The Development and Characterization of Ni-Cu/Al_2O_3 Catalyst for Hydrogen Production via Multi-Fuel Reforming

By

Marcin Khzouz

A thesis submitted to
The University of Birmingham
for the degree of
DOCTOR OF PHILOSOPHY

School of Chemical Engineering
College of Engineering and Physical Sciences
The University of Birmingham
May 2014

Abstract

Developing a catalyst that accepts a wide range of fuels for hydrogen production is an important design aspect for the successful multi-fuel reformer. This thesis aims to synthesize and evaluate Ni-Cu/Al_2O_3 catalysts for methanol and methane steam reforming. Detailed characterizations of catalysts, as well as the role of the bimetallic nature of Ni-Cu metals on the catalytic reaction are presented and discussed.

A series of Ni_x-Cu_y/Al_2O_3 catalysts with various metals loadings (x= 10, 7, 5, 3 and 0% weight and y= 0, 3, 5, 7 and 10%, respectively) were prepared. The temperature programed reduction revealed that bimetallic catalysts displayed a new hydrogen uptake peak compared with monometallic metal catalyst and this was attributed to NiCuO reduction. The X-ray diffraction patterns indicated $Ni_xCu_{1-x}O$ phase formation.

The methanol steam reforming was evaluated over the prepared catalysts over the range of temperatures 225-325°C in a fixed bed reactor. It was found that bimetallic Ni-Cu had a strong influence on the amount of CO_2 and CO by controlling the water gas shift reaction and decomposition reaction. The highest amount of hydrogen produced among the other prepared catalysts was 2.2 mol/mol-CH_3OH for 5%Cu-5%Ni at 325°C.

Low temperature methane steam reforming at 500-700°C was investigated. The synergetic effect between Cu and Ni metals was also investigated, showing that Cu provides a stabilizing effect by forming Ni-Cu alloy and controlling the catalyst structure. The 7%Ni-3%Cu revealed the highest conversion of 71.1% methane and produced the maximum amount of hydrogen at 2.4 mol/mol-CH_4 among the other prepared catalysts at 600°C and S/C of 3. The bimetallic reacted Ni-Cu catalysts revealed less carbon selectivity (0.9% for 5%Ni-5%Cu) compared to 10%Ni (4.6%) catalyst at 600°C.

Dedication

To my family,

And

To the ones I love

Acknowledgements

First and foremost, I would like to express my deepest gratitude to my supervisor Prof. Joe Wood for his encouragement and valuable advice throughout my research. I would also like to thank Dr. Waldemar Bujalski (late) for his positive support and finding a financial assistance throughout the course of my studies. I would like to thank Dr. Andrew Rollinson for assistance with calculation and Dr. Shangfeng Du for his great help during writing the thesis. Also, thanks to all my friends and colleagues for their assistance. Above all, I am grateful to my parents and all my family for their support, love and sacrifices throughout my studies.

Marcin Khzouz

Contents

LIST OF FIGURES

LIST OF TABLES

NOMENCLATURE

a.u.	Arbitrary unit
APS	Active particle size
BDDT	Brunauer, Deming, Deming and Teller
BET	Brunauer Emmett Teller
C	A constant for a particular system
D_{calc}	Calculated metal density, g/cm^3
DTG	Derivative thermo gravimetric, %/min
DTGS	Deuterated triglycine sulfate
E_a	Activation energy, J/mol
EDS	Energy dispersive X-ray spectroscopy
ER	Elementary reaction
FID	Flame ionization detector
GC	Gas chromatograph
GHSV	Gas hourly space velocity, min^{-1}
GMW_{calc}	Gram molecular weight, g/g-mole
IR	Infrared
IUPAC	International union of pure and applied chemistry
K	constant
K_{WGS}	Water gas shift reaction equilibrium constant
L	crystallite size, nm
LHSV	Liquid hourly space velocity, min^{-1}
m_i	Mass fraction of species i, g
MW_i	Molecular weight of species i, g/mol

n_p	Molar sum of the product, mol
P	Pressure, mmHg
P/P_0	Relative pressure
P_0	Saturated vapour pressure of gas, mmHg
PD	Percent dispersion, %
PEMFC	Polymer electrolyte membrane fuel cell
R	Universal gas constant , J mol^{-1} K^{-1}
RDS	Rate determining step
RGA	Refinery gas analyzer
S	Surface of the catalyst
S/C	Steam to carbon ratio
SA_{calc}	Calculated specific surface area
$SA_{Metallic}$	Metallic surface area, m^2/g of metal
SEM	Scanning electron microscope
SF_{calc}	Calculated stoichiometry factor
SOFC	Solid oxide fuel cell
SW	Sample weight, g
T	Temperature , K
TCD	Thermal conductivity detector
TG	Thermo gravimetric, %
TGA	Thermo gravimetric analyses
TPR	Temperature programmed reduction
V	Volume of gas adsorbed at pressure P , cm^3
V_m	Volume of gas for monolayer formation , cm^3
V_S	Volume sorbed , cm^3

W_s	Sample weight, g
X_{con}	Conversion, %
XRD	X-ray diffraction
XRF	X-ray fluorescence
y_i	Mole fraction of species i
β	Peak width
$\Delta H°$	Change in enthalpy, kJ
Δm	Percentage mass change, %
λ	X-ray wavelength, nm
σ	Variation for produced gas, %
$\%V_i$	Percentage volume of species i, %
ΔG	Change in Gibbs free energy, kJ
ΔG_{WGS}	Change in Gibbs free energy for water gas shift reaction, kJ
μ	Mean value for produced gas, %

CHAPTER 1

INTRODUCTION

In the last decades, the economic and social implications of the inevitable approach towards peak oil production has led to increased interest in alternative energy sources and the possibility to employ hydrogen as an energy carrier [1]. Hydrogen can be produced from natural gas, coal, biomass and water. It can be used either in internal combustion engines or in fuel cells to produce electricity [2]. Providing the hydrogen is obtained from a renewable source, its utilization with fuel cell technology could potentially resolve the current problem of dependency on fossil fuels, and concerns related to greenhouse gas emissions and global warming [3]. This chapter introduces fuel cell technology and hydrogen as energy source/carrier. Then, steam reformers for hydrogen generation are described. Finally, the scope of the thesis and motivation are stated.

1.1 Fuel cells

Fuel cells generate electricity via electrochemical reactions. Figure 1.1 shows that the fuel cell consists of an anode, cathode and electrolyte. A chemical reaction takes place in an electrochemical cell which provides a special separation of reduction and oxidation reactions [4]. The oxidation reactions take place at the anode side and the reduction reactions take place at the cathode. Those reactions happen when hydrogen fuel is supplied to the anode side while oxygen is delivered through cathode side. An electrical current is generated due to the electron movements from the anode through an external circuit to the cathode [5]. Different types of fuel cells may be selected depending upon their applications, with fuel type used to produce hydrogen and the operating temperature of the fuel cell being key considerations [6].

The most popular fuel cells are Solid Oxide Fuel Cell (SOFC) [7] and Polymer Electrolyte Membrane Fuel Cell (PEMFC) [8] as presented below.

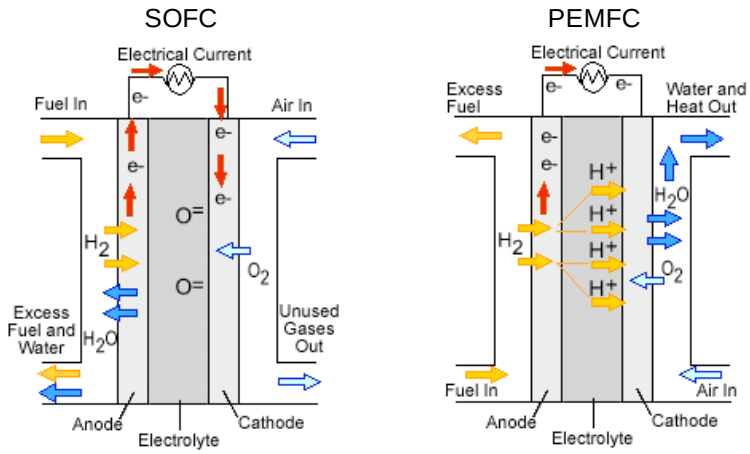

Figure 1.1. Schematic diagrams for fuel cells [9].

1.1.1 Solid oxide fuel cell

Solid oxide fuel cells (Figure 1.1) are designed to operate at high temperatures usually between 700-1000°C [10]. The overall electrochemical reaction which occurs on cathode and anode sides is provided in Eq. 1.3 [11]. SOFCs are classified into tubular and planar SOFCs based on the shape of the ceramic electrolyte employed in the fuel cell. The main advantage of the high operating temperature of SOFCs is the possibility to perform both internal and external reforming of any type of fuel such as; natural gas and hydrocarbons to generate hydrogen [7, 12]. The fuel for SOFCs can be a mixture of H_2, CO and CH_4 to generate electricity. Furthermore SOFCs are not poisoned by carbon monoxide and are very tolerant to syngas, comprised of hydrogen and carbon monoxide. The main applications of SOFC are stationary power generation and auxiliary power units with efficiency around 50% [13]. Figure 1.2 explains the application of SOFC and power range.

Cathode side: $O_2 + 4e^- \rightarrow 2O^{2-}$ (Eq. 1.1)

Anode side: $2H_2 + 2O^{2-} \rightarrow 2H_2O + 4e^-$ (Eq. 1.2)

Overall reaction: $2H_2 + O_2 \rightarrow 2H_2O$ (Eq. 1.3)

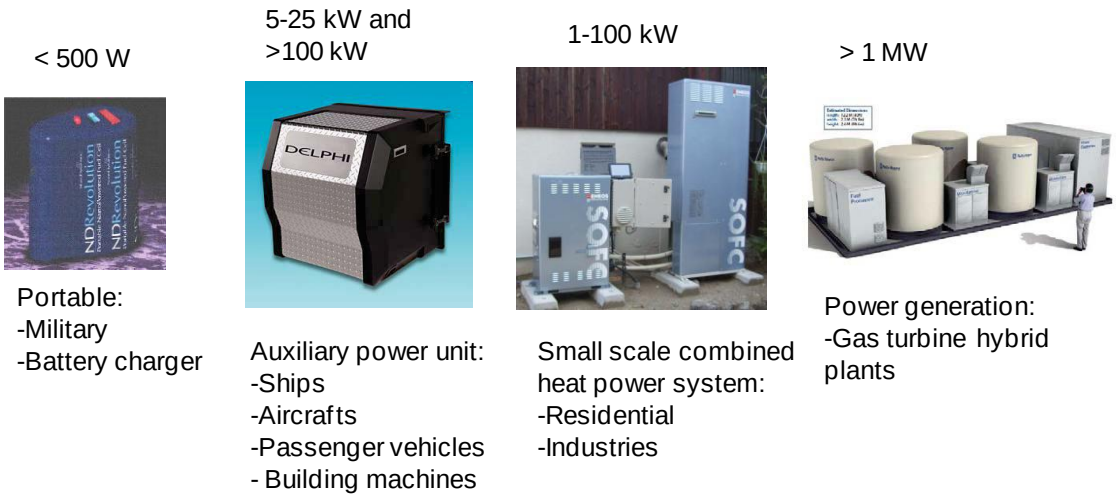

Figure 1.2. Applications of SOFCs [11].

1.1.2 Polymer electrolyte membrane fuel cell

The PEMFC consists of a polymer conductive membrane as electrolyte that allows protons to cross from the anodic side to the cathodic side as shown in Figure 1.1 [7]. The overall electrochemical reaction on anode and cathode sides is given in Eq. 1.6 [11]. This type of fuel cell is sometimes called Proton Exchange Membrane Fuel Cell (PEMFC). PEMFCs can be classified into two types; low temperature operation which operates at a temperature lower than 90°C and high temperature operation for temperatures up to 180°C [5]. The PEMFC has the advantage of a faster start up than SOFC [10]. However, the PEMFC requires high purity hydrogen as fuel since it is susceptible to CO poisoning [5]. The anode of the PEMFC catalyst is made from platinum, which may become deactivated by the adsorption of impurities such as CO, causing a decrease in the catalytic activity. The recommended CO concentration limit

is 10 ppm for low temperature PEMFC [5] and it is significantly higher (3%) for high temperature PEMFC (160°C) [14, 15]. The main applications (Figure 1.3) for PEMFC are; portable power generation , stationary applications with reformer for on-site power generation and fuel cell vehicles with calculated efficiency of 35-60% [8, 10].

Cathode side: $O_2 + 4H^+ + 4e^- \rightarrow 2H_2O$ (Eq. 1.4)

Anode side: $2H_2 \rightarrow 4H^+ + 4e^-$ (Eq. 1.5)

Overall reaction: $2H_2 + O_2 \rightarrow 2H_2O$ (Eq. 1.6)

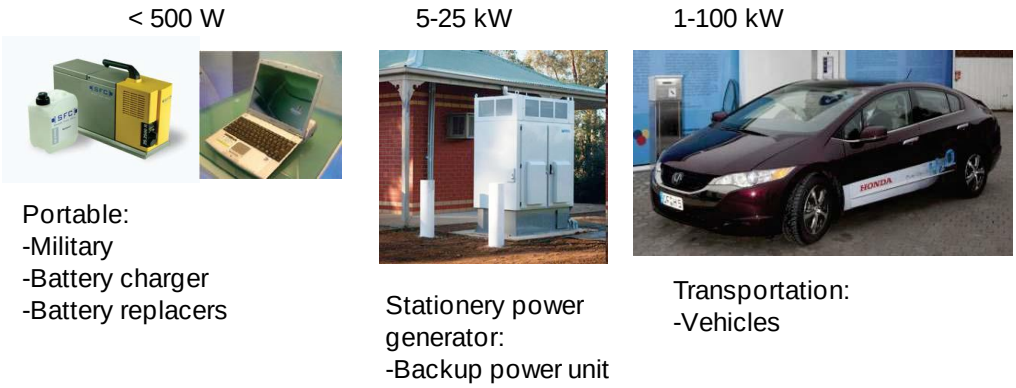

Figure 1.3. Applications of PEMFCs [4, 11].

1.2 Hydrogen as an energy vector

Hydrogen is an intermediate fuel, which must be generated from some other source and then burnt or converted to electrical energy and thus is known as an 'energy carrier' [3] rather than an energy source. Hydrogen can be produced from a wide range of energy sources such as natural gas, gasoline, coal, methanol, ethanol, biomass and water [16]. Hydrogen can be extracted from its energy source by several methods such as thermo-chemical, biological and electro-chemical techniques, as shown in Figure 1.4 [3, 17, 18].

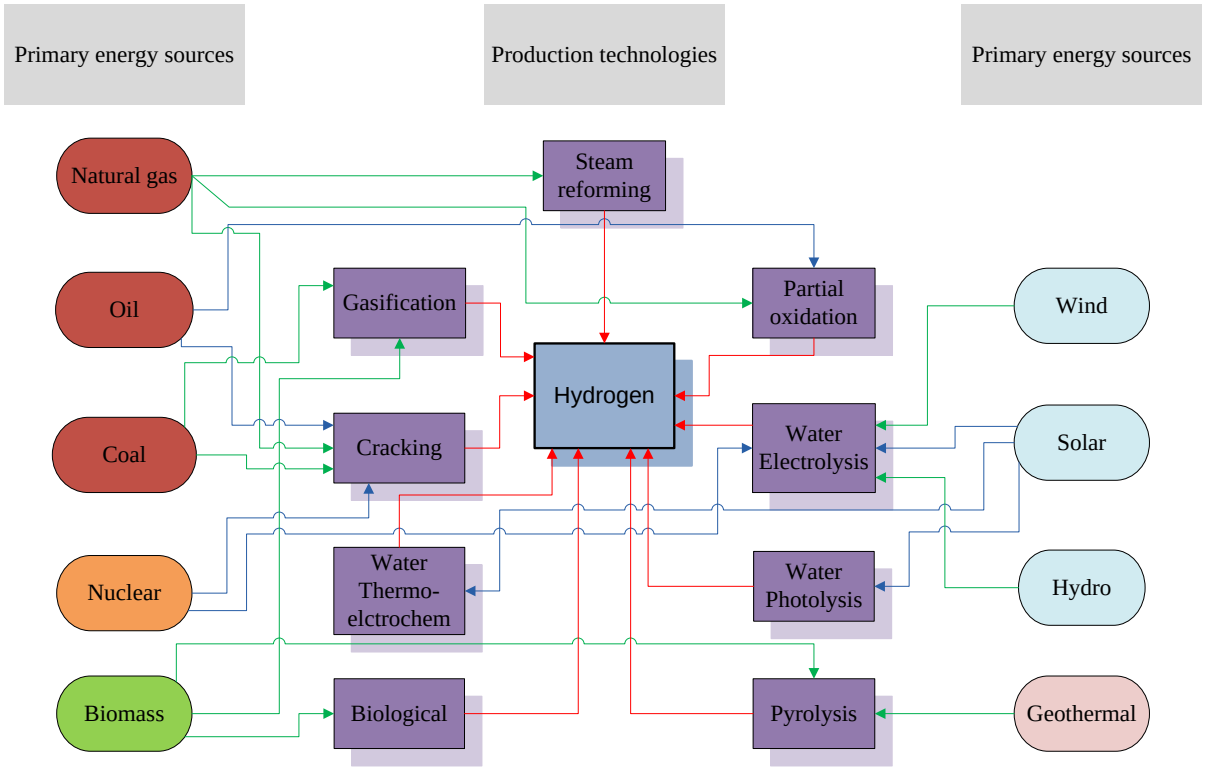

Figure 1.4. Hydrogen primary energy sources and extraction technologies [18] .

The total annual world production of hydrogen is around 368 trillion cubic meters [16]. 48 % of the global demand for hydrogen was produced from natural gas, about 30 % from oil, 18 % from coal and 4 % from water electrolysis [18] as shown in Figure 1.5. Of this amount, about 49% is used in ammonia production, 37% in petroleum refining, 8% in methanol production and the other 6% in a miscellaneous smaller-volume uses [18]. About 96% of hydrogen is produced from fossil fuels via a thermo-chemical process that converts hydrocarbons into a syngas [17] as shown in Figure 1.5 [18, 19]. Large-scale hydrogen production from natural gas is currently the lowest cost method for hydrogen production [16, 18]. Small-scale production for vehicle refuelling stations and stationary fuel cells in buildings are being developed. Hydrogen can also be extracted from water via electrolysis; however, it is a very expensive process [16]. Water electrolysis represents 3.9% of the primary energy sources for hydrogen production [18, 19].

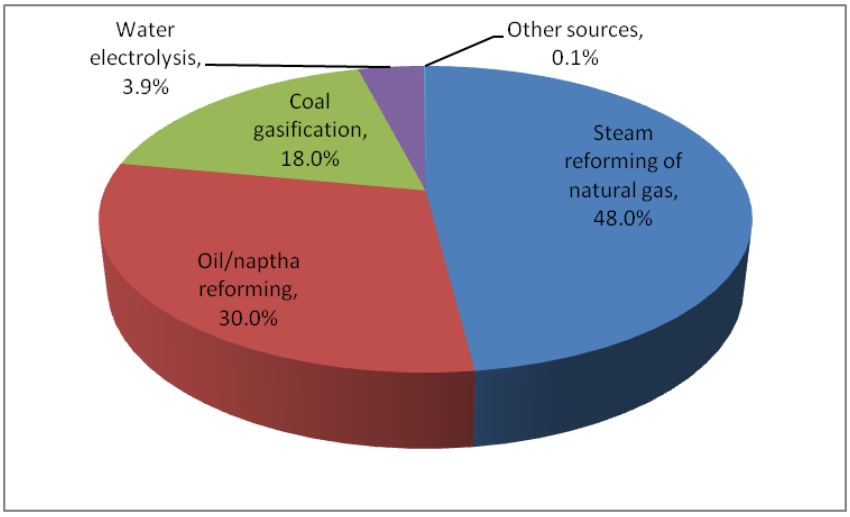

Figure 1.5. Global hydrogen productions from primary energy sources [19].

Methane steam reforming is considered a widely available method to produce hydrogen at large-scale due to a well-developed methane infrastructure and the favourably high hydrogen to carbon ratio of methane [20]. Methane can be converted to hydrogen and carbon monoxide at high temperatures (>800°C) [20, 21]. On the other hand, methanol as an alternative fuel is reformed at much lower temperatures in the range 200-300°C [22, 23].

The methanol is also known ‘‘wood fuel’’ and was widely used as the motor fuel in Germany during the World War II [24] . The first commercial methanol process, based on the destructive distillation of wood, dates back to 1830 [25]. After the 1920s modern technologies were developed to produce commercial methanol from different sources such as natural gas, coal and petroleum [24, 25]. The total world demand for methanol (2010) was 41 million metric tons [25]. While not currently economically viable, methanol is also produced from bio-based resources as landfill gas, pig manure, sugar beets, driftwood, rice straw, and paper mill black liquor [9]. Although methanol is presently obtained commercially from hydrocarbon fossil fuels, biomass is identified as a viable alternative route [24, 26, 27]. Methanol is made from

synthesis gas which is a mixture of CO, CO_2 and H_2 according to Eq. 1.7-1.8. A detailed literature survey of the production of hydrogen from methanol and methane is presented in Chapter 2.

$CO + 2H_2 \rightleftharpoons CH_3OH$, $\Delta H°_{298} = -90.7$ kJ/mol (Eq. 1.7)

$CO_2 + 3H2 \rightleftharpoons CH_3OH + H_2O$, $\Delta H°_{298} = -49.5$ kJ/mol (Eq. 1.8)

The problem with hydrogen production is the storage of the produced gas [3] . Unlike liquid fuels that can be easily stored, the very low density and flammability of hydrogen made its storage expensive or impractical. Hydrogen can be either stored in the gaseous, liquid or solid forms [28]. In the gaseous form, hydrogen is compressed in a huge specially engineered tank at 350 or 700 bar pressure. This consumes a lot of storage energy which was calculated as up to 20% of the internal energy available from the stored hydrogen [28]. In the liquid phase, hydrogen can be stored in smaller tanks compared to the gas phase. This requires cooling down hydrogen to cryogenic temperatures (-243°C), thus again requires a high amount of energy estimated as about 30% of the hydrogen energy content [28]. Solid materials are also used for hydrogen storage. Hydrogen is stored in metals hydrides via combination with the metal by an exothermic reaction and the release of hydrogen for use occurs by an endothermic reaction that requires heat [28, 29]. Metal hydride storage is compact compared with compressed hydrogen tanks but heavier. Hydrogen represents 1-2% of the total weight [30, 31]. It can be concluded that each method of hydrogen storage has disadvantages concerning energy losses, high cost and safety issues. For this reason, hydrogen could be produced on-board vehicles and devices using reforming technology and provide a solution for the hydrogen storage problem as discussed below.

Hydrogen can be produced on-board from its energy carrier based on the reforming of hydrocarbons and alcohols using fuel processors [32]. This could potentially solve hydrogen storage and transportation difficulties concerning small-scale applications [33, 34]. Methane, methanol, ethanol and dimethyl ether are considered hydrogen carriers for on-board reforming [20, 21, 25, 35-39]. The reforming temperature is an important factor in the design of a fuel processor, whether it can be used either in transportation, stationary applications or both [34]. Methane is reformed above 800°C [40]. Ethanol reacts at a temperature around 500°C [20] and dimethyl ether in the range of 300-450°C [41]. Methanol represents the lowest reforming temperature range at 200-300°C [23]. Low temperature methane steam reforming is also possible at temperature above 500°C [42]; however, low temperature catalysts should be developed [21] which are active in this temperature range. Methanol and methane steam reforming for fuel processor development for PEMFC and SOFC applications has been studied as addressed in Section 1.3.

1.3 Steam reformer applications

A methanol steam reformer prototype for vehicle applications has been developed since 1997 [29]. An on-board methanol reformer was coupled with a PEMFC to power fuel cell vehicles Necar 3 and Necar 5 developed by DaimlerChrysler [29]. A compact reformer system was a target for the manufacturer. Casio developed a small scale reformer for portable devices [40], for example the methanol micro-reformer and PEMFC system powered Casio laptop. A methanol reformer was also used in military portable applications to provide continuous power for a long period (72 hours) [24, 41, 42]. In 2010, a prototype of 5kW hydrogen reformer coupled with PEMFC was developed by Element One [43]. Currently researchers are developing multi-

flexible power PEMFC systems that can be fuelled by a wide range of fuels such as methane, diesel, dimethyl ether, ethanol and methanol [44-46].

Methane steam reformers for hydrogen production have been developed for fuel cell applications in stationary applications [21]. The small-scale reformers at refuelling stations are an option for supplying hydrogen to vehicles [47]. Methane steam reformers are being developed for combined heat and power system units coupled with SOFCs for stationary applications and providing heat and power for residential use [48]. The fuel cell technology requires compact and low cost reformers [49]. For this reason, a number of industries have investigated compact steam methane reformers such as Ballard power systems and Sanyo electric, which built residential PEMFCs powered by hydrogen generated from steam methane reforming [50, 51]. The power generated by the stand-alone steam methane reformers are in the range of 0.4-3 kW with efficiency of 70-80% [21]. The compact reformers should operate at low temperature (<700°C) and low-pressure (<3 bar). Thus, the currently existing large-size reformer technology with high temperature and high-pressure operation is not suitable for small-size reformers for fuel cell applications [51].

1.4 Motivation

Bimetallic catalysts can improve the catalytic properties of the single metal or develop new properties for application in steam reforming reactions. Different metal compositions could be used to synergistic effect of catalytic performance by engineering the desired bimetallic particle size and its surface composition. Both methanol and methane steam reforming reactions are investigated on Ni-Cu bimetallic catalysts to understand the resulting reactivity and product distribution.

The objective of this research is to state the effect of adding Ni to Cu on the catalyst properties, catalyst activity and catalyst selectivity for methanol steam reforming reaction and to understand the effect of adding Cu to Ni on catalyst performance for low temperature methane steam reforming reaction. This has been achieved by preparing, characterizing and testing Ni-Cu catalyst systems with various metal loadings supported on Al_2O_3. The objective of the work was to design an active, selective and stable catalyst that could be applied for developing a multi-fuel reformer for hydrogen generation from methanol and methane fuels.

The Ni-Cu catalyst system could potentially achieve high selectivity for H_2 production at low operation temperatures for both methanol (225-325°C) and methane (500-700°C) steam reforming reactions. Methanol steam reforming reaction over Ni-Cu catalyst system could be used to reduce the amount of CO produced due to an increase of the catalyst selectivity for CO_2 by balancing the amount of CO/CO_2 ratios of water gas shift reaction. On other hand, The Ni-Cu catalyst system could reduce the amount of coke formed during methane steam reforming reaction and increase the selectivity for H_2 and CO_2 at low reforming temperatures.

1.5 Scope of the thesis

The pace of development of on-board hydrogen production for stationary and portable fuel cell applications as well as fuel cell vehicles has been recently increased [21, 25, 32, 43-52]. The technology to produce hydrogen on-board from its energy carrier could potentially solve the problem of storing and distribution of gaseous hydrogen. Therefore, the requirements for a reformer that accepts a wide range of fuel to generate hydrogen and using a common catalyst are still under development [32, 38, 53-56]. Methanol and methane fuels are promising primary

hydrogen energy sources for both PEMFC and SOFC applications. Thus the development of compact, fast start-up, highly efficient and low cost fuel reformers are challenges that could partly be solved by catalyst development. Accordingly, this thesis aims to investigate in-house synthesized Ni_x-Cu_y/Al_2O_3 catalyst for hydrogen production from methanol and methane steam reforming.

This work is presented in eight chapters. In Chapter 1, the introduction of fuel cells is discussed and a general overview of hydrogen production from its primary energy sources is explained. Steam reformer applications and the research motivation are also addressed. In Chapter 2, a literature review of methanol and methane steam reforming catalysts is presented. Materials and experimental methods to synthesise and characterize Ni_x-Cu_y/Al_2O_3 catalyst are explained in Chapter 3. The reactions equilibrium investigations of methane and methanol steam reforming are described in Chapter 4. In Chapter 5, the characterization results of prepared catalyst are presented. The reaction of methanol steam reforming over the prepared catalyst and spent methanol steam reforming catalyst characterization are described in Chapter 6. In Chapter 7, the investigations of methane steam reforming and methane spent catalyst characterization are reported. Finally, the conclusions along with future work are presented in Chapter 8.

1.6 Publications

Publications resulting from work in this thesis are listed below:

1.6.1. Journals

1. Khzouz, M., J. Wood, K. Kendal and W. Bujalski, *Characterization of Ni–Cu-based catalysts for multi-fuel steam reformer.* International Journal of Low-Carbon Technologies, 2012. **7**(1): p. 55-59.

2. Khzouz, M., J. Wood, B. Pollet and W. Bujalski , *Characterization and activity test of commercial Ni/Al_2O_3, Cu/ZnO/Al_2O_3 and prepared Ni–Cu/Al_2O_3 catalysts for hydrogen production from methane and methanol fuels.* International Journal of Hydrogen Energy, 2013. **38**(3): p. 1664-1675.

1.6.2. Conference presentations

1. Khzouz, M., J. Wood and W. Bujalski., *Multi-fuel steam reformer for hydrogen production from methane and methanol fuels.* European PEFC and H_2 Forum 2013, Lucerne, Switzerland. Poster presentation.

2. Khzouz, M., J. Wood and W. Bujalski., *Multi-fuel steam reformer for hydrogen production from methane and methanol fuels.* 8th Annual International Hydrogen and Fuel Cells Conference, Birmingham, UK, March 2012. Poster presentation.

3. Khzouz, M., J. Wood and W. Bujalski., *Multi-fuel steam reformer for hydrogen production from methane and methanol fuels.* Hydrogen and Fuel Cells Conference 2011, Xcaret, Mexico, December 2011. Oral and poster presentations.

4. Khzouz, M., J. Wood and W. Bujalski., *Multi-fuel steam reformer for hydrogen production from methane and methanol fuels.* MEGS II Annual Conference, Nottingham, UK, September 2011. Poster presentation.

5. Khzouz, M., J. Wood and W. Bujalski., *Multi-fuel steam reformer for hydrogen production from methane and methanol fuels.* 7th Annual International Hydrogen and Fuel Cells Conference, Birmingham, UK, March 2011. Poster presentation.

CHAPTER 2

LITERATURE REVIEW

This chapter reviews the literature for methanol and methane steam reforming in terms of the catalyst used, the reaction mechanism, modes of catalyst deactivation, as well the concept of multi-fuel reforming and catalyst preparation methods. Section 2.1 explains the steam reforming process in general and type of fuel reforming. Sections 2.2-2.4 introduce methanol steam reforming catalyst including the promoters and supports used in the catalyst, then the methanol steam reforming mechanism and methanol catalyst deactivation are discussed. Sections 2.5-2.7 describes the methane reforming catalyst as well as promoters and supports used in such catalysts, then methane steam reforming catalyst deactivation and reaction mechanism are explained. The multi-fuel processor concept and the progress of multi-fuel reforming are explained in Section 2.8. Finally, the catalyst preparation methods and catalyst testing techniques are explained in Section 2.9.

2.1 Steam reforming process

Hydrocarbon feedstocks can be converted to a hydrogen rich gas by a controlled steam reforming reaction, which requires heat and water to produce syngas (H_2 and CO). The steam reforming process was developed in 1926 to produce hydrogen and CO [25, 57] and became most popular for hydrogen production from methane and methanol for fuel cell applications [58]. The process is endothermic, which requires an external source of heat to maintain the reaction. Therefore, owing to the time required for heating to the reaction temperature, the slow dynamic response and slow start up time are drawbacks of steam reforming process when it is used for the fuel reformer [59]. While steam reforming is the most popular method for hydrogen

production, partial oxidation and auto-thermal reforming are two other attractive methods for hydrogen production [20, 25, 32, 34, 60].

Table 2.1. Comparison of various reforming methods [20, 25, 32, 34, 60, 61].

	Steam reforming (SR)	**Partial oxidation (PO)**	**Auto-thermal reforming (ATR)**
Chemical reaction	$C_nH_mO_z+(n-z)H_2O \rightarrow nCO+\left(n+\frac{m}{2}-z\right)H_2$	$C_nH_mO_z+\frac{1}{2}(n-z)O_2 \rightarrow nCO+\frac{m}{2}H_2$	$C_nH_mO_z+yO_2+2\left(n-y-\frac{z}{2}\right)H_2O \rightarrow nCO_2+2\left(n-y-\frac{z}{2}+\frac{m}{4}\right)H_2$
Steam availability	Steam is part of process	Partially burns a fuel , no steam is required	Both steam and air are required
Maximum H_2 yield (mol H_2 per mol $C_nH_mO_z$)	$2n+0.5m-z$, combined steam reforming and water gas shift reaction	$n+0.5m$, combined partial oxidation and water gas shift reaction	$2n-2y-z+0.5m$, auto-thermal reforming as shown in equation above
Maximum percent purity of H_2 in the products mix (vol%)	$100\times\left(\frac{2n+0.5m-z}{3n+0.5m-z}\right)$ combined steam reforming and water gas shift reaction	$100\times\left(\frac{n+0.5m}{2n+0.5m}\right)$ combined partial oxidation and water gas shift reaction	$100\times\left(\frac{2n-2y-z+0.5m}{3n-2y-z+0.5m}\right)$ auto-thermal reforming as shown in equation above
Heat requirments	Largely endothermic , consume a lot of heat, disadvantage	Exothermic, produce heat, advantage	Must be controlled under slightly exothermic reaction, start-up requires heat , advantage
Start-up period for reformer application	Long start-up period, since steam is required, disadvantage	Short start-up period, since no steam is required, advantage	Short start-up period, steady state conditions must be controlled, advantage

2.1.1 Methane and methanol fuels

Currently methane and methanol are being used as sources of fuel to produce hydrogen in small-scale fuel reformers [62]. Methane is a widely available fuel and is a major source of hydrogen worldwide due to the higher production cost of hydrogen. The well-developed natural gas infrastructure makes methane the best choice for hydrogen production for fuel cell stationary applications.

Methanol, also known as wood alcohol, can be produced mainly from coal and natural gas [25, 63]. The total world demand for methanol was estimated to be about

41 million metric tons [25]. Although methanol is toxic and until now doesn't have a well-established infrastructure compared to the other fuels, the below mentioned advantages make methanol an appropriate fuel for hydrogen production [25].

Methanol became very attractive as liquid fuel for low temperature fuel cell applications due to the following reasons [64]; methanol has high hydrogen to carbon ratio, it is liquid at ambient conditions and so is a dense and transportable hydrogen energy carrier, it is miscible with water so can be premixed with water in the same fuel tank, is free of sulphur and biodegradable. The conversion of methanol to the hydrogen takes place over a lower range of temperatures 200-350°C compared to other liquid fuels which are only converted at temperatures above 500 °C, which is due to the absence of C-C bonds in methanol. A further advantage for fuel cell applications is that methanol reformers produce relatively low levels of CO at low reforming temperature with selective catalysts (as explained in Chapter 4) so secondary conversion such as water gas shift reaction is unnecessary. Because of methanol's low energy chemical bonds, reforming of methanol ensures faster start-up, lower fuel processor cost as well as methanol being one of the only chemicals that can be converted directly to electricity in a direct methanol fuel cell. Of course, there are also some disadvantages; methanol is toxic, being ingestion or inhalation the main concern, and the hydrogen yield is relatively low (18.75 wt.% of steam reformed methanol) compared with other fuels (50 wt.% of steam reformed methane) [64]. The oxygen content of methanol fuel causes a hydrogen yield penalty for steam reforming ($2n + 0.5m - z$) [61]. In addition, methanol is presently obtained commercially from hydrocarbon fossil fuels which has high carbon emissions footprint from manufacturing. Table 2.2 explains the major differences of using methane and methanol fuels in a steam reformer.

Table 2.2. Methane and methanol fuels comparison for fuel reformer application.

Feature	Methane	Methanol
H_2 produced	High	Low
Temperature	Up to 800 °C	Up to 350 °C
CO produced	High	Low
Maximum percent purity of H_2 in the products mix (vol%)	80%	75%
Maximum H_2 yield	4 mol/mol of CH_4 (or 50 wt% of CH4)	3 mol/mol of CH_3OH (or 18.75 wt% of CH_3OH)
Catalyst composition	Nickel based	Copper based
Selectivity	Hydrogen and CO	Hydrogen and CO_2
Purity of fuel used	Not available for commercial	Available for commercial
Phase	Gas	Liquid
Size	Large (three purification units and gas cleaning unit)	Small (one purification unit)
Material	Incoloy	SS 316 L
Weight	High	Low
Volume	Large	Small

2.1.2 Steam reforming catalyst

A basic definition of a catalyst is a substance that affects the rate of the reaction without itself becoming permanently involved in the reaction [65]. This simplified scenario suggests that the catalyst emerges from the process unchanged [66], although in practice a catalyst may undergo changes such as oxidation state and becoming deposited with coke.

The function of the catalyst is to accelerate a chemical reaction by forming bonds with the reactants and allowing these reactants to form a product. The product must detach from the catalyst so that the active site can be used in the next reaction cycle [57, 65-67]. Figure 2.1 shows the potential energy of both catalysed and non-catalysed reaction paths. It is clear that the non-catalysed reaction has to overcome the large energy barrier to produce a product. In contrast, the catalysed reaction has a lower energy barrier due to the adsorption process or spontaneous process which

lowers the free energy of the reactants. The most important aspect is that the overall changes in the free energy are the same for both reaction pathways. This means that the catalyst changes the kinetics of the reaction only and has no effect on the thermodynamics of the reaction.

Mainly, the catalyst used for steam reforming is a heterogeneous catalyst at which the reactants and the catalysts exist in different phases [65]. The catalyst consists of either a single substance or more than one component distinguished as; active metal component, a support and promoters. Table 2.3 classifies the catalyst used in steam reforming as; oxide catalysts, the noble metal catalysts and the base metal catalysts [60].

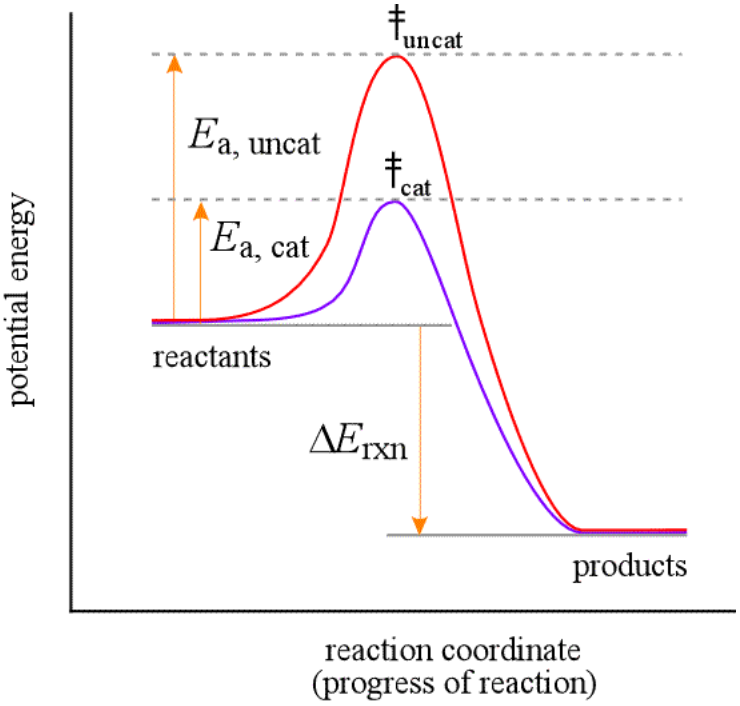

Figure 2.1. Role of catalyst and potential energy diagram [68].

Table 2.3. Main advantages and disadvantages of catalysts used for fuel processors [60].

Category	Example	Properties
Oxide catalysts	MgO, Al_2O_3, V_2O_5, ZnO, TiO_2, La_2O_3, CeO_2, La_2O_3–Al_2O_3, CeO_2–Al_2O_3, MgO–Al_2O_3	Normally good activity but low selectivity.
Noble metal catalysts	Rh, Ru, Pt and Pd	Active, high selectivity but the cost is high.
Base metal catalysts	Co-based (Co/ZnO), Cu-based (Cu/Al_2O_3), Ni-based (Ni/Al_2O_3)	- Co-based: good catalytic performance, but rapidly deactivate. - Cu-based: good activity at low reaction temperature, while H_2 selectivity is poor. - Ni-based: high conversion and the H_2 selectivity, but coke deposition and a severe deactivation may occur.

2.2 Methanol steam reforming

The steam reforming of methanol (Eq. 2.1) ideally produces dry gases consisting of 75 vol% of hydrogen and 25 vol% carbon dioxide with complete stoichiometric conversion. However, this is not usually the case in a real reaction since the reformate gases usually also contain unconverted reactants and by product, for example CO, CO_2, H_2, H_2O, CH_3OH [69]. The process is carried out at a temperature in the range of 200-300°C [32] and usually employs copper based catalysts such as commercial $Cu/ZnO/Al_2O_3$ catalysts [32]. The methanol steam reforming process (Eq. 2.1) [70-74] is represented by summation of decomposition reaction of methanol (Eq. 2.2) and water gas shift reaction (Eq. 2.3) [71, 75, 76].

$$CH_3OH + H_2O \rightleftharpoons CO_2 + 3H_2 \quad , \Delta H°_{298} = +49.5 \text{ kJ/mol} \qquad \text{(Eq. 2.1)}$$

$$CH_3OH \rightleftharpoons CO + 2H_2 \quad , \Delta H°_{298} = +90.2 \text{ kJ/mol} \qquad \text{(Eq. 2.2)}$$

$CO + H_2O \rightleftharpoons CO_2 + H_2$, $\Delta H°_{298} = -41$ kJ/mol (Eq. 2.3)

According to the stoichiometry of the reactions, complete steam reforming of methanol notwithstanding equilibrium limitations is predicted using highly active and selective copper-based catalyst to produce hydrogen and carbon dioxide at a reforming temperature of (200-300°C) and at atmospheric pressure [71, 75, 76]. The equilibrium analyses of reformate produced for methanol steam reforming reaction are simulated and discussed in detail in Chapter 4.

Methanol conversion to hydrogen rich gas by catalytic steam reforming for fuel cell applications interested the US army in 1975, although the idea was originally developed in 1963 [58]. After that, the activity of various commercial catalysts for steam reforming was investigated and it was found that low temperature water gas shift catalyst $CuO/ZnO/Al_2O_3$ is most active [58, 77]. Several studies of the kinetics and thermodynamics of methanol steam reforming were carried out, such as studies by Amphlett et al. [78, 79] to explain the thermodynamic aspects of catalytic steam reforming. Kinetic analysis of methanol steam reforming process by Peppley et al. [70] gave the basic theoretical foundation for methanol steam reforming studies. After that, studies of methanol reforming reactions and catalyst were carried out to investigate hydrogen production from methanol for fuel cell application, as explained in detail below.

2.2.1 Methanol steam reforming catalyst

The process of catalyst development for methanol steam reforming was an extension of studies into the catalyst used for the methanol synthesis process [80]. The most popular catalyst is $CuO/ZnO/Al_2O_3$ which was developed by BASF [57]. Catalysts operated for the methanol reforming process can be classified in the literature as

commercial and non-commercial catalysts, although details of the commercial catalysts may be scarce due to reasons of intellectual property. Commercial catalysts are those manufactured for hydrogen production such as BASF S3-85, Cu-0203-T and G-66 MR which are used as a reference for comparison with other non-commercial catalysts [81, 82]. Commercial catalysts may be classified as copper containing and non-copper containing (Group VIIIB metals) with various promoters and various preparation methods [25].

The objectives for developing an active methanol catalyst in the literature were to increase the amount of hydrogen and suppress CO produced during the reforming process. Several proposed solutions for reaction conditions and mechanisms for improving the performance of the overall process will be discussed in the following sections.

2.2.2 Active metals for methanol reforming catalyst

Methanol steam reforming is carried out over two types of catalysts, the copper-based catalyst and the VIIIB group metals catalysts such as Pd, Pt and Ni. Each type of catalyst has its unique properties to perform the reaction which will be discussed in the upcoming sections.

2.2.2.1 Copper based active metals

Methanol steam reforming over copper based catalyst has been studied as an extension to the use of copper catalyst in the methanol synthesis reaction (Eq. 1.7-1.8) [83]. The most widely used copper based catalyst is the commercial $Cu/ZnO/Al_2O_3$ catalyst. It is clear from the literature that the active component of the catalyst is the copper. A catalyst with the highest copper loading gives a high conversion of the methanol and the high selectivity for hydrogen production [84]. The

$Cu/ZnO/Al_2O_3$ catalyst has well dispersed copper crystallites over the catalyst support which gives high accessible metal surface area and thus good catalyst formulation [85]. The role of the promoter such as ZnO is to improve the dispersion of the Cu and the reducibility of the CuO [23, 86]. Furthermore the promoter such ZnO provides a structural support for the Cu based catalyst [80]. The role of the support Al_2O_3 in the $Cu/ZnO/Al_2O_3$ catalyst is to provide high surface area and increases the copper dispersion in the catalyst [87-89]. In addition, the Al_2O_3 support improves the mechanical strength of the catalyst and prevents the catalyst from sintering [88, 89].

Although the $Cu/ZnO/Al_2O_3$ catalyst is well-discussed in the literature and gives satisfactory results for methanol conversion and the hydrogen production, the $Cu/ZnO/Al_2O_3$ catalyst suffers from sintering and deactivation during prolonged operation, which reduces the efficiency of the methanol steam reforming [80]. Also, achieving high dispersion of Cu metals during catalyst preparation is a difficult process [90]. Thus several researchers have studied the effect of adding promoter materials such as ceria (CeO_2) [91-96], yttrium-doped ceria (YDC) [97], zirconium (ZrO_2) [23, 89, 98-107], chromium (Cr) [108-112], Gold (Au) [80, 113, 114] and manganese (Mn) [115, 116] to the copper based catalyst in order to improve the catalyst performance, as discussed in Section 2.2.4.

2.2.2.2 VIIIB Group active metals

Catalysts based upon Group VIIIB metals such as Pd [94, 117-128] , Pt [117, 129] and Ni [94, 130-133] have been developed for methanol steam reforming. These metals exhibit different performance for methanol steam reforming than copper based catalysts. Mainly the decomposition reaction will transform methanol to CO and H_2 and the slow water gas shift reaction will convert CO to CO_2 [134]. Although

these metals are active for methanol conversion, they produce a large amount of CO which makes them an unattractive option for hydrogen production for PEMFC [25]. However, Group VIIIB metals for hydrogen production are still in research due to its ability to produce hydrogen at high temperature above 300°C at high stability [25] as reported below.

2.2.2.2.1 Palladium (Pd) based catalysts

Palladium supported on ZnO catalyst is thoroughly discussed in the literature. Iwasa et al. [117-121] studied the activity of Pd/ZnO catalyst which is reduced at temperatures above 300°C and concluded that a PdZn alloy formed during reduction, rather than Pd metallic phase, was responsible for the high activity and selectivity to CO_2 and H_2. The conclusions of Iwasa et al. [117-121] encouraged other researchers to carry out further studies on Pd catalysts. Cao et al. [122] studied the behaviour of $Pd/ZnO/Al_2O_3$ catalyst by optimizing the Pd/ZnO ratio on the Al_2O_3 supported catalyst and compared it to the copper based catalyst. They mentioned that $Pd/ZnO/Al_2O_3$ and Cu based catalysts exhibit high activity and selectivity in producing hydrogen. However, Pd produced a comparable amount of CO as a Cu based catalyst. It was mentioned that Pd is more thermally stable than Cu-based catalyst when the reaction temperature is above 300°C.

Ranganathan et al. [123] compared the Pd/ZnO catalyst to the Pd/CeO_2 catalyst. They found that the Pd/ZnO is favourable for steam reforming reaction instead of the decomposition reaction that occurred predominantly over the Pd/CeO_2 catalyst. This was explained by the high density of acidic sites on the Pd/ZnO compared to the high density of basic sites on the Pd/CeO_2 catalyst. Karim et al. [124] explained the Pd/ZnO selectivity in terms of the structures of the crystallite and alloy. Small metallic

particles of Pd have low selectivity for the steam reforming reaction, however, the alloy phase with Zn particles increases the reaction selectivity. In addition, they found that large particles of Pd do not have a negative effect on the reaction performance over an alloy phase. In contrast, Agrell et al. [125] found a correlation between Pd crystallite size and CO formation, where the small PdZn crystallite particle will produce more CO. The effect of adding Mg, Al, Zr, Ce, La, or Ru or a first-row transition metal to Pd/ZnO catalysts have shown that Cr, Fe, or Cu addition increases the selectivity to H_2 production by decreasing the CO formation, illustrating that the formation of a Pd-Zn alloy is critical for high selectivity in hydrogen production [94]. Penner et al. [126, 127] studied the differences in Pd/Ga_2O_3 catalyst activity and selectivity for the steam reforming reaction. These differences were interpreted in terms of different catayst (bi-) metallic–oxide contact areas.

Iwasa et al. [117, 118, 121] studied the performance of Pd on different supports such as ZnO, In_2O_3, ZrO_2, Ga_2O_3 and CeO_2, and showed that the Pd-Zn alloy was the most active and selective for the methanol reaction followed by Pd-In and Pd-Ga alloys. Furthermore, in the same study it was reported that Pd/ZnO/CeO_2 catalyst has a good thermal stability as well as a good activity and selectivity at 350°C [117, 121]. On the other hand, Pd-Zn deactivation was reported in the literature due to sintering [135]. Therefore the study of Pd/Zn catalyst performance on different supports shows that Pd-Zn/C catalyst has the lowest deactivation rate. In a further study a highly structured and thermally stable Pd-Zn catalyst was achieved using SiO_2 support and reduction at a temperature up to 600°C [128].

2.2.2.2.2 Platinum (Pt) based catalysts

The catalyst prepared from this metal is not studied thoroughly in the literature. The most commonly used catalyst in VIIIB Group is Pd supported catalyst, due to its anomalous high performance [136]. Iwasa et al showed the superiority performance of the Pd/ZnO catalyst compared to Pt/ZnO catalyst [136]. Pd/ZnO achieved lower selectivity for CO which was evaluated on a carbon basis, $P_{CO}/(P_{CO}+P_{CO2})$; where P_{CO} and P_{CO_2} represent the partial pressures of CO and CO_2 gasses in the effluent, respectively, and a higher methanol conversion (56.3% conversion and 1.9% CO selectivity) than Pt based catalyst (27.6% conversion, 4.6% CO selectivity). Iwasa et al. [117] studied the Pt based catalyst on different supports such as ZnO, In_2O_3 and Ga_2O_3. The Pt formed an alloy with Zn, In and Ga, improving the selectivity for the methanol steam reforming. Pt metals deposited on carbon were prepared by Tolmacsov et al. [129]. The carbon supported catalyst was shown to effectively produce H_2 and CO above 350°C. The advantage of using Pt and carbon support was reported to be the high thermal stability achieved [129] .

2.2.2.2.3 Nickel (Ni) based catalysts

Nickel based catalysts are used on a large scale for hydrogen production because they are cost effective [94]. The reaction over Ni-based catalyst proceeds via the methanol decomposition and is then followed by the forward water gas shift reaction [130-132]. Hydrogen and carbon monoxide are produced at temperatures in the range of 310-340°C [133].

The Ni/Al catalyst is used for methanol steam reforming at temperatures above 300°C. The Ni/Al catalyst activity and selectivity depends on the structure and the composition of the catalyst after pre-treatment and activation [130-133]. However, the

catalysts undergo severe changes in their structure after a reaction due to the high operation temperature (> 340°C), which causes a reduction of oxidic nickel, deposition of carbonaceous species and destruction of the support [133]. Qi et al. [133] assumed that reduction of oxidic Ni took place simultaneously with dehydrogenation of methanol at around 290 °C. The reformate composition when the reaction temperatures are above 340°C showed high levels of CO_2 and CH_4 where the methanation reaction decreases the amount of hydrogen in the reformate. The methanol reforming reaction is predominant in the temperature range 310-340°C for Ni based catalyst. The increase in the reaction temperature suggested the loss of oxidic Ni during reaction. Qi et al. [130, 132] observed a stable and a selective Ni/Al catalyst at temperature greater than 300°C in the presence of potassium and sodium.

2.2.3 Support for methanol reforming catalyst

The support for methanol steam reforming catalysts is ZnO, Al_2O_3, or ZnO with Al_2O_3. The support plays an important role during methanol steam reforming. It provides high surface area for active parts of catalyst and maintains stable reaction conditions against active metal sintering [137].

The Cu based catalysts employ solid material supports. Those supports such as ZnO and Al_2O_3 increase the surface area of active copper particles as well as leading to catalyst stability during the reaction. It was reported that the oxide support improves the stability of copper based catalyst by physically separating the copper crystallites, since Cu is very susceptible to thermal sintering [138, 139]. This was explained by the ability of the support to form oxygen vacancies, which leads to partial re-oxidation of reduced Cu metals to Cu_2O. Therefore, the rapid deactivation of copper catalyst

due to irreversible alloy formation from active copper metal is avoided, as well as the thermal sintering of small copper particles being suppressed [140].

For VIIIB group metals catalyst (Ni, Pd and Pt), various supports were investigated such as SiO_2, Al_2O_3, ZnO, MgO, La_2O_3, NdO_3, MnO_2, Cr_2O_3, HfO_2 and Nb_2O_5 [141, 142]. It was revealed that Pd/ZnO catalyst has higher activity than other prepared catalysts due to high support area of ZnO as well as the interaction between Pd and ZnO [143]. It was shown that PdZn alloy formed increases the catalyst activity toward CO_2 rather than CO, as discussed in methanol reaction mechanism in Section 2.4.2. The existence of the metallic phase of Pd enhances CO production so the support plays an important role of forming alloy particles which help to avoid producing CO, which subsequently leads to coke formation [124].

2.2.4 Promoter for methanol reforming catalyst

The catalyst activity is improved by adding promoters to the catalyst. In this section, the effect of promoters on copper based catalyst is discussed. For VIIIB group based active metal catalyst, the effects of promoters was discussed in Section 2.2.2.2.

2.2.4.1 Cerium (CeO_2) promotion

Various studies of adding cerium to the copper based catalyst (CuO-CeO_2) were investigated. Men et al. [91] showed that preferential dispersion of the copper on the ceria occurs, which leads to optimize the copper dispersion. It was also found that CeO_2 promoters decrease the sintering of copper micro-particles and increase the copper dispersion of the catalyst [92, 93, 107]. The promoted copper catalyst with CeO_2 has high thermal stability which reduces the amount of CO produced during the methanol steam reforming [92, 93]. This was attributed to the synergistic interaction between copper atoms and CeO_2 [94].

On the other hand, the CeO_2 addition to the $Cu/ZnO/Al_2O_3$ reduces the interaction between CuO and ZnO. Therefore, it hinders the reducibility of the copper catalyst [89]. However, the addition of the CeO_2 promoter to ZrO_2 on Al_2O_3 and Y_2O_3 supports was found to enhance the activity of $CuO\text{-}CeO_2$ catalyst [95, 96]. Although the CeO_2 hinders the reducibility of the copper catalyst, doping a small amount of Zn on to $CuO\text{-}CeO_2$ has shown an improvement for the steam reforming compared to the effect of doping other metals such as La, Zr, Mg, Gd, Y, Ca which had a negligible effect on catalyst activity [96].

2.2.4.2 Yttrium-doped ceria (YDC) promotion

The YDC promotion effect on copper based catalyst was studied by Cheng et al. [97]. The YDC was reported to enhance the activity of Cu supported on Al_2O_3 catalyst. This was related to increase the amount of Cu^+ sites on the catalyst, illustrating that YDC facilitates the oxidation of Cu by CO_2 during reaction. However, the copper dispersion was decreased by adding the YDC.

2.2.4.3 Zirconium (ZrO_2) promotion

The effect of adding ZrO_2 to the copper based catalyst was studied in the literature due to its positive effect on the catalyst performance. The copper-based catalyst activity and stability was improved by adding ZrO_2. It was explained that ZrO_2 can enlarge the surface area of the copper catalyst, stabilize the crystal size of the Cu and prevent the Cu particles from aggregation [23, 89, 98-102]. ZrO_2 leads to stabilize Cu^+ species on the surface of the catalyst which reduces the CO formation [89, 101, 104, 144]. Purnama et al. [103, 104] studied the CuO/ZrO_2 catalyst activity and compared it with the commercial copper catalyst. They found that ZrO_2 promotion

was more effective than ZnO particles by preventing the copper particles from sintering and had reduced the CO formation at high methanol conversion.

Jones and Hagelin [105] studied the effect of adding ZrO_2 to Cu/ZnO catalyst supported on nanoparticles alumina and concluded that ZrO_2 promotes methanol reforming and suppresses the methanol decomposition reaction. Matsumura and Ishibe [106] interpret that the particle sizes of Cu and ZnO with ZrO_2 promotion are significantly smaller than those for Cu/ZnO alone and BET surface area is 2-3 times as high as that for Cu/ZnO.

Reports in the literature showed that Cu/ZnO/ZrO_2 catalyst has good stability in operation, and it has low selectivity to carbon monoxide production [23, 89, 106, 107]. Matsumura and Ishibe [106] explained that the ZrO_2 particles act as an inhibitor for the growth of the ZnO particles. However, the deactivation of Cu/ZnO/ZrO_2 catalyst was interpreted as being due to the growth of ZnO particles which affects the interaction between copper and zinc oxide [106].

2.2.4.4 Chromium (Cr) promotion

Small amounts of Cr additives serve as catalytic and structural promoters [108-110]. Idem and Bakhshi [111] have investigated the effect of Cr on Cu-Al catalyst and concluded a high methanol conversion occurs (91 mol% at temperature 250°C) upon the addition of Cr since it enhanced the activity of Cu by maintaining optimum amounts of Cu^0 and Cu^{1+} species. The activity test of Cu/Zn/Cr supported on Al_2O_3 was investigated by Kearns et al. [112], which demonstrated higher activity than the Cu/Zn/Al catalyst with the spent catalyst of Cu/Zn/Cr showing evidence of crystallites of Cu metal.

2.2.4.5 Gold (Au) promotion

Takahashi et al. [113] studied the effect of adding gold to Cu based catalyst. The methanol conversion had increased and the carbon dioxide selectivity was almost unity. The copper dispersion increased in copper-gold alloy. However, the copper catalyst promoted with Au showed instability after a period of time (200 minutes) due to the deposition of coke on the catalyst surface [80, 113, 114].

2.2.4.6 Manganese (Mn) promotion

The steam reforming of methanol over Cu-Mn oxide catalysts showed the formation of the Cu-Mn spinel phase with high activity [115]. It was proved that the pathway of the reaction of Cu-Mn catalyst includes a methyl formate intermediate as for the commercial copper catalyst [116].

2.2.4.7 Promoting of methanol reforming catalyst using Ni

The Cu based catalysts promoted or doped with Ni metals are reviewed in this section. It was difficult to find direct literature related to methanol steam reforming and Ni-Cu based catalysts. Ni-Cu based catalysts are usually discussed in the literature under ethanol steam reforming [145-147]. However, some recent works have studied Ni-Cu for methanol reforming as reported below.

Ni-Cu supported on carbon nanotubes have been studied recently. An Ni-Cu alloy supported on carbon nanotubes and a bimetallic catalyst of Ni and Cu supported in carbon nanotubes were compared at a reaction temperature of 360°C [148]. The formation of Ni-Cu alloy was responsible for active hydrogen production. It was observed that the absence of Ni-Cu alloy leads to strong adsorption between Ni and hydrogen leading to decrease the activity of the catalyst due to the reduction of methanol contact with Ni particles. The effect of Ni loading showed an enhancement

in catalyst performance by decreasing the Ni content. It was reported 98.6% of hydrogen yield, calculated from the formula $100 \times F_{H2} /(3 \times F_{CH3OH,0})$ where F_{H2} represents molar flow rate of H_2 and F_{CH3OH} is the feeding rate of methanol, and 41.5% of CO selectivity, determined as $100 \times F_{CO} /(F_{CO} + F_{CO2})$ where F_{CO} and F_{CO2} represent molar flow rate of CO and CO_2, respectively, at 20wt% of Ni of the total loading of Ni-Cu.

Ni_xCu_y-Al catalysts were synthesised with different Ni-Cu contents up to 10wt% of the total metal loading in order to compare methanol and ethanol steam reforming reactions [149]. The catalytic performance study at temperature range 230-700°C was reported, showing promising results for bimetallic systems in terms of reducing the undesirable product such as methane during reforming. No deactivation was observed for two consecutive runs. The results showed that NiCu alloy have improved catalyst stability compared to the monometallic Cu. The composition of the bimetallic systems showed no change in product distribution at temperature above 300°C compared to mono Cu catalyst. However, some differences were reported at temperatures below 300°C when Ni contents increased, leading to corresponding increase in CO yield.

Recently the literature has reported a list of Ni catalysts modified with a second metal such as; Au, Ag, Sn, Cu, Co, Mo, Fe [150]. The current work [151] was referred as a recent work for Ni-Cu catalyst for steam reforming [150, 152].

2.3 Methanol catalyst deactivation

Deactivation or degradation of a catalyst is defined as the loss of catalyst activity [65]. It could be a result of mechanical, thermal and chemical factors. These factors cannot be treated independently since each factor can have an interdependent effect. Coking, sintering and poisoning are the most important causes of the catalyst deactivation during methanol steam reforming process. Table 2.4 explains types and causes of catalyst deactivation and their effects on catalyst characteristics and operation.

Various literature investigations based their explanation for deactivation upon results obtained using an experimental scale reactor for catalyst testing, observation of catalyst deactivation as well as characterization of spent catalyst samples, as described in the following sections.

Table 2.4. Types and causes of catalyst deactivation [65].

Type	Causes	Results
Mechanical	Particle failure	Bed channelling, plugging
	Fouling	Loss of surface area
Thermal	Component volatization	Loss of component
	Phase changes	Loss of surface area
	Compound formation	Loss of component and surface area
	Sintering	Loss of surface area
Chemical	Poison adsorption	Loss of active sites
	Coking	Loss of surface area, plugging

2.3.1 Sintering and carbon formation

Thurgood et al. [153] attributed deactivation of copper based catalysts to a decrease in capacity to adsorb and dissociate hydrogen. They developed a copper-based catalyst deactivation model and proved the sites responsible for hydrogen adsorption decline at greater rate than those responsible for the adsorption of oxygenated species. The author assumed in the model two active sites; one active site supports hydrogen adsorption only, while the other adsorbs carbon- and oxygen containing species. Both sites must be physically close to each other so that adsorbed hydrogen can react with the adsorbed species at the other site. The loss of hydrogen adsorption sites indicate a decline in the activity for hydrogen adsorption and subsequent dissociation into adsorbed atomic hydrogen. Hence, several causes of copper based catalyst deactivation are summarised in the following:

- Copper crystallites are susceptible to thermal sintering and to high steam concentrations [74, 80].
- Polymeric deposition of coke occurs [80].
- Oxidation state changes from active Cu^{+} state to Cu^{0} inactive state [80, 106, 154].

The sintering mechanism was related to the vacancy diffusion and copper stability compared to other metals [80]. Polymeric deposition is a result of intermediate products and by-products formed during reaction that will cause fouling of the catalyst. The active site of copper catalyst Cu^{+2} is readily changed causing initial deactivation of catalyst [155]. Furthermore decreasing the ratio Cu^{+}/Cu^{0} causes permanent deactivation due to ZnO covering of active Cu phase during growth of ZnO particles [106, 154].

The temperature rise is a major cause of catalyst deactivation by thermal sintering and avoidance of copper crystallites from sintering has been suggested to be achieved by carrying out the steam reforming reaction at temperatures below 300°C [80]. Despite that, the uncontrolled temperature inside the reactor may still cause thermal sintering.

Group VIIIB metals have high stability during the reforming process. Their ability to operate at high temperatures (>300°C) compared to the copper based catalyst showed resistivity for thermal sintering [25]. Catalyst deactivation and poisoning of Group VIIIB metals are not covered in the literature as widely as copper based catalysts. However, a lifetime test of the catalyst prepared from VIII Group metals was studied by several researchers. Suwa et al. [135] studied the lifetime of Pd/ZnO and other Pd prepared catalysts for 50h and concluded the deactivation was caused by coverage of Pd-Zn alloy particles with zinc carbonate hydroxide. Group VIIIB metals were reported to produce a lot of CO that might decompose to produce deposited carbon on the catalyst surface [32] .

2.3.2 Poisoning

Metal catalysts are extremely sensitive to poisons such as sulphur, chloride and carbon deposits. Trace amounts of sulphur might exist in methanol fuel, chlorine can be introduced in the reaction steam or in the reformer during cleaning processes from water and carbon can be a result of coke formation.

Twigg et al. [80] studied the deactivation of metal copper catalysts and concluded that the copper catalysts are susceptible to thermal sintering via surface migration by presence of chloride. Steam methanol reforming catalysts are extremely sensitive to site-blocking poisons by sulphur species. Lindström and Pettersson [156] studied the

effect of adding poisons such as sulphur and chlorine and concluded that copper catalyst deactivation happens by chemical deactivation. Table 2.5 illustrates the various types of poisons and their effects on copper based catalyst.

Due to the fact that the methanol steam reforming reaction requires to produce hydrogen with high purity using a high quality feed, the amount of contaminants should be controlled and monitored in order to avoid poisoning of the catalyst metal. Methanol feedstock sulphur and chloride contents must be controlled and monitored by trapping these poisons as illustrated in Figure 2.2 [156]. A catalyst formulation can be controlled to become highly resistant to poisoning, such as by adding ZnO to copper based catalysts. For instance, ZnO acts as an inhibitor of sulphur poisoning. Furthermore catalyst treatment and regeneration (activation) using nitrogen or air may remove poisons from the catalyst [80, 156].

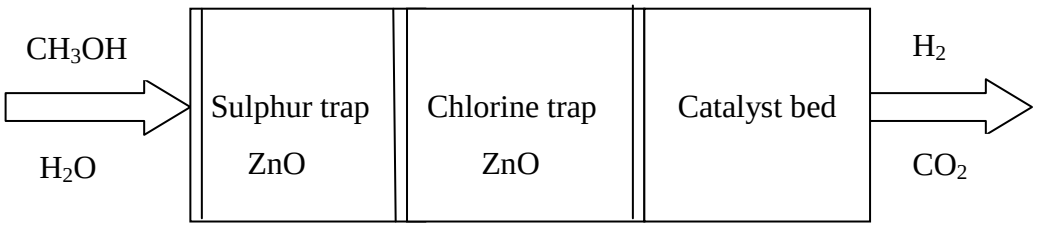

Figure 2.2. Steps of controlling and avoiding poisons [156].

Table 2.5. Types of poisons and their effect on the copper based catalyst.

Type of poisons	Poisons effect	Comments and reactions responsible
Chloride poison	• Adsorbed chlorine atoms block catalytic site. • Low melting point of Cu (I) chloride (430°C) accelerates the sintering of Cu catalyst [80]. • Cu (I) chloride exacerbates the poisoning of Cu catalyst by sulphur compounds due to low melting point of Cu (I) chloride. • Zn halides have low melting point (283°C) [80] which will cause sintering problems.	• $Cu_{(s)} + HCl_{(g)} \rightarrow CuCl_{(s)} + 0.5\ H_{2(g)}$ $\Delta H°_{298} = -43.5$ kJ mol^{-1} [80] • To avoid catalyst poisoning by chloride, concentration of HCl in gas phase should be of order 1ppb. • $ZnO_{(s)}+2HCl_{(g)} \rightarrow ZnCl_{2(S)} + H_2O_{(g)}$ $\Delta H°_{298} = -121.8$ kJ mol^{-1} [80]
Sulphur poison	• Adsorption of sulphur on the copper surface is thermodynamically favourable which will cause formation of bulk copper sulphide and hence site blocking.	• $2Cu + H_2S \rightarrow Cu_2S + H_2$ $\Delta H°_{298} = -59.4$ kJ mol^{-1} [80] • ZnO act as a buffer by removing H_2S from gas stream by formation zinc sulphide. • $ZnO_{(s)}+H_2S_{(g)} \rightarrow ZnS_{(S)}+ H_2O_{(g)}$ $\Delta H°_{298} = -76.7$ kJ mol^{-1} [80] • Gas sulphur concentration must be kept below 1 ppm and some referred it to 0.1 ppm [80].
Carbon deposition (coking)	• Physical damage of catalyst pores. • Wax and carbon formation on catalyst bed. • Obstruction of active sites	• $2CO \rightarrow CO_2 + C$ [80] • Wax can be generated from impurities in catalyst such as silica that can react with alumina to form acidic sites.
By-products, intermediates poisons	• Polymeric deposition.	• Significant amount of formaldehyde and methyl formate intermediate will cause polymeric deposition on catalyst [156].

2.4 Methanol reaction mechanism

The reaction mechanism was discussed in the literature for copper based catalyst and Group VIIIB based catalyst. Each catalyst has its unique path for reaction to produce hydrogen. The mechanism of the reaction and catalytic function of copper based catalyst and Group VIIIB metals based catalyst are discussed below.

2.4.1 Reaction mechanism over Cu based catalyst

The methanol steam reforming which is discussed in the Section 2.2 (Eq. 2.1) is a sequence of methanol decomposition (Eq. 2.2) followed by the water gas shift reaction (Eq. 2.3) [157]. The discrepancy in the amount of carbon monoxide produced and whether it is above or below equilibrium value has revealed two concepts for reaction mechanism [71, 83].

In the first case, the amount of carbon monoxide produced in the reaction is significantly greater or equal to the amount of CO produced by the water gas shift reaction [73, 158, 159]. The CO produced was attributed to the decomposition reaction followed by water gas shift reaction. In the second case, the amount of CO produced is less than that produced by water gas shift reaction, where an intermediate mechanism of methyl formate is suggested [160].

As a result, the mechanism for methanol steam reforming over copper based catalyst was proposed based on the amount of CO formation. A comprehensive model including methanol steam reforming reaction, water gas shift reaction and decomposition reaction of methanol were proposed [70]. The comprehensive model assumes two active sites on the catalyst. One site is responsible for steam reforming reaction and water gas shift reaction while the second site is responsible for activating the decomposition reaction. This means the hydrogen species is adsorbed

upon one site (Elementary Reaction ER. 2.19) and oxygen-containing species are adsorbed upon another active site. On the other hand, some studies did not consider the decomposition reaction due to low concentration of CO [73, 158, 159] which led to develop a reaction mechanism based on the formation of formic acid, surface hydroxyls from formate species and reverse water gas shift reaction for adsorbed CO [158, 159].

Several studies presented Langmuir-Hinshelwood mechanisms explaining the various reaction paths for methanol reforming [161]. Methanol steam reforming was studied assuming two distinct types of active sites on catalyst; those that are responsible for hydrogen adsorption which will not compete with another active site upon which methoxy adsorbs on [158], as shown in the Elementary Reaction (ER) steps (ER. 2.1-2.3). It was noticed from the reaction steps that oxygen-containing species are neglected except methoxy. Then, dehydrogenation of the adsorbed methoxy (ER. 2.3) to the adsorbed oxymethylene is considered a Rate-Determining Step (RDS).

$$CH_3OH + S_1 + S_{1a} \rightleftharpoons CH_3O^{(1)} + H^{(1a)} \quad \text{(ER. 2.1)}$$

$$CH_3O^{(1)} + S_{1a} \rightleftharpoons CH_2O^{(1)} + H^{(1a)} \quad \text{(RDS)} \quad \text{(ER. 2.2)}$$

$$2H^{(1a)} \rightleftharpoons H_2 + 2S_{1a} \quad \text{(ER. 2.3)}$$

Since the above reaction path neglects the oxygen containing species, another reaction mechanism is proposed in which all oxygen or carbon species are adsorbed on a common active site and hydrogen adsorbs in a different one [159]. It was explained in the elementary reaction steps (ER. 2.4-2.11) that the rate limiting reaction was the formation of formic acid from formaldehyde as shown in ER. 2.8 [159].

$$CH_3OH + S_1 + S_{1a} \rightleftharpoons CH_3O^{(1)} + H^{(1a)} \quad \text{(ER. 2.4)}$$

$$H_2O + S_1 + S_{1a} \rightleftharpoons OH^{(1)} + H^{(1a)} \quad \text{(ER. 2.5)}$$

$$CH_3O^{(1)} + S_{1a} \rightleftharpoons CH_2O^{(1)} + H^{(1a)} \quad \text{(ER. 2.6)}$$

$$OH^{(1)} + S_{1a} \rightleftharpoons O^{(1)} + H^{(1a)} \quad \text{(ER. 2.7)}$$

$$CH_2O^{(1)} + O^{(1)} \rightleftharpoons HCOOH^{(1)} + S_1 \quad \text{(RDS)} \quad \text{(ER. 2.8)}$$

$$HCOOH^{(1)} + S_{1a} \rightleftharpoons HCOO^{(1)} + H^{(1a)} \quad \text{(ER. 2.9)}$$

$$HCOO^{(1)} + S_{1a} \rightleftharpoons H^{(1a)} + CO_2^{(1)} \quad \text{(ER. 2.10)}$$

$$HCOO^{(1)} + S_1 \rightleftharpoons OH^{(1a)} + CO^{(1)} \quad \text{(ER. 2.11)}$$

$$2H^{(1a)} \rightleftharpoons 2S_{1a} + H_2 \quad \text{(ER. 2.12)}$$

$$CO^{(1)} \rightleftharpoons S_1 + CO \quad \text{(ER. 2.13)}$$

$$CO_2^{(1)} \rightleftharpoons S_1 + CO_2 \quad \text{(ER. 2.14)}$$

The last Langmuir-Hinshelwood mechanism is known as a comprehensive model since it includes all possible reactions for methanol steam reforming (ER. 2.15-2.26) [70]. The reaction path assumed that oxygen-containing species adsorbs on one type of active site while hydrogen adsorbs on a different type of site. In this case, the dehydrogenation of adsorbed methoxy is a rate-determining step as shown in ER. 2.20.

The key feature of the above reaction path over the copper based catalyst is summarised by Peppley et al. as follow [70]:

- Hydrogen adsorption does not compete for the active sites (ER. 2.19) at which the oxygen-containing species adsorb.
- There are separate active sites for the decomposition reaction distinct from the active sites for the methanol steam reaction and the water-gas shift reaction.

- The rate-determining step for both the methanol steam reaction and the methanol decomposition reaction is the dehydrogenation of adsorbed methoxy groups.
- The Rate Determining Step (RDS) for the water-gas shift reaction is the formation of an intermediate formate species.

$$CH_3OH + S_1 + S_{1a} \rightleftharpoons OH^{(1)} + H^{(1a)} \quad \text{(ER. 2.15)}$$

$$H_2O + S_1 + S_{1a} \rightleftharpoons OH^{(1)} + H^{(1a)} \quad \text{(ER. 2.16)}$$

$$CO^{(1)} \rightleftharpoons S_1 + CO \quad \text{(ER. 2.17)}$$

$$CO_2{}^{(1)} \rightleftharpoons S_1 + CO_2 \quad \text{(ER. 2.18)}$$

$$2H^{(1a)} \rightleftharpoons H_2 + 2S_{1a} \quad \text{(ER. 2.19)}$$

$$CH_3O^{(1)} + S_{1a} \rightleftharpoons CH_2O^{(1)} + H^{(1a)} \quad \text{(RDS)} \quad \text{(ER. 2.20)}$$

$$CH_3O^{(1)} + CH_2O^{(1)} \rightleftharpoons CH_3OCH_2O^{(1)} + S_1 \quad \text{(ER. 2.21)}$$

$$CH_3OCH_2O^{(1)} + S_{1a} \rightleftharpoons CH_3OCHO^{(1)} + H^{(1a)} \quad \text{(ER. 2.22)}$$

$$CH_3OCHO^{(1)} + OH^{(1)} \rightleftharpoons HCOOH^{(1)} + CH_3O^{(1)} \quad \text{(ER. 2.23)}$$

$$HCOOH^{(1)} + S_{1a} \rightleftharpoons H^{(1a)} + HCOO^{(1)} \quad \text{(ER. 2.24)}$$

$$OH^{(1)} + CO^{(1)} \rightleftharpoons HCOO^{(1)} + S_1 \quad \text{(ER. 2.25)}$$

$$HCOO^{(1)} + S_{1a} \rightleftharpoons H^{(1a)} + CO_2{}^{(1)} \quad \text{(ER. 2.26)}$$

Busca et al. [162] claimed that methanol steam reforming is not a sequence of the methanol decomposition and the water gas shift reaction because a low amount of CO is produced by reverse water gas shift reaction only. Methyl formate intermediate is produced from direct methanol dehydrogenation (Eq. 2.4) and afterwards hydrolyzed to form formic acid (Eq. 2.5) then formic acid decomposes to form carbon dioxide (Eq. 2.6), which explains the low amount of CO produced [163, 164]. In addition, the low amount of CO was suggested to be due to the reverse water gas

shift reaction (Eq. 2.7) [73, 158, 159]. Therefore, it can be concluded that the decomposition reaction determines the possible pathway of the reaction mechanism [157].

$2CH_3OH \rightarrow HCOOCH_3 + 2H_2$ (Eq. 2.4)

$HCOOCH_3 + H_2O \rightarrow CH_3OH + HCOOH$ (Eq. 2.5)

$HCOOH \rightarrow H_2 + CO_2$ (Eq. 2.6)

$CO_2 + H_2 \rightleftharpoons CO + H_2O$ (Eq. 2.7)

The other possible pathway for producing a low amount of CO is formaldehyde intermediate as shown in Eq. 2.8-2.10. The possible formaldehyde formed in this mechanism by methanol dehydrogenation may react with hydroxyl groups. Then, formic acid is produced which decomposes afterwards to H_2 and CO_2 [116]. Papavasiliou et al. [116] have recently mentioned the major path of the reaction is a methyl formate intermediate however parallel paths appear to be operative over copper based catalyst.

$CH_3OH \rightarrow HCHO + H_2$ (Eq. 2.8)

$HCHO + H_2O \rightarrow HCOOH + H_2$ (Eq. 2.9)

$HCOOH \rightarrow H_2 + CO_2$ (Eq. 2.10)

In summary, the reaction of methanol steam reforming includes the decomposition reaction followed by water gas shift reaction in cases where the amount of CO produced is equal or greater than equilibrium. So, the decomposition reaction of methanol should be included as part of the overall reaction sequence [70]. Some studies excluded the decomposition reaction due to low concentration of CO observed and they referred the CO produced to the reverse water gas shift reaction only [158, 159].

2.4.2 Reaction mechanism over Group VIIIB based metal catalysts

The reaction mechanism for Group VIIIB metals such as Pd, Pt and Ni exhibits different performance for methanol steam reforming reaction than the copper-based catalysts [165]. It was suggested that the decomposition reaction mainly transforms methanol to CO and H_2 and slow water gas shift reaction converts CO to CO_2 [137, 141, 166] . The composition of both CO and CO_2 determines the reaction mechanism of methanol steam reforming which depends on the reaction temperature as well as the catalyst structure [130-133]. The existence of the alloy phase of metal or metal phase determines CO_2 and CO composition [119, 141, 142, 166, 167].

Methanol steam reforming reaction for VIIIB group metals was mainly studied on Pd based catalyst. Iwasa et al. [117, 118, 137] studied the reaction paths over Pd catalyst. Methanol steam reforming is carried out by decomposition reaction followed by water gas shift reaction as explained in detail below.

The reaction path depends on the metallic phase or the alloy phase appearing on the catalyst [124]. It was suggested that the C=O bond adsorbed upon the alloy phase prevents the decomposition of aldehyde (HCHO) directly to CO and H_2 as illustrated in Figure 2.3 [137, 141, 167]. The difference in the reactivity of HCHO species in the metallic phase or the alloy phase determines the reaction path. In the metallic phase [119, 142], methanol decomposes directly to CO and H_2 via formation of aldehyde (HCHO) species as shown in Eq. 2.11-2.12; then the water gas shift reaction is responsible for CO_2 production. In the alloy phase [119, 135, 142], the aldehyde (HCHO) intermediate reacts with H_2O to produce formic acid (HCOOH) as shown in Eq. 2.13, which decomposes directly to CO_2 and H_2, as shown in Eq. 2.14. Part of the formic acid (HCOOH) is also formed from methanol dehydrogenation to methyl

formate ($HCOOCH_3$) and H_2, as shown in Eq. 2.15 following by hydrolysis of methyl formate ($HCOOCH_3$) in the Eq. 2.16 then formic acid decomposes to produce CO_2 and H_2.

$$CH_3OH \rightarrow HCHO + H_2 \quad \text{(Eq. 2.11)}$$

$$HCHO \rightarrow CO + H_2 \quad \text{(Eq. 2.12)}$$

$$HCHO + H_2O \rightarrow HCOOH + H_2 \quad \text{(Eq. 2.13)}$$

$$HCOOH \rightarrow CO_2 + H_2 \quad \text{(Eq. 2.14)}$$

$$HCHO + CH_3OH \rightarrow HCOOCH_3 + H_2 \quad \text{(Eq. 2.15)}$$

$$HCOOCH_3 + H_2O \rightarrow HCOOH + CH_3OH \quad \text{(Eq. 2.16)}$$

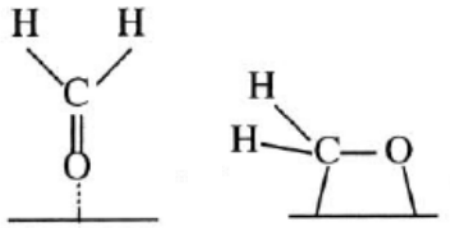

a b

Figure 2.3. Reaction intermediate for the steam reforming of methanol over Pd alloys and metallic Pd: a) HCHO at Pd alloy phase and b) HCHO at Pd metallic phase [117].

2.5 Methane steam reforming

The purpose of the catalytic methane steam reforming is to produce the maximum amount of hydrogen by introducing steam into methane. Methane steam reforming is a strongly endothermic reaction as shown in Eq. 2.17. Methane steam reforming also includes exothermic water gas shift reaction as shown in Eq. 2.18 which is favoured by a low temperature. The methane steam reforming process is represented in Eq. 2.19 as a combination of reactions 2.17 and 2.18 [168-171].

$$CH_4 + H_2O \rightleftharpoons CO + 3H_2 \quad , \Delta H°_{298} = +206 \text{ kJ/mol} \quad \text{(Eq. 2.17)}$$

$$CO + H_2O \rightleftharpoons CO_2 + H_2 \quad , \Delta H°_{298} = -41 \text{ kJ/mol} \quad \text{(Eq. 2.18)}$$

$$CH_4 + 2H_2O \rightleftharpoons CO_2 + 4H_2 \quad , \Delta H°_{298} = +165 \text{ kJ/mol} \quad \text{(Eq. 2.19)}$$

The reactions in Eq. 2.17-2.19 are reversible. The product of methane steam reforming is a mixture of CO, CO_2, H_2, unconverted methane and steam. The product depends on the reaction temperature, the operating pressure and the ratio of steam fed into the reactant [57].

In a conventional reactor (large-scale reactors), methane is reformed to CO_2 and H_2 at relatively high temperature and pressure (above 800-1000°C and 30-40 bar) by using a catalyst to achieve a maximum conversion of methane [172, 173]. The stoichiometry of the methane reaction (Eq. 2.17) shows the steam to carbon ratio of one. However, this is not the case in practice; an excess of steam is required to suppress the carbon formation, with steam to carbon ratio of 3 to 4 being normally used. However; the economic implications tend to favour the use of a lower steam to carbon ratio by developing new catalysts which resist carbon formation. For small-scale reactors, the target is to handle the reaction at low temperature (500-800°C) as well as low pressure (atmospheric pressure) in order to handle fuel cell applications [168-171]. The equilibrium concentration analysis of reformate produced for methane steam reforming reaction are simulated and discussed in Chapter 4.

2.5.1 Methane steam reforming catalyst

The nickel-based catalyst is normally used for methane steam reforming. The catalyst is designed to operate at severe reaction temperatures ranging from 700°C to 1000°C and high pressure (30 bar) [174]. To maximize the overall efficiency (and hence economics) of the conversion to carbon dioxide and the production of hydrogen, reformers are operated at high temperature and pressure, followed by shift process. The Ni catalyst is the most popular catalyst used for methane reforming due to its favourable economics and its commercial availability.

It was reported in the literature that methane steam reforming catalyst should achieve the following [65, 169, 175]:

- The methane steam reforming catalyst must be active and tolerant for carbon formation.
- The catalyst in methane steam reforming is assumed as an active catalyst when it achieves the target reformates concentration at specific reformer operation conditions.

It is known that ceramic supported commercial Ni catalyst deactivates by particle sintering, thermal degradation of the support and carbon deposition. Therefore, the studies on the development of deactivation resistant methane reforming catalysts are as summarized below.

2.5.2 Active metals of methane reforming catalyst

A heterogeneous catalyst used for methane steam reforming is typically a metal oxide supported material. The most popular metal oxide catalysts for steam methane reforming are oxides of Ni, Pt, Pd, Ru, Rh and Ir [176, 177].

The most important aspect of active metals is the particle size. It was mentioned that a small particle size ensures a large surface area and as a consequence a better catalytic activity [178]. Concerning the reaction activity, it was concluded the smaller NiO crystals have a more open metal surface which are more resistant to carbon formation than large NiO crystals [178, 179]. It was explained that carbon formation is a structure dependent reaction and will not proceed when crystals are below a critical size [178]. A higher carbon deposition rate was noticed on large Ni particles during the reforming reaction, consequently reducing the catalyst activity [180]. The initiation

or nucleation of carbon was not observed on the smaller Ni particles, which result in a low coking rate [181, 182].

The activity of methane steam reforming catalyst is also related to the metal surface area (the number of active metal sites) [183-185]. It was reported that an Ni catalyst achieved a dispersion of 2-5% at metal particle size of 20-50nm. Assuming spherical Ni crystals, the crystal size d is determined from the dispersion D of Ni particles,($d = 101/D$), where d in nm and D is %. Higher dispersions are achieved as very small crystallites. Hence, the Ni loading above 15-20wt.% will not increase the catalyst activity, due to the additional metal being poorly dispersed. The catalyst activity decreases per unit metal surface area with increasing the Ni metals loading above 20wt.%. The reason for this is due to a decrease of large ensemble landing sites on the smaller particles. This was related to a change in electronic state of the active metal particles which will reduce the number of large ensemble adsorption sites on the smaller particles. For instance, the Ni based catalysts with high dispersion may result in a low metallic and low reactive character for Ni particles causing a structural change of the available metal. In turn this has an influence on the catalyst activity [186, 187] by reducing the catalyst ability for activating C-H bonds during methane steam reforming.

A series of platinum catalysts were studied for methane reforming, including Pt/Al_2O_3, Pt/ZrO_2 and Pt/CeO_2 catalysts prepared by an impregnation method [188]. Pt showed a rapid deactivation due to coke formation leading to active site coverage and pore-plugging [185].

2.5.3 Support for methane reforming catalyst

The support provides a surface for dispersion of active metal and determines the catalyst resistance to sintering [189]. The support should have high mechanical strength, high surface area and sufficiently large pores in order to allow gas diffusion. The most popular supports used in methane steam reforming are α-Al_2O_3 and γ-Al_2O_3. The other supports are found in the literature are; MgO, $MgAl_2O_4$, SiO_2 and ZrO_2 [190].

The most important characteristic for these supports are that they should have a good porosity which determines a large surface area for the catalyst [191]. The support also determines the final particle size of the metal within the pore structure, morphology and phase transition during the reaction. Finally, the stable catalyst was found to have strong interaction between the metal and the support which makes the catalyst highly resistant to sintering and coking. On other hand, the literature reported the influence of the support on methane steam reforming reaction efficiency (activity) is small. It was reported the major contributor for catalyst activity is the active metal upon which hydrogen is adsorbed [192].

The size of the supported particles plays an important role in the steam reforming reaction. It was found that Ni (10-15 nm) supported by small nano-particles of ZrO_2 (7-25 nm) can be active and stable in the temperature range 700-800°C [193]. The major difference between conventional support (Al_2O_3) and the nano-support (ZrO_2) is that the conventional support has discrete metal nano crystals sizing from 1 to 20 nm supported on oxide particles that are several magnitudes larger than metal nano crystals. It was concluded that Ni catalyst supported on large oxide particles was deactivated more rapidly than nano-particles supported oxide via coke formation.

Ni catalyst was studied for methane steam reforming with various oxides as support such as [190] ; Al_2O_3, MgO, SiO_2, CeO_2 and ZrO_2. A summary of these studies is reported below:

Al_2O_3 is the most popular support used in methane steam reforming because of its industrial availability [194-197]. Ni-αAl_2O_3 and Ni-γAl_2O_3 are used in methane steam reforming due to the nature of interaction between Ni and Al_2O_3. For instance, nickel aluminate spinel ($NiAl_2O_4$) is formed due to high calcination temperatures. The drawback of $NiAl_2O_4$ is difficult to reduce which high concentrations influence the final metal content for nickel alumina catalyst. The major drawback of Ni-γ-Al_2O_3 is its instability at temperature above 700°C due to thermal deterioration of γ-Al_2O_3 which leads to sintering and pore blockage and as a result leading to surface area loss and phase transformation into α-Al_2O_3 leading to further loss in active surface area.

A range of other supports than Al_2O_3 were reported in the literature. For instance, silica has increased the strength of the interaction between Ni and support. The problem of silica support is its propensity to melt at high steam reforming temperature [194]. Mg is used as a support but it can hydrate in presence of steam causing a weak catalyst at temperature below 425°C [194]. However, MgO support [198] enhances the catalytic reaction by activation under steam since it dissociates steam into OH^- and H^+ species. ZrO_2 is able to oxidize the deposited carbon so it can suppress the carbon deposition. Finally, Ni supported on $CeZrO_2$ showed [195] a good example of the effect of the support on the reaction. Ceria is able to store, release and transfer O_2 species which would prevent carbon formation. A 10 wt% Ni catalyst supported on Ce-ZrO_2 was investigated at temperatures in the range 500-

800°C [199]. It was shown that the catalyst achieved 66.6% CH_4 conversion at temperature 800°C.

2.5.4 Promoters for methane reforming catalyst

The catalyst modification using promoter metal plays an important role in increasing the activity and suppressing the carbon deposition. It was reported that metal oxides suppress the carbon formation [200]. Therefore, several studies reported the enhancement of active metal function of catalysts by introducing a promoter and modifying the support.

The effect of addition of Pt to Ni/Al_2O_3 catalyst was studied [201]. The methane reforming activity was improved where less than of 0.3wt.% of Pt was added to 15wt.% of Ni. It was also mentioned that addition of a small amount of Pt to $Ni/MgAl_2O_4$ had increased the surface area and this probably was responsible for an increase in the methane steam reforming conversion.

Molybdenum (Mo) was added to Ni catalyst as promoter [202]. It was found that doping 0.5wt.% of Mo significantly enhances the Ni catalyst ($Ni\text{-}Mo/\gamma Al_2O_3$) resistance to coking. It was noticed that a change of the oxidation state of Mo promoter atoms occurs due to surface reaction of vapour and Mo. The presence of oxygen atoms increases the gasification of CH_4 so it decreases the carbon deposit [180, 203].

The effect of addition zirconia and Ni/SiO_2 was investigated [204]. It was reported that Ni/SiO_2 catalysts deactivate due to high steam temperature. Steam will cause silica coarsening leading to cover the active surface of Ni. The addition of Zr increased the catalyst activity by increasing the silica resistivity for steam.

For such studies, it was reported that doping Ni/Al_2O_3 catalysts with rare earth oxides achieved great improvements in catalyst stability and high temperature resistance [205, 206]. This was related to the effect of rare earth metals by preventing the growth of Ni particles, suppressing the oxidation of active Ni particles and the formation of $NiAl_2O_4$.

Rhodium supported catalyst was investigated in the study of methane conversion and CO selectivity within the temperature range 500-800°C [199]. The study showed that 3wt.% Rh supported on $Ce_{0.15}Zr_{0.85}O_2$ achieved a methane conversion of 28.1% at 500°C.

Ruthenium added to Ni catalyst and supported on Al_2O_3 catalyst was studied [207-209]. It was reported that doping small amount of Ru (0.5wt.%) suppresses the growth of carbon whiskers on Al_2O_3 supported Ni catalyst. The presence of Ru in a highly dispersed state facilitates the reduction of NiO and decreases the coking during steam reforming of CH_4. The catalyst showed a maximum conversion of 30% at temperature 650°C.

Cerium was added to palladium supported on γ-Al_2O_3 catalyst [210]. The presence of CeO_2 improved the catalytic performance since it has good thermal and mechanical resistance as well as having good oxygen storage capacity. It was reported that the reaction over $Pd/CeO_2/Al_2O_3$ catalyst was more efficient than Pd/Al_2O_3 catalyst since Pd sites are agglomerated as large clusters during the reaction.

2.5.4.1 Promoting of methane reforming catalyst using Cu

Investigations have been carried out upon methane steam reforming catalysts modified by adding Cu metal [150, 152, 211]. Cu metal was used to enhance the

decomposition reaction of methane and ethane and to improve the water gas shift reaction at high temperature as reported below.

The theory of introducing Cu promoter is to improve the stability of the catalyst by controlling the number of adjacent active sites (ensemble size) [212-215]. The activity and selectivity of the mixed metal Ni-Cu catalyst was claimed to increase due to the dilution of Ni surface atoms, compared with only Ni metal. It was mentioned that a geometrical effect of Cu addition is the dominant one rather than an electronic effect. This explained that small formed ensembles of nickel surface atoms decrease the amount of adsorbed carbon species so the carbon formation rate is minimized [216-218].

The catalyst prepared using samaria-doped ceria and Al_2O_3 supported Ni-Cu catalysts via impregnation was studied [219]. The results showed that the water gas shift reaction activity decreased with increasing the temperature from 400-550°C for doped ceria, more than Al_2O_3 supported Ni-Cu catalyst. The rate of water gas shift reaction for ceria was higher at 400°C than Ni-Cu/Al_2O_3, then with increasing the temperature, the Ni-Cu was superior. It was mentioned that the addition of Cu (0.01wt.%, 0.1wt.%, 0.5wt.%) to Ni (0.5wt.%) catalyst improved the activity of water gas shift reaction and it was related the amount of the bimetallic Cu-Ni species.

The introduction of Cu to Ni alumina catalysts was investigated for methane decomposition reaction conversion and the results showed an enhancement of the catalyst stability within the temperature range 500-900°C. It was reported that the maximum conversion of methane was 54% at 700°C for a run of 20 hours duration [220].

The addition of Cu to Ni/SiO_2 was studied. The results showed an increase in the stability of Ni/SiO_2 catalyst due to an increase in the synergetic effect of Ni-Cu during the methane decomposition reaction [221]. The overall performance of methane decomposition over Ni-Cu catalyst was found to increase compared to Ni/SiO_2 catalyst [222]. Ni-Cu alloy catalysts showed that adsorption of methane could not be assumed to be close to equilibrium. It was assumed that a dissociative mechanism of methane followed by dehydrogenation of the adsorbed methyl species occurred [223, 224].

The carbon formation over unsupported Ni-Cu catalyst was studied during ethylene decomposition reaction and it was compared to pure Ni [225, 226]. It was inferred that Cu limits the number of Ni sites so inhibits the formation of encapsulating carbon [225]. For the same study, it was found that 70wt.%Ni-30wt.%Cu achieved a maximum conversion of ethylene over the temperature range 600-700°C.

Methane decomposition was studied over unsupported Ni-Cu catalyst [220, 227-233]. The ensemble effect of Cu showed the decrease in carbon formation and it improved the Ni catalyst activity at a temperature of 600°C.

Copper-nickel alloys were studied as hydrogenolysis catalysts [234-237]. It was reported that adding more than 5wt.%Cu to nickel decreases the activity of ethane hydrogenolysis. The loss of activity was related to geometric and electronic effects of copper to nickel. The number of available sites for adsorption was affected by geometrical change. It was mentioned that it is possible to have Ni and Cu atoms, Ni-Ni, Cu-Cu and Ni-Cu sites on the catalyst. The difference between Ni catalyst and Ni-Cu catalyst is that the amount of chemisorbed hydrogen is low in Ni-Cu catalyst compared to Ni catalyst and the adsorbed hydrogen on copper is negligible. It was

concluded that Cu atoms dilute the available Ni atoms on the surface. The electronic effect was explained since Ni-Cu causes a change in the metallic bond so the adsorption capability on the metal surface is lower than monometallic Ni catalyst.

2.6 Methane catalyst deactivation

The methane steam reforming catalysts lose their activity during the reaction. It was reported in the literature that the catalyst is deactivated via three possible routes; carbon formation, sintering and poisoning [169, 178, 212, 238-249].

2.6.1 Carbon formation

Generally, any steam reforming process is accompanied by reactions producing carbon. The carbon formation is increased with the number of carbon molecules in the reactants [178, 238, 239]. The carbon formation via methane steam reforming was categorized into three types; whisker, coke and gum carbon [212]. The main carbon formation routes are shown in Eq. 2.20-2.22 [169] (methane decomposition (Eq. 2.20), Boudouard reaction (Eq. 2.21), CO reduction (Eq. 2.22) and explained in Table 2.6 [240].

$CH_4 \rightleftharpoons C + 2H_2$, $\Delta H°_{298} = +75$ kJ/mol (Eq. 2.20)

$2CO \rightleftharpoons C + CO_2$, $\Delta H°_{298} = -172$ kJ/mol (Eq. 2.21)

$CO + H_2 \rightleftharpoons C + H_2O$, $\Delta H°_{298} = -131$ kJ/mol (Eq. 2.22)

Table 2.6. Routes for carbon formation [240].

Carbon type	Formation	Temperature range	Critical parameters	phenomena
Whisker carbon	Diffusion of carbon through Ni crystal causing nucleation and whisker growth at Ni crystal at top (Eq. 2.20-.2.22) $C_nH_m = nC + \frac{m}{2} H_2$	>450°C	High temperature Low steam to carbon ratio	Breakup of catalyst pellets
Coke (pyrolytic carbon)	Thermal cracking of hydrocarbon and deposition of carbon on catalyst C_nH_m=olefins=coke	>600°C	High temperature Low steam to carbon ratio High pressure	Encapsulating of catalyst pellets
Gum (polymer film)	Polymerization of CH_4 radicals on Ni surface into encapsulating film $C_nH_m=(CH_2)_n$=gum	<500°C	Low temperature Low steam to carbon ratio Absence of H_2	Blocking of metal surface

The carbon formed chemisorbs as a monolayer or adsorbs in multilayers leading to prevent the access of reactants to the metal surface sites. Moreover, the carbon formed might encapsulate a metal particle causing deactivation of the particle. The carbon accumulated in pores causes a fracture of metal support leading to reactor plugging and it can also lead to poor heat distribution inside the reactor bed [248]. Finally, the carbon leads to fouling of the metal surface and causes the blockage of the catalyst pores, which results in a change in physical characteristics of the catalyst support. Whisker carbon and coke formation are the main sources of carbon formation in methane reforming as explained in detail below.

2.6.1.1 Whisker Carbon

Whisker carbon is the main source of carbon formation during methane steam reforming. This type of carbon has high mechanical strength leading to damage of the catalyst particle [169]. The mechanism of whisker formation was explained in the literature via two possible routes. The first route was related to carbon transport over the bulk of the nickel particles [241-243] and the second interpretation was related to carbon transport along the graphene Ni interface [244].

In the bulk case [241-243], the methane is adsorbed on the Ni catalyst surface and several surface reactions take place, converting methane to adsorbed carbon. The carbon surface formed is segregated into layers then it diffuses through Ni so that carbon precipitates on the rear side of Ni particle. After a while, the growing carbon whisker will leave the Ni particle and the Ni particle changes the shape [169]. The carbon whisker leaves small fragments of nickel behind in the whisker. The limitation of this mechanism is that the bulk case was studied under high pressure rather than low pressure as in second mechanism explained below.

The carbon transport along the graphene Ni interface was reported [244]. The carbon nanofibers were observed during methane decomposition over supported Ni catalyst. Graphene layers were observed around the nickel crystals causing a change in the adsorption rate of C and Ni atoms. The transport of C atoms from the free surface to the graphene Ni interface was achieved by breaking of the C bond to the Ni free surface and the diffusion occurs at the graphene Ni interface.

The formation of carbon with Ni catalyst can be minimized by increasing the steam to carbon ratio [242]. This depends on reaction conditions including temperature and pressure [250]. The minimum recommended steam to carbon ratio was estimated to

be three based on thermodynamic analysis and the type of carbon formed during methane steam reforming reaction. Increasing the amount of steam will avoid the reversible reactions responsible for producing carbon.

2.6.1.2 Coke

The coke formation on Ni catalyst is due to the reaction mechanism of methane and carbide formation [243]. Methane proceeds via dissociative adsorption to form carbonaceous intermediates. Carbide is formed during the reaction and reducing the formation of carbide is required to minimize the amount of coke formed on the catalyst surface [243]. Therefore, several techniques were mentioned in the literature for coke reduction based on methane reaction mechanism.

The adsorption process itself depends on the activation energy of adsorption upon Ni, that is structure sensitive [251]. It was suggested that carbon formation needs a larger ensemble of surface sites than steam reforming [252]. As a consequence, it was suggested to control the ensemble size in order to eliminate the coke formation [212]. It is known that Ni favours carbon deposition [239, 241, 253]. Therefore; dopants are added to decrease the coke formation without affecting the reaction process [243].

The other possible way to decrease the coke formation is to use a support. The support causes a spillover of steam (OH) from the support to the nickel surface [254]. The function of the support is to provide larger surface area coverage of H_2O or OH than unsupported catalysts, which cause a low heat of adsorption preventing coke formation [255, 256]. It was concluded that methane dissociation and water adsorption are important factors to increase the catalyst resistivity for coking.

The coke deposited on the catalyst is removed using several treatment methods. The encapsulation of carbon on Ni catalyst can be removed via introducing hydrogen at 500°C. Increasing the amount of steam can also be used to remove the fresh formed carbon in the methane steam reforming process. Aged coke is removed by introducing air at temperature 500°C [257] which depends on the reactivity of carbon; during this process the air diffuses through carbon causing the burn off process. In this case, the metallic phase of catalyst will be oxidized so the controlled addition of air to nitrogen or steam was recommended.

2.6.2 Sintering

Sintering of methane reforming catalyst was reported as the major source of catalyst deactivation during methane steam reforming [169, 245-247]. The nickel sintering process took place at high reaction temperature above 500°C. Sintering causes a loss of catalytic surface area due to metal crystallite growth, a loss of the support area due to support fracture occurs and pores collapse, as it causes a chemical transformation of catalyst to non-active phase. In fact, the sintering process is slow and irreversible so the sintering should be prevented to guarantee active methane steam reforming. The sintering process is affected by many parameters such as; temperature, time, chemical medium, catalyst structure and morphology [248]. Majorly in methane steam reforming catalyst the reaction temperature and steam are the most strongly contributing factors to sintering [258].

Two nickel sintering mechanisms were proposed in the literature [249]. The particle growth can happen either by particle migration or atom migration [248, 259]. The atom migration of metals is a transfer of one atom of a metal particle to another metal

particle. In particle (crystallite) migration, the particles move to the support and collide to form larger particles as shown in Figure 2.4 [248].

In particle (crystallite) migration, the crystallites over the support migrate to another crystallite including collision and coalescence. In atomic migration, the atom migrates by detachment of metal atoms from crystallite and then it is captured by large [248] crystallites over the support surface. The difference between these two mechanisms is that atomic migration results in a particle size distribution toward small particle sizes rather than large particle size distribution as in the particle migration mechanism. This leads to fast growth at beginning of sintering and slows down later. The sintering resulting from the crystallite migration mechanism [260-262] was observed and it was affected by mass transport via diffusion of nickel atoms to nickel crystallite surfaces [263].

Finally, the sintering process in methane steam reforming is affected by high temperature (500°C) and steam. It is known that metal crystallite stability decreases with decreasing the melting temperature of the metals, however; this is not the case in the supported metals due to strong interaction between metal and the support [248]. The presence of a high amount of steam increases the sintering rate due to the formation of Ni_2-OH species at the nickel surface, which has higher diffusion energy than nickel atoms [248], this phase transformation causes loss of surface area of the support leading the nickel dispersed atoms to accelerate the sintering mechanism.

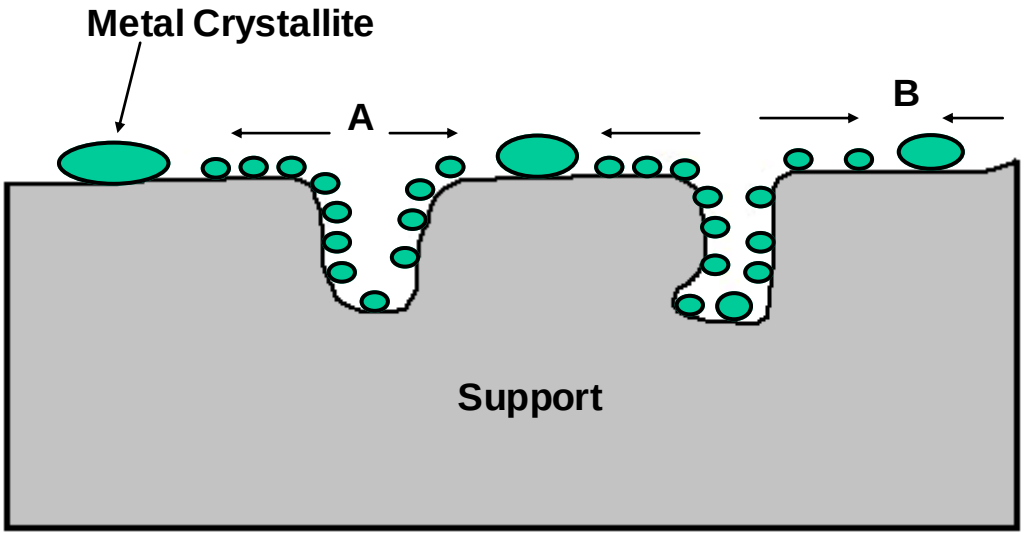

Figure 2.4. Two models for crystallite growth due to sintering by A: atomic migration or B: particle (crystallite) migration [248].

2.6.3 Poisoning

Poisoning of a nickel catalyst is majorly caused by sulphur, as for methanol steam reforming catalyst discussed in Section 2.3.2. Sulphur might exist in the feedstock and leads to the formation of hydrogen sulphide (H_2S) which chemisorbs on the metal, causing deactivation [243]. Zinc oxide catalyst is used to remove the sulphur as pre-treatment reaction to avoid catalyst poisoning [169]. The poisoned catalyst is regenerated using an oxidation reaction and is controlled by catalyst reduction.

2.7 Methane steam reforming reaction mechanism

Studying the methane steam reforming mechanism is an important consideration in order to understand the reaction process. Literature reports have discussed methane reaction mechanism as part of the methane reaction kinetics [168]. Various reaction mechanisms were explained in terms of the kinetic models, including Langmuir Hinshelwood [170], Temkin identity, two-step kinetic power law, pellet kinetics and micro kinetic analysis [255, 264]. In these models, the reaction mechanism was part of the studies which are summarized below.

In the Langmuir Hinshelwood model, it was suggested that methane adsorbs on the catalyst surface and the adsorption of methane is the rate-determining step based on methane concentration [170]. The Temkin identity proposed that the methane reaction is dependent upon the reactants and products pressure. A micro kinetic model of methane steam reforming was suggested [255]. The model showed that the surface reactions included both adsorption and dehydrogenation [255]. In addition, the micro kinetic model expanded the analysis of carbon formation and the catalyst deactivation [264]. It can be concluded from the reaction models that there is disagreement about the single rate-determining step for methane steam reforming.

The complex model of methane reaction based on Langmuir Hinshelwood was suggested [170]. The model included the three main reactions for methane steam reforming; steam reforming reaction to CO and H_2 (Eq. 2.17), water gas shift reaction (Eq. 2.18) and steam reforming of methane to CO_2 and H_2 (Eq. 2.19). The model concluded that the rate-determining step for these reactions is a surface reaction. The surface reactions for methane steam reforming reaction are listed below where S represents the surface of the catalyst [170]. The model elementary reactions are provided in equations (ER. 2.27-2.39).

$$CH_4 + S \rightarrow CH_4{}^*S \quad \text{(ER. 2.27)}$$

$$H_2O + S \rightleftharpoons O^*S + H_2 \quad \text{(ER. 2.28)}$$

$$CO^*S \rightleftharpoons CO + S \quad \text{(ER. 2.29)}$$

$$CO_2{}^*S \rightleftharpoons CO_2 + S \quad \text{(ER. 2.30)}$$

$$H^*S + H^*S \rightleftharpoons H_2{}^*S + S \quad \text{(ER. 2.31)}$$

$$H_2{}^*S \rightleftharpoons H_2 + S \quad \text{(ER. 2.32)}$$

$$CH_4{}^*S + S \rightleftharpoons CH_3{}^*S + H^*S \quad \text{(ER. 2.33)}$$

$CH_3{}^*S + S \rightleftharpoons CH_2{}^*S + H^*S$ (ER. 2.34)

$CH_2{}^*S + O^*S \rightleftharpoons CH_2O^*S + H^*S$ (ER. 2.35)

$CH_2O^*S + S \rightleftharpoons CHO^*S + H^*S$ (ER. 2.36)

$CHO^*S + S \rightleftharpoons CO^*S + H^*S$ (RDS) (ER. 2.37)

$CHO^*S + O^*S \rightleftharpoons CO_2{}^*S + H^*S$ (RDS) (ER. 2.38)

$CO^*S + O^*S \rightleftharpoons CO_2{}^*S + S$ (RDS) (ER. 2.39)

The above model was modified and discussed by Rostrup-Nielson in order to explain the steps of hydrogen generated as shown in elementary reactions (ER. 2.40-2.43) below [169]:

$CH_4 + 2^*S \rightarrow CH_3{}^*S + H^*S$ (ER. 2.40)

$CH_3{}^*S + S \rightarrow CH_2{}^*S + H^*S$ (ER. 2.41)

$CH_2{}^*S + S \rightarrow CH^*S + H^*S$ (ER. 2.42)

$H_2 + 2^*S \rightleftharpoons 2H^*S$ (ER. 2.43)

The CO_2 formation during methane steam reforming process was also explained in elementary reactions (ER. 2.44-2.49) below. The condition for CO_2 formation is to have both the water step reaction and CO step reaction at equilibrium [265].

$CH_4 + S \rightarrow CH_2{}^*S + H_2$ (ER. 2.44)

$CH_2{}^*S + H_2O \rightleftharpoons CHOH^*S + H_2$ (ER. 2.45)

$CHOH^*S \rightleftharpoons CO^*S + H_2$ (ER. 2.46)

$CO^*S \rightleftharpoons S + CO$ (ER. 2.47)

$S + H_2O \rightleftharpoons O^*S + H_2$ (Equilibrium) (ER. 2.48)

$O^*S + CO \rightleftharpoons S + CO_2$ (Equilibrium) (ER. 2.49)

Finally, the mechanism for methane steam reforming suggested that the activation of C-H bonds is responsible for methane reaction [187]. The C-H bonds showed irreversibility and desorption steps of H atoms with OH groups to form H_2 or H_2O. The reaction was dependent upon CH_4 partial pressure and independent of CO_2 and H_2O partial pressures. The reactions steps are explained below in ER. 2.50-2.60.

$$CH_4 + 2^*S \rightarrow CH_3{}^*S + H^*S \quad \text{(RDS)} \quad \text{(ER. 2.50)}$$

$$CH_3{}^*S + S \rightarrow CH_2{}^*S + H^*S \quad \text{(ER. 2.51)}$$

$$CH_2{}^*S + S \rightarrow CH^*S + H^*S \quad \text{(ER. 2.52)}$$

$$CH^*S + S \rightarrow CS + H^*S \quad \text{(ER. 2.53)}$$

$$CO_2 + 2^*S \rightleftharpoons CO^*S + O^*S \quad \text{(ER. 2.54)}$$

$$CS + O^*S \rightleftharpoons CO^*S + O^*S \quad \text{(ER. 2.55)}$$

$$CO^*S \rightleftharpoons CO + S \quad \text{(ER. 2.56)}$$

$$H^*S + H^*S \rightleftharpoons H_2{}^*S + S \quad \text{(ER. 2.57)}$$

$$H^*S + O^*S \rightleftharpoons OH^*S + S \quad \text{(ER. 2.58)}$$

$$OH^*S + H^*S \rightleftharpoons H_2O^*S + S \quad \text{(ER. 2.59)}$$

$$H_2O^*S \rightleftharpoons H_2O + S \quad \text{(ER. 2.60)}$$

From all the above mentioned models, it is concluded the reaction of carbon intermediates with oxygen are important steps. This means that oxygen has an important role in directing the reaction. This suggested the reactivity of the catalyst metal towards C-H bond activation is the governing reaction [187].

Reviewing the above models, it is concluded that methane steam reforming reaction and the relative concentrations of the products (CO and CO_2) depend on the catalyst performance and water gas shift reaction. The mechanisms of producing H_2, CO_2 and CO are explained later.

It is agreed in the literature that the methane reforming reaction is a first order reaction and it is dependent on the concentration or partial pressure of methane itself. Thus, it was realized that formation of adsorbed carbon species is the rate-determining step for the reforming process [266]. The methane steam reforming mechanism was investigated at a temperature below 700°C and it was observed that the most important issue for studying the reaction mechanism of methane was the selection of reactant and the product concentrations, which are responsible for determination of the CH_4 activation steps on the catalyst surface [171].

Since CH_4 derived intermediates chemisorb on the catalyst surface and react with H_2O, so the reaction depends on the initial activation of C-H bonds. The catalysed CH_4 derived intermediates and chemisorbed carbon are rapidly reacted with derived H_2O intermediates. This means the methane decomposes via elementary H abstraction steps to chemisorbed carbon. The chemisorbed carbon formation becomes faster as H atoms are abstracted from CH_4. After that, CH and C are formed as intermediates after couple of elementary steps in the reaction. Chemisorbed carbon reacts with H_2O co-reactants. It was found that the activation energy of the first H abstraction in CH_4 is 142 kJ/mol and the first activation energy of the C-H bond is independent of H_2O concentration [171].

The available steam oxidizes the surface of Ni, thus it speeds up the decomposition of methane as well as the formation of hydrogen and carbon oxides. The carbon oxide at the beginning of the reaction is high due to the presence of surface oxygen species [192]. Therefore, the carbon monoxide is formed due to the reaction of methane with the NiO containing catalyst. This means the reduction of Ni catalyst occurs, leading to produce carbon monoxide. The formation of hydroxyl group on the

nickel surface was investigated [192]. This group is very reactive to methane and CO compared with lattice oxygen of NiO. Thus, the oxygen accumulates on the catalyst surface at the beginning of the reaction due to steam, which results in producing CO, and then the amount of CO declines due to continuous injection of steam to the reactants. After that, hydrogen and CO_2 are formed in the reaction. CO_2 is formed due to surface reaction of hydroxyl groups and carbon. In this case, the catalyst surface is saturated with OH due to steam and the reaction producing CO does not occur. Finally, the formation of CO_2 from CO is possible in the water gas shift reaction.

2.8 Multi-fuel processor

The work carried out on research and development of a fuel reformer, which is suitable for variety of fuels, is reported in this section. Table 2.7 presents a summary of fuel reformer development worldwide. It was reported that an important objective is that a multi-fuel reformer for hydrogen production should be as reliable and efficient as those designed for a single specific fuel [32]. Therefore, the US department of energy has issued targets for multi-fuel reformer development as presented in Table 2.8.

Table 2.7. Fuel reformer developments [53, 267].

Company	**National laboratory**
Epyx Corp, Toyota , Nissan ,Praxair , Shell , Haldor Topsoe, Exxon , Innovatek, General Motors , Ford Motor Co, Ballard Power Systems, DaimlerChrysler, Johnson Matthey, Hydrogen Burner Technology	Argonne National Laboratory, Forschungszentrum Julich, Los Alamos National Laboratory

Pettersson and Westerholm [53] reported several activities for multi-fuel reformer development. The literature addressed that the multi fuel reformer has not yet

reached beyond the prototype stage and laboratory experiments are still performed. Therefore, several important issues were raised for multi-fuel reformers systems; those are summarized in Table 2.9 [38, 53-56].

A unique example of a multi fuel reformer is the model that was developed by Innovatek [48, 268] as shown in Figure 2.5. It was claimed that a fuel processor sized for 1 kW_{el} PEM fuel cell employs variety of fuels such as; methane, methanol and biofuels.

Table 2.8. US Department of Energy technical targets for fuel processor [269].

Characteristic	**Target**
Energy efficiency	80%
Power density	800 W/L
Specific Power	800 W/kg
Cost	10$/$kW_{el}$
Start-up	<1 min
Transient response	1 s
CO content (transient)	100 ppm
CO content (steady state)	10 ppm
Durability	5000 h

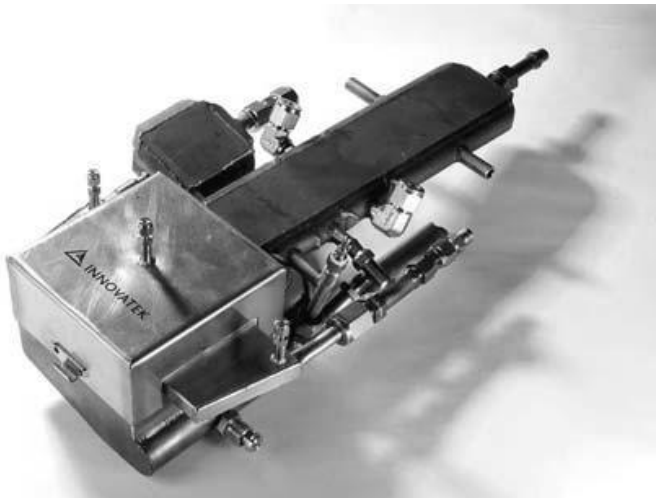

Figure 2.5. Multi-fuel processor developed by Innovatek for 1 kW_{el} PEM fuel cell [32].

Table 2.9. Multi-fuel reformers problems and possible further research.

Problem	Further required research
Catalyst development for fuel processing	• Catalyst should be active, durable, and resistant to the following: vibrations, sudden changes in flow and temperature, poisoning. • Very active for water gas shift reaction. • Developed to reduce CO contents. • Accept wide range of fuels.
Catalyst deactivations studies	• Extensive catalyst deactivation studies should address the problems associated with catalyst deactivation due to poisoning which affect the system efficiency.
Reactor development	• Reformer volume must be minimized. • The residence time should be minimized to achieve a quick response. • Fast warm up period. • Develop reactor material with high heat conductivity.
Designed fuels	• Cost of fuel • Availability of fuel • Fuel purity; sulphur content • Reforming simplicity including important fuel parameters for fuel cell application; hydrogen to carbon ratio, energy content, ease of storage, flammability.
Emission	• Minimize emissions at start up, transients and shutdown such as H_2S, NH_3, CO, CO_2.
Price	• Catalyst, reformer and heat exchangers cost including system auxiliaries costs.
System design and energy integration	• Efficient transfer of heat is needed for endothermic reaction and heat management is required to avoid catalyst deactivation.

2.9 Catalyst preparation and catalyst testing

Metal catalysts are prepared and synthesised using the appropriate selected metal salt of the material interest. Different techniques are mentioned in the literature for preparing catalysts. The procedure of catalyst development is different from one study to another. However, the principle method of catalyst development and design

criteria does not change and the steps carried out for catalyst preparation are quite similar. Catalyst testing and evaluation methods are used to study the characteristics of the prepared catalyst and the proper feedback of synthesised catalyst can be recognized.

2.9.1 Catalyst preparation

Different researchers use different procedures for preparing their catalysts and therefore the general principles are discussed below but for specific procedures the reader should refer to the literature.

2.9.1.1 Co-precipitation

In co-precipitation, the objective is to obtain a solid precipitate from a solution containing soluble precursors of both the support and the surface oxides of active metal [85]. The co-precipitation method forms a solid precipitate by changing the solution pH value that leads to precursor condensation and the formation of oxides or hydroxide of the metal. In addition, co-precipitation can be carried out by introducing ions at which the solubility of the product for the required precipitate is achieved. The final solid is obtained by further filtration and washing out of counter ions in the precipitate. This method produces better interaction between the support and the active species.

The choice of metal salt precursor or alkali used for catalyst preparation by this technique and other techniques depends on the final quality of catalyst to be synthesised. The most important factor when choosing the precursor is to avoid possible harmful effects on the prepared catalyst such as the contaminants introduced in the catalyst formulation [65].

2.9.1.2 Impregnation

The simplest method of synthesising supported metal oxide catalysts is the impregnation method. Preparation of catalyst by the impregnation method is performed by introducing a solid support material with high surface area with the liquid solution which contains dissolved oxide precursor. The impregnation solution can be aqueous or organic and the solid support material can be metal oxide or metal oxide precursor [85]. The relation between impregnating liquid volume and support volume determines the type of impregnation method. When the impregnating liquid volume equals the support pore volume, impregnation is known as incipient wetness. On the other hand, when the impregnating liquid volume is greater than the support pore volume, impregnation is known as equilibrium adsorption [85].

Catalysts for steam reforming prepared by the incipient wetness method are easy to handle. However, uniform surface coverage is not achieved using this method. The equilibrium adsorption method will produce better dispersion of surface metal oxide than the incipient wetness method but it doesn't necessarily provide uniform distribution of active species on the support surface [85]. Impregnation methods for catalyst preparation are often used due to their ease and simplicity compared to the other methods, achieving a maximum metal loading of 10wt.%.

2.9.1.3 Microemulsion

Catalysts for methanol steam reforming can be synthesised by the microemulsion technique. The microemulsion technique is used for preparing nanoparticles of catalyst. A microemulsion consists of a mixture of water, a surfactant, a surface-active agents and oil [85]. This method is based on mixing two microemulsions and aqueous solutions composed of the desired reactants in order to obtain the desired

particles. Particles are formed during collision of the water droplets in the microemulsions. Once the reactants are mixed, interchange between reactants takes place inside the water droplets which will control the final size of the metal particles and as a result the surfactant molecules will attach to the metal [85].

2.9.1.4 Sol-gel

The latest technique for catalyst preparation is the sol-gel process. A sol is a colloidal suspension of solid particles in a liquid. A gel is a continuous solid and liquid phase of colloidal dimensions and the colloid is a suspension in which the dispersed phase is so small that gravitational forces are negligible [85]. Thus, gel is formed from particles of sol when an attractive force causes them to link together. So the sol-gel process can be defined as the formation of a gel by aggregation of particles in a sol [85].

The most important advantage of the sol-gel process is its ability to produce solid phase particles from a homogeneous solution. Also it allows the preparation of both support and active sites in one single step process [85]. The sol-gel process can be also described as a multistep process in which xerogel is prepared and loaded with active metals of interest to prepare the required catalyst.

2.9.2 Catalyst drying, calcinations and activation

Catalyst synthesized by the above mentioned methods often contains precursor material, water and other contaminants. Therefore further processing is required to make the catalyst ready for use by applying drying, calcination and then activation.

2.9.2.1 Catalyst Drying and Calcination

The process of removing a large volume of moisture (70%-75%) from prepared catalyst is achieved by drying [65, 85]. A large amount of moisture inside the catalyst

pore should be evaporated. This can be achieved by using drying process at low temperature up to 100 °C. The high surface area of the catalyst and the high catalyst porosity can be achieved by carefully controlling the drying process. The drying process has a strong effect on the size of the metal particles and will lead to a fine distribution of the metal over support by chemical bonds [65, 85]. However, it was reported that un-controlled drying processes such as fast drying, slow drying and temperature gradient will lead to structure collapse with the loss of pore volume and surface area of the catalyst.

Calcination is the important step in catalyst preparation where the catalyst is exposed to high temperatures for the final formation of metal oxide catalysts. The calcination process can be achieved using one of the following thermal energy sources such as microwave oven, electric oven and gas fired furnace. The role of the calcination process can be summarised in the following points [65, 85]:

1. Thermally decompose non-oxidic precursors and unwanted ligands.
2. Oxidize the support and surface species.
3. Clean the surface from impurities by volatizing hydrogen, carbon or nitrogen.
4. Remove poisons from catalyst surface such as sulphide and halides.
5. Thermal energy will control the crystalline phase and the size of the support grain and surface oxides.
6. Active phase generation.
7. Stabilize the mechanical properties of catalyst.

Although calcination has the above mentioned advantages, calcination can cause loss of surface area and loss of surface density. This may happen during rapid increases in the calcination temperature, which may cause the support damage [85].

As a consequence of this, the pore walls of the support material cannot withstand the growing internal stress which will cause the pores to collapse. Furthermore, as an example of uncontrolled calcinations performed above 600°C, Ni salts deposited on alumina increase the amount of Ni $[Al_2]O_4$ that influences the final metal content. Ni $[Al_2]O_4$ will lower the mobility of Ni^0 atoms which will affect the rate of nucleation of particle size [65].

2.9.2.2 Catalyst Activation

Once the catalyst is prepared and calcined it should be activated before use by reduction to the metal. The reduction process is an important step for obtaining the highest catalyst surface area. The reduction is affected by several variables; the reduction temperature, time and the composition of the reducing gas. This can be accomplished by catalyst pre-treatment or catalyst activation process in the reactor before use. Twigg [57] suggested three reasons for activation of the catalyst inside the reactor, or *in-situ* reduction:

- Reduced metal catalysts are very sensitive to air.
- Correct activation is essential to achieve the proper catalyst structure.
- Activation gives a final opportunity to remove poisons and moisture from the catalyst.

Steam reforming catalysts are metal based supported catalysts. Thus, activation of catalysts requires reduction of the precursor metal oxide to the pure crystallite metals [57, 85]. Hydrogen is the most used reduction agent. Hydrogen can achieve a high surface area of metal while temperature is kept under control during the reduction process. Un-controlled temperature will cause active metal sintering during activation and will cause metal aggregation due to the loss of support materials. So as for the

calcination process, the activation process should also be controlled to avoid any structural change in the catalyst.

The reduction temperature depends on the chemical nature of the catalyst support with metal. The correct reduction temperature can achieve the highest surface area using pure hydrogen. The commercial Cu based catalysts are normally reduced at a temperature of 250°C [105]. The commercial Ni catalyst is normally reduced at 600°C. However, the reduction temperature above 600°C can cause sintering and below this temperature can lead to an incomplete and slow reduction process. The effect of reduction temperature was reported that Ni supported on γ-alumina is active when it is reduced at temperature 700°C [192], silica and zirconia are active at 500°C and NiMgO is reduced above 800°C.

The catalyst reduction period can vary from several minutes up to twenty-four hours, depending on the amount of the catalyst reduced and the reduction gas involved. An over estimated reduction time will damage the catalyst and an under estimated time gives an incompletely reduced catalyst. Pure hydrogen is recommended for the reduction since it gives the highest surface area of reduced metal.

2.9.3 Catalyst testing

The synthesized catalyst should be tested, both by characterization and reaction under realistic conditions. Testing all the properties which can affect catalyst activity, selectivity and life of catalyst should be investigated using catalyst characterization. Fresh catalyst and spent catalyst characteristics must be determined in order to understand the catalyst behaviour before and after reaction which will gives an opportunity for catalyst improvement. Thus, catalyst properties that can be tested can be classified as bulk chemical properties, surface chemical properties and physical

properties [57]. Table 2.10 explains some of general techniques used for catalyst characterization and related properties determined by these techniques.

Catalyst performance is measured in a reactor. Experimental reactors for steam reforming are developed to evaluate the activity of catalyst and selectivity for hydrogen production. The lifetime activity test of catalyst is also carried out in experimental reactors to test the catalyst durability, performance and its behaviour after an extended time of operation [57, 65].

The type of reactor used for testing depends on several pre-determined factors such as reactor feed, temperature, pressure and expected product compositions. Operation conditions are major factors which must be considered during the study of the catalyst activity [67]. In general, experimental scale steam reactors are tubes measuring 6-25 mm internal diameter by 200-300 mm length and usually contain several grams of catalyst.

The majority of the experimental scale reactors use a fixed bed reactor configuration as shown in Figure 2.6. The fixed bed reactor is externally heated to study the performance of the catalyst prepared. The reason behind using a fixed bed reactor is that this reactor can be easily implemented in the lab to test the prepared catalyst effectively. It offers close approximation to plug flow and isothermal operation, low pressure drop and is suitable for use with gas feeds.

Table 2.10. Some techniques used for determination catalyst properties [57].

Technique	Catalyst properties	Properties determined
X-ray diffraction (XRD)	Bulk chemical properties	Crystallite size, crystalline phases present
Electron microscopy	Bulk chemical properties Surface properties of catalysts	Particle shape and sizes Chemical identity and structure of surface layers
Elemental analysis	Bulk chemical properties	Bulk elemental composition
Temperature programmed reduction (TPR)	Bulk chemical properties	Size and temperature range of reduction stages
Combined gas chromatography and mass spectrometry (GC-MS)	Bulk chemical properties	Analysis of volatile and poisons over catalyst
Surface reaction of N_2O	Surface properties of catalysts	Surface area of metal components
Chemisorptions of CO,H_2, O_2	Surface properties of catalysts	Surface area of metal components
Physisorption of gases (N_2)	Surface properties of catalysts	Total surface area
Photoelectron spectroscopy	Surface properties of catalysts	Chemical identity of surface layers
Temperature-programmed desorption	Surface properties of catalysts	Chemical identity of adsorbed surface species
Spectroscopy	Surface properties of catalysts, bulk chemical properties	Types of chemical bonds
Pellet crushing	Physical properties	Catalyst compression strength
Porosimetry	Physical properties	Pore size distribution
Non-steady state gas flow through catalyst bed	Physical properties	Diffusion characteristics
Physical adsorption isotherms	Physical properties	Textural properties of catalyst

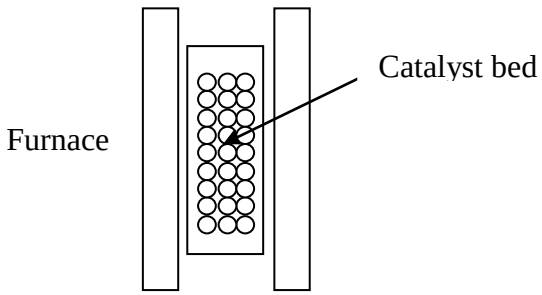

Figure 2.6. Fixed bed reactor configuration.

2.10 Chapter summary

The literature review surveyed the research carried out for methanol and methane steam reforming for hydrogen production. The literature also showed the current work developed for multi-fuel reforming. There were several works carried out for catalyst development to increase the selectivity for hydrogen production and fuel conversion. Progress was also reported for using a new active material on the catalyst for methanol and methane reactions. It was also mentioned that catalyst doping or promoting should enhance the catalyst reactivity towards hydrogen production and it would reduce the amount of CO produced and carbon formation. Several studies reported the reaction mechanism principle based on the active catalyst material used. Furthermore, the types of catalyst deactivation and source of carbon formation were investigated in order to increase the lifetime of the catalyst. Finally, the literature reported several methods and techniques for catalyst preparation and testing for methanol and methane steam reforming which might affect the overall catalytic reaction process.

CHAPTER 3

EXPERIMENTAL METHODS

This chapter discusses the experimental methods, apparatus and materials used for catalyst preparation and characterization. In addition, the test rig and experimental conditions for carrying out the methanol and methane reactions are described. The catalysts prepared and their preparation methods are explained in Section 3.1. The catalyst characterization techniques and apparatus used are described in Section 3.2. The catalyst reactivity test procedure for methanol and methane fuels and reaction parameters are explained in Section 3.3.

3.1 Catalyst preparation

The Ni_x-Cu_y/Al_2O_3 catalyst, displayed in Figure 3.1, was synthesised via an impregnation method. Both mono-metallic catalyst (10%wt.Cu/Al_2O_3 and 10%wt.Ni/Al_2O_3) and bi-metallic catalysts (7%wt.Ni-3%wt.Cu/Al_2O_3, 5%wt.Ni-5%wt.Cu/Al_2O_3 and 3%wt.Ni-7%wt.Cu/Al_2O_3) were prepared using 0.8M metal solution. Nickel nitrate ($Ni(NO_3)_2.6H_2O$) and/or copper nitrate ($Cu(NO_3)_2.3H_2O$) provided by (Fisher Scientific) were dissolved in high purity ethanol (99.8%) using a magnetic stirrer with masses of the metal salt added being listed in Table 3.1. To ensure good mixing and dissolution, the mono-metal solution was mixed for 30 minutes. However, for the bi-metallic catalyst type, a copper metal solution was prepared by mixing it for 30 minutes then nickel nitrate was added to the prepared solution and it was further mixed for 30 minutes. To the above-prepared solution, 6 grams of trilobe Al_2O_3, as shown in Figure 3.1, provided by Johnson Matthey were added and mixed for two hours using an ultrasonic mixer/heating bath (Bandelin Sonorex bath) set at a temperature of 27°C. The catalyst was dried overnight in a static oven at 100°C. In the final preparation stage the catalyst was heated for

calcination to 500°C at rate of 5°C/min, held at that temperature for 5 hours, then finally cooled at rate 5°C/min to ambient room temperature. The metal content in the prepared catalyst samples were theoretically estimated as shown in Table 3.1.

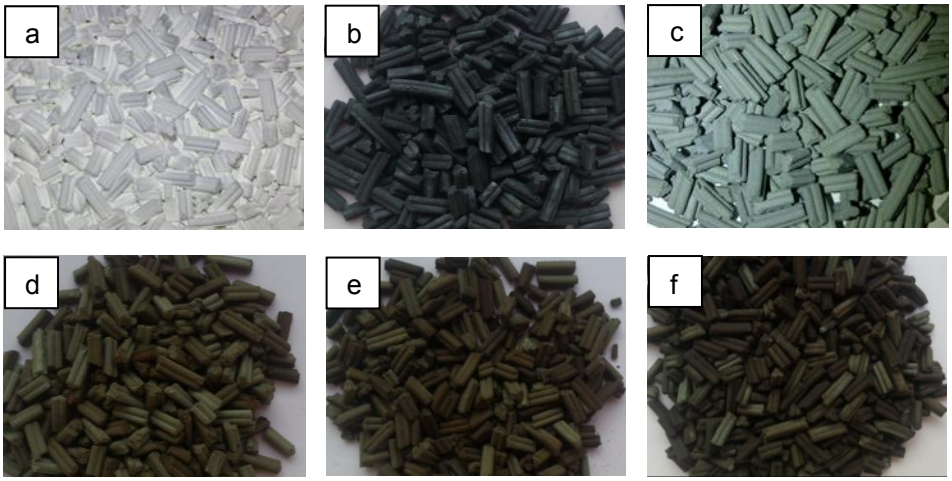

Figure 3.1. The prepared catalyst: a) Al_2O_3, b) 10%wt.Cu/Al_2O_3, c) 10%wt.Ni/Al_2O_3, d) 7%wt.Ni-3%wt.Cu/Al_2O_3, e) 5%wt.Ni-5%wt.Cu/Al_2O_3 and f) 3%wt.Ni-7%wt.Cu/Al_2O_3.

Table 3.1. Ni_x-Cu_y/Al_2O_3 catalyst preparation.

%wt.Cu	%wt.Ni	Copper nitrate added (g)	Nickel nitrate added (g)	Ethanol volume (ml)	XRF results*
10	0	2.53	0.0	13.1	9.8%Cu
0	10	0.0	3.30	14.2	9.7%Ni
3	7	0.70	2.31	13.5	6.8%Ni-3.2%Cu
5	5	1.29	1.65	13.8	5.1%Ni-4.8%Cu
7	3	1.81	0.99	13.6	2.9%Ni-7.2%Cu

*Measured by X-ray Fluorescence spectrometer (XRF).

The prepared mono-metallic catalyst (10%wt.Cu/Al_2O_3 and 10%wt.Ni/Al_2O_3) and bi-metallic catalyst (7%wt.Ni-3%wt.Cu/Al_2O_3, 5%wt.Ni-5%wt.Cu/Al_2O_3 and 3%wt.Ni-7%wt.Cu/Al_2O_3) in the rest of this work will be denoted as 10%Cu , 10%Ni , 7%Ni-3%Cu, 5%Ni-5%Cu and 3%Ni-7%Cu for brevity.

3.2 Catalyst characterization

The catalysts were characterized using X-ray Fluorescence (XRF) spectrometer, Scanning Electron Microscope (SEM), nitrogen adsorption-desorption cycles analysed by the Brunauer Emmett Teller (BET) method to determine surface area, CO chemisorption, X-ray Diffraction (XRD), Infrared (IR), Temperature Programmed Reduction (TPR) and Thermo Gravimetric Analyses (TGA). Both fresh and used catalysts were characterized and these testing methods are described in detail in the following sections.

3.2.1 XRF

A Bruker S8 Tiger X-ray Fluorescence (XRF) spectrometer was used to determine the elemental composition of the prepared catalyst samples in the solid form. The apparatus uses a dispersive wavelength XRF system. It was applied to give a quantitative analysis of the metal contents for the prepared catalyst. The apparatus is able to detect elements from oxygen through to uranium. The features of the apparatus were optimized for detecting and quantifying the elemental components of small sample sizes below one gram.

The catalysts contents were experimentally validated using XRF apparatus for which a 13 mm diameter cylindrical shaped pellet catalyst mixed with wax in ratio 5:1 was prepared. The flat surface of pellet is required. After that, the XRF measurement was set for 30 minutes scan to guarantee full elemental scan for the 13 mm diameter pellet. The elemental results were reported on the apparatus screen, providing the metal content of the prepared catalyst samples as reported here in Table 3.1.

3.2.2 SEM

A Philips XL-30 with LaB6 filament SEM fitted with an Oxford Instruments INCA Energy Dispersive X-ray Spectroscopy (EDS) system was used to study the catalyst morphology for both fresh and spent catalysts. In principle, an electron beam is scanned over the catalyst surface which will generate signals. The signals detection produces the image. The SEM apparatus uses a NordlysS camera which is able to produce images with minimal geometric distortion at a resolution of 1344x1024 pixels. The SEM captures adjusted angle from 15°-130° upon a 50x50 mm stage. The images were displayed and recorded using INCA software. The fitted EDS allowed the study of elemental composition of the scanned samples. The EDS provides quantitative analysis for elemental composition providing the elemental distribution across the scanned sample.

SEM images (Philips XL-30) of the catalyst were performed for both fresh and spent catalysts. The scanned samples were coated with gold before being introduced to the microscope chamber in order to make electrically insulating samples conducting. The external morphology of the samples was recorded in the range of 1 µm up to 100 µm and a two-dimensional image was displayed on the computer screen using INCA software. The SEM images for scanned metals species are presented in Chapter 5.

3.2.3 CO chemisorption

A Micrometrics AutoChem 2920 Analyzer was used to determine the active surface area, the percent of metal dispersion and the average particle size of catalyst, pulses of CO gas were applied to the sample. The difference between the amount of CO gas injected and the amount of CO detected in the exhaust from the sample tube can be used to determine the amount of chemisorbed CO gas [270, 271].

The flow diagram of the chemisorption analysis is shown in Figure 3.2. One gram of fresh crushed catalyst was placed inside a 10 mm diameter fused quartz sample tube and secured in place with quartz wool. In 10%H_2/90%Ar was flowed over the catalyst for 2 hours at a rate of 10 ml/min at the corresponding reduction temperature of the catalyst obtained from the TPR test (Section 3.2.7 and Section 5.6 of Chapter 5) to reduce the oxidised catalyst to the metallic form. Then, for purging purposes helium gas was flowed through the sample tube at a rate of 10 ml/min and the sample was cooled to ambient temperature of 30°C. Finally, the CO pulse adsorption test was performed at a CO flow rate of 20 ml/min using helium as carrier gas at a flow rate 50 ml/min. A loop volume of 0.5389 ml CO was injected until the area of the peaks were equal, indicating no further adsorption on the sample or up to a maximum of twenty pulse injections. The remaining of CO in the exhaust from the sample tube which was not adsorbed on the catalyst was recorded by Thermal Conductivity Detector (TCD).

CO pulse chemisorption was applied to the prepared catalysts in order to determine percent metal dispersion, active metal surface area and active metal particle size. The injected CO gas reacts with active sites until all active sites are consumed or covered with chemisorbed CO. Therefore, the amount of adsorbed gas is measured in order to calculate percent metal dispersion and active metal surface area. CO pulse chemisorption carried out in this study determines percent metal dispersion as shown in Eq. 3.1, the effective metallic surface area per gram of sample as shown in Eq. 3.2 and the active particle size as given in Eq. 3.3.

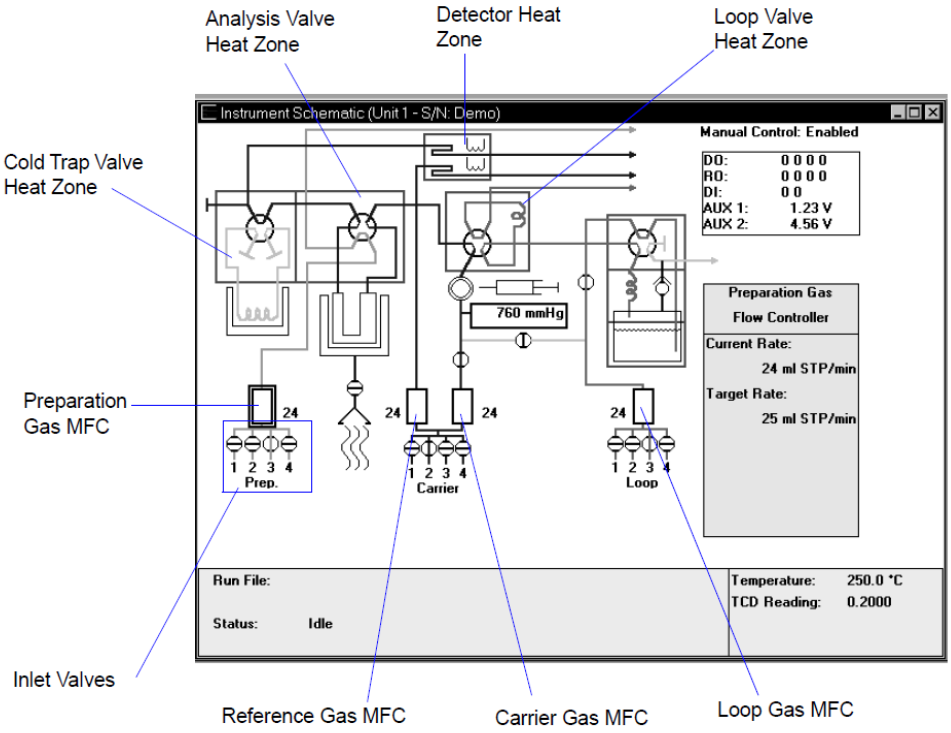

Figure 3.2. The flow diagram for chemisorption apparatus [270].

$$PD = 100\left(\frac{V_s \times SF_{calc}}{SW \times 22414}\right)GMW_{calc} \qquad \text{(Eq. 3.1)}$$

Where:

PD : percent dispersion (%)

V_S : Volume sorbed (cm^3 at STP)

SF_{calc} : calculated stoichiometry factor

SW : sample weight (g)

GMW_{calc} : gram molecular weight (g/g-mole)

$$SA_{Metallic} = \left(\frac{V_s}{SW \times 22414}\right) \times (SF_{calc}) \times (6.123 \times 10^{23}) \times (SA_{calc}) \qquad \text{(Eq. 3.2)}$$

Where:

$SA_{Metallic}$: metallic surface area (m^2/g of metal)

SA_{calc} : calculated specific surface area

$$APS = \frac{6}{(D_{calc}) \times \left(\frac{W_s}{GMW_{calc}}\right) \times (6.023 \times 10^{23}) \times (SA_{calc})} \quad \text{(Eq. 3.3)}$$

Where:

APS : active particle size

D_{calc} : calculated metal density (g/cm^3)

W_S : sample weight (g)

From Eq. 3.1-3.3 [270], SF_{calc} , GMW_{calc}, SA_{calc} and D_{calc} were determined in order to estimate percent dispersion as illustrated in Appendix 9.1.

3.2.4 Nitrogen adsorption-desorption

In order to determine the catalyst surface area and average pore size for fresh and spent catalysts, the samples were analysed by the nitrogen adsorption-desorption method. The technique enables to understand the physical changes to the catalyst structure as well as the sintering effects to be probed and quantified in terms of changes to the surface area. The measurements were carried out over approximately 1.4 g of catalyst sample using a Micrometrics ASAP 2010 analyser. Accelerated Surface Area and Porosimetry (ASAP) uses the static volumetric technique to determine surface area using N_2 physisorption isotherms at -196°C. The sorption measurements were conducted over the range of relative pressures from 0.01 to 0.99 during adsorption and the relative pressure was subsequently reduced to 0.14 during the desorption stage. The volume of gas adsorbed was recorded by the instrument. Then the experiment data collected was used to calculate the BET [272] surface area and average pore size as explained in calculated example in Appendix 9.2. The calculations were performed using the linearized form of the BET equation as given in Eq. 3.4 [65, 273]. Furthermore, the analysis of Brunauer, Deming, Deming and Teller (BDDT) were also performed to understand the porosity of the

tested samples, as explained below, by plotting the isotherms graphs, as will be explained in Section 5.2 of Chapter 5, Section 6.3.2 of Chapter 6 and Section 7.3.2 of Chapter 7.

$$\frac{P}{V(P_0 - P)} = \frac{1}{V_m C} + \frac{(C-1)}{V_m C}\frac{P}{P_0} \quad \text{(Eq. 3.4)}$$

Where:

P : pressure (mmHg)

P_0 : saturated vapour pressure of gas (mmHg)

V : volume of gas adsorbed at pressure P (cm^3)

V_m: volume of gas for monolayer formation (cm^3)

C : a constant for a particular system

Physical adsorptions isotherms plots can be classified into six types, labelled I through VI as shown in Figure 3.3 [272-274]. Type I is referred to as physisorption on microporous materials that have extremely fine pores at which Langmuir area can be calculated. Physical adsorption upon non-porous or possibly macroporous samples, associated with high energy of adsorption, is represented by Type II. Conversely, the characteristic of materials that are non-porous or macroporous and with low energy of adsorption is shown in Type III. The materials which contain mesoporosity and hysteresis gives rise to a Type IV isotherm shape with a high energy of adsorption and a Type V shape with a low energy of adsorption. Type VI is the stepped isotherm and is attributed to several possibilities including multiple pore sizes.

Hysteresis loops are classified into four types as shown in Figure 3.4 [273]. Each hysteresis loop type has its own characteristics and interpretations with respect to pores of the tested material [275]. The H1 Type indicates regular even pores without interconnecting channels. Narrow pores and interconnecting channels can be found in Type H2. Hysteresis loop Type H3 can be a yield of Type II isotherms without

pores. The hysteresis loop of Type H4 covers a large range of relative pressures with slit-like pore for Type I isotherm.

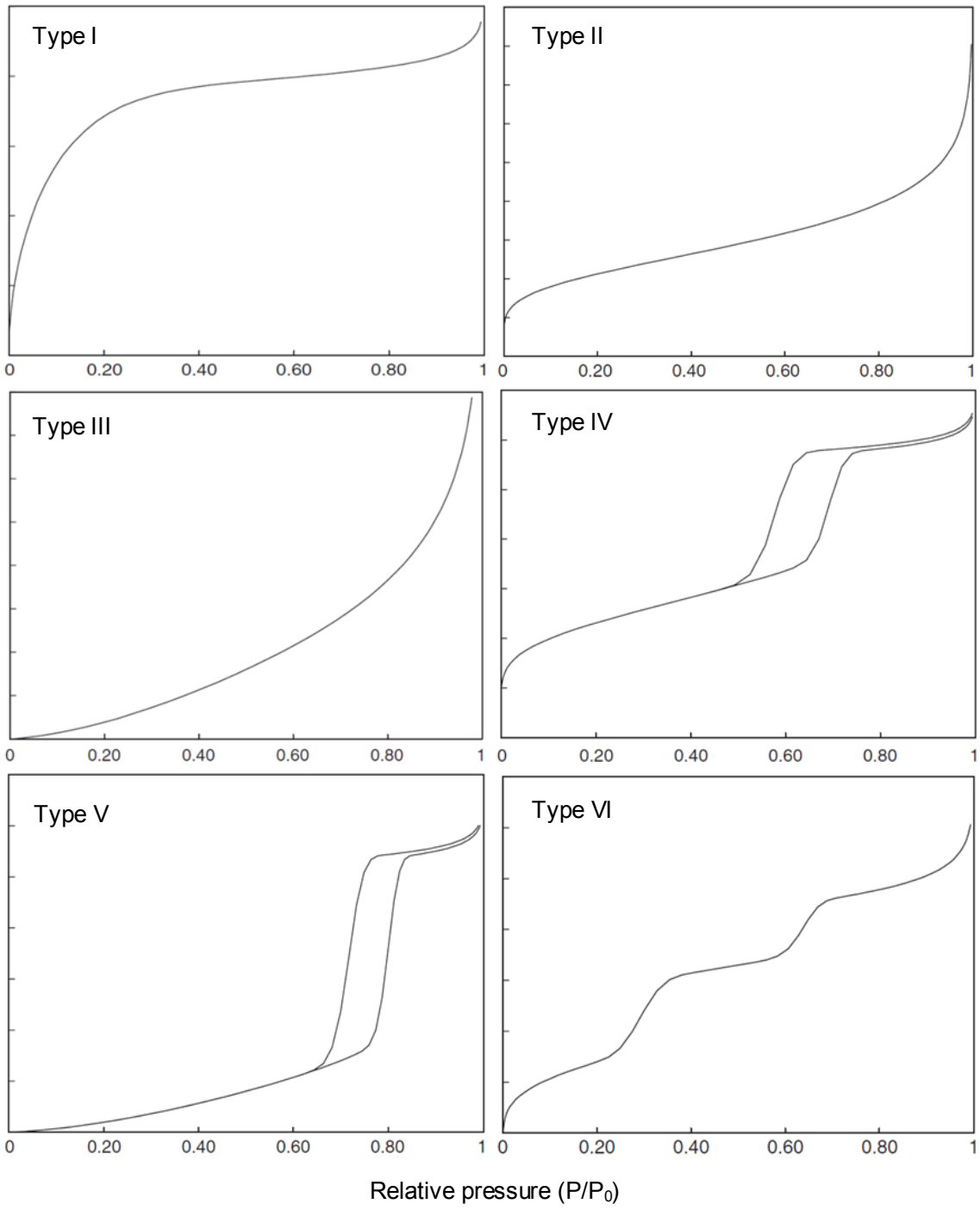

Figure 3.3. Types of adsorption isotherm in the classification of BDDT [273].

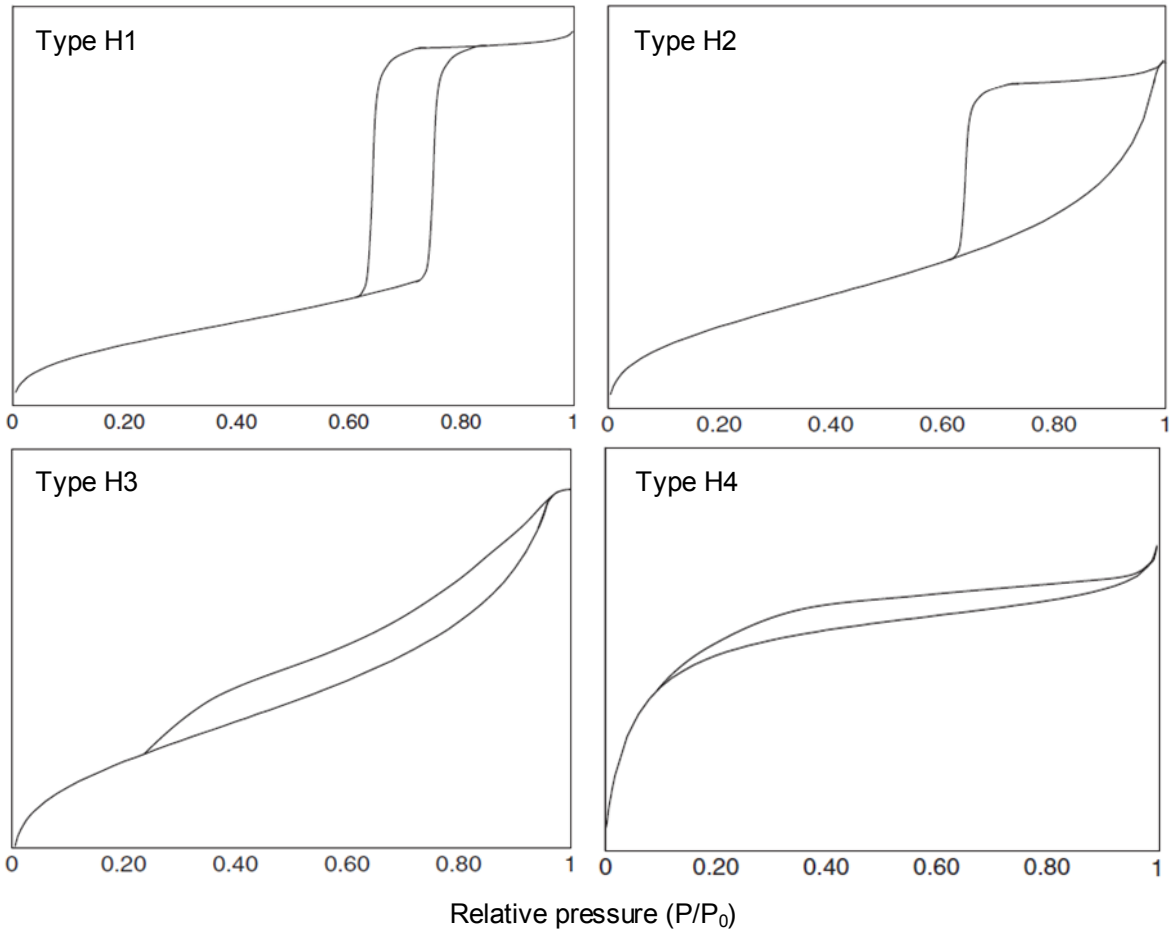

Figure 3.4. The four types of hysteresis loops according to IUPAC [273].

3.2.5 XRD

In order to identify the crystal phases of catalysts and to determine the crystal particle sizes, XRD characterization was performed using a Bruker D8 Advanced Diffractometer. The apparatus is applied to routine measurements of powder X-ray diffraction patterns to identify the crystalline phases and determine the crystal structure. The measurements using the apparatus can generate X-ray diffraction patterns up to 1100°C in air. The coupled high resolution powder X-ray LynxEye position detector and monochromatic Cu radiation enables to generate diffraction lines. In powder particles, an elastic scattering of X-ray photons by atoms occurs and

diffraction lines appear. The Scherrer formula relates crystal size to line width as shown in Eq. 3.5 [65, 276]:

$$L = \frac{K\lambda}{\beta \cos\theta} \qquad \text{(Eq. 3.5)}$$

Where:

L : crystallite size (nm)

K : a constant

λ : X-ray wavelength (nm)

β : the peak width (degree)

θ : the Bragg angle (degree)

The catalyst was crushed using a mortar and pestle in order to obtain a powder of the catalyst then it was scanned and recorded at room temperature in the two theta range from 30° to 90°, with 0.02° step size and Cu*Kα* radiation, *λ*=0.154 nm and *K*=0.9. The XRD patterns were matched and assigned according to the XRD database (PDF-4+2012) provided by International Centre for Diffraction Data (ICDD).

3.2.6 IR

The surface composition of the catalyst was studied by applying infrared spectroscopy to identify adsorbed species on the catalyst surface. Absorption of photons in infrared range wave number 4000-400 cm^{-1} occurs and gives rise to absorption bands which can be identified as being associated with the vibrations of particular functional groups or bonds adsorbed upon the active sites of the catalyst. Infrared spectra of catalyst were recorded using a Bruker Tensor 37 spectrometer. Before the infrared spectrum of the catalyst was determined, a background signal was run on pure KBr powder in air. This is performed in order to remove the signal from water vapour and CO_2 that are considerable absorbers of infrared from the final spectrum by subtracting the background signal from the experimental signal of

interest. Then, the catalyst was crushed using a pestle and mortar then it was mixed with KBr powder at ratio of 1:10. All samples were sieved at a particle size of less than 75µm. The sieved sample was loaded into the cup of diffuse reflectance collector location. The used diffuse reflectance apparatus was a Harrick Praying Mantis Diffuse Reflection Accessory which is specially designed for examining powders by reflection spectroscopy [277]. Spectra over the range 4000-400 cm^{-1} at room temperature were collected with 64 scans and a resolution of 4 cm^{-1} using a Deuterated TriGlycine Sulfate (DTGS) detector.

3.2.7 TPR

The TPR analysis is used to record hydrogen uptake by a catalyst sample as a function of a programmed ramp increase and therefore indicates peaks of hydrogen consumption by adsorption and corresponding temperatures at which reduction of the sample occurs. It is also used to identify the number of reducible species that appear upon the catalyst surface [270, 271]. Therefore, the catalyst should contain reducible metals in order to apply the TPR test. Typically, hydrogen gas is flowed over the sample and the unreacted gas at the exhaust from the sample tube is measured by a TCD while the temperature of the sample is increased at a defined rate. The hydrogen uptake volume and corresponding reduction temperature are recorded.

The TPR runs were conducted using a Micrometrics AutoChem 2920 Analyzer on one gram of fresh catalyst ground by pestle and mortar. The catalyst sample was pretreated using argon as preparation gas at flow rate 50 ml/min for cleaning the entire lines of the apparatus (Figure 3.2). The sample was pretreated by increasing the temperature up to 500°C at 10°C/min and held for one hour in order to remove

any moisture from the sample and tube, then the sample was cooled down to ambient temperature. After that, 10%H_2/90%Ar at flow rate of 50 ml/min was introduced and the temperature was increased to 900°C at 10°C/min to record hydrogen uptake using TCD.

3.2.8 TGA

A TGA was carried out using a NETZSCH TG 209 F1 instrument [278]. The mass of the used catalyst was monitored against the programmed temperature in order to study the mass changes of carbon formed on the used catalyst [279]. The sample was introduced to the TGA instrument in an aluminium crucible that can resist a high increase in the temperature. During the TGA process carbon deposited on the sample in the reaction was removed from the catalyst by oxidation in air at a flow rate of 50ml/min and heating the sample (20 mg) in the oven chamber from 25°C to 900°C at a ramp rate of 10°C/min. Then, the percentage mass changes with temperature were recorded. The mass loss recorded in Figure 3.5 represents the two counteracting effects of carbon burn off and metal oxidation. Therefore, the carbon formation was calculated in this work. The measured mass loss by TGA is assumed as sum of complete metal oxidation to NiO and Cu_2O and carbon burn off. The calculation assumed that the catalyst was fully reduced before performing TGA as explained in Section 6.3.4 and Section 7.3.4 of Chapter 6 and Chapter 7, respectively.

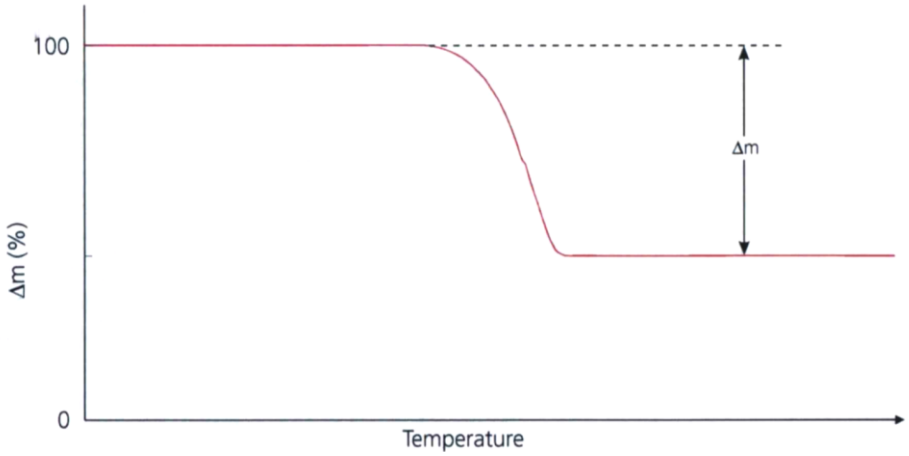

Figure 3.5. Typical TG curve presenting mass change versus temperature [279].

3.3 Catalytic reactivity test

Methanol and methane steam reforming reaction were investigated in terms of reaction conditions, fuel conversion and amount of H_2, CO_2 and CO produced. The prepared catalysts were examined for the reforming of both fuels in a multi-fuel reformer experimental test rig as described in the following sections.

3.3.1 Experimental multi-fuel reformer test rig

The multi-fuel reformer experimental test rig was used to test the catalyst activity for methanol and methane reactions. The experimental rig consists of three modules; the feed, reactor and gas analysis modules as illustrated on the flow sheet in Figure 3.6. A photograph of the physical rig used for carrying out the reaction is shown in Figure 3.7.

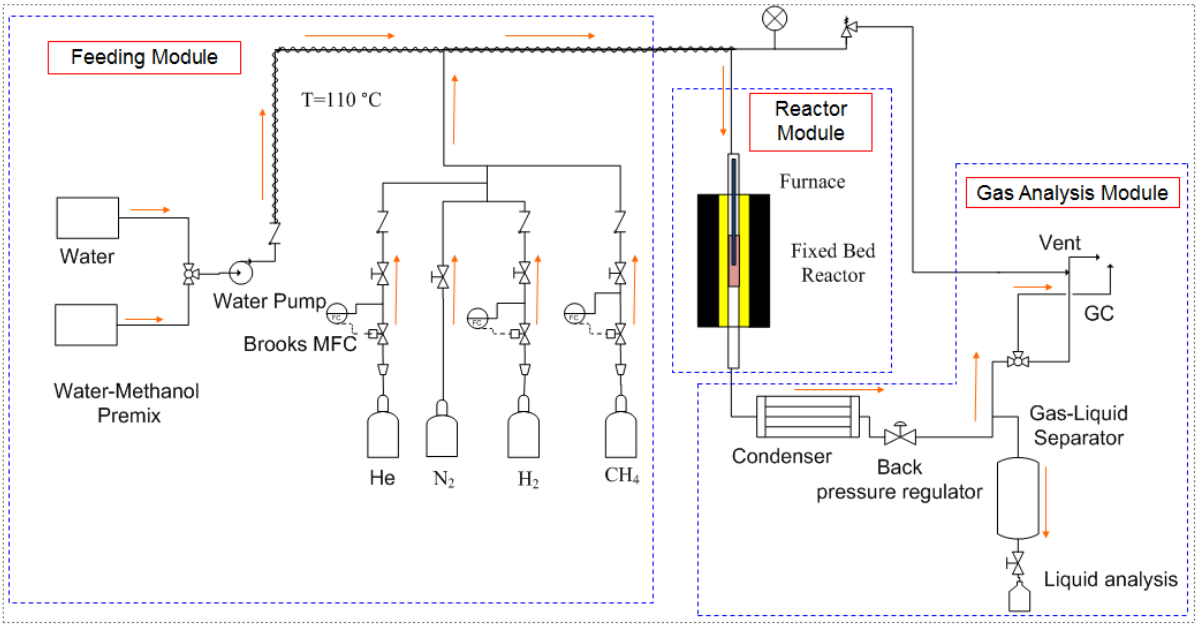

Figure 3.6. Experimental test rig flow sheet diagram.

Figure 3.7. Experimental test rig.

The feeding module is composed of a Cole-palmer EW-74930-05 series one pump which can supply water or water-methanol premix to the vaporization zone and reactor. A vaporizer constructed from trace heating tape (OMEGA FGR-100) wrapped around the feed pipe is used to generate steam at 110°C, the temperature of which was controlled using a West 2300 PID controller. Digital Brooks mass flow controllers were used to control the flow rate of the various gases fed to the reactor during the catalytic tests.

The reactor module consists of a high temperature furnace (Severn Thermal Solutions Ltd.) that can withstand temperatures up to 1200°C and controlled via EUROTHERM PID controller. Inside the furnace, the fixed bed reactor was constructed of stainless steel tube (316L) with inner diameter 10.9 mm, wall thickness 0.89 mm and tube length of 395 mm. To ensure satisfactory heat conductivity between reactor wall and inner furnace wall, marble chips (2-3 mm particle size) provided from Fisher Scientific were packed into the annulus between the reactor and the furnace walls. Three grams of catalyst were packed into the reactor and the void space above and below was filled with glass beads; the catalyst bed height was 50mm in the centre of the reactor as shown in Figure 3.8. The temperature of the reactor was measured using a K type thermocouple fixed near the centre of the bed.

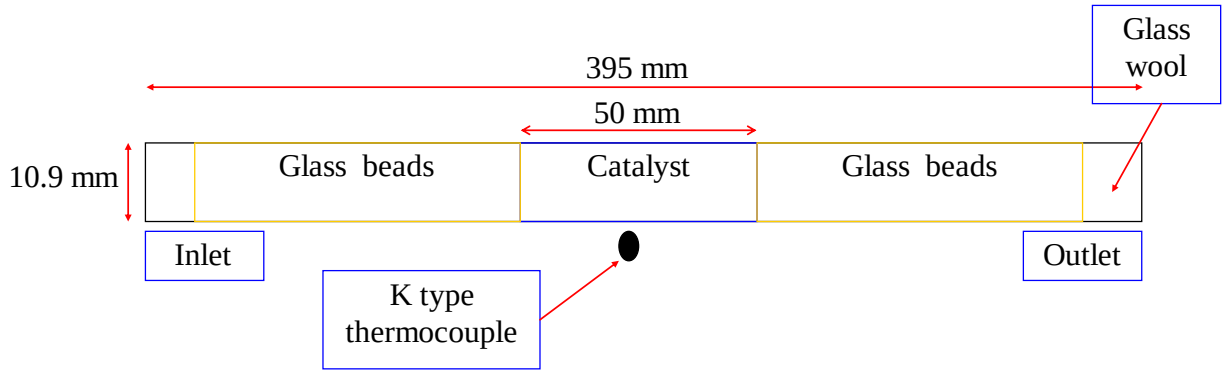

Figure 3.8. Fixed bed tube diagram.

The reformate stream at the outlet of the reactor was cooled before proceeding for gas analysis. Therefore, a condenser facilitated by ice cubes in a bath surrounding a coiled section of the reactor outlet pipe at a temperature of -2°C was used. After cooling, the unreacted liquid was separated from gaseous stream in a specially designed gas-liquid separator unit. The various gases generated in the reaction were transferred for analysis via an unheated direct transfer line and analysed using a Refinery Gas Analyzer (RGA) manufactured by Agilent. The reformate gases were sampled using an online connection to Agilent 7890A model gas analyzer. The gas sample duration was five minutes before the generated gas was withdrawn out to the vent.

The refinery gas analyzer is equipped with seven columns, five valves and three detectors consisting of Flame Ionization Detector (FID) and two TCD [280]. A schematic diagram of the RGA is shown in Figure 3.9. The FID was used to detect all hydrocarbons to C5, C6, C6+ components in column 6 and 7. Gases that cannot be ionized were detected using TCD2 and TCD3. TCD2 signal detected methane, CO_2 and CH_4 in column 2 and CO, N_2, O_2 in column 3. The third TCD was dedicated to measuring hydrogen in column 4. The methods of analysis including types of

columns used are explained in Table 3.2 and the GC calibration is illustrated in Appendix 9.3.

Table 3.2. GC conditions for gas analysis.

Oven temperature program	60°C hold 1 min, to 80°C at 20°C/min , to190°C at 30°C/min , then 45°C/min to100°C hold 4 min
Valve temperature	120°C
FID channel	
Front inlet	120°C, split ratio 200:1
Column	#6: DB-1 #7: HP-AL-S
Column flow (He)	3 ml/min (13.8 psi), constant flow mode
FID	
Temperature	250°C
H_2 flow	40 ml/min
Air flow	400 ml/min
Make up (N_2)	25 ml/min
Second TCD channel	
Column	#1: HayeSep Q 80/100 mesh #2: HayeSep Q 80/100 mesh #3: Molecular sieve 5A, 60/80 mesh
Column flow (He)	22 ml/min , constant flow mode
Procolumn flow (He)	3 psi, constant pressure mode
TCD	
Temperature	250°C
Reference flow	45 ml/min
Make up	2 ml/min
Third TCD channel	
Column	#4: HayeSep Q 80/100, mesh #5: Molecular sieve 5A, 60/80, mesh
Column flow (N_2)	22 ml/min , constant flow mode
Procolumn flow (N_2)	3 psi, constant pressure mode
TCD	
Temperature	250°C
Reference flow	45 ml/min
Make up	2 ml/min

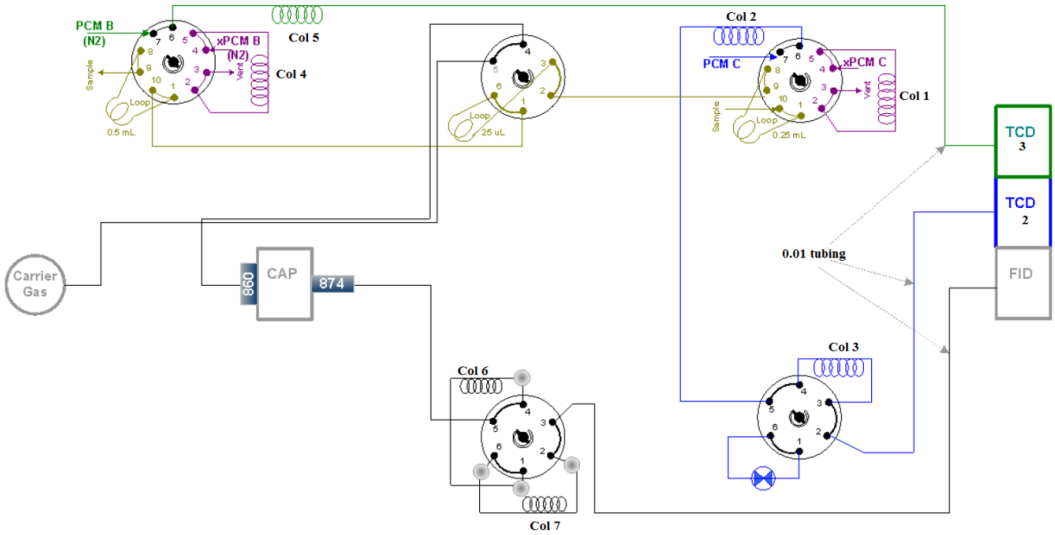

Figure 3.9. Schematic diagram of RGA [281].

3.3.2 Methanol steam reforming activity test

Measurements of the steam reforming of methanol were conducted in a fixed tubular bed reactor. Three grams of catalyst were packed in the middle of the reactor to a bed height of 50 mm. Glass beads were used to hold the catalyst in the middle of the reactor and glass wool was added to the reactor outlet to prevent any traces of consumed catalyst to enter the analysis module. Before the reaction commenced, the system was purged with N_2 for five minutes to remove the air from the pipes and reactor bed. Then, hydrogen at flow rate of 10 ml/min was introduced to reduce the catalyst at its reduction temperature determined from TPR test (Section 5.6 of Chapter 5). The reduction process was carried out by raising the temperature to its target point at a rate of 5°C/min and maintaining it for 30 minutes in hydrogen flow before switching to pure N_2 for purging.

Methanol steam reforming was carried out at temperatures of 225, 250, 275, 300 and 325°C in order to study the catalyst reactivity and methanol conversion as will be explained in Sections 6.1 and 6.2 of Chapter 6. Distilled water mixed with pure

methanol (99.99%) in a specific mole ratio of 1.3 and 1.7 was injected using the pump at constant flow rate of 0.06 ml/min. Then, the reactor was left for one hour in order for the temperature to stabilize under the reaction conditions. Once stable operation was achieved, samples were withdrawn for gas analysis, which was repeated every 15 minutes and recorded for three hours run duration of the catalyst reactivity test. Helium gas was used as carrier gas at flow rate 8 ml/min to facilitate the flow of reformate to RGA. The output flow rate was measured manually using bubble flow meter and stopwatch to calculate the flow rate of reformate. In order to study methanol conversion and products yields; an elemental analysis using reactor exist concentrations of CO, CO_2, CH_4 and H_2 and the inlet flow of methanol was performed as explained in Section 6.1 of Chapter 6.

3.3.3 Methane steam reforming activity test

Measurements of the steam reforming of methane were conducted according to similar methods as methanol steam reforming. However, the tested operation conditions such as temperature, flow rate and steam to carbon ratio were changed in order to study the effect of these variables upon the reaction performance. Three grams of catalyst were packed in the middle of the reactor to a bed height of 50 mm, with again the remainder of the volume being filled with glass beads and glass wool. Methane steam reforming was carried out at temperatures 500, 550, 600, 650 and 700°C in order to study the catalyst reactivity and methane conversion as explained in Sections 7.1 and 7.2 of Chapter 7. Pure methane (99.99%) was injected into the reactor feed line at a flow rate of 25 ml/min. Helium gas was used as carrier gas at flow rate 8 ml/min to facilitate the flow of reformate to RGA. The steam generated through the trace heating was mixed with methane at mole ratios of 2:1 and 3:1, with the flow rate being controlled using the pump. Then the reformate was analysed

using the RGA. In order to study conversions and products yields; an elemental analysis using reactor exist concentrations of CO, CO_2, CH_4 and H_2 and the inlet flow of methane was performed as explained in Section 7.1 of Chapter 7.

CHAPTER 4

CHEMICAL EQUILIBRIUM ANALYSIS OF METHANOL AND METHANE STEAM REFORMING

In this chapter, the chemical equilibrium analysis of methanol and methane reforming reactions are discussed. The chemical equilibria for both reactions (Sections 4.1 and 4.2) were calculated by the use of freely available CEA program from http://www.grc.nasa.gov/WWW/CEAWeb/. CEA is a program which calculates chemical equilibrium product concentrations from any set of reactants based on minimization of Gibbs free energy. The results of equilibrium analysis were presented in terms of fuel conversions and products yields from the predicted mole fractions of CEA program. The calculated results of methanol and methane reforming reactions were plotted to illustrate the trends of fuel conversions and products yields and at different temperatures and steam to carbon ratios, as discussed later in this chapter.

4.1 Chemical Equilibrium analysis of methanol steam reforming

The chemical equilibrium of methanol steam reforming reaction is studied in order to predict the amount of reformate produced during the reaction. The methanol steam reforming in Eq. 4.1 [70-74] is comprised of the decomposition reaction of methanol (Eq. 4.2) and water gas shift reaction (Eq. 4.3) [71, 75, 76].

$CH_3OH + H_2O \rightleftharpoons CO_2 + 3H_2$, $\Delta H°_{298} = +49.5$ kJ/mol (Eq. 4.1)

$CH_3OH \rightleftharpoons CO + 2H_2$, $\Delta H°_{298} = +90.2$ kJ/mol (Eq. 4.2)

$CO + H_2O \rightleftharpoons CO_2 + H_2$, $\Delta H°_{298} = -41$ kJ/mol (Eq. 4.3)

In order to study the conversions and products yields; the total number of moles in the equilibrium product is calculated by performing a carbon balance as presented in

Eq. 4.4. The moles of carbon entering the reaction from methanol will equal the carbon leaving the reaction. The Eq. 4.4 contains unknown n_{out}.

$$\left(1\times y_{CO}+1\times y_{CO_2}+1\times y_{CH_4}+1\times y_{CH_3OH}+1\times y_C\right)\times n_{out}=n_{CH_3OH,in} \quad \text{(Eq. 4.4)}$$

$$y_i = mol\ \ fraction\ of\ species\ i,\ \ obtained\ \ from\ CEA\ program$$

$$n = total\ \ moles$$

Where, in and out subscribts denote releveant mol enetring or leaving the reaction.

The conversions for methanol and water were obtained by:

$$x_{CH_3OH}=\frac{n_{CH_3OH,in}-n_{CH_3OH,out}}{n_{CH_3OH,in}} \quad \text{(Eq. 4.5)}$$

$$x_{H_2O}=\frac{n_{H_2O,in}-n_{H_2O,out}}{n_{H_2O,in}} \quad \text{(Eq. 4.6)}$$

The moles of products from the reaction were calculated by:

$$n_{i,out}=y_i\times n_{out} \quad \text{(Eq. 4.7)}$$

Where $n_{i,out}$ is total moles of species i.

The products yields for hydrogen, carbon dioxide and carbon monoxide were obtained in mol per mol of methanol:

$$H_2 yield=\frac{n_{H_2,out}}{n_{CH_3OH,in}} \quad \text{(Eq. 4.8)}$$

$$CO_2 yield=\frac{n_{CO_2,out}}{n_{CH_3OH,in}} \quad \text{(Eq. 4.9)}$$

$$CO\ yield=\frac{n_{CO,out}}{n_{CH_3OH,in}} \quad \text{(Eq. 4.10)}$$

CEA in methanol steam reforming was programmed to run with all possible products by entering the moles of methanol (1 mol) and water (1.3 and 1.7 mol). All products were considered but whose mole fractions were less than $5x10^{-6}$ were negligible in calculations. Reaction temperatures were set to a range between 225-325°C with output values obtained for every 25°C interval at atmospheric pressure. The methanol conversion was complete and the products of methanol steam reforming were CH_4, CO_2, CO and H_2 as shown in Figures 4.1-4.4.

Figure 4.1 reveals that methane is the dominant product in methanol steam reforming. The two methanation reactions shown in Eq. 4.11 and Eq. 4.12 are strongly exothermic. This explains that the amount of methane in the products decrease with increasing the reaction temperature. Methanation reactions would consume CO_2, CO and valuable H_2 in the syngas products as shown in Figures 4.2-4.3, respectively. Methanation of both CO and CO_2 produce water, which explains the negligible effect of increasing S/C from 1.3 to 1.7.

$$CO + 3H_2 \rightleftharpoons CH_4 + H_2O \quad , \Delta H°_{298} = -206.2 \text{ kJ/mol} \qquad \text{(Eq. 4.11)}$$

$$CO_2 + 4H_2 \rightleftharpoons CH_4 + 2H_2O \quad , \Delta H°_{298} = -165.0 \text{ kJ/mol} \qquad \text{(Eq. 4.12)}$$

According to the results obtained in Figures 4.1-4.4, methanol steam reforming catalysts should have no methanation activity and therefore copper-based catalysts are used for methanol steam reforming. The presence of metallic Ni in the catalyst would promote the methanation reaction.

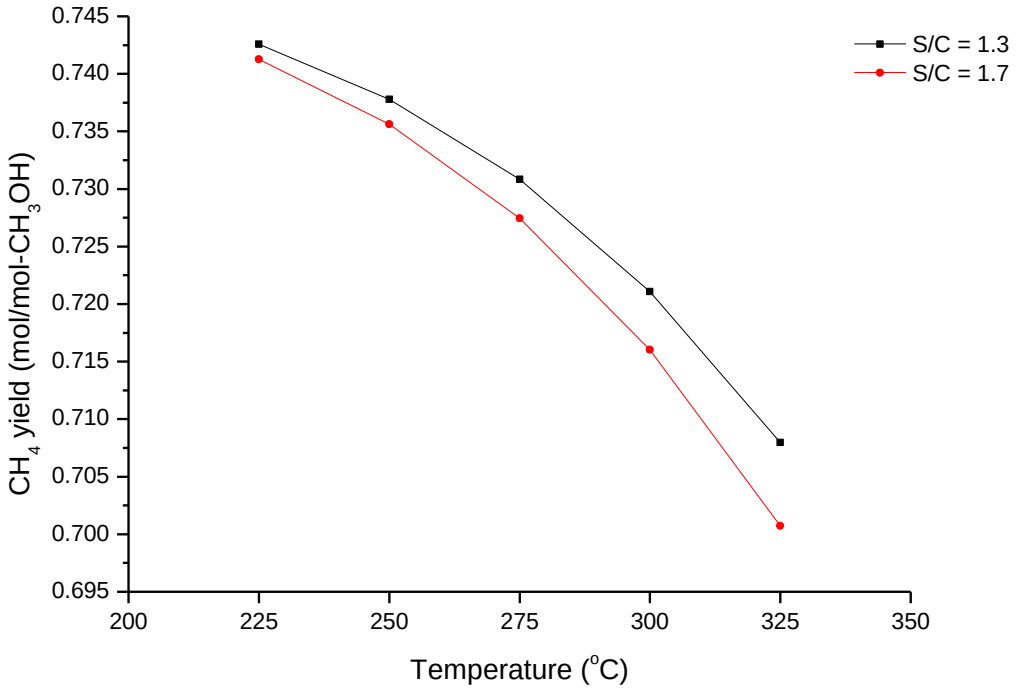

Figure 4.1. Equilibrium methane yield at various methanol reaction temperatures at S/C of 1.3 and 1.7.

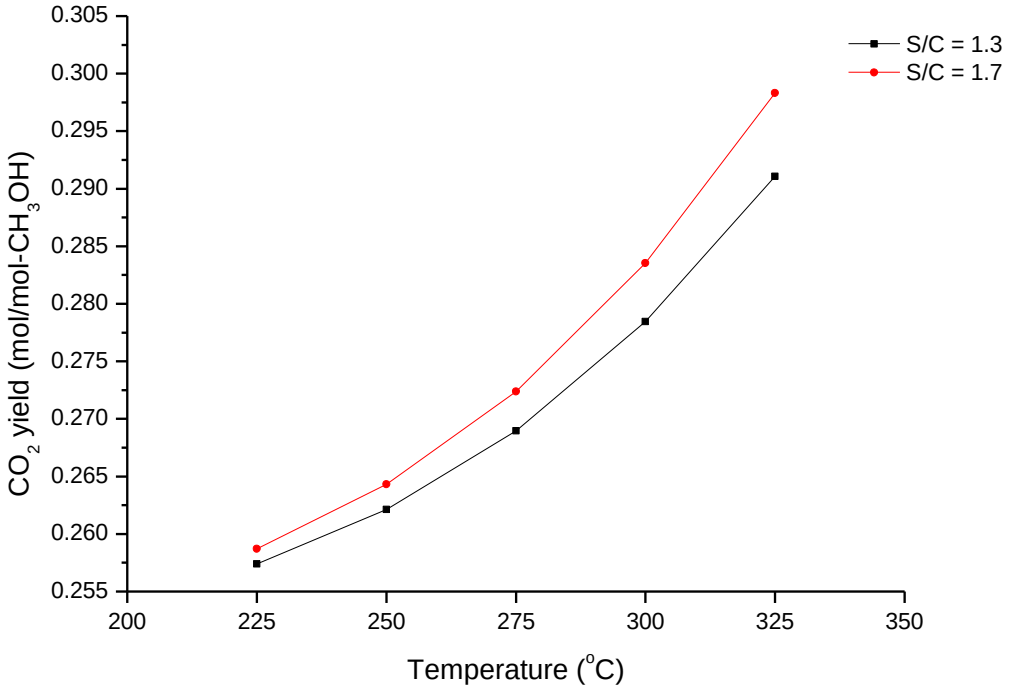

Figure 4.2. Equilibrium CO_2 yield at various methanol reaction temperatures at S/C of 1.3 and 1.7.

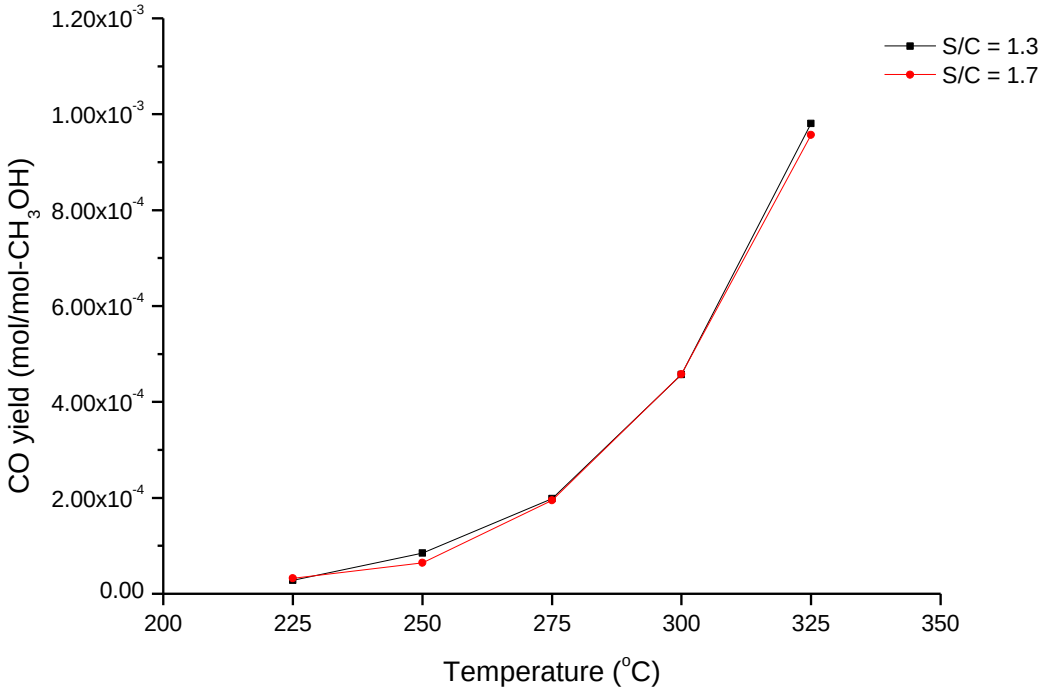

Figure 4.3. Equilibrium CO yield at various methanol reaction temperatures at S/C of 1.3 and 1.7.

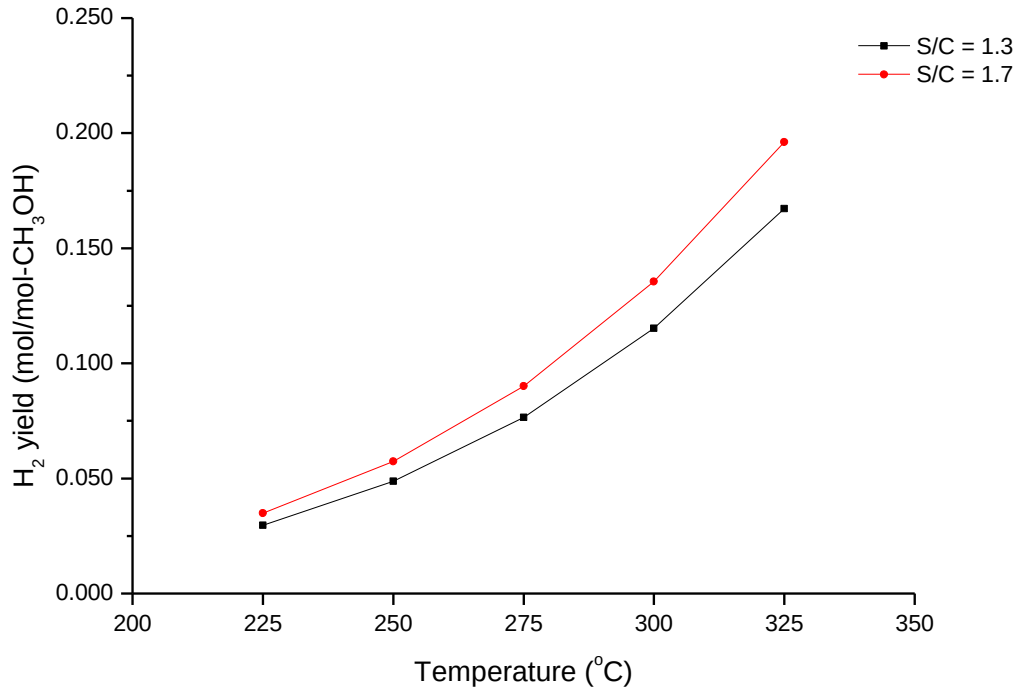

Figure 4.4. Equilibrium H_2 yield at various methanol reaction temperatures at S/C of 1.3 and 1.7.

In order to predict the equilibrium products for methanol steam reforming over active methanol catalyst, CEA in methanol steam reforming was programmed to run by omitting CH_4 as a product (just CO and CO_2 as potential carbon products) by entering the moles of methanol (1 mol) and water (1.3 and 1.7 mol). Reaction temperatures were set to a range between 225-325°C with output values obtained for every 25°C interval at atmospheric pressure. The methanol conversion was complete (Figure 4.5) and the products of methanol steam reforming were CO_2, CO and H_2 as shown in Figures 4.6-4.8.

The methanol conversion in Figure 4.5 revealed a complete conversion at S/C of 1.3 and 1.7 and temperatures between 225-325°C. The water conversion decreases with increasing temperatures from 225°C to 325°C. This indicates that water consumption by steam reforming of methanol reaction (Eq. 4.1) or water gas shift reaction (Eq. 4.2) decrease with increasing temperature and the methanol decomposition reaction (Eq. 4.3) has a predominant effect in methanol fuel conversion. The decrease in water consumption was larger for S/C of 1.3 than S/C of 1.7 indicating the positive effect of extra steam on methanol steam reforming reaction as explained by the increase of CO_2 produced and the decrease in CO produced at S/C of 1.7 in Figure 4.6 and Figure 4.7, respectively.

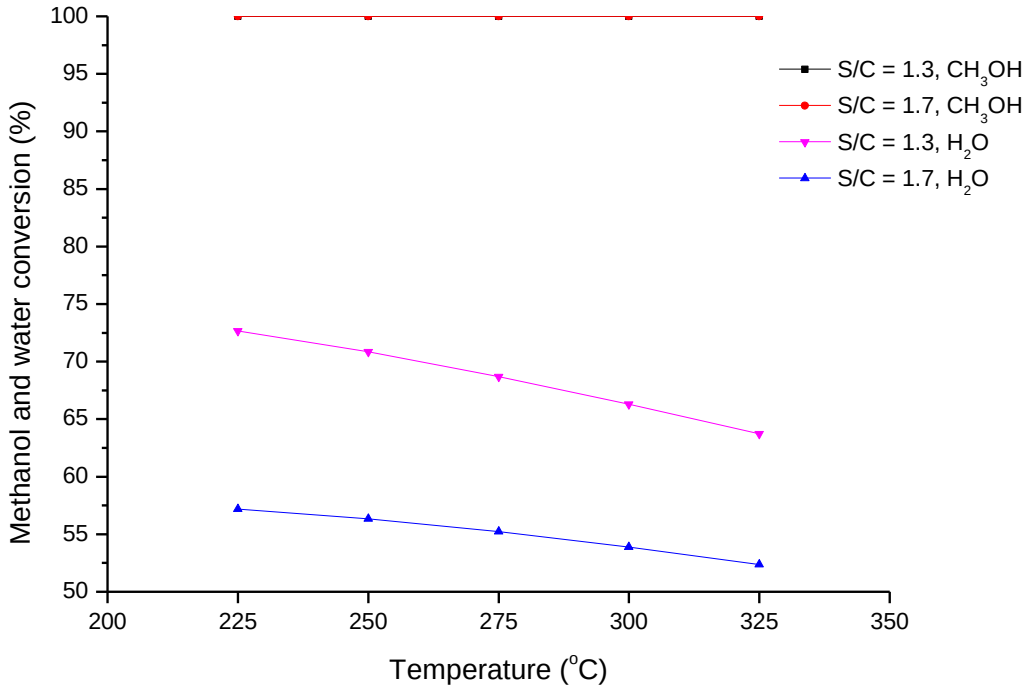

Figure 4.5. Equilibrium methanol and water conversions at various methanol reaction temperatures at S/C of 1.3 and 1.7, (CO and CO_2 as potential carbon products).

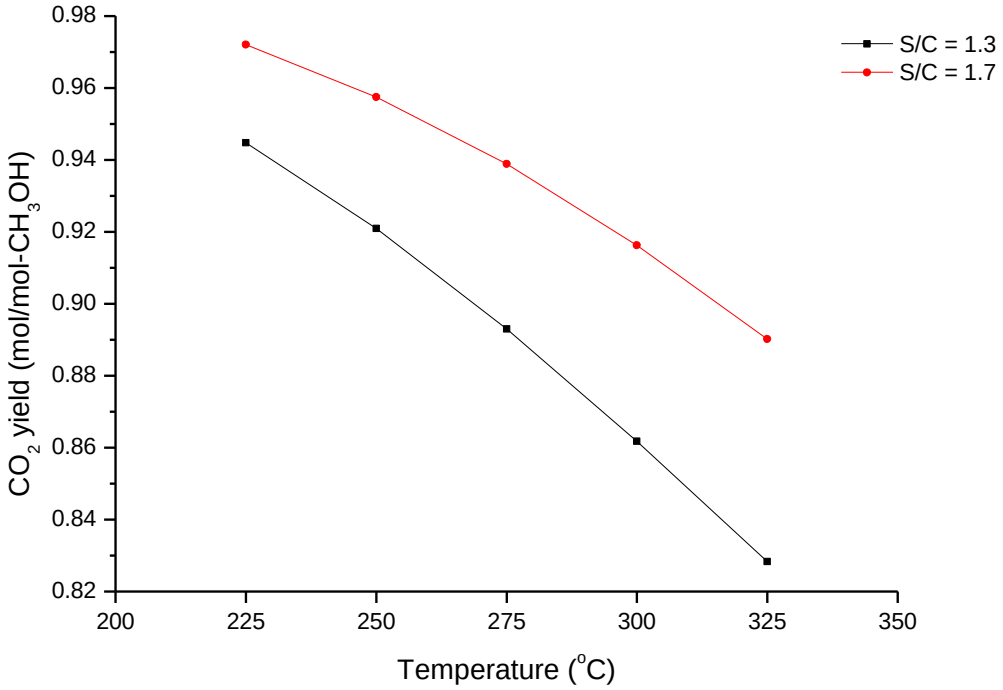

Figure 4.6. Equilibrium CO_2 yield at various methanol reaction temperatures at S/C of 1.3 and 1.7, (CO and CO_2 as potential carbon products).

The equilibrium CO_2 yield for both steam to carbon ratios of 1.3 and 1.7 is presented in Figure 4.6. The CO_2 yield decreases with increasing temperatures from 225°C to 325°C. This is related to the mole balance of carbon since the CO increases with increasing the temperature due to both reverse water gas shift reaction and decomposition reaction as shown in Figure 4.7. On the other hand, the amount of CO_2 increases with increasing the steam to carbon ratio in the reactants. The maximum calculated yield of CO_2 is 0.97 mol/mol-CH_3OH obtained at 225°C and S/C of 1.7.

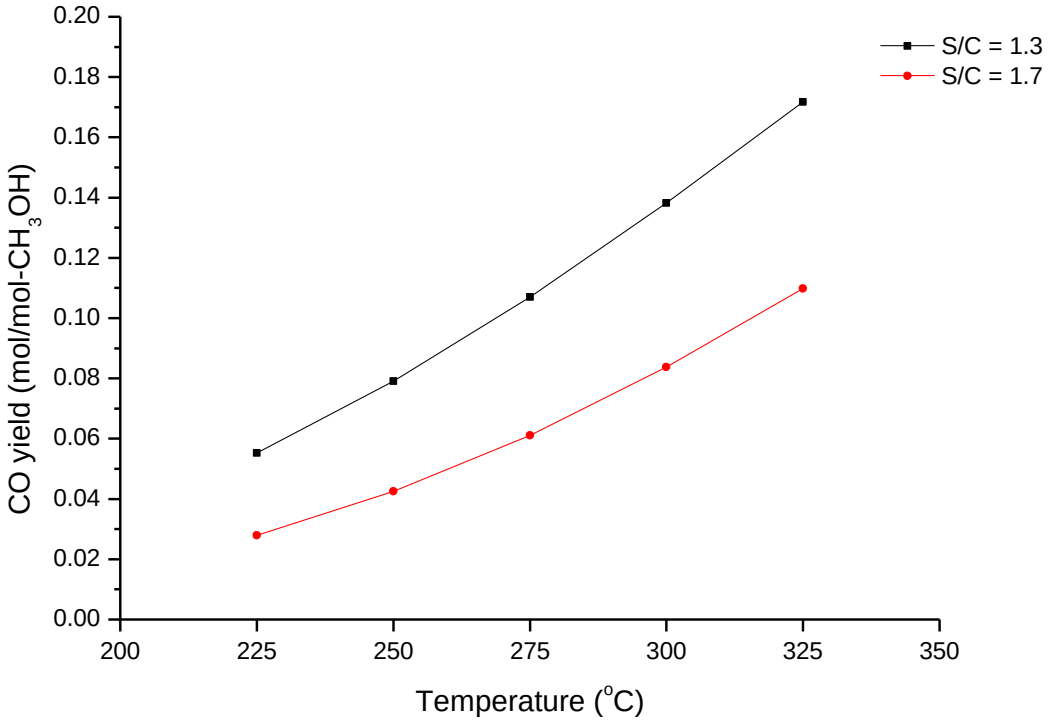

Figure 4.7. Equilibrium CO yield at various methanol reaction temperatures at S/C of 1.3 and 1.7, (CO and CO_2 as potential carbon products).

The calculated equilibrium yield of CO increases with increasing temperatures and it decreases with increasing the amount of water in the reactants as shown in Figure 4.7. The temperature increase causes the equilibrium of the water gas shift reaction (Eq. 4.3) to move towards the left side, increasing in the amount of CO. Increasing

the amount of steam decreases the amount of CO in the products while the amount of CO_2 increases. The minimum CO yield is 0.028 mol/mol-CH_3OH, which is achieved at 225°C and S/C of 1.7. The maximum CO yield is 0.17 mol/mol-CH_3OH obtained at S/C of 1.3 and at temperature of 325°C.

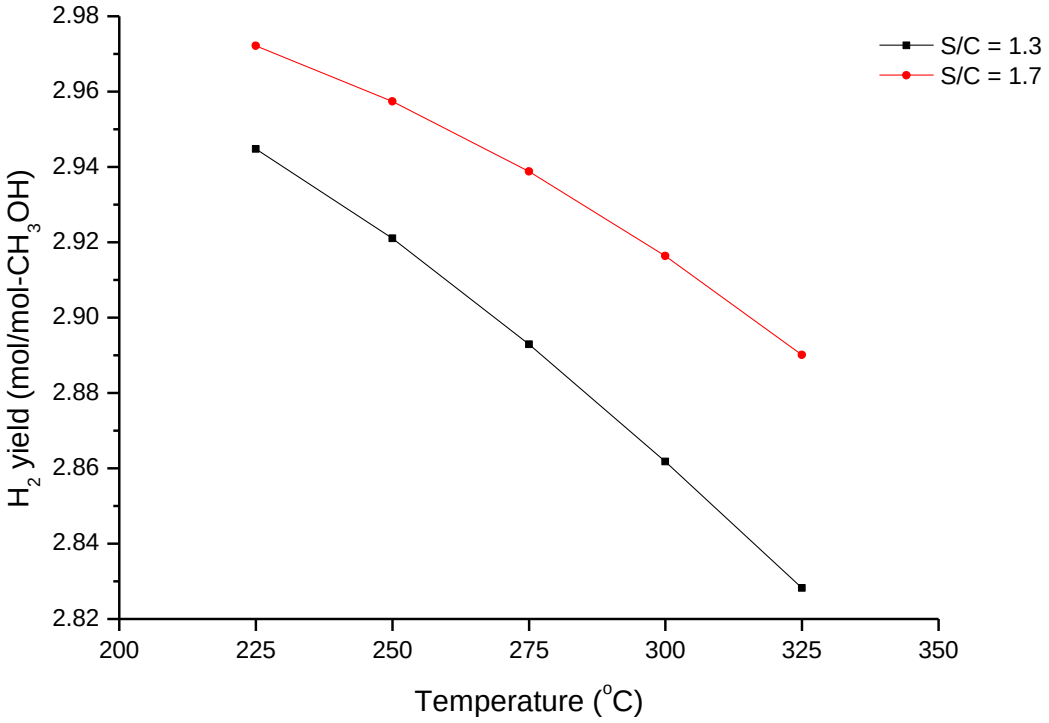

Figure 4.8. Equilibrium H_2 yield at various methanol reaction temperatures at S/C of 1.3 and 1.7, (CO and CO_2 as potential carbon products).

As shown in Figure 4.8, the calculated yield of H_2 decreases with increasing temperature due to reverse water gas shift reaction which consumes H_2. The H_2 yield increases when increasing the amount of water in the reactants. The maximum H_2 yield is 2.97 mol/mol-CH_3OH obtained at S/C of 1.7, 225°C.

4.2 Chemical equilibrium analysis of methane steam reforming

The steam reforming of methane shown in Eq. 4.13 is comprised of the methane reforming reaction (Eq. 4.14) followed by the water gas shift reaction (Eq. 4.14) [168-171]. The reforming reaction (Eq. 4.14) is endothermic and is favoured at high reaction temperature while the water shift reaction (Eq. 4.15) is an exothermic reaction and it is strongly favoured at low reaction temperature.

$CH_4 + 2H_2O \rightleftharpoons CO_2 + 4H_2$, $\Delta H°_{298}$= +165 kJ/mol (Eq. 4.13)

$CH_4 + H_2O \rightleftharpoons CO + 3H_2$, $\Delta H°_{298}$= +206 kJ/mol (Eq. 4.14)

$CO + H_2O \rightleftharpoons CO_2 + H_2$, $\Delta H°_{298}$= −41 kJ/mol (Eq. 4.15)

In order to study the conversions and products yields; the total number of moles in the equilibrium product is calculated by performing a carbon balance as presented in Eq. 4.16. The moles of carbon entering the reaction from methane will equal the carbon leaving the reaction. The Eq. 4.16 contains unknown n_{out}.

$$\left(1\times y_{CO} + 1\times y_{CO_2} + 1\times y_{CH_4} + 1\times y_C\right)\times n_{out} = n_{CH_4,in} \quad \text{(Eq. 4.16)}$$

$y_i = mol\ \ fraction\ of\ species\ i,\ \ obtained\ \ from\ CEA\ program$

$n = total\ \ moles$

Where, *in* and *out* subscribts denote releveant mol enetring or leaving the reaction.

The methane conversion was calculated using Eq. 4.17 and the water conversion was obtained by Eq. 4.6. The moles of products from the reaction were calculated by Eq. 4.7.

$$x_{CH_4} = \frac{n_{CH_4,in} - n_{CH_4,out}}{n_{CH_4,in}} \quad \text{(Eq. 4.17)}$$

The products yields for hydrogen, carbon dioxide and carbon monoxide were obtained in mol per mol of methane:

$$H_2 yield = \frac{n_{H_2,out}}{n_{CH_4,in}} \quad \text{(Eq. 4.18)}$$

$$CO_2 yield = \frac{n_{CO_2,out}}{n_{CH_4,in}} \quad \text{(Eq. 4.19)}$$

$$CO\ yield = \frac{n_{CO,out}}{n_{CH_4,in}} \quad \text{(Eq. 4.20)}$$

CEA in methane steam reforming was programmed to run with all possible products by entering the moles of methane (1 mol) and water (2 and 3 mol). All products were considered but whose mole fractions were less than $5x10^{-6}$ were negligible in calculations. Reaction temperatures were set to a range between 500-700°C with output values obtained for every 50°C interval at atmospheric pressure. The methane and water conversions and the products of methane steam reforming were CO_2, CO and H_2 as shown in Figures 4.9-4.12.

Figure 4.9 shows that the equilibrium methane conversion increases with increasing the reaction temperature and the amount of steam in the reactants. A lot of unconverted methane is obtained between 500-600°C and S/C of 2 and 3. The maximum methane conversion is 97.1% obtained at 700°C and S/C of 3. The water conversion in Figure 4.9 represents the amount of water consumed in methane steam reforming reaction. It is observed that a lot of water is consumed between 500-600°C, and then it becomes approximately constant at 650-700°C. This means that water is consumed in water gas shift reaction and methane steam reforming reaction.

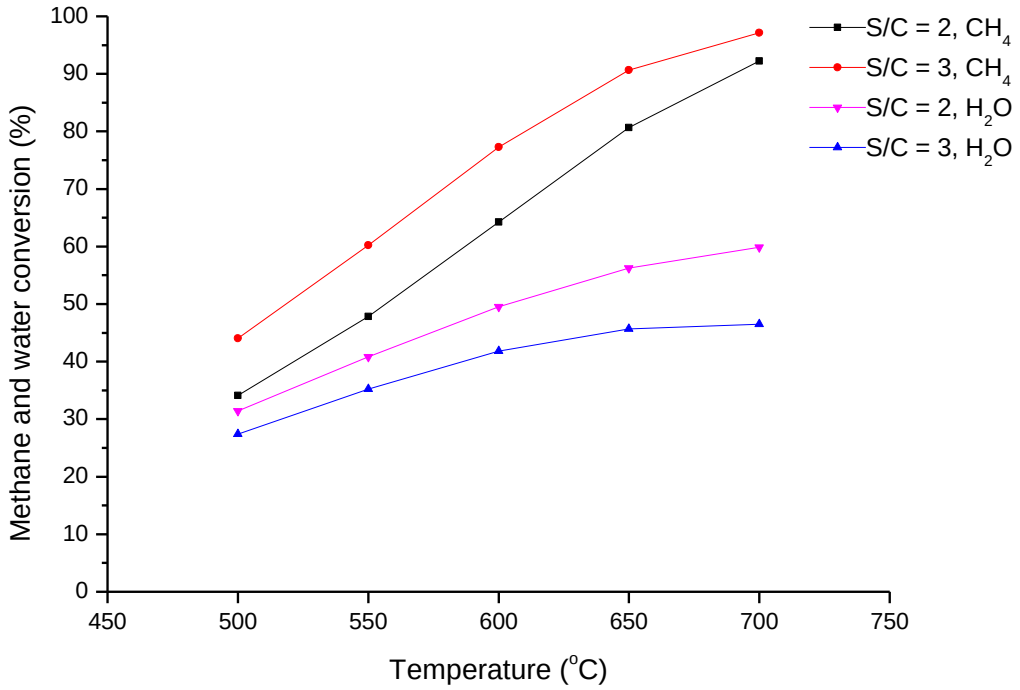

Figure 4.9. Equilibrium methane and water conversions at various methane reaction temperatures at S/C of 2 and 3.

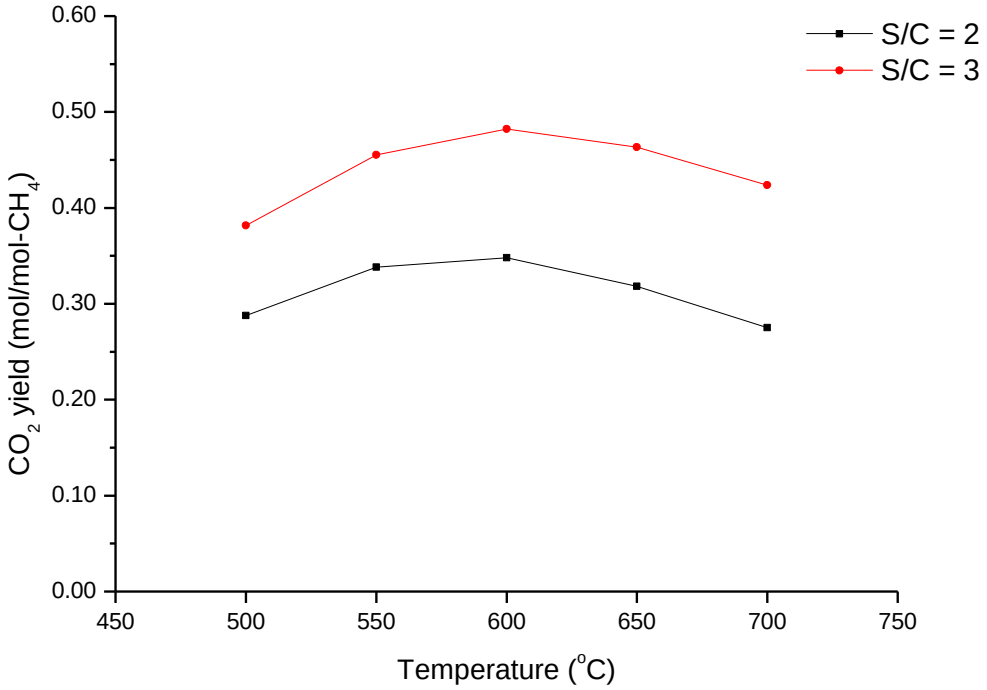

Figure 4.10. Equilibrium CO_2 yield at various methane reaction temperatures at S/C of 2 and 3.

Figure 4.10 shows that the amount of CO_2 increases with increasing temperature reaching a maximum peak at 600°C, then it decreased at temperatures 650-700°C. This is predicted due to water gas shift reaction since the water consumption is observed at 500-600°C in Figure 4.9. The amount of CO_2 increases with increasing steam to carbon ratio in the reactants due to water gas shift reaction. The maximum yield of CO_2 is 0.48 mol/mol-CH_4 obtained at 600°C and S/C of 3.

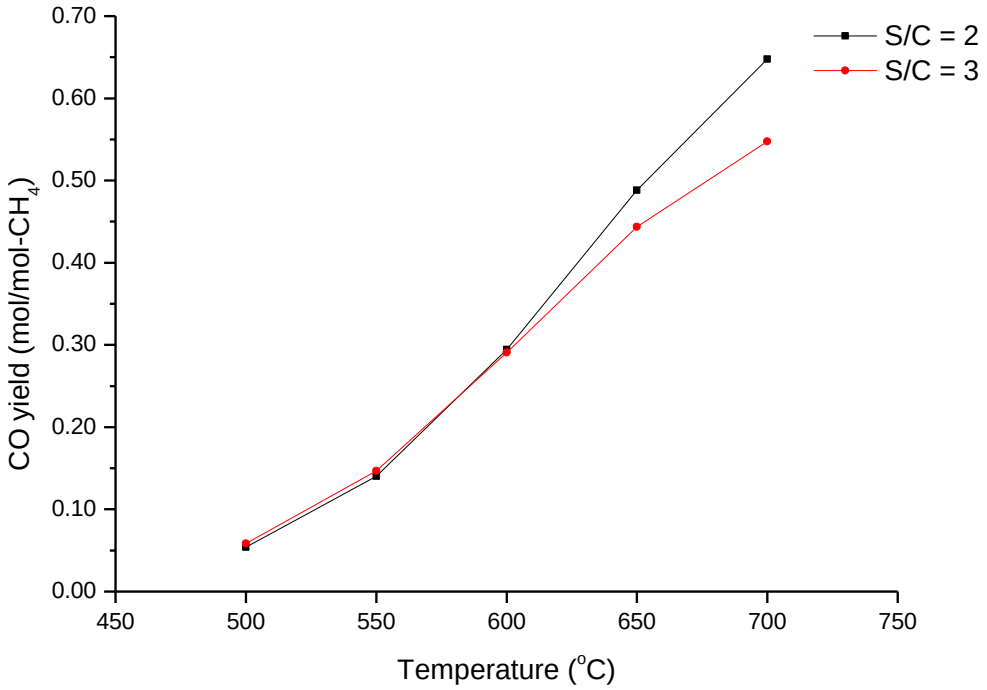

Figure 4.11. Equilibrium CO yield at various methane reaction temperatures at S/C of 2 and 3.

The equilibrium CO yield increases with increasing temperature as shown in Figure 4.11. Both methane steam reforming and reverse water gas shift reaction produce CO. The reverse water gas shift reaction consumes CO_2 and H_2 to produce CO and H_2O explaining the drop in CO_2 yield at temperatures 650-700°C in Figure 4.10. The increase in the amount of water in the reactants tends to increase the amount of CO_2 (Figure 4.10) and reduces the amount of CO (Figure 4.11). The minimum CO yield is

0.054 mol/mol-CH_4 which is achieved at 500°C and S/C of 2. The maximum CO yield is 0.65 mol/mol-CH_4, obtained at low S/C of 2 and at 700 °C.

As shown in Figure 4.12, the calculated yield of H_2 increases with increasing temperature in methane steam reforming. The H_2 yield increases when increasing the amount of water in the reactants. The maximum H_2 yield is 3.34 mol/mol-CH_4 obtained at 700°C and S/C of 3.

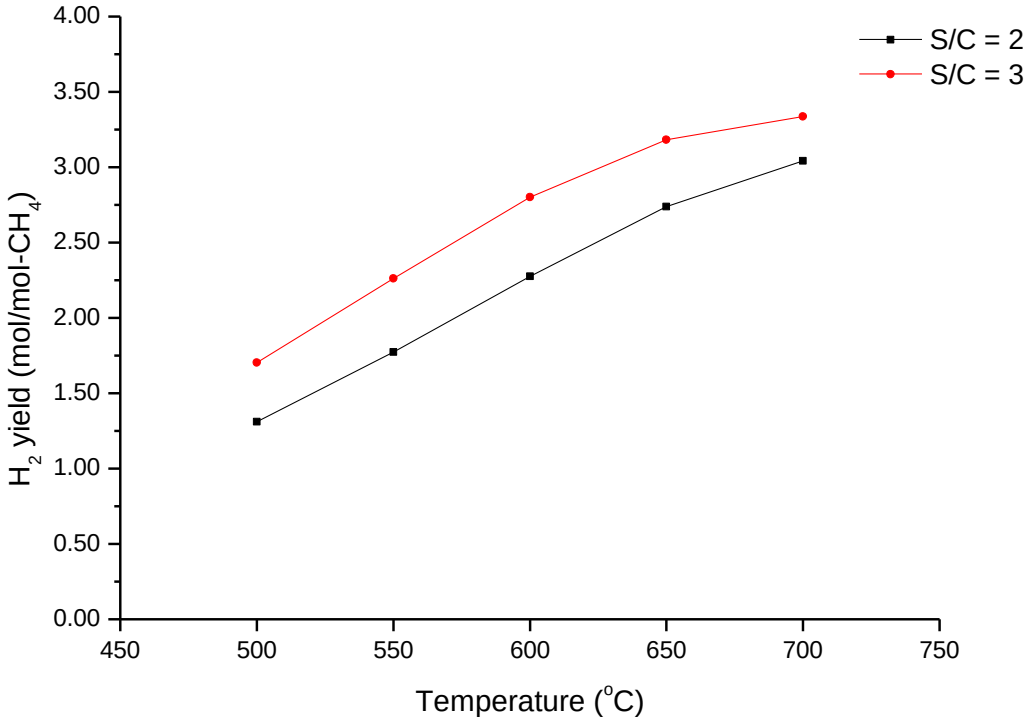

Figure 4.12. Equilibrium H_2 yield at various methane reaction temperatures at S/C of 2 and 3.

4.3 Chapter summary

The chemical equilibrium analysis of methanol and methane reforming reactions were investigated using a CEA program using a carbon balance to determine the total number of moles in the equilibrium product.

For methanol steam reforming, the methanol conversion and products yield were calculated at operating temperatures within 225 -325°C and steam to carbon ratios of 1.3 and 1.7. The methanol conversion was complete for all operating conditions. Methanol steam reforming showed that methane was a potential product of equilibrium via methanation reaction. The case when the catalyst is not active for methanation reaction, the equilibrium products were CO_2, CO and H_2. The CO_2 yield decreased with increasing temperature from 225°C to 325 °C. The amount of CO_2 increased with increasing steam to carbon ratio in the reactants. For CO, the yield followed the opposite trend of CO_2. The calculated H_2 yield decreased with increasing temperature and increased with increasing the amount of water in the reactants.

For methane steam reforming, the methane conversion and products yield were calculated at operating temperatures within 500-700°C and steam to carbon ratios of 2 and 3. The methane conversion increased with increasing the reaction temperature and the amount of water in the reactants. The CO_2 yield increased and reached a peak at 600°C then decreased with increasing temperature. The CO_2 yield increased with increasing water in the reactants. The CO yield increased with increasing temperature and decreased with the amount of water in the reactants. The H_2 yield increased with increasing temperature and increased with increasing the amount of water in the reactants.

CHAPTER 5

CATALYST CHARACTERIZATION OF PREPARED NI-CU/AL_2O_3 CATALYST

The characterization of the in-house prepared catalysts will be presented and described in this chapter and the results obtained will also be compared to commercially available 50%wt.Cu/25%wt.ZnO/25%wt.Al_2O_3 (HiFUEL R120 obtained from Alfa Aesar) and 40%wt.Ni/60%wt.Al_2O_3 (HiFUEL R110 obtained from Alfa Aesar) catalysts. Characterization results of the fresh prepared catalyst samples (10%Cu/Al_2O_3, 10%Ni/Al_2O_3, 7%Cu-3%Ni/Al_2O_3, 5%Cu-5%Ni/Al_2O_3, 7%Ni-3%Cu/Al_2O_3) are presented and discussed in this chapter. Physical and chemical properties of the catalyst are examined using the following techniques; SEM, nitrogen adsorption-desorption, CO chemisorption, XRD, IR and TPR.

The catalyst morphology has been probed using SEM as described in Section 5.1. The catalyst surface area (BET) and pore size were calculated using nitrogen adsorption-desorption as explained in Section 5.2. The active particle diameter and surface area of the catalyst metal were estimated using CO chemisorption data as detailed in Section 5.3. The crystallite phase and crystallite size were estimated using XRD patterns in Section 5.4. IR spectra (Section 5.5) have been recorded to present the occurrence of bonds associated with characteristic wavenumbers. Finally, TPR has been used to detect the reducible species and the reduction temperature of the in-house catalysts in Section 5.6.

5.1 SEM

The morphological appearance of Al_2O_3 support and the fresh prepared catalyst (10%Cu, 10%Ni, 7%Cu-3%Ni, 5%Cu-5%Ni, 7%Ni-3%Cu) are shown in Figure 5.1. The EDS results for prepared catalysts are illustrated in Appendix 9.7.

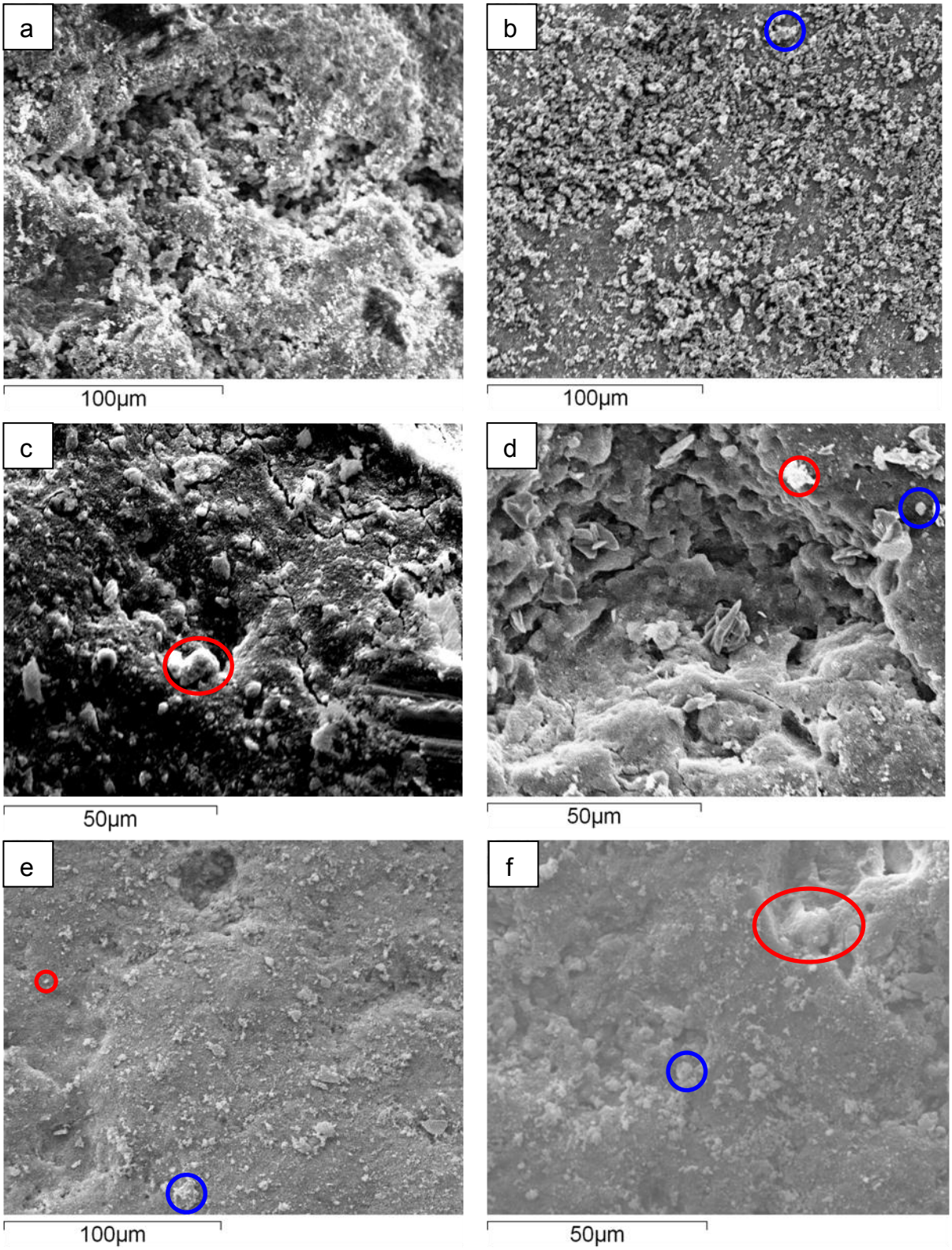

Figure 5.1. SEM of prepared catalysts: a) Al_2O_3, b) 10%Cu, c) 10%Ni, d) 7%Cu-3%Ni, e) 5%Cu-5%Ni and f) 7%Ni-3%Cu.

The Al_2O_3 support in Figure 5.1a displays the surface of the support and it is composed of irregular particles. The Al_2O_3 support used for the preparation of catalysts in this study has the same morphology as the sample presented in Figure 5.1a. Variation in darkness from light grey (low aluminium concentrations) to dark grey (high aluminium concentrations) in Figure 5.1a indicates an increase in concentration of aluminium species throughout the support [282].

Copper species in Figure 5.1b are seen as shaded white patches (highlighted by a marked blue circle) distributed over a light grey background of Al_2O_3 support [282]. The distribution of particles in 10%Cu seems to be practically uniform with some small agglomerates of particles apparent. The estimated size of particles is 5-15 µm.

A typical SEM image of 10%Ni/Al_2O_3 catalyst in Figure 5.1c shows an irregular distribution of bright white spherical Ni species (highlighted by a marked red circle) [230] upon a dark grey background of Al_2O_3, indicating a large concentration of Al_2O_3 support. Agglomerates of larger size of Ni particles are apparent in Figure 5.1c with particle size 6-12 µm.

Figure 5.1d shows the surface morphology of 7%Cu-3%Ni/Al_2O_3 catalyst. The particles of the catalyst are evenly distributed over the support [227]. In contrast to a monotype catalyst, 7%Cu-3%Ni showed smaller agglomerates in comparison to 10%Cu and 10%Ni catalysts. Copper species (shaded white, highlighted by a marked blue circle) and Ni species (bright white, highlighted by a marked red circle) are shown in Figure 5.1d and they are distributed throughout the light grey area characteristic of the alumina support. It is noticed that Ni and Cu clusters [283] are formed on the support. The approximate size of species is 6.5 µm.

Performing SEM for 5%Cu-5%Ni showed that both Cu particles (shaded white, highlighted by a marked blue circle) and Ni particles (bright white, highlighted by a marked red circle) are distributed throughout the light grey of the Al_2O_3 support as shown in Figure 5.1e. Clusters of both Ni and Cu particles are noticed and the SEM of 5%Cu-5%Ni has also shown small agglomerates of particles compared to the monotype 10%Cu and 10%Ni catalyst with approximate sizes 4.4-10.9 µm.

Agglomerates of larger particle sizes (highlighted by a marked red circle) are apparent in the 7%Ni-3%Cu sample (Figure 5.1f) compared to 7%Cu-3%Ni (Figure 5.1d) and 5%Ni-5%Cu (Figure 5.1e) samples. Copper species in Figure 5.1f are seen as shaded white patches (highlighted by a marked blue circle). Introducing additional Ni to the bimetallic system caused morphological changes compared to 7%Cu-3%Ni and 5%Ni-5%Cu samples [227]. As mentioned previously, 10% Ni catalyst displayed larger agglomerates compared to 10%Cu catalyst. This is related to the fact that Ni species normally reveal more agglomerates with increasing Ni concentration [229]. In Figure 5.1f clusters of Ni and Cu species are apparent over the light grey indicating the Al_2O_3 support with approximate sizes 3.3-8.7 µm.

The SEM image of commercial 50%Cu/25%ZnO/25%Al_2O_3 is shown in Figure 5.2a. It displays a similar morphological appearance as the prepared 10%Cu catalyst presented in Figure 5.1b. However, more white patches (highlighted by a marked blue circle) are visible due to a higher concentration of Cu species (50wt.%) and small agglomerates of species are displayed throughout the light grey Al_2O_3 support [284] with approximate sizes 2-16 µm. Figure 5.2b shows the surface morphology of the 40%Ni/60%Al_2O_3 catalyst. It displays agglomerates of Ni species throughout the Al_2O_3 support (highlighted by a marked red circle). The commercial catalyst showed

a uniform distribution of Ni clusters with approximate sizes 4-7.8 µm. It is noticeable that Ni species in Figure 5.2b revealed more agglomerates compared to Cu species in Figure 5.2a. In contrast, the samples prepared in this study afforded less agglomerates than commercial catalysts due to the low concentration of metals species (10wt.%) [285]. The SEM results suggest that the prepared catalyst with low metal contents can be more effective than conventional high metal content in terms of having more widely dispersed species distribution.

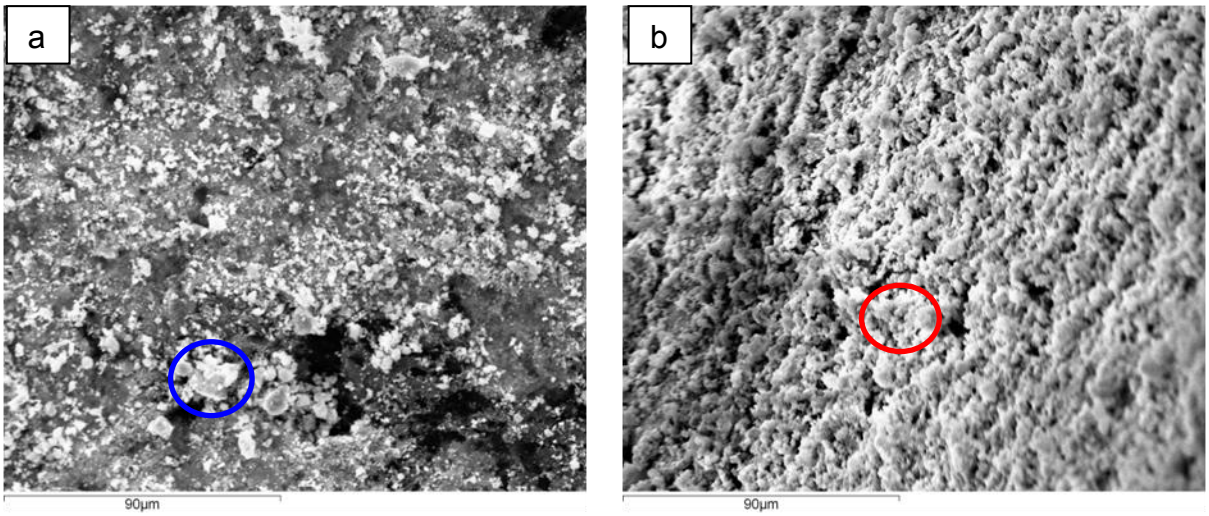

Figure 5.2. SEM of: a) 50%Cu/25%ZnO/25%Al_2O_3, b) 40%Ni/60%Al_2O_3.

5.2 Nitrogen adsorption-desorption

In order to determine the catalyst surface area and pore size diameter, the samples were analysed by the nitrogen adsorption-desorption method. The adsorption-desorption isotherm graph for the in-house prepared catalysts and the commercial catalysts are shown in Figure 5.3.

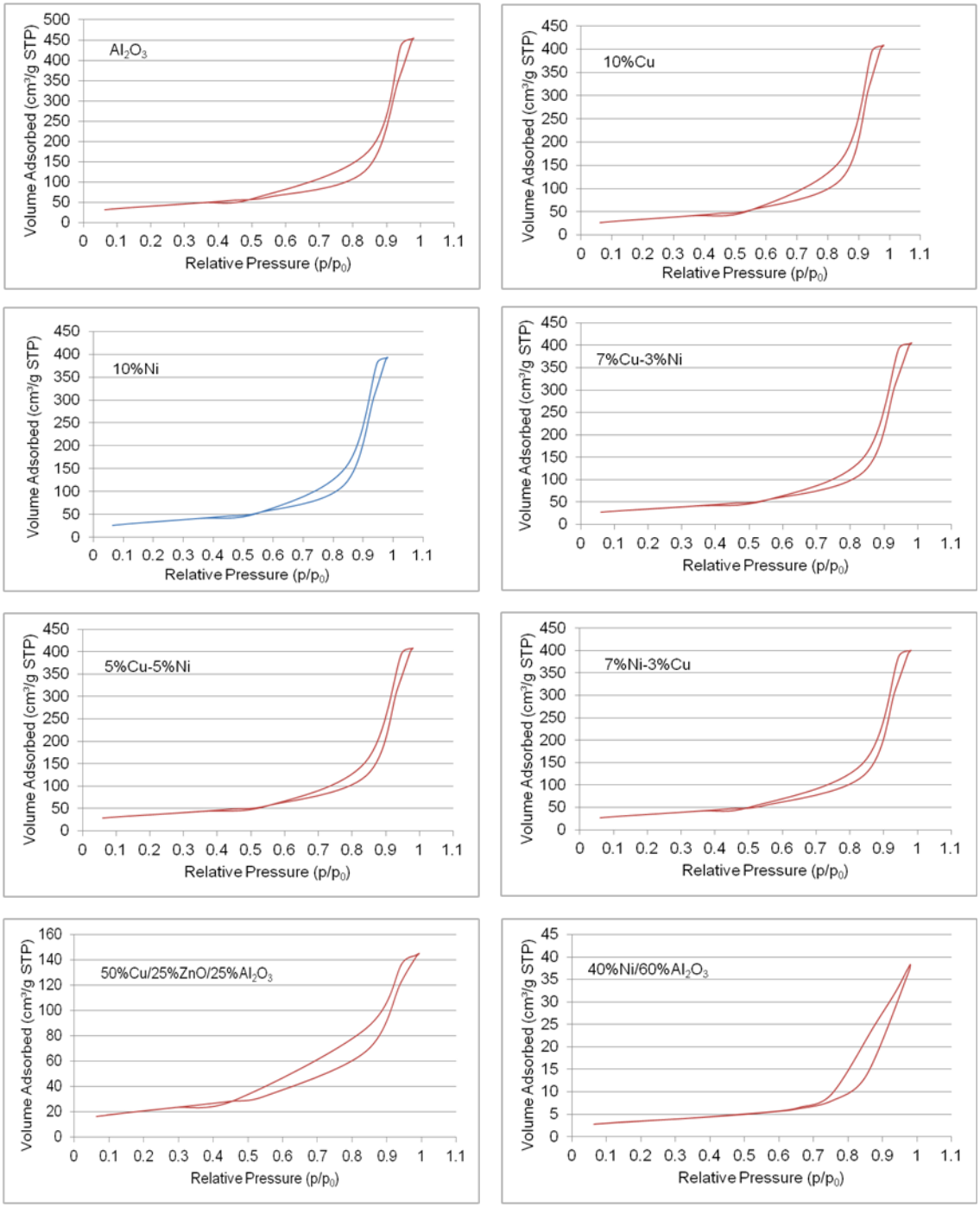

Figure 5.3. The sorption isotherms of nitrogen at 77K of prepared and commercial catalysts.

As observed in Figure 5.3, nitrogen uptake for the prepared catalyst was less at low relative pressure ($P/P_0 < 0.50$), with a very low initial gradient in the uptake curve. An increase in adsorption with increase in relative pressure was noticed at ($0.60 < P/P_0 < 0.95$). All prepared catalysts have shown very similar isotherm shapes

with hysteresis in each of the adsorption-desorption tests. Based on the isotherm classification explained in Figure 3.3 (displayed in Section 3.2.4 of Chapter 3), the prepared catalysts in this study are classified as Type IV indicating mesoporosity of material with high energy of adsorption. The hysteresis related to mesoporosity of material is classified into as Type H1, as shown in Figure 3.4 (displayed in Section 3.2.4 of Chapter 3). This suggests that regular even pores without interconnecting channels exist in the Al_2O_3 support used to prepare catalysts for this work.

Figure 5.3 also shows the adsorption isotherms of the 50%Cu/25%ZnO/25%Al_2O_3 and 40%Ni/60%Al_2O_3 commercial catalysts. Both catalysts showed a Type IV adsorption isotherm with hysteresis Type H1 indicating a regular even mesoporous structure of the support. 50%Cu/25%ZnO/25%Al_2O_3 catalyst showed low N_2 adsorption over the range of relative pressures ($P/P_0 < 0.40$) and it increased with increasing relative pressure ($0.50 < P/P_0 < 0.95$). The 40%Ni/60%Al_2O_3 displayed low N_2 adsorption over the range of relative pressures ($P/P_0 < 0.70$) then increased steeply at a relative pressure ($0.80 < P/P_0 < 0.95$) indicating a high adsorption of nitrogen.

The prepared catalysts showed a higher volume of adsorption compared to commercial catalysts because the prepared catalysts have a different type of Al_2O_3 support. In addition, the commercial catalysts have relatively high metal content (40%wt.Ni) and (50%wt.Cu/25%wt.ZnO) in comparison with the in-house prepared catalyst (10wt.%) which might cause a blockage of the pores of its corresponding Al_2O_3 support and thus reduce the volume of nitrogen adsorbed.

The analysis of nitrogen adsorption-desorption has shown that all tested catalysts indicated negligible microporous volume. Furthermore, BET surface area calculations were performed using the linearised form of the BET equation (Eq. 3.4) as illustrated in Appendix 9.2 and summarized in Table 5.1. The calculation in Appendix 9.2 shows a BET plot and working of the method for a selected sample to confirm the validity of results calculated using a computer, and ensure that the linear region of the graph was used in the calculations.

Table 5.1. BET surface area for prepared and commercial catalysts.

Catalyst	**BET surface area m^2/g**	**Average pore diameter (nm)**
Al_2O_3	142	19.2
10%Cu	120	21.1
10%Ni	122	19.9
7%Cu-3%Ni	125	20.1
5%Cu-5%Ni	128	19.6
3%Cu-7%Ni	125	19.8
50%Cu/25%ZnO/25%Al_2O_3	74	12.0
40%Ni/60%Al_2O_3	12	18.7

For fresh prepared catalyst, the surface area of trilobe alumina used as support for the impregnated samples was 142 m^2/g. The impregnated samples revealed a lower surface area with respect to the pure alumina. The surface area ranged from 120 m^2/g for 10%Cu to 128 m^2/g for 5%Cu-5%Ni catalyst. This is due to the fact that Ni and/or Cu particles might block pores of Al_2O_3 during metal deposition. It was noticed that the bimetallic catalyst presented a slightly higher surface area than the monotype catalyst. This finding might have occurred since the SEM images of bimetallic catalysts revealed a more even distribution of metal particles compared to the mono-metallic catalysts. This could lead to less blockage of the catalyst pore

structure compared with monometallic catalysts displaying large aggregates of metal particles, and therefore the bimetallic catalyst retains a slightly higher surface area. De Rogatis et al. [149, 211] prepared a Ni-Cu/Al_2O_3 catalyst via impregnation method which showed a BET surface area of 80 m^2/g. Their findings have shown that impregnated samples resulted in a lower surface area and pore volume with respect to pure Al_2O_3 due to pore blockage during metal deposition.

The commercial nickel catalysts showed a low surface area (12 m^2/g) which could be partly due to high metal loadings and also a low surface area of the starting support. The SEM displayed agglomerates of Ni species throughout the Al_2O_3 support, which can cause blockage of the support pores. The commercial copper catalyst revealed a surface area of 74 m^2/g and it can be attributed by the SEM results that small agglomerates of species are displayed throughout the support. This might result in a lower amount of pores being blocked as well as a more even distribution of metals particles owing to the inclusion of ZnO as a promoter. In conclusion, the differences in surface area of the various prepared and commercial catalysts reported here depends on several factors, which include; the type of alumina support, the amount of metal loading throughout the support and the treatment conditions during catalyst preparation such as calcination temperature and promoters added [90].

5.3 CO chemisorption

CO pulse chemisorption was applied to prepared and commercial catalysts in order to determine percent metal dispersion, active metal surface area and active metal particle size. The injected CO gas reacts with active sites until all active sites are consumed or covered with chemisorbed CO. The pulse chemisorption is a commonly established technique for determining metal dispersions and average metal particle

sizes in supported monometallic catalysts [286]. CO chemisorption is also performed on bimetallic catalysts. However, CO chemisorbs indiscriminately on both metal components (Ni and Cu) for the bimetallic catalysts [286]. Therefore, the test is limited to determine the total number of metal surface sites irrespective of the individual metal components on the surface of a catalyst. In spite of this limitation, various studies have been performed of CO chemisorption on bimetallic catalysts such as Pd-Cu [287], Pt-Au [288] and Ni-Cu [149, 211]. In these studies, the dispersions of bimetallic catalysts were measured and investigated for total metals of the catalyst support and compared with monometallic catalyst. Assuming that the difference is due to the second metal, the dispersion of each metal may be inferred. However this is complicated if the different metals have different adsorption strengths with CO. De Rogatis et al. [149] studied the dispersion of bimetallic Ni-Cu catalyst and compared it with monometallic Cu and Ni catalysts. They considered the small differences between the chemisorption results of their investigated samples could be attributed to experimental errors and the fact that a complex combination of various possible reactions may occur during the CO chemisorption investigation. This means that metal dispersion data strongly depends on adsorption characteristics of such prepared catalyst [286].

As explained in Chapter 3 (Section 3.2.3), repeated injections of CO gas are made and the surface is considered saturated when five successive peaks detected by TCD at the outlet achieve equal areas as illustrated in Figure 5.4. The TCD signal versus time shows successive injections of CO adsorptive gas onto the sample. The first two peaks show that the sample became saturated and no further adsorption occurred after the third peak. The area presented under the peak represents the volume of gas in the outlet stream which has not been adsorbed. Therefore, the

difference between gas injected and the amount in the exhaust from the sample tube outlet may be used to determine the volume of chemisorbed CO gas on active sites of the catalyst.

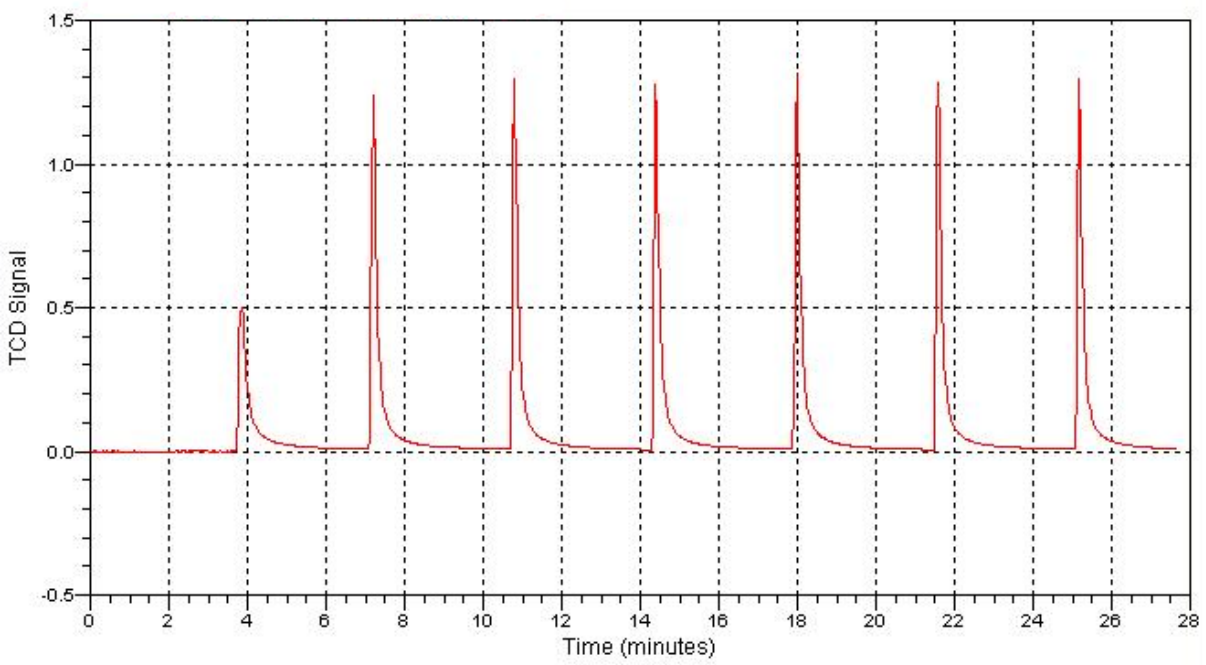

Figure 5.4. The TCD signal of CO pulse chemisorption performed on 10%Cu/Al_2O_3 catalyst.

Table 5.2 shows CO pulse chemisorption characteristics for the prepared mono-metallic catalyst of Ni and Cu with various loadings (10wt.%, 7wt.%, 5wt.%, 3wt.%), bimetallic catalysts (7%wt.Cu-3%wt.Ni, 5%wt.Cu-5%wt.Ni, 3%wt.Cu-7%wt.Ni) and commercial copper and nickel catalysts.

Table 5.2. Metal dispersion, metal surface area and active particle diameter for prepared and commercial catalysts.

Catalyst	**Metal dispersion (%)**	**Metal surface area m^2/g**	**Active particle diameter (nm)**
10%Cu	0.92%	0.60 m^2/g sample 6.0 m^2/g metal	113
10%Ni	1.74%	1.16 m^2/g sample 11.6 m^2/g metal	58
7%Cu-3%Ni	1.38%	0.90 m^2/g sample 9.0 m^2/g metal	75
5%Cu-5%Ni	1.63%	1.10 m^2/g sample 10.7 m^2/g metal	64
3%Cu-7%Ni	1.95%	1.30 m^2/g sample 12.9 m^2/g metal	53
7%Cu	1.46%	0.66 m^2/g sample 9.40 m^2/g metal	72
5%Cu	3.16%	1.02 m^2/g sample 20.34 m^2/g metal	33
3%Cu	4.31%	0.83 m^2/g sample 27.77 m^2/g metal	24
7%Ni	2.89%	1.35 m^2/g sample 19.30 m^2/g metal	35
5%Ni	4.07%	1.35 m^2/g sample 27.07 m^2/g metal	25
3%Ni	6.56%	1.31 m^2/g sample 43.67 m^2/g metal	16
50%Cu/25%ZnO/25%Al_2O_3	0.31%	1.01 m^2/g sample 2.02 m^2/g metal	334
40%Ni/60%Al_2O_3	1.29%	1.29 m^2/g sample 8.62 m^2/g metal	78

From the results in Table 5.2, 3%Ni had higher dispersion compared to 10%Ni catalyst and similarly 3%Cu achieved higher dispersion compared to 10%Cu catalyst. It can be inferred that a catalyst impregnated with low metal content has highly dispersed metals throughout the support. Samples with low metal contents of Cu or Ni particles have low active particle diameter which present highly dispersed metals over the Al_2O_3 support [289]. The CO chemisorption ability of bimetallic catalysts decreases with increasing Cu addition from (1.95%) in 3%Cu-7%Ni to (1.38%) in 7%Cu-3%Ni. This is attributed to some Cu metal particles becoming inaccessible to the adsorption gas because they could be part of large clusters of metal or have become trapped in pores which are not accessible to the outside surface of the catalyst. This finding agrees with previous studies that copper addition during preparation over alumina support decreases the amount of chemisorbed CO on the Ni surface [287, 290, 291]. Based on the XRD analysis as will be discussed in Section 5.4, the bimetallic catalyst revealed the presence of both metallic copper and metallic nickel, therefore, the obtained CO chemisorption data includes all metal phases formed on the surface of the catalyst.

Performing CO pulse chemisorption for commercial 50%Cu/25%ZnO/25%Al_2O_3 revealed a dispersion of 0.32% throughout the Al_2O_3 support. A high metal loading of Cu gives a large active particle diameter of 334 nm that may be interpreted as due to a low CO adsorption accessibility owing to a particle size effect [287]. This particle diameter is significantly higher than the crystallite size obtained from XRD, which could be explained if the clustered Cu particles are composed of multiple crystallites and part of these particles are in contact with ZnO and the support [149]. Gine´s et al. [90] studied the metallic copper dispersion over various types of copper based catalysts. It was reported that the dispersion values ranged from 0.9% for

42.6%wt.CuO/43.7%wt.ZnO/13.7%wt.Al_2O_3 catalyst reaching up to 5% for 42%wt.Cu/51%wt.ZnO/7%wt.Al_2O_3 catalyst. It should be pointed out that various studies reported the low dispersion of Cu particles throughout the support as being attributed to a large particle size of copper and various investigations have thus been carried out to increase the metallic dispersion by improving the catalyst preparation [90, 292-295]. The Ni dispersion for commercial Ni/Al_2O_3 catalyst was 1.29%. This value is similar to the values reported by Oliveira et al. [296] (1.42%) and by Seo et al. [297] (1.5%) for commercial Ni/Al_2O_3 catalyst. The CO chemisorption revealed an active particle diameter of 78 nm and this is significantly higher than the value of crystallite size obtained from XRD, suggesting that Ni particles are composed of multiple crystallites and some of the particles are in contact with the support using CO pulse test [149].

5.4 XRD

The XRD spectra of all prepared catalysts are shown in Figure 5.6, from which information about the crystalline structure can be deduced. XRD patterns can be matched to peaks for corresponding pure metals oxides that can be found in the database (PDF-4+2012) provided by International Centre for Diffraction Data (ICDD). For the Al_2O_3 support, peaks may be matched with XRD patterns of two different phases of alumina, namely γ-Al_2O_3 and traces of θ-Al_2O_3. Broad and diffuse diffraction lines of Al_2O_3 support as observed in Figure 5.6 indicate a low degree of crystallinity. According to Sohlberg et al. [298], the presence of both γ-Al_2O_3 and θ-Al_2O_3 is consistent with low calcination temperature (500°C) and α-Al_2O_3 is absent with relative high surface area (142 m^2/g).

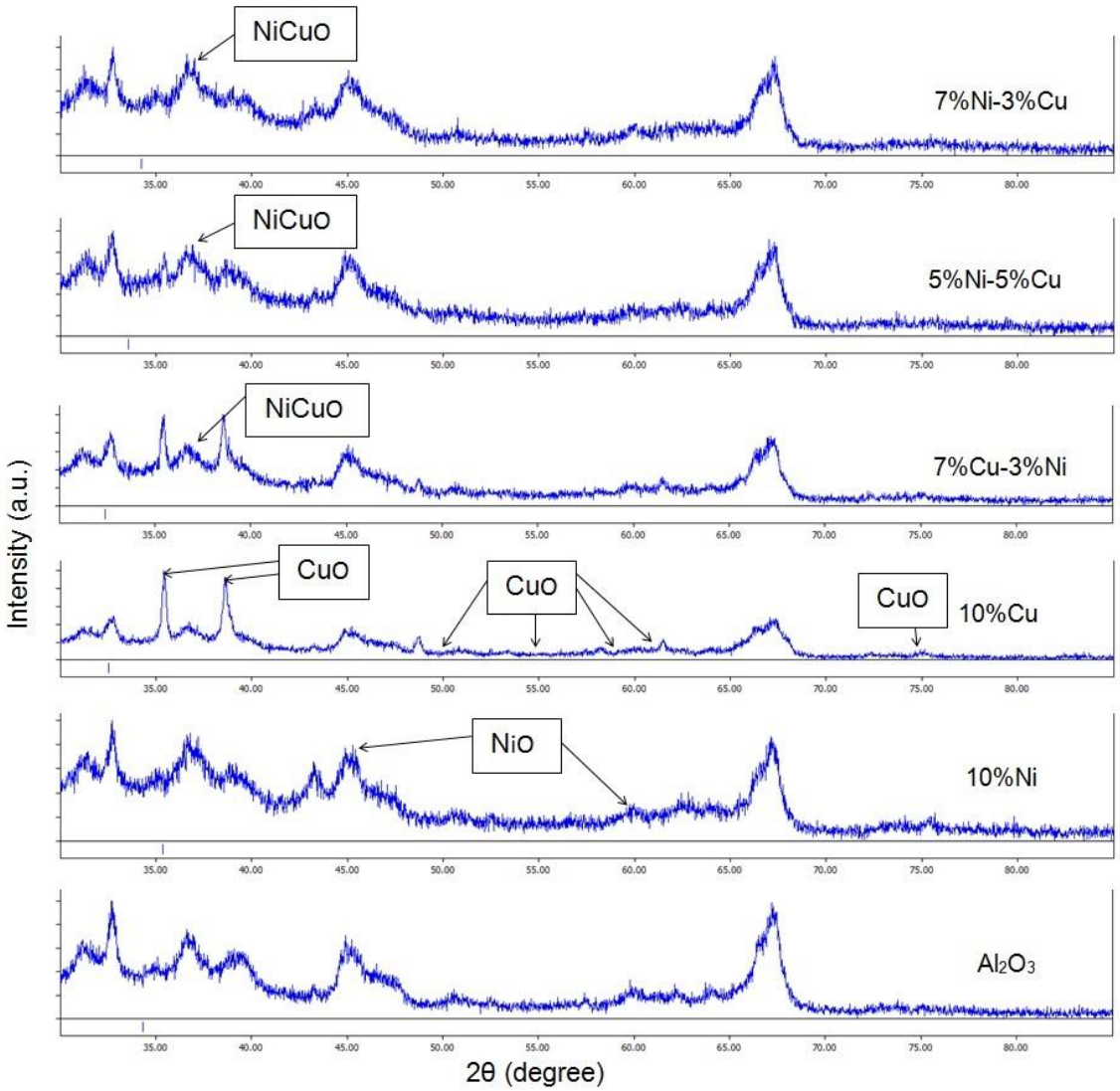

Figure 5.6. XRD pattern for various types of prepared catalysts.

The XRD spectra performed for the monotype catalyst suggested the existence of NiO in the 10%Ni catalyst sample at (2θ = 45°, 60°) with the average crystallite diameter calculated by Scherrer's equation (Eq. 3.5) of 17.8 nm. The monotype catalyst of 10%Cu showed XRD patterns of CuO spectra at (2θ = 35°,39°,50°,55°,58°,61°,75°) and the average crystallite size of CuO was 17.9 nm. On the other hand, the bimetallic catalysts indicated the formation of NiO, CuO phases and $Ni_xCu1_{-x}O$ phase at (2θ = 36°). For instance, the crystallite diameter size of $Ni_xCu1_{-x}O$ for 5%Cu-5%Ni was 16.7 nm. This estimated value is lower than that found in both types of monometallic catalysts. It was noticed that the position of the

diffraction peaks is changed because Cu addition leads to a shift towards higher angles for NiO diffraction peaks since the ionic radius of Ni^{2+} is bigger than that of Cu^{2+} [149]. This leads to the different ability of the two ions to create crystallite structure [149].

The crystal phase was also identified for commercially available catalysts as shown in Figure 5.7. XRD patterns of the commercial sample $Cu/ZnO/Al_2O_3$ exhibited CuO patterns (2θ = 36°, 45°, 63°) and achieved a crystallite size of 17.5nm. In the XRD of commercial Ni catalyst, the existence of NiO (2θ = 44°, 63°) was identified and the crystallite size was 17.9 nm. The results obtained from XRD in relation to the particle diameter are lower than the value obtained from CO chemisorptions since the samples were not reduced. In fact, the active particle diameter estimated via CO chemisorption for reduced samples reveals a larger active particle diameter than the non-reduced sample [211]. The oxide phase of metal appears in the XRD patterns due to non-reduced samples. Accordingly, the reduced metal particles are thought to be composed of multiple crystallites and part of the metal is in strong interaction with the support as will be discussed later in Section 5.6, which reports the TPR analysis.

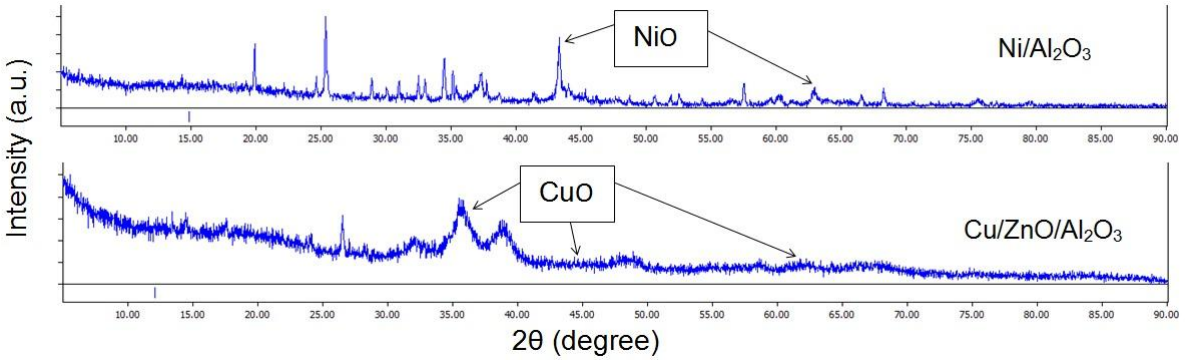

Figure 5.7. XRD for commercial $Cu/ZnO/Al_2O_3$ and Ni/Al_2O_3 catalysts.

5.5 IR

Figure 5.8 displays the IR spectra of monotype and bimetallic catalysts. The spectra of monotype 10%Ni and 10% Cu showed only one peak at 1375 cm^{-1} and 1502 cm^{-1}, respectively. However, the bimetallic catalysts showed three peaks which are assigned as NiO (1375 cm^{-1}), CuO (1502 cm^{-1}) and an alloy of Ni-Cu (1430 cm^{-1}). The IR spectra were also recorded for comparison purposes on available commercial catalysts of copper and nickel as shown in Figure 5.9 and peaks at similar wavenumber to the in-house prepared catalysts were observed. Three different oxides phases were detected in commercial Ni catalyst. Those are attributed to Al_2O_3 (3386 cm^{-1}), NiO (1444 cm^{-1}) and nickel surface spinel (1028 cm^{-1}) as reported by Ryczkowski [299]. The commercial copper spectra showed a low wavenumber band at (1515 cm^{-1}) which is related to CuO, ZnO at (1368 cm^{-1}) and a high wavenumber band at (3311 cm^{-1}) attributed to Al_2O_3, which agree with the band assignments reported by Edwards and Schradar [300]. The positions of the bands are affected by several conditions such as; temperature at which catalyst was calcined and the surface concentrations of metals throughout the support [299, 300]. For instance, the commercial catalysts have a larger amount of metal concentration than prepared catalysts, which will increase bond strength of metals oxides causing the wavenumber to shift towards larger values.

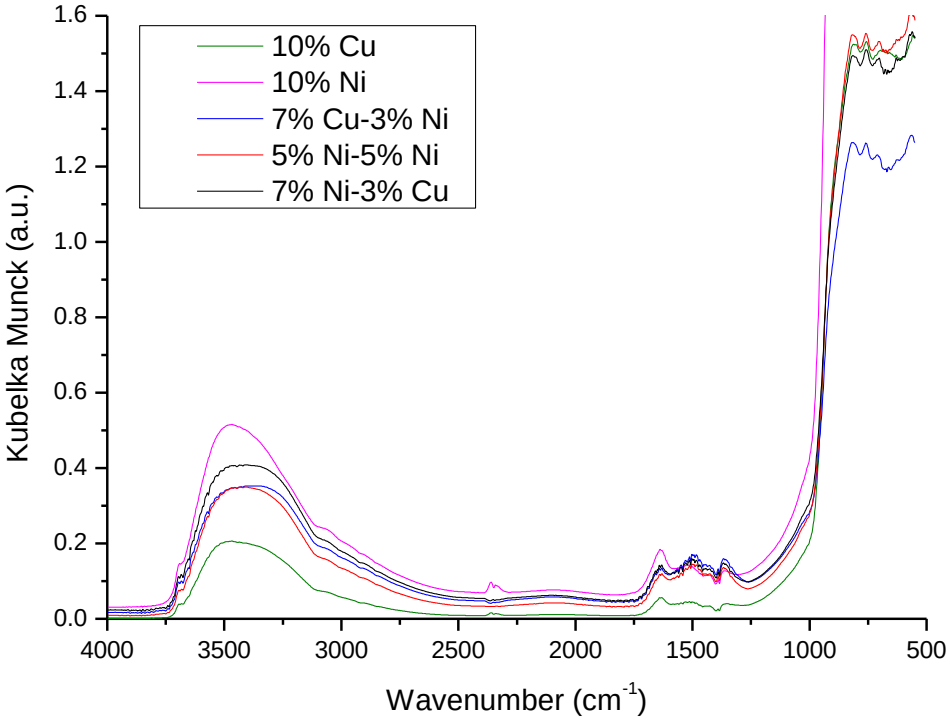

Figure 5.8. Infrared spectra for various prepared catalysts.

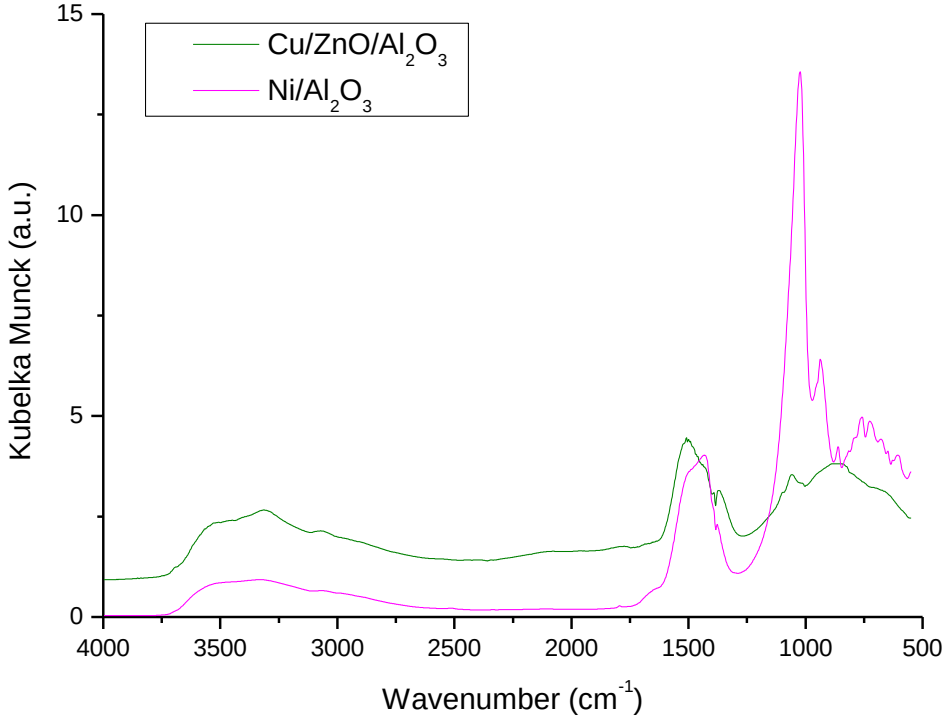

Figure 5.9. Infrared spectra for commercial catalyst.

5.6 TPR

The hydrogen uptake of the TPR profile for each catalyst is given in Figure 5.10. The 10%Cu catalyst exhibited one wide peak with maximum reduction temperature at 250°C. The reduction peak is attributed to the dispersion of CuO over the Al_2O_3 support and the amount of hydrogen consumed corresponds to the amount of hydrogen required to react with reducible particles on the catalyst. The finding is similar to that found in tested commercially available catalyst as shown in Figure 5.11 and the result agrees with that found by Jones and Hagelin [105].

The 10%Ni catalyst displayed broad multi peaks at 400°C and 650°C (Figure 5.10). Two peaks are attributed to a range of interactions between NiO and the Al_2O_3 support. The low reduction temperature corresponds to a weak interaction between NiO and Al_2O_3 support and the high reduction temperature is likely to be related to a strong interaction of NiO and Al_2O_3 [211, 301, 302]. Figure 5.11 shows the TPR test and hydrogen uptake of commercially available Ni catalysts. Two prominent peaks appeared at 650°C and 776°C. However, the hydrogen uptake began at 400°C, which explains that the reduction of Ni can occur at this point. Various reduction peaks are affected by the nature of metal support interaction [303]. NiO species supported on Al_2O_3 are reduced at around 500-700°C and the reduction of nickel aluminates occurs at high temperature above 800°C [297, 304]. The discrepancy between prepared and commercial Ni catalysts might be the result of low percentage of metal loading on the prepared catalyst in comparison with high metal loadings in the commercial catalyst.

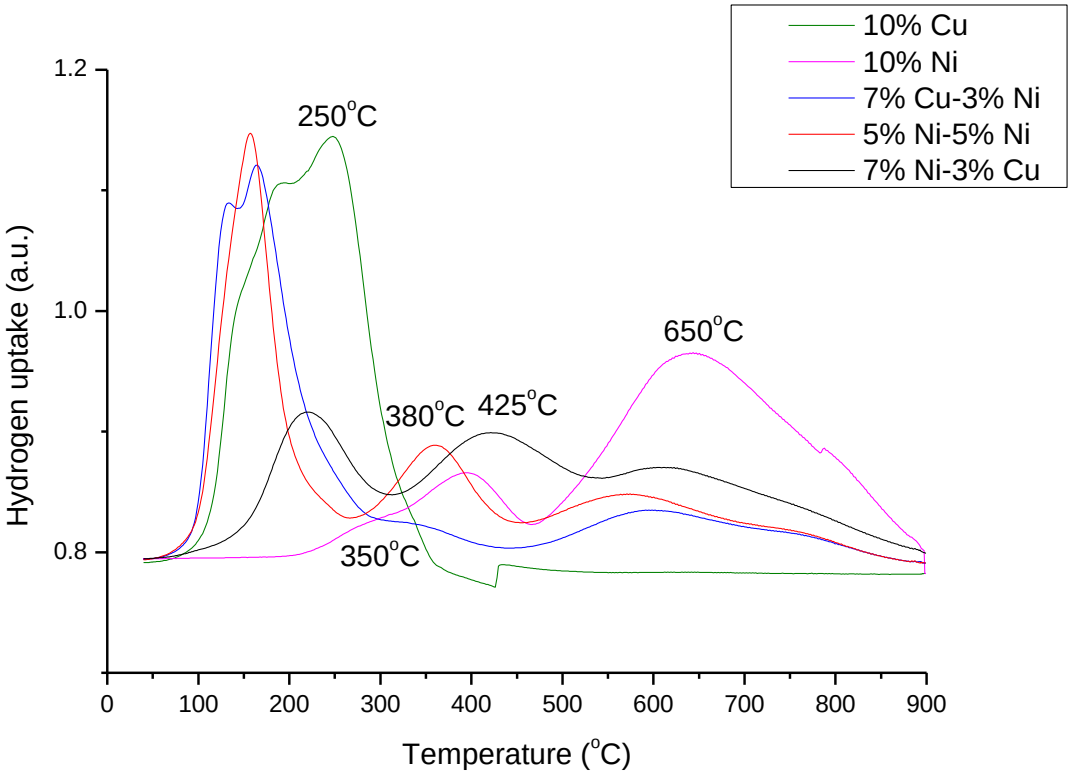

Figure 5.10. TPR for prepared catalysts.

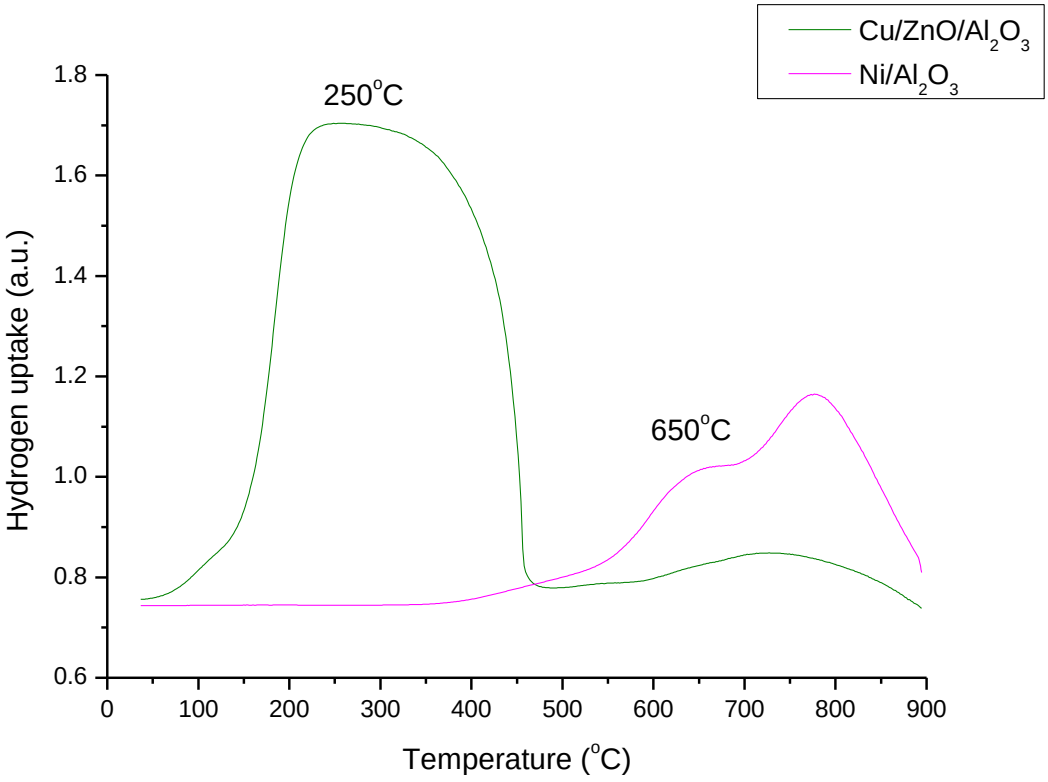

Figure 5.11. TPR for commercial catalysts.

The TPR profile of the bimetallic Ni-Cu catalysts (Figure 5.10) shows three hydrogen uptake peaks. The first obtained peak on 7%Cu-3%Ni and 5%Cu-5%Ni showed high hydrogen uptake compared to 7%Ni-3%Cu. This indicates that a high area of hydrogen uptake peaks is related to the amount of reducible species of CuO, which increases in samples containing higher percentages of Cu. Therefore, the first sharp peak is associated with pure CuO and is shifted compared to the monotype Cu catalysts due to different amounts of Cu loadings and the rate of hydrogen uptake on CuO species. The broad peak in the middle (350°C for 7%Cu-3%Ni, 380°C for 5%Cu-5%Ni, 425°C for 7%Ni-3%Cu) of the TPR trace for the bimetallic catalyst can be associated with NiCuO interaction with support which was used to determine the reduction temperature for the subsequent reaction study. In addition, it can also indicate a weak interaction of NiO with support. The last peak is related to a strong interaction of NiO with the support. Ni–Cu catalyst supported on Al_2O_3 was prepared by De Rogatis et al. [211] and their findings agree with the TPR results reported. In their study, the first reduction peak appeared at about 160°C and was associated with the reduction of CuO. The second peak at 390°C was attributed to the reduction of Ni-based species promoted by the presence of metallic Cu, as also mentioned by Lee et al. [305]. The third peak at about 770°C was related to strong interaction of Ni oxides species with the Al_2O_3. The difference in the position of reduction peaks reported here is related to the fact that the temperature of the reduction peaks strongly depend on the particle dimension and the interaction strength between metal particles and the support.

5.7 Chapter summary

Various characterization techniques for fresh prepared catalyst (10%Cu/Al_2O_3, 10%Ni/Al_2O_3, 7%Cu-3%Ni/Al_2O_3, 5%Cu-5%Ni/Al_2O_3, 7%Ni-3%Cu/Al_2O_3) were performed in order to compare the bimetallic catalyst with monometallic prepared catalyst. The prepared catalysts were also compared with commercially available 50%Cu/25%ZnO/25%Al_2O_3 and 40%Ni/60%Al_2O_3 catalysts. The SEM showed that increasing the loading of Ni to 7wt.% loading gave larger agglomerates compared to other prepared catalysts. The prepared catalyst showed less agglomerates and more evenly dispersed species compared to the commercial catalyst due to a low contents of metals. The adsorption isotherm explained the mesoporosity of material characteristics with high energy of adsorption. The CO pulse chemisorption for monometallic and bimetallic prepared catalyst was applied. A limitation of this test was that it is principally designed to study the dispersion on monometallic catalysts. The results obtained for bimetallic catalyst present the total number of metal sites irrespective of the individual metal components on the surface of the catalyst. The increase of loading of Cu in Ni-Cu catalyst has an adverse effect upon the metals dispersion. The XRD spectra for reference Al_2O_3 support showed γ-Al_2O_3 and traces of θ-Al_2O_3. The results for the impregnated catalyst revealed an oxide phase of the corresponding metals. It was found by IR that the positions of bands in the catalyst are affected by the concentration of the metals over the support. Finally, the hydrogen uptake and the corresponding reduction temperature were determined using TPR. The 10%Ni catalyst displayed broad multi peaks. The 10%Cu catalyst exhibited one wide peak and the TPR profile of the bimetallic Ni-Cu catalysts showed three hydrogen uptake peaks related to CuO , NiCuO and NiO reduction.

CHAPTER 6

METHANOL STEAM REFORMING

This chapter describes the research carried out for the methanol steam reforming reaction over in-house prepared catalysts (10%Cu, 7%Cu-3%Ni, 5%Cu-5%Ni and 3%Cu-7%Ni). The reaction was carried out in a fixed bed reactor to study the catalyst reactivity under various operating conditions as will be discussed in Section 6.1. The reactions were carried out for 4 hours at various temperatures of 225, 250, 275, 300 and 325°C at atmospheric pressure. A constant flow rate of 0.06 ml/min of premixed water and methanol at ratios of 1.3 and 1.7 was fed into the reactor system in order to study the fuel conversion and the catalyst selectivity for products. The effects of Ni contents in a bimetallic Ni-Cu catalyst (Section 6.2) were also studied and compared with 10%Cu monometallic catalyst for methanol steam reforming reaction.

The spent catalyst was characterized and a comparison with a freshly prepared catalyst are drawn and discussed in Section 6.3. The morphology and textural properties of the used catalysts were probed by SEM. The surface area of the spent catalyst recovered following reactions at the high (325°C) and low temperatures (225°C) was determined by nitrogen adsorption-desorption analysis. Crystallite size and its phase were determined using XRD. The amount of carbon formation was studied for all used catalyst samples.

Finally, a long stability reaction test for 20 hours is also reported in Section 6.4 for some selected in-house prepared catalysts at 325°C and steam to carbon ratio of 1.7, in order to deduce the catalytic behaviour during a long-term operation.

6.1 Effects of methanol reaction temperature and steam over prepared 10%Cu/Al_2O_3 catalyst

The catalytic activity measurements were performed in the packed fixed bed reactor as discussed earlier in Chapter 3. The experiments were performed over the temperature range of 225-325°C, with the S/C ratio of 1.3 and 1.7, atmospheric pressure and liquid hourly space velocity (LHSV) of 0.77 h^{-1}. Both effects from increasing the reaction temperature and increasing the amount of the water in the reactants upon the product produced were compared to the calculated equilibrium product yields.

In order to study conversions and products yields; an elemental analysis using reactor exit concentrations of CO, CO_2, CH_4 and H_2 and the inlet flow of methanol was performed. The unmeasured H_2O was calculated. It was assumed that the total molar flow of carbon entering the reactor from methanol equals the carbon leaving the reactor outlet. The accumulation of coke is assumed zero in the carbon balance as shown in Eq. 6.1. The carbon balance Eq. 6.1 contains two unknowns, $\dot{n}_{out,dry}$, $\dot{n}_{CH_3OH,out}$.

$$\left(y_{CO} + y_{CO_2} + y_{CH_4}\right) \times \dot{n}_{out,dry} + 1 \times \dot{n}_{CH_3OH,out} = 1 \times \dot{n}_{CH_3OH,in} \quad \text{(Eq. 6.1)}$$

$y_i = mol\ \ fraction\ of\ species\ i.$

$\dot{n} = total\ \ molar\ \ flow\ \ rate\ \ (mol/\min)$

$\dot{n}_i = molar\ \ flow\ \ rate\ of\ species\ \ i\ \ (mol/\min)$

where, in and out subscribts denote releveant mol enetring or leaving the reaction.

The hydrogen balance analysis was performed as shown in Eq. 6.2. Hydrogen entering the reaction from water and methanol equals the hydrogen leaving the reaction. The Eq. 6.2 contains three unknowns, $\dot{n}_{out,dry}$, $\dot{n}_{H_2O,out}$ and $\dot{n}_{CH_3OH,out}$

$$\left(2y_{H_2}+4y_{CH_4}\right)\times\dot{n}_{out,dry}+2\times\dot{n}_{H_2O,out}+4\times\dot{n}_{CH_3OH,out}=4\times\dot{n}_{CH_3OH,in}+2\times\dot{n}_{H_2O,in} \quad \text{(Eq. 6.2)}$$

$y_i = mol\ \ fraction\ of\ species\ i.$

$\dot{n}\ = total\ \ molar\ \ flow\ \ rate\ \ (mol/\min)$

$\dot{n}_i = molar\ \ flow\ \ rate\ of\ species\ \ i\ \ (mol/\min)$

From the above elemental analysis, the unknown $\dot{n}_{out,dry}$ was measured in the experiment from bubble meter after water condensation, $\dot{n}_{CH_3OH,out}$ and $\dot{n}_{H_2O,out}$ were calculated.

The conversions for methanol and water were obtained by Eq.6.3-6.4 and displayed in Figure 6.1:

$$x_{CH_3OH}=\frac{\dot{n}_{CH_3OH,in}-\dot{n}_{CH_3OH,out}}{\dot{n}_{CH_3OH,in}} \quad \text{(Eq. 6.3)}$$

$$x_{H_2O}=\frac{\dot{n}_{H_2O,in}-\dot{n}_{H_2O,out}}{\dot{n}_{H_2O,in}} \quad \text{(Eq. 6.4)}$$

The molar flow rates of products from the reaction were calculated by:

$$\dot{n}_{i,out}=y_i\times\dot{n}_{out,dry} \quad \text{(Eq. 6.5)}$$

The products yields for hydrogen, carbon dioxide and carbon monoxide were obtained in mol/min per mol/min of methanol as shown in Eq.6.6-6.8 and presented in Figures 6.2-6.4:

$$H_2 yield=\frac{\dot{n}_{H_2,out}}{\dot{n}_{CH_3OH,in}} \quad \text{(Eq. 6.6)}$$

$$CO_2 yield=\frac{\dot{n}_{CO_2,out}}{\dot{n}_{CH_3OH,in}} \quad \text{(Eq. 6.7)}$$

$$CO\ yield=\frac{\dot{n}_{CO,out}}{\dot{n}_{CH_3OH,in}} \quad \text{(Eq. 6.8)}$$

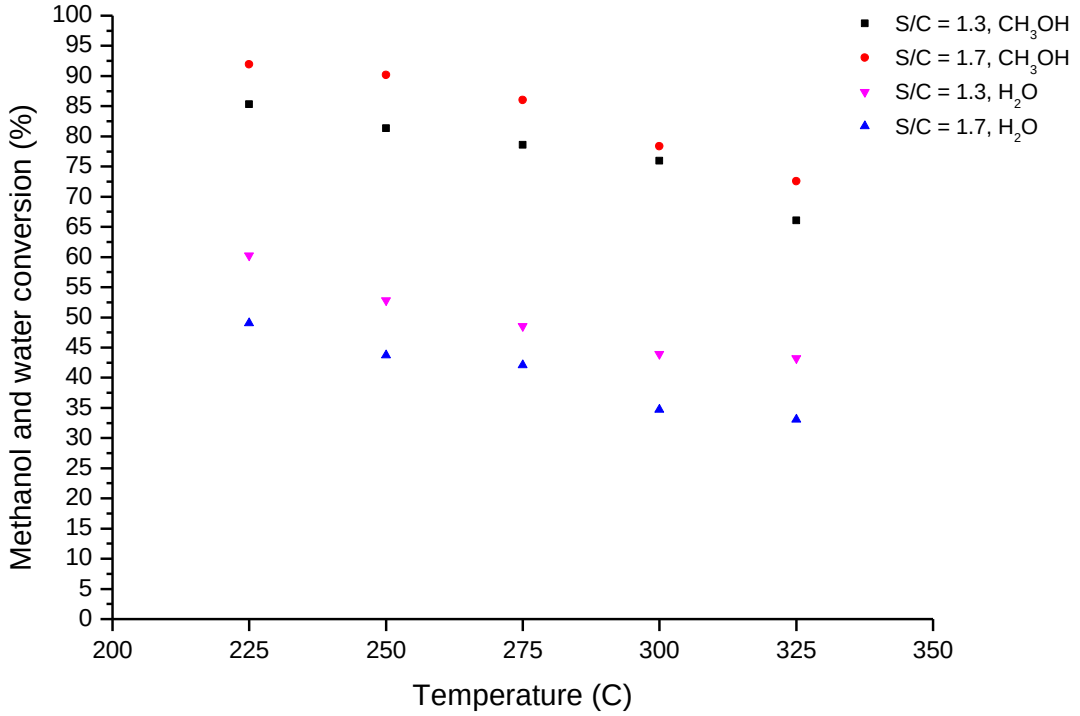

Figure 6.1. Methanol and water conversions for 10%Cu/Al_2O_3 methanol catalyst within 225-325°C for the S/C of 1.3 and 1.7.

The methanol conversion, shown in Figure 6.1, decreased with increasing the temperature. The conversion of methanol at S/C ratio of 1.7 was observed to decrease from 92% at 225°C to 73% at 325°C. The reported decrease in methanol conversion with increasing the temperature in Figure 6.1 is related to the concentration of reformate in the reactor. The inhibiting effect of H_2, CO_2 and CO was noticed as the water consumption decreased with increasing the operating temperature. The amount of water consumed was less than predicted by equilibrium analysis in Figure 4.5. It was also observed that an increase of the water amount in the reactants via a higher S/C ratio led to a decrease of the unreacted methanol at 225-325°C. The excess of steam over the amount required by the reaction stoichiometry facilitated the steam reforming reaction and suppressed the reverse water gas shift reaction [69, 306].

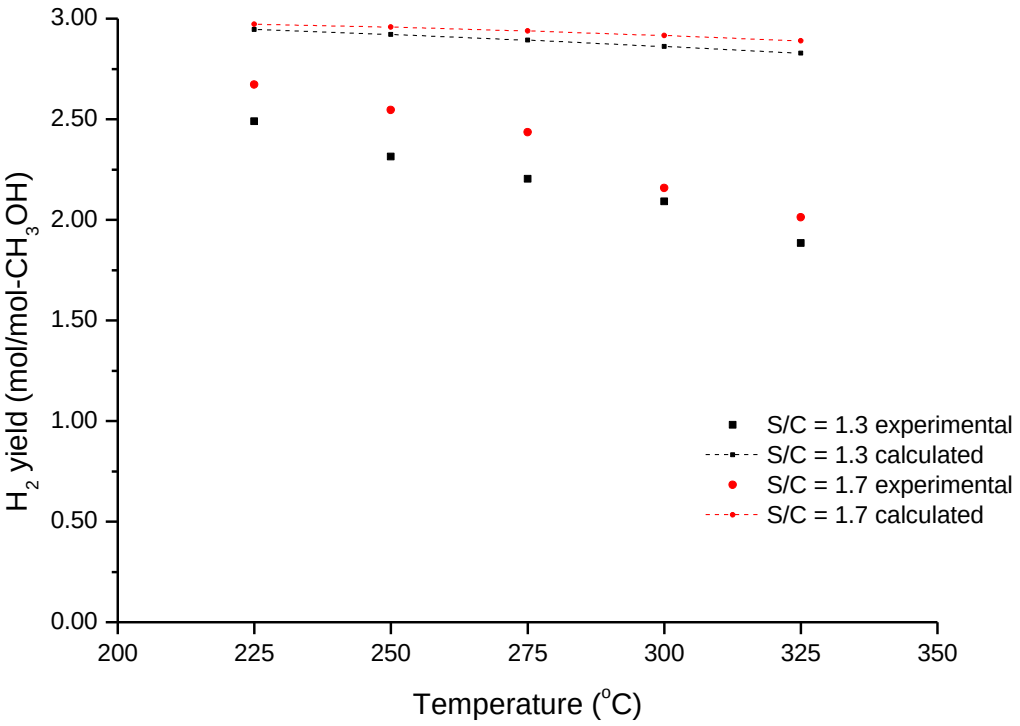

Figure 6.2. Experimental and calculated H_2 yield for 10%Cu/Al_2O_3 methanol catalyst within 225-325°C for the S/C of 1.3 and 1.7.

It is shown in Figure 6.2 that the amount of hydrogen produced decreased with increasing the reaction temperature. The amount of hydrogen produced in the experiment was less than predicted by equilibrium calculations due to kinetic limitation. It was observed that the hydrogen amount changed from 2.7 mol/mol-CH_3OH at 225°C to 2.0 mol/mol-CH_3OH at 325°C for S/C= 1.7 and from 2.5 mol/mol-CH_3OH at 225°C to 1.9 mol/mol-CH_3OH at 325°C for S/C =1.3. Thus, it is concluded experimentally that increasing the amount of steam has a small effect upon hydrogen production. The results obtained in Figure 6.2 agree with the reported hydrogen amount studied in the literature [306]. It was mentioned that hydrogen yield decreases as the reforming temperature increases due to the increase of CO in the product. The decrease in hydrogen amount was ascribed to reverse water gas shift reaction since it would consume hydrogen.

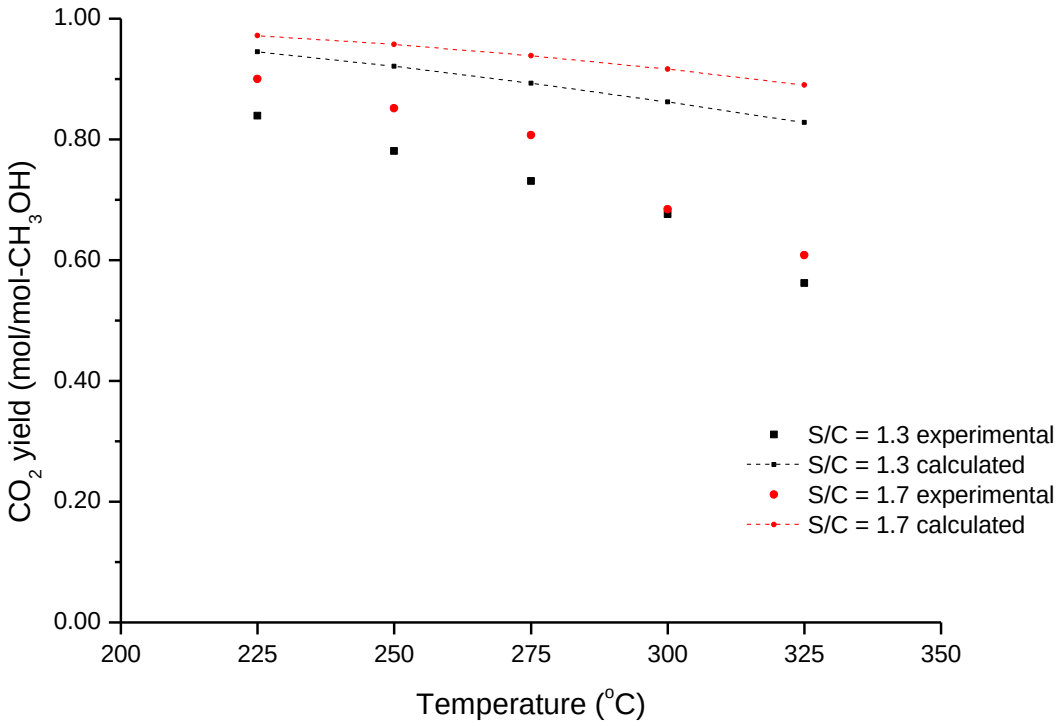

Figure 6.3. Experimental and calculated CO_2 yield for 10%Cu/Al_2O_3 methanol catalyst within 225-325°C for S/C of 1.3 and 1.7.

Figure 6.3 shows the amount of CO_2 produced as a function of temperature. It is clear that the amount of CO_2 is less than that found from equilibrium calculations within 225°C-325°C. The yield of CO_2 was decreasing with increasing the reaction temperature. This observation may be explained, since the water gas shift reaction in the experiment consumed more water at lower reaction temperature than the one at higher reaction temperature. The amount of CO_2 decreased from 0.90 mol/mol-CH_3OH at 225°C to 0.61 mol/mol-CH_3OH at 325°C. This suggests that CO_2 is consumed to produce CO with increasing temperature by the reverse water gas shift reaction as explained below.

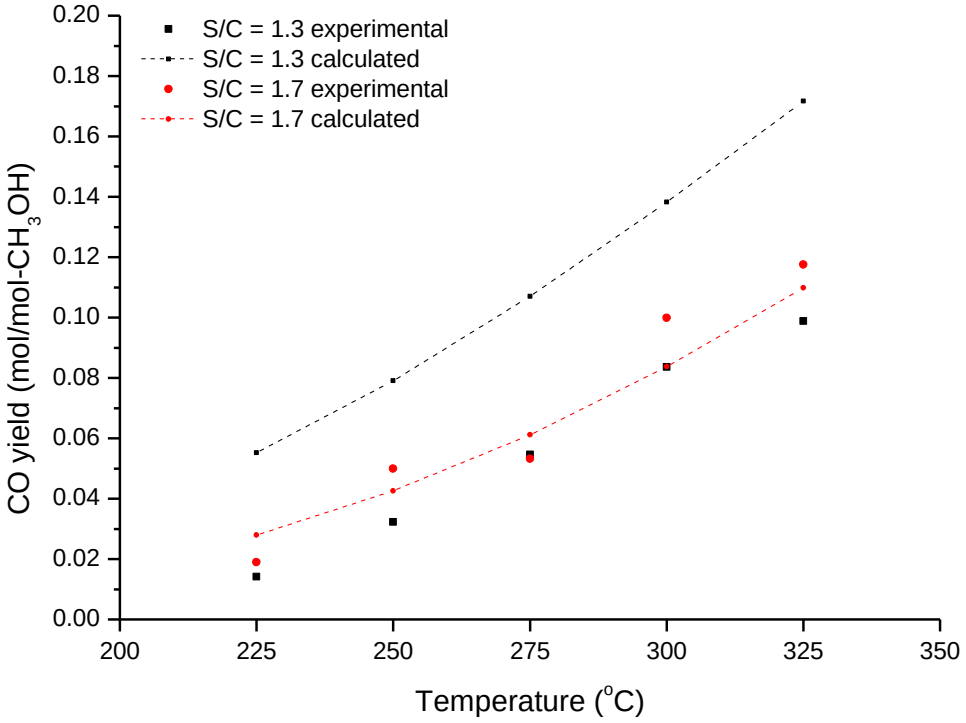

Figure 6.4. Experimental and calculated CO yield for 10%Cu/Al_2O_3 methanol catalyst within 225-325°C for the S/C of 1.3 and 1.7.

Figure 6.4 shows that the amount of CO produced was less than the equilibrium values within 225°C-325°C for S/C of 1.3 and nearly equal at temperatures of 225°C-275°C for the S/C of 1.7 and a slightly greater at 300-325C for S/C of 1.7. This trend could be explained because the low activity of the reverse water gas shift reaction is responsible for low CO production [73, 158-160]. The amount of CO was slightly larger than the estimated equilibrium values in the range of temperatures 300-325°C, which indicates that the decomposition reaction of methanol would be responsible for CO production in parallel with reverse water gas shift reaction [70]. It was reported in the literature [69, 82, 306] that increasing the amount of the steam in the reactants would decrease the amount of CO produced by suppressing the reverse water gas shift reaction as displayed in Figure 6.4 for calculated equilibrium. The reported literature indicated that excess steam of the amount required by stoichiometry would

effectively suppress CO formation [69, 306]. However, it was shown experimentally that increasing the amount of water in the reactants by changing S/C from 1.3 to 1.7 had a very small effect on the amount of CO produced. The experimental measurements of CO yield displayed an increase from 0.02 mol/mol-CH_3OH at 225°C up to 0.12 mol/mol-CH_3OH at 325°C for S/C of 1.7

In conclusion, the methanol steam reforming over monometallic 10% Cu/Al_2O_3 catalyst was carried out from 225°C to 325°C at atmospheric pressure. The hydrogen yield was less than calculated equilibrium. The concentration of carbon monoxide was less or nearly equal than the equilibrium calculation, which suggests that reverse water gas shift reaction is a main contributor for CO [70]. According to the methanol reaction mechanism suggested in Chapter 2, the amount of CO detected suggests that the catalyst in methanol steam reforming is responsible for methanol steam reforming reaction in which CO_2 is produced, as well as for the slow water gas shift reaction in which CO is consumed. Finally, a conversion (92%-73%) was achieved from 225°C to 325°C in the operated catalyst and this was further improved by adding more water to the reactants because of the enforced steam reforming reaction [57].

6.2 Effects of Ni content on methanol steam reforming

In this section, the effects of Ni content in the prepared catalysts (7%Cu-3%Ni, 5%Cu-5%Ni and 3%Cu-7%Ni) are compared with results for the 10%Cu catalyst and the effects of Ni content on product yield and conversion are explained. The reactions were carried out for catalysts from 225°C to 325°C with the S/C of 1.7 at atmospheric pressure.

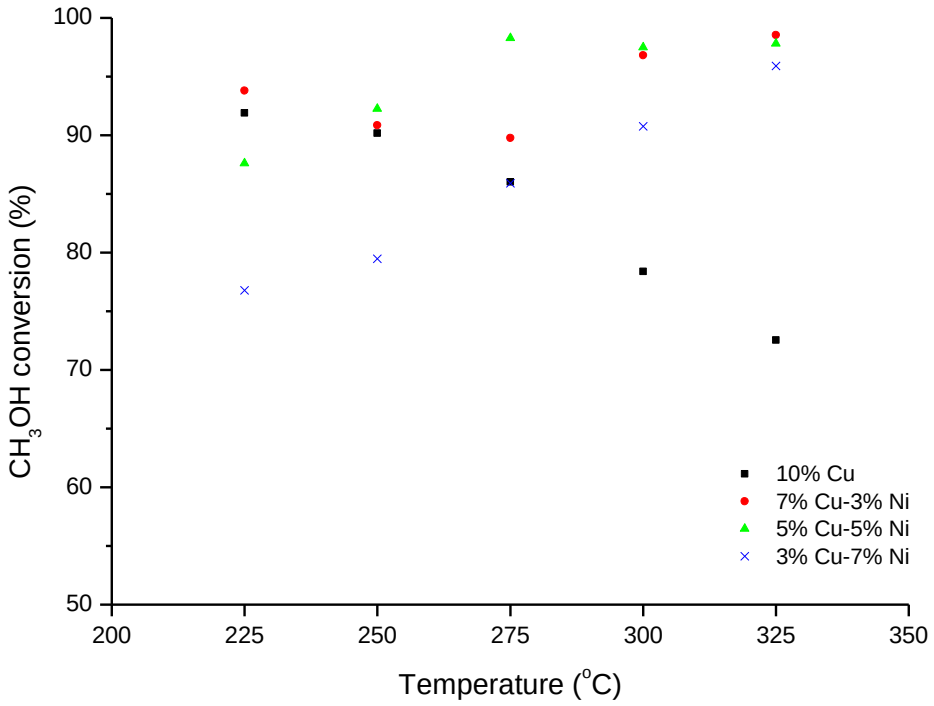

Figure 6.5. Methanol conversion within 225-325°C and S/C of 1.7 for 10%Cu, 7%Cu-3%Ni, 5%Cu-5%Ni and 3%Cu-7%Ni methanol catalysts.

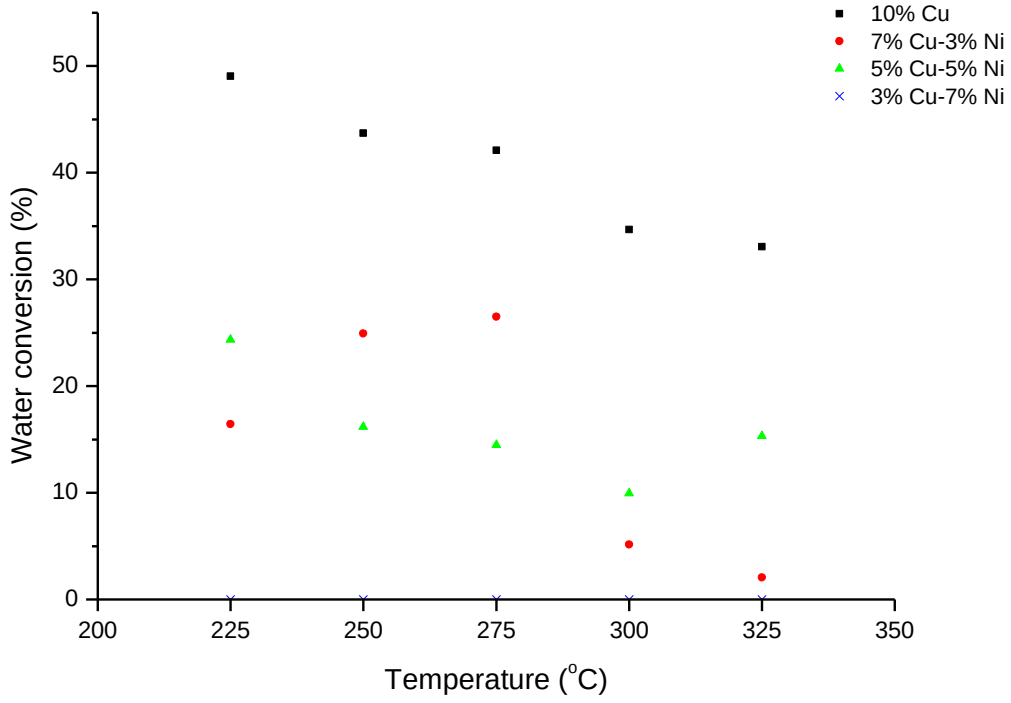

Figure 6.6. Water conversion within 225-325°C and S/C of 1.7 for 10%Cu, 7%Cu-3%Ni, 5%Cu-5%Ni and 3%Cu-7%Ni methanol catalysts.

The methanol and water conversions are displayed in Figure 6.5 and Figure 6.6, respectively. The bimetallic catalyst revealed a lower water conversion than 10%Cu catalyst at all operating temperatures and the bimetallic catalyst showed a superior methanol conversion at 300-325°C. For 7%Cu-3%Ni catalyst, the methanol conversion decreased from 94% at 225°C to 90% at 275°C, then it showed an increase up to 98.5% at 325°C . The 7%Cu-3%Ni catalyst revealed a slight increase in water conversion within 225-275°C then it decreased rapidly within 300-325°C. The slight increase in water consumption indicates that methanol steam reforming is a part of the reaction. However, the water consumption was less than 10%Cu catalyst for all temperatures which explains the existence of decomposition reaction as explained from the amount of CO produced later in this section. Both 5%Cu-5%Ni and 3%Cu-7%Ni catalysts showed an increase in conversions with increasing the reaction temperature (87.6%-97.8% for 5%Cu-5%Ni and 76.8-95.9% for 3%Cu-7%Ni) which is explained by the possible methanol decomposition reaction that occurs on Ni species in bimetallic catalyst [137, 141, 166] where CO was produced. The water consumption for 5%Cu-5%Ni was less than 10%Cu and it decreased with increasing the reaction temperature. There was no water consumption for 3%Cu-7%Ni, this explains the low methanol conversion at low reaction temperature (225-250°C) since the decomposition reaction is the dominant reaction for such catalyst and the conversion increase with increasing the reaction temperature.

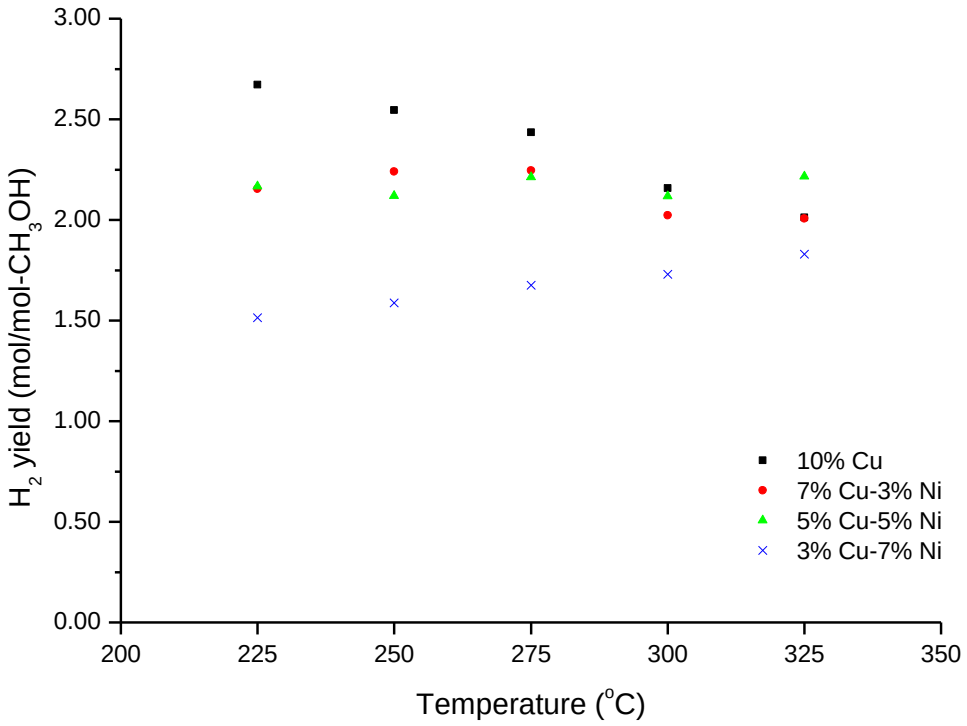

Figure 6.7. Hydrogen yield within 225-325°C and S/C of 1.7 for 10%Cu, 7%Cu-3%Ni, 5%Cu-5%Ni and 3%Cu-7%Ni methanol catalysts.

The steam reforming reaction on various prepared catalysts showed that 10%Cu produced the highest amount of hydrogen within 225-300°C compared to other prepared catalysts, as shown in Figure 6.7. It was noticed that adding Ni metal to the Cu catalyst reduced the amount of hydrogen produced and it suggests that the bimetallic catalyst is less selective for hydrogen production than the monometallic Cu catalyst at such an operating temperature. The hydrogen yield of 2.2 mol/mol-CH_3OH was observed over 5%Cu-5%Ni catalyst at 325°C which is the highest amount at such temperature for all prepared catalyst. The hydrogen yield was approximately constant (2.0-2.2 mol/mol-CH_3OH) for 7%Cu-3%Ni and 5%Cu-5%Cu catalysts. The hydrogen yield increased from 1.5 mol/mol-CH_3OH at 225°C to 1.8 mol/mol-CH_3OH at 325°C for 3%Cu-7%Ni catalyst. More Ni metal in the catalyst made the catalyst less selective to hydrogen as observed for the 3%Cu-7%Ni catalyst. This confirms

that Ni rich catalysts (with more than 5wt.%) are favourable for the decomposition reaction rather than the steam reforming reaction itself. For bimetallic catalyst, the decrease in hydrogen amount compared to 10%Cu could be due to the active methanol decomposition reaction over Ni and the reverse water gas shift reaction affecting the concentration of hydrogen produced as both reactions are thermodynamically favoured [130-133].

The carbon oxides yields are shown in Figures 6.8 and 6.9 as a function of temperature for various catalysts. The influence of increase the Ni content in the catalyst on reformate yield had shown an increase in CO and decrease in CO_2. It is observed from Figure 6.8 that increasing the amount of Ni content in the catalyst negatively affects CO_2 production compared to 10% Cu. The amount of CO_2 formed in operated bimetallic catalyst is less than the amount obtained with the monometallic Cu catalyst. It was also observed that with 10%Cu, 7%Cu-3%Ni, 5%Cu-5%Ni catalysts, the amount of CO_2 decreased when increasing the temperature in the range of 225-325°C. However, the amount of CO_2 formed with 3%Cu-7%Ni decreased within 225-275°C and then increased within 300-325°C, this observation is discussed below. From Figure 6.9, the amount of CO produced increased with the increase of Ni content upon the catalyst. The trend in CO yield with catalyst type is opposite to the trend of CO_2 shown in Figure 6.8.

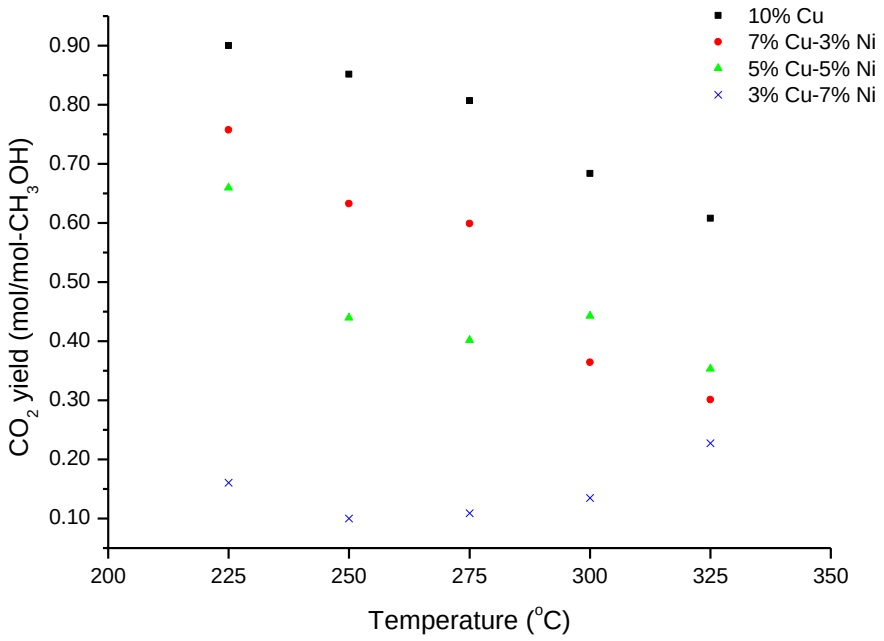

Figure 6.8. CO_2 yield within 225-325°C and S/C of 1.7 for 10%Cu, 7%Cu-3%Ni, 5%Cu-5%Ni and 3%Cu-7%Ni methanol catalysts.

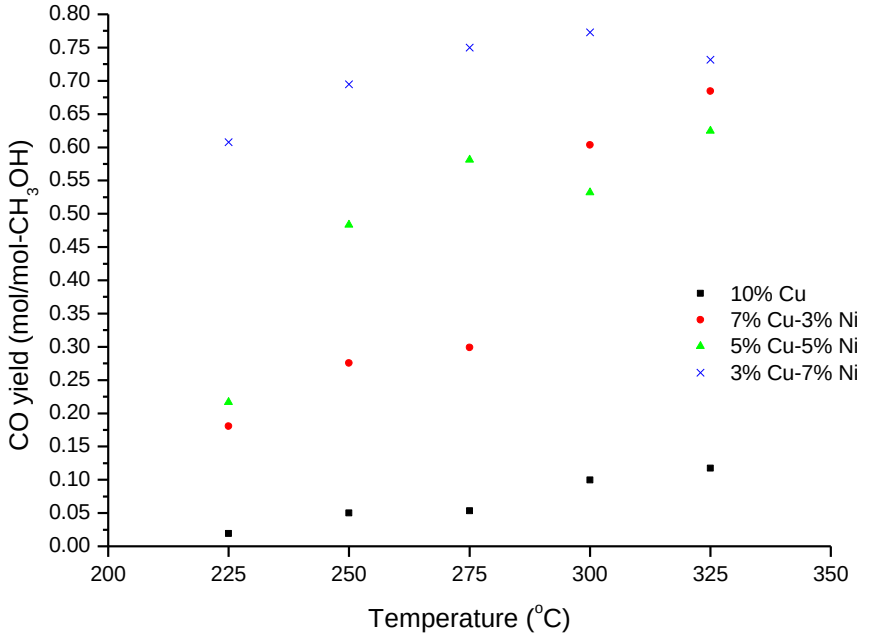

Figure 6.9. CO yield within 225-325°C and S/C of 1.7 for 10%Cu, 7%Cu-3%Ni, 5%Cu-5%Ni and 3%Cu-7%Ni methanol catalysts.

In order to understand the effect of Ni content, methanol steam reforming over 10% Ni catalyst was tested. The main products over 10% Ni (Table 6.1) were CO and H_2, which were produced from the methanol decomposition reaction. The formation of a small amount of CO_2 is related to the water gas shift reaction. The methanol steam reforming over 10%Ni produced a significant amount of CH_4 due to CO and CO_2 hydrogenation [149] which was not observed in 10%Cu and bimetallic Ni-Cu catalysts. The difference between 10%Ni catalyst and 10%Cu catalyst is that the latter one promotes the water gas shift reaction as observed from the formation of large quantities of CO_2 and small quantities of CO in Figure 6.8 and Figure 6.9, respectively. As a result, the water gas shift reaction equilibrium shifts towards the reactants with increasing the temperature at which the conversion of CO to CO_2 is decreased as observed for 10%Cu in Figure 6.9.

Table 6.1. Product yield for methanol reaction for 10%Ni and for physical mixture of single metal 10%Cu and 10%Ni catalysts.

	10%Ni	**10%Ni, 10%Cu***	**10%Ni, 10%Cu***	**10%Ni ,10%Cu***
Temperature (°C)	325	325	325	275
S/C	1.7	1.7	1.3	1.3
Methanol Conversion (%)	70.9	96.1	91.6	86.9
Water conversion (%)	15.0	22.5	15.3	27.0
H_2 yield	1.47	2.08	1.84	2.03
CO_2 yield	0.11	0.71	0.68	0.72
CO yield	0.50	0.13	0.14	0.11
CH_4 yield	0.10	0.11	0.09	0.03

*Physical mixture of single metal (1.5 g of 10%Cu and 1.5 g of 10%Ni).

The bimetallic effect for Ni-Cu catalyst was also compared with the physical mixture of single metal 10%Cu and 10% Ni catalysts. The reaction over the physical mixture

of single metal 10%Ni and 10% Cu (Table 6.1) showed significant formation of CH_4 which was not observed for 10% Cu and Ni-Cu catalysts. Copper-based catalysts have good activity for the water gas shift reaction, and have no methanation activity, as discussed in equilibrium analysis in Chapter 4. The existence of single Ni catalyst in the reactor promotes CH_4 formation by CO and CO_2 hydrogenation [149]. The reaction over physical mixture showed less CO and more CO_2 than the bimetallic system. This indicates that the 10%Cu catalyst in the mixture controls the high activity of the water gas shift reaction.

By comparing the carbon oxide yield over monometallic 10%Cu, 10%Ni and physical mixture of single metals 10%Cu and 10%Ni catalysts, it was observed that the CO amount is strongly dependent on the Cu content in the bimetallic Ni-Cu catalysts, which affects the water gas shift reaction equilibrium. The decrease in Cu content with respect to Ni in the catalyst showed an increase in CO formation, suggesting that the water gas shift reaction moves towards reactants. The increase in Ni content with respect to Cu on the bimetallic catalyst revealed additional CO derived from the methanol decomposition reaction. The bimetallic Ni-Cu catalyst did not produce CH_4, suggesting an inhibiting effect of Cu alloying for CO and CO_2 hydrogenation on Ni. It was reported that Cu has a low CO dissociation activity where CO remains on the catalyst surface [149]. As a result, the Cu presented in Ni-Cu catalyst prevents the CO activation on Ni sites in Ni-Cu catalyst.

The reaction activity profile (Figures 6.8 and 6.9) for carbon oxide yield for 3%Cu-7%Ni revealed slightly different trends over 5%Ni-5%Cu and 7%Cu-3%Ni catalysts. The amount of CO_2 formed with 3%Cu-7%Ni decreased within 225-275°C then increased at temperatures in the range of 300-325°C. It is well known that Cu

promotes the water gas shift reaction at low temperature and the reaction equilibrium moves towards the reactants by increasing the temperature. Hence, the CO amount will increase. On the other hand, Ni promotes methanol decomposition reaction and the reaction becomes very operative with increasing the temperature. Accordingly, it is expected that the amount of CO would increase and CO_2 decrease with increasing the reaction temperature as observed for 5%Ni-5%Cu and 7%Cu-3%Ni catalysts. Indeed, the reverse water gas shift reaction was found to be active at temperatures of 300-325°C for 7%Cu-3%Ni and 5%Cu-5%Ni catalysts, evidenced by a drop in water consumption (Figure 6.7) at these high temperatures. For 3%Cu-7%Ni catalyst, the Ni rich alloy effect was observed. The Ni-Cu alloy phase is responsible for balancing the amount of CO with respect to CO_2. According to the methanol reforming on VIIIB Group metals discussed in Chapter 2, it was mentioned that methanol reaction over metallic phase exhibited a different path than alloy phase [119, 141, 142, 166, 167]. The C=O bond adsorbed upon the alloy phase prevents the direct decomposition of aldehyde (HCHO) to from CO and hydrogen, which is not the case in the metallic phase. For the metallic phase, CO is directly produced from methanol decomposition and in the alloy phase CO_2 is formed via formic acid. It is reasonable to infer that the alloy phase has a balancing effect in CO_2 and CO yield for 3%Cu-7%Ni at a temperature above 275°C.

It is concluded that a higher metal content of Ni over Cu has a strong influence upon the amount of CO_2 by controlling the dominant reaction paths [119, 141, 142, 166, 167]. When increasing the amount of Ni, the effect of bimetallic Ni-Cu becomes dominant in the reaction. The decomposition reaction on the metallic phase of Ni-Cu is responsible for producing a high amount of CO in the products. From the above results, it can be concluded that the decomposition reaction occurs predominantly on

the metallic phase of Ni-Cu and the reverse water gas shift reaction occurs at the Cu site and increase with increasing the reaction temperature, where these reactions are the major contributors for the CO production. Based on the results above it is also concluded that the bimetallic Ni-Cu catalyst produced negligible amount of CH_4. It was validated experimentally in this work that performing methanol steam reforming reaction over pure 10%Ni catalyst or over physical mixture of single metal 10%Ni and 10%Cu catalysts at 325°C and S/C of 1.7 produced a noticeable amount of CH_4 (up to 0.11 mol/mol-CH_3OH). The effects of the Ni-Cu alloy phase in the reaction for all bimetallic catalysts were observed from the negligible amounts of CH_4 produced during the reaction, which means that the alloy phase is responsible for decreasing the hydrogenation effects of CO or CO_2 [149]. This suggests that the added Ni significantly decreases the CO or CO_2 hydrogenation activity of nickel catalysts by alloying, which means that no further hydrogen is consumed to generate CH_4.

6.3 Characterization of used methanol steam reforming catalysts

In this section, characterization results and discussion are presented for the spent catalysts in order to understand the catalyst properties during the reaction. The morphology of the used catalyst operated at 225°C and 325°C and S/C of 1.7 was examined using SEM. Then the catalyst surface area (determined using the BET method) and pore size were calculated using nitrogen adsorption-desorption isotherm data. The crystallite phase and size were estimated using XRD analysis. Finally, the TGA measurement was performed in order to study the carbon formation on the catalyst surface.

6.3.1 SEM of used methanol catalysts

The morphological appearance of the spent catalysts (10%Cu, 7%Cu-3%Ni, 5%Cu-5%Ni and 3%Cu-7%Ni) operated at 225°C and 325°C and the S/C of 1.7 are shown in Figures 6.10 and 6.11, respectively. The SEM images of the used 10%Cu catalyst which had been previously exposed to a temperature of 225°C during reaction, depicted in Figure 6.10a, shows a shade of white spots which correspond to Cu species (highlighted by a marked blue circle) distributed over grey Al_2O_3 support. Small agglomerates of particles are apparent on the left side of the image (highlighted by a marked green circle). The distribution of particles showed uniformity over the support. The SEM image of the used 10%Cu catalyst reacted at 325°C in Figure 6.11a showed shade white spots (highlighted by a marked blue circle) which represent Cu species distributed over shades of grey Al_2O_3 support but more agglomeration (highlighted by a marked green circle) have appeared on the catalyst compared to the SEM image of the used 10%Cu catalyst reacted at 225°C. This would be explained by the fact that increasing the reaction temperature to 325°C may lead to the sintering of copper crystallites, causing coarsening [80].

The surface morphology of the used 7%Cu-3%Ni catalyst reacted at 225°C is showed in Figure 6.10b. Shades of white spots which represent Cu species (highlighted by a marked blue circle) and bright white spots which refer to Ni species (highlighted by a marked red circle) are distributed uniformly across the surface of the aluminium support with small agglomerates of particles appearing on the catalyst surface (highlighted by a marked green circle). Figure 6.11b shows the SEM image of the used catalyst operated at 325°C in the reaction, from which it is observed that larger agglomerates of particles appear on the catalyst surface (highlighted by a marked green circle) compared to 7%Cu-3%Ni reacted at temperature 225°C.

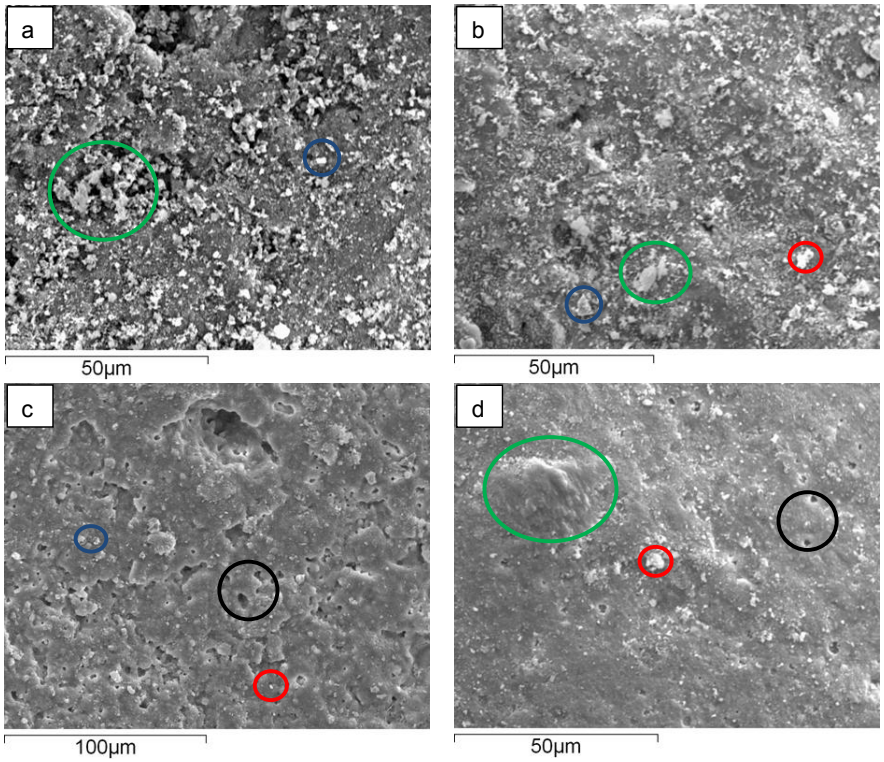

Figure 6.10. SEM images of the used methanol catalysts reacted at 225°C and S/C of 1.7: a) 10%Cu, b) 7%Cu-3%Ni, c) 5%Cu-5%Ni and d) 3%Cu-7%Ni.

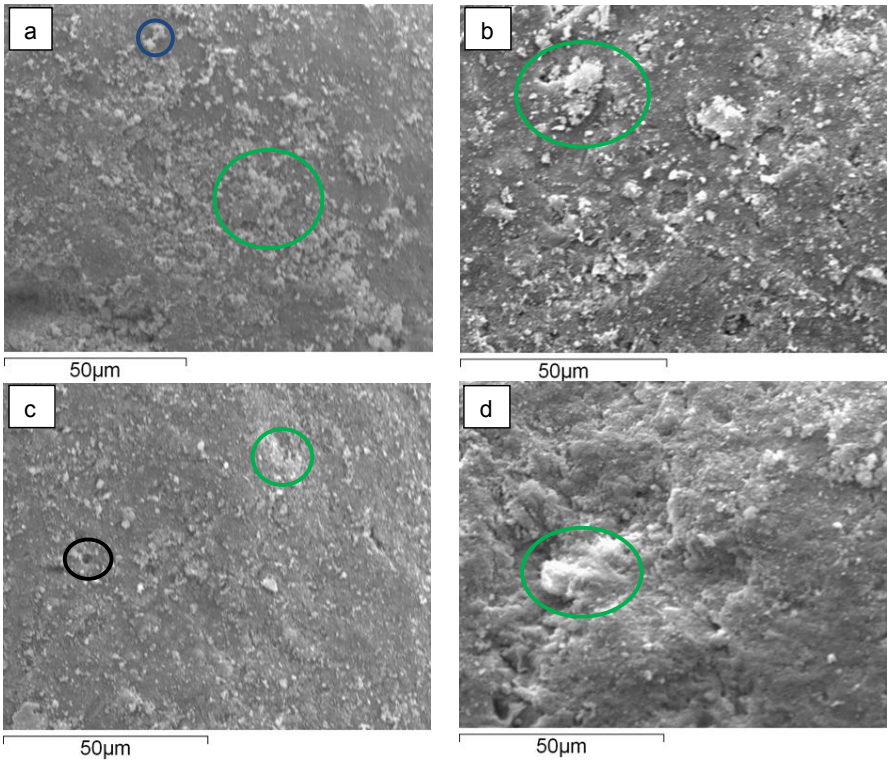

Figure 6.11. SEM images of the used methanol catalysts reacted at 325°C and S/C of 1.7: a) 10%Cu, b) 7%Cu-3%Ni, c) 5%Cu-5%Ni and d) 3%Cu-7%Ni.

The SEM image of the used 5%Cu-5%Ni reacted at 225°C in Figure 6.10c shows shades of white spots which correspond to Cu species (highlighted by a marked blue circle) and bright white spots which represent Ni species (highlighted by a marked red circle) distributed across the surface of the Al_2O_3 support. Figure 6.11c shows the distribution of species throughout the support for the used catalyst reacted at 325°C. It is observed that a uniform distribution of species occurs with smaller agglomerates (highlighted by a marked green circle) compared to the used 10%Cu and 7%Cu-3%Ni catalysts reacted at 325°C. However, some cracks (highlighted by a marked black circle) are visible for the used 5%Cu-5%Ni reacted at 225°C and 325°C.

The SEM image in Figure 6.10d for the used 3%Cu-7%Ni reacted at 225°C showed bright white spots which refer to Ni species (highlighted by a marked red circle) throughout the support with large agglomerates (highlighted by a marked green circle) and cracks observed on the surface (highlighted by a marked black circle). From Figure 6.11d, the used 3%Cu-7%Ni catalyst reacted at 325°C showed large agglomerates of bright white spots which correspond to Ni species agglomeration (highlighted by a marked green circle).

6.3.2 Nitrogen adsorption-desorption for the used methanol catalysts

The changes to the catalyst surface area and pore diameter after the reaction were studied and compared with respect to the fresh catalyst in order to understand the effects of the reaction on catalyst characteristics. Therefore, the used catalysts reacted at 225°C and 325 °C and S/C of 1.7 were investigated using nitrogen adsorption-desorption analysis. The isotherm adsorption-desorption graphs for the used catalysts are shown in Figures 6.12 and 6.13.

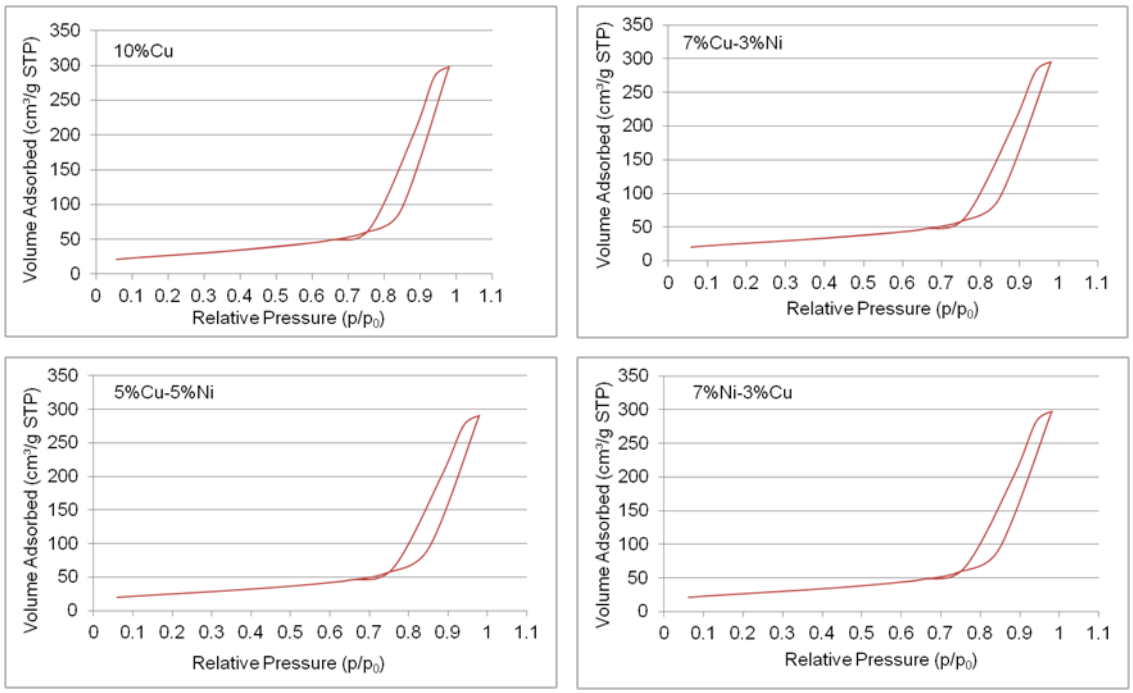

Figure 6.12. The sorption isotherms of nitrogen at 77K for the used methanol catalysts reacted at 225°C and S/C of 1.7.

The adsorption-desorption isotherm for the used catalysts at 225°C and 325°C showed a low nitrogen uptake at a low relative pressure (P/P_0＜0.75). The increase in the adsorption with the increase in the relative pressure was obtained at (0.85＜P/P_0＜0.95). Based on the isotherm classification discussed in Figures 3.3 and 3.4, illustrated in Section 3.2.4 of Chapter 3, the used catalysts were found to be of Type V and hysteresis H1. This means that, based on the classification, the used catalysts reacted at 225°C and 325°C indicated the mesoporosity with a low energy of adsorption, including a regular and even pore distribution in the Al_2O_3 support [273].

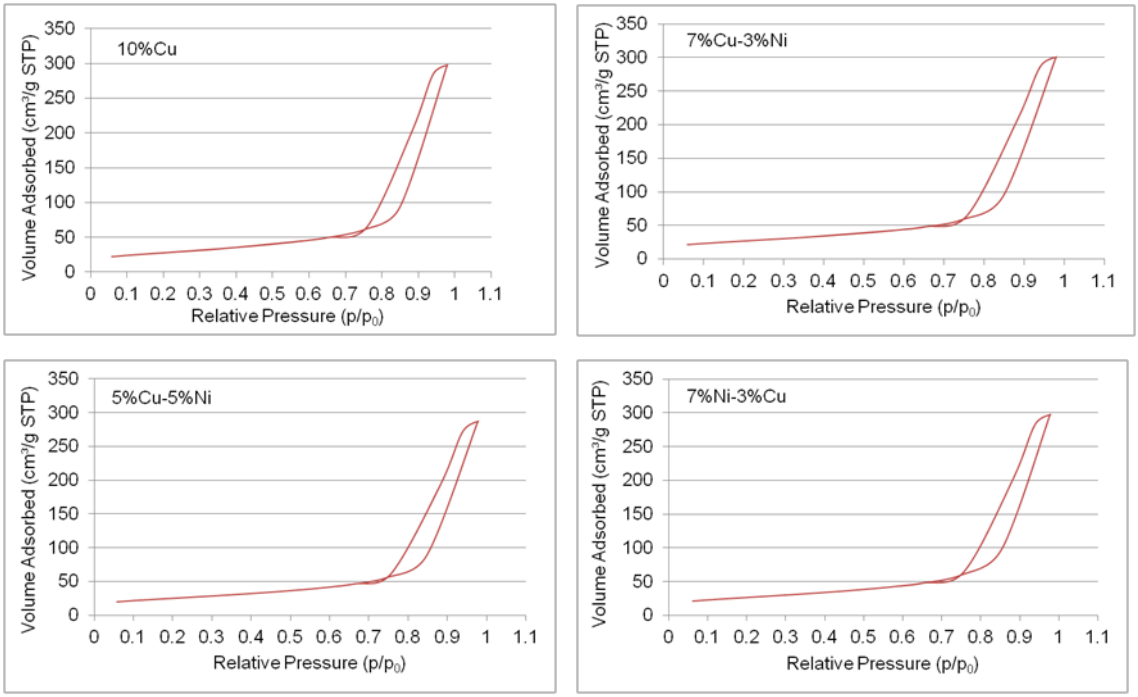

Figure 6.13. The sorption isotherms of nitrogen at 77K for the used methanol catalysts reacted at 325°C and S/C of 1.7.

Comparing the isotherms for the fresh catalysts in Figure 5.3, displayed in Section 5.2 of Chapter 5, with the used catalysts in Figures 6.12 and 6.13, the used catalysts displayed a lower volume of adsorption. This is likely to be caused by the blockage in the pores of the corresponding Al_2O_3 support for the used catalysts leading to a reduction in the volume of N_2 adsorbed. Both types of the used catalysts showed a similar adsorption-desorption isotherm. Furthermore, the analysis of nitrogen adsorption-desorption had shown that the used catalyst indicated negligible microporous volume. The BET surface area calculations using the linearized form of BET equation (Eq. 3.4), discussed in Section 3.2.4 of Chapter 3, showed that the used catalysts had a lower surface area than the fresh catalysts as summarized in Table 6.2. This can be explained by the pore-blockage of the support after the reaction. Both temperatures showed similar results indicating that increasing the

reaction temperature from 225°C to 325°C causes only minor changes to the catalyst surface area and pore size.

Table 6.2. BET surface area and pore diameter for the fresh and used methanol catalysts reacted at 225°C, 325°C and S/C of 1.7.

	10%Cu	**7%Cu-3%Ni**	**5%Cu-5%Ni**	**3%Cu-7%Ni**
Surface area, fresh (m^2/g)	120	125	128	125
Surface area ,reacted at 225°C (m^2/g)	96	94	90	94
Surface area , reacted at 325°C (m^2/g)	98	94	89	95
pore diameter, fresh (nm)	19.2	20.1	19.6	19.8
pore diameter, reacted at 225°C (nm)	19.2	19.6	20.0	19.5
pore diameter, reacted at 325°C (nm)	18.9	19.8	20.0	19.4

6.3.3 XRD analysis for the used methanol steam reforming catalysts

The XRD patterns for the used catalysts operated at 225°C and 325°C and S/C of 1.7 are shown in Figures 6.14 and 6.15. The differences in XRD patterns between the fresh (Figure 5.6, displayed in Section 5.4 of Chapter 5) and the spent catalysts can be identified below. The XRD patterns of all the used catalysts showed peaks related to the metallic phases of Ni or Cu and γ-Al_2O_3 and a trace amount of θ-Al_2O_3.

The monotype catalyst 10%Cu showed XRD patterns of Cu metals at 2θ = 44°, 50° and 72° and the average crystallite size of Cu was 18.1 nm. The bimetallic used catalysts showed patterns related to metallic Ni and metallic Cu and for Ni-Cu. The average crystallite size of bimetallic catalysts is 16.8 nm at 2θ = 37°. The XRD patterns for the used bimetallic catalysts showed the metallic phase of an alloy when increasing the amount of Ni in Cu in the catalyst. The formation of a Ni-Cu alloy

reported in the literature depends on the amount of Ni contents, indicating the Ni rich alloy or Cu rich alloy catalyst [149, 305]. The rich Ni alloy phase or rich Cu alloy phase reported in the literature determines the reaction paths discussed in Section 6.2. For instance, a dominant decomposition reaction occurred with 7%Ni-3%Cu over the metallic phase of Ni which was concluded from the high concentration of CO produced (Figure 6.9) at 225-275°C. However, 7%Cu-3%Ni showed a dominant decomposition reaction over the metallic phase of Cu as a large amount of CO was produced at 300-325°C. The XRD patterns for used catalyst operated at 225°C and 325°C showed similar patterns, such that the effects of reaction temperature on the metal phase cannot be deduced. However, the XRD patterns displayed less diffuse and sharper patterns for the catalysts reacted at 325°C than 225°C. This would be possible due to crystallite growth with increasing the reaction temperature.

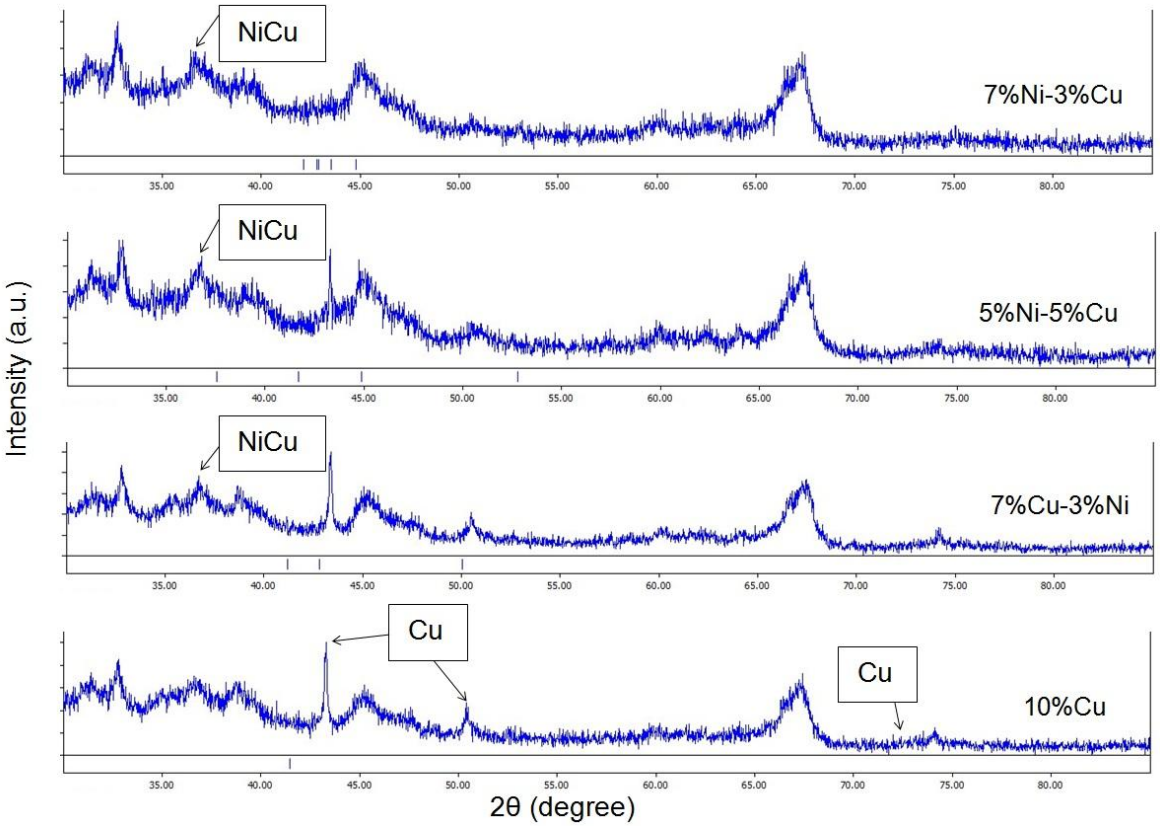

Figure 6.14. XRD patterns for the used methanol catalysts reacted at 225°C and S/C of 1.7.

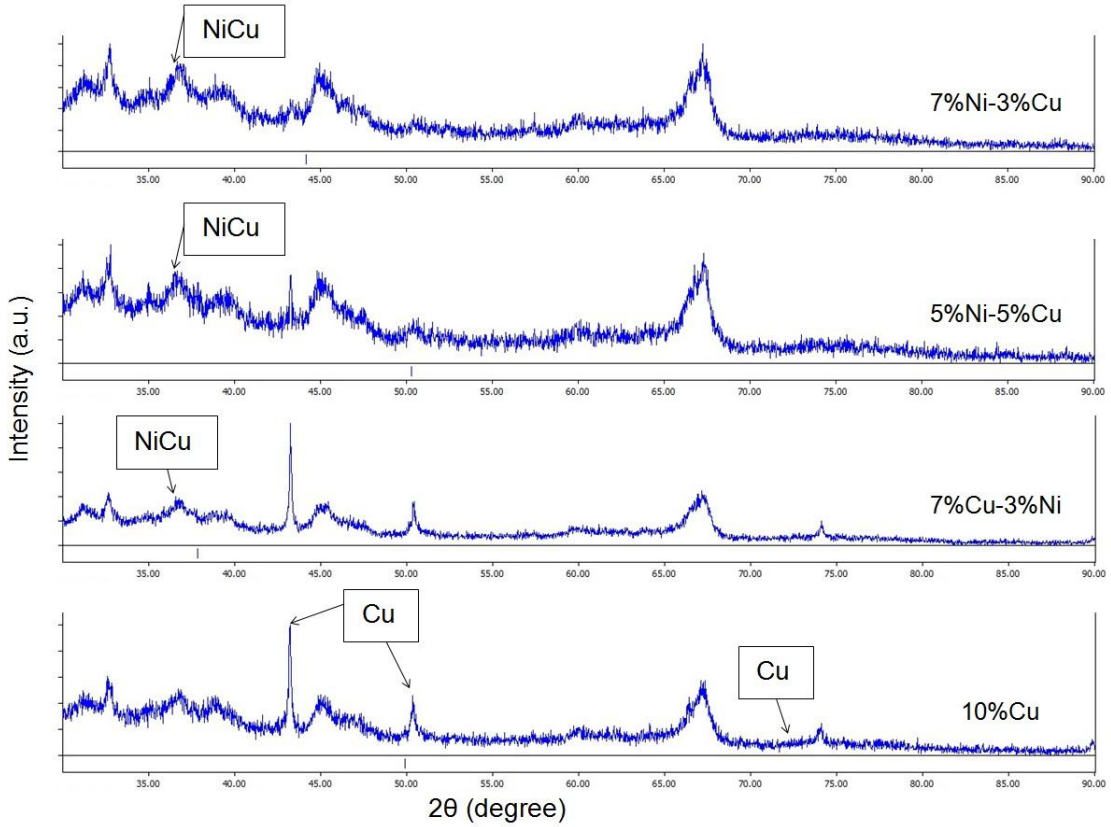

Figure 6.15. XRD patterns for the used methanol catalysts reacted at 325°C and S/C of 1.7.

The XRD for the used catalysts are also proof that the catalyst was reduced properly since no metal oxide phase was detected, except for aluminates related to the support material, but a comparison of the XRD patterns for the fresh catalysts (Figure 5.6, displayed in Section 5.4 of Chapter 5) and used catalysts showed the presence of metal oxide phases in the fresh catalyst. It is also demonstrated that the metals in the catalysts were not oxidised after 4 hours reaction, meaning any observed deactivation was not as a result of oxidation of the catalyst metals [80, 306, 307].

6.3.4 Carbon formation analysis for used methanol steam reforming catalysts

As discussed in Chapter 2, carbon formation is a major cause of catalyst deactivation during methanol steam reforming, which can lead to the loss of surface area of the catalyst and catalyst pore-mouth plugging [65]. In addition, carbon deposition

(coking) may lead to physical damage of the catalyst pores as well as obstruction of the active sites on the catalyst [80].

The TGA discussed in Chapter 3 was carried out to study the amount of carbon formation on the catalyst during the reaction for all operated catalysts at 225-325°C and S/C of 1.3 and 1.7. This was achieved by introducing air into 20 mg of the used sample and heating the sample in the oven from 25°C to 900°C at a ramp rate of 10°C/min. A typical TGA plot for the operated catalyst is shown in Figure 6.16. The mass loss in Figure 6.16 represents the two counteracting effects of carbon burn off and metal oxidation. Therefore, the carbon formation was calculated. The measured mass loss by TGA is assumed as sum of complete metal oxidation to NiO and Cu_2O as shown in Eq. 6.9 and Eq. 6.10, respectively, and carbon burn off. The mass gain is calculated from wt. % of metal loading. The mass of oxygen, based on stoichiometry, that reacts to form NiO and Cu_2O was calculated and deducted from the value obtained from TGA curve. The remainder gives an estimate of carbon formation. The calculation assumed that the catalyst was fully reduced before performing TGA. Then, the accumulated carbon in grams for the reaction duration was calculated as well as the catalyst selectivity for solid carbon (Sel_C) was estimated as shown in Eq. 6.11.

$2Cu + 0.5O_2 \rightarrow Cu_2O$, $\Delta H°_{298}$= -168.6 kJ/mol (Eq. 6.9)

$Ni + 0.5O_2 \rightarrow NiO$, $\Delta H°_{298}$= -239.5 kJ/mol (Eq. 6.10)

$$Sel_C\ (\%) = 100 \times \frac{n_{carbon}}{n_{CH3OH,in}} \quad \text{(Eq. 6.11)}$$

Where n_i is total moles for reaction duration for species i (mol)

The total mass change with the increase in the temperature is shown in Figure 6.16. The peak at temperature 66.4°C (98.60%) shows the loss in the moisture on the catalyst. The prepared catalyst showed a continuous drop in the percentage of mass to 93.95%. The differences between percentages of mass changes (4.65 wt.%) represent the total amount of carbon removed and mass gain due to oxidation of metals of the catalyst. The calculated accumulated solid carbon within the reaction duration (four hours) was 88.5 mg with catalyst selectivity for carbon was 3.2%.

It was valuable to compare the carbon formation of the prepared catalyst with the commercial copper catalyst, discussed in Chapter 5, operated at the same conditions. The same TGA analysis was performed and the result is presented in Figure 6.17. It can be noticed that commercial catalyst has a higher mass change and two regions were observed. The first peak occurred at temperature 151°C with 5.23 wt.% mass change and the second peak at temperature 711°C with 6.80 wt.% mass change. The calculated accumulated solid carbon within reaction duration was 172.0 mg with catalyst selectivity for carbon was 6.2%. Comparing the two TGA graphs, the prepared catalyst is less susceptible for carbon formation than the commercial copper catalyst. The limitation of this comparison is that the commercial catalyst 50%wt.Cu/25%wt.ZnO/25%wt.Al_2O_3 consists of higher active metal loadings. In fact, the carbon formation on the catalyst surface depends on the nature of the active metal phase and the metal-support interaction [248]. The effect of metal loading has not been discussed thoroughly in the literature, however; the carbon formation upon the highly loaded catalyst was found to cause rapid deactivation [308]. The parameters mentioned above would affect carbon removal rate by diffusion as a result the diffusion rate is being faster on small particles due to shorter diffusion path [248]. The CO chemisorption results reported in Table 5.2 (presented

in Section 5.3 of Chapter 5) revealed that active particle diameter of 7%Cu-3%Ni was 75 nm and the active particle diameter for commercial copper catalyst was 334 nm.

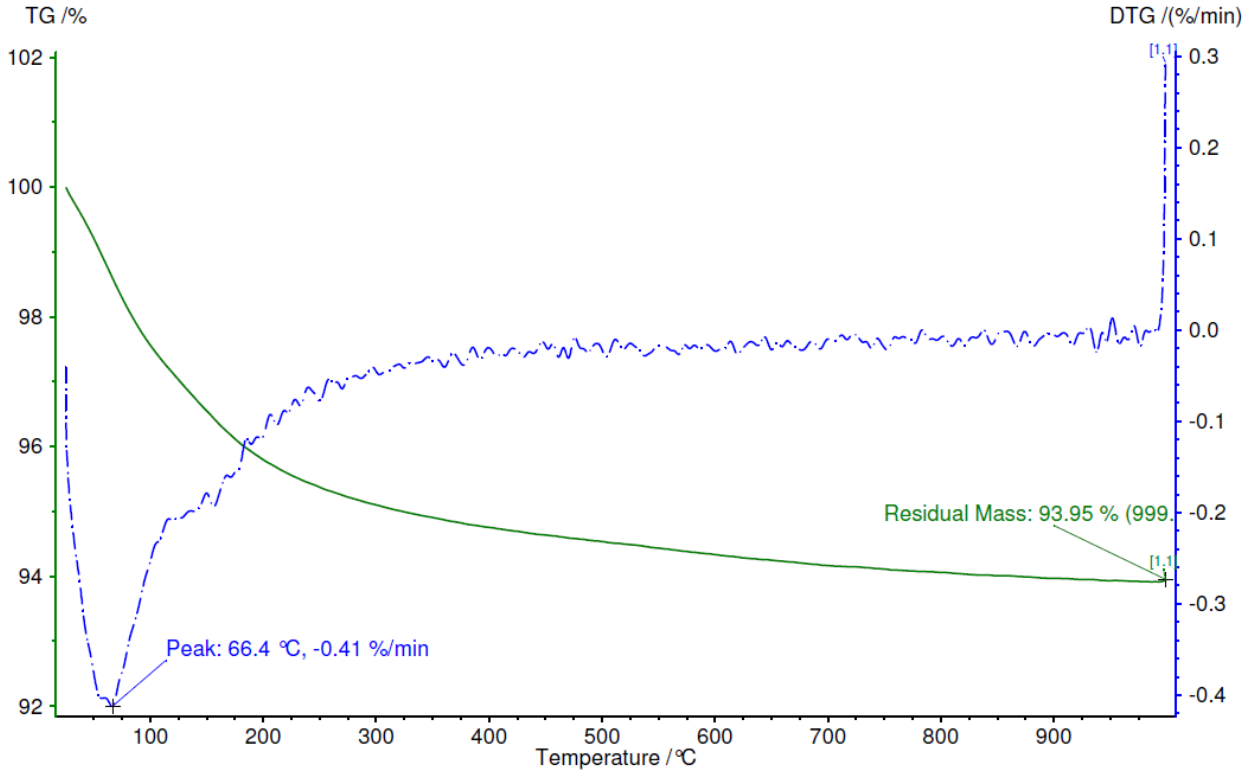

Figure 6.16. Typical TGA graph for the spent methanol 7%Cu-3%Ni catalyst reacted at 325°C and S/C of 1.3, the primary TG axis presents the percentage mass loss and the secondary Derivative Thermo Gravimetric (DTG) axis presents the derivative of percentage mass loss with respect to time as obtained from the NETZSCH software.

Tables 6.3 and 6.4 explain the amount of carbon formation occurring over the spent catalysts for methanol steam reforming. When the steam to carbon ratio was increased from 1.3 to 1.7, the amount of carbon decreased. Accordingly, the results are in agreement with the one reported in the literature where the increase of steam revealed a decrease in the amount of coke formed [69, 306]. Generally, the carbon formation depends on the catalyst composition and the reaction temperature [248]. Both parameters are affecting the carbon formed on the catalyst surface. It was reported and calculated in the literature that carbon will form at the operating temperature below 670°C for S/C of 1 and below 600°C for S/C of 2 [306]. Hence,

the entire reaction temperature reported in Figures 6.16 and 6.17 are within carbon formation region.

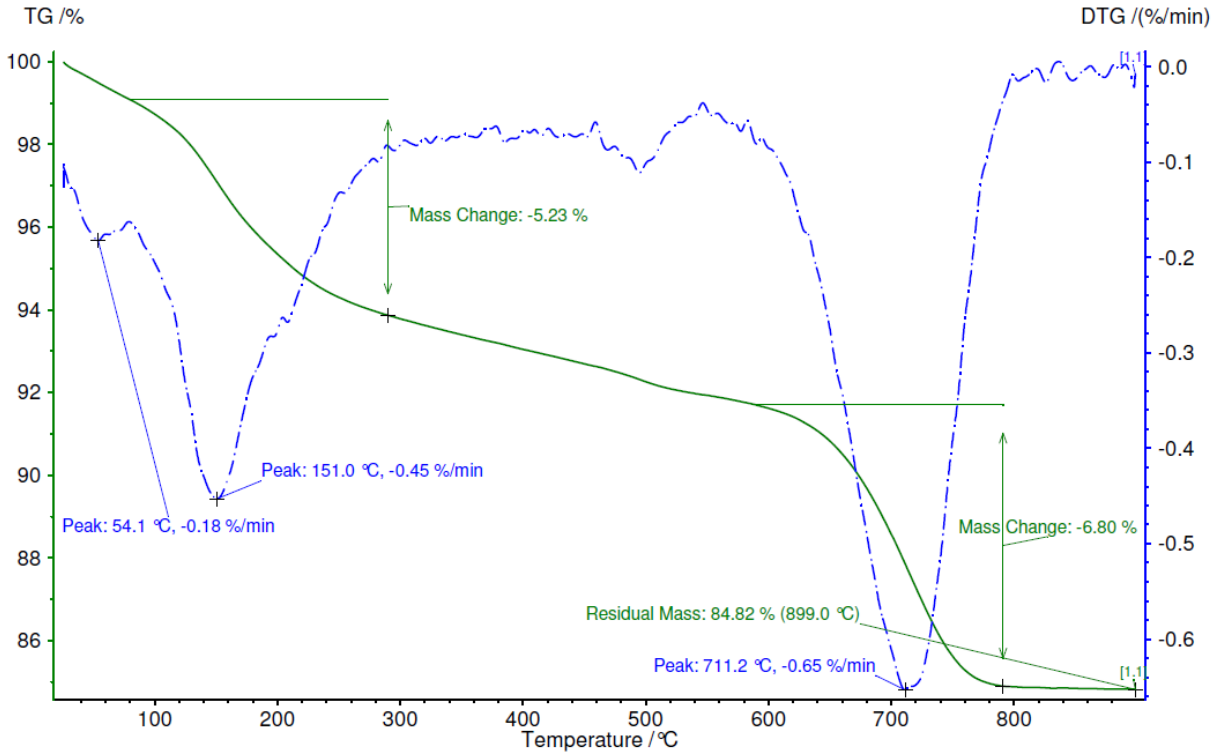

Figure 6.17. Typical TGA graph for the spent methanol copper commercial catalyst reacted at 325°C and S/C of 1.3, the primary TG axis presents the percentage mass loss and the secondary DTG axis presents the derivative of percentage mass loss with respect to time as obtained from the NETZSCH software.

The catalyst composition plays an important factor in the amount of carbon formation. For instance, the prepared catalysts which were reacted at 225-325°C and S/C of 1.7 in Table 6.4 are explained. The bimetallic rich Ni catalyst (5%Cu-5%Ni and 3%Cu-7%Ni) reacted at temperature 300°C showed less carbon deposition than 10%Cu and 7%Cu-3%Ni. On other hand, 7%Cu-3%Ni and 3%Cu-7%Ni showed less carbon deposition than 10%Cu reacted at temperature 250°C. The 10%Cu catalyst produced less carbon than 7%Cu-3%Ni and 5%Cu-5%Ni reacted at temperature 225°C.

Table 6.3. Carbon deposition and selectivity on the used methanol catalysts reacted at 225-325°C and S/C of 1.3.

	10%Cu		**7%Cu-3%Ni**		**5%Cu-5%Ni**		**3%Cu-7%Ni**	
T (°C)	Carbon amount (mg)	Sel_C (%)	Carbon amount (mg)	Sel_C (%)	Carbon amount (mg)	Sel_C (%)	Carbon amount (mg)	Sel_C (%)
225	54.6	2.0	51.0	1.8	43.4	1.6	43.3	1.6
250	66.3	2.4	33.9	1.2	46.7	1.7	27.1	1.0
275	33.3	1.2	28.8	1.0	44.0	1.6	33.7	1.2
300	48.3	1.7	35.1	1.3	27.8	1.0	36.1	1.3
325	60.9	2.2	47.7	1.7	59.9	2.1	32.8	1.2

Table 6.4. Carbon deposition and selectivity on the used methanol catalysts reacted at 225-325°C and S/C of 1.7.

	10%Cu		**7%Cu-3%Ni**		**5%Cu-5%Ni**		**3%Cu-7%Ni**	
T (°C)	Carbon amount (mg)	Sel_C (%)	Carbon amount (mg)	Sel_C (%)	Carbon amount (mg)	Sel_C (%)	Carbon amount (mg)	Sel_C (%)
225	6.9	0.3	22.5	0.9	16.4	0.6	7.3	0.3
250	35.1	1.4	5.1	0.2	28.7	1.1	6.7	0.3
275	20.1	0.8	21.0	0.8	19.4	0.8	36.4	1.4
300	27.3	1.1	34.5	1.4	6.8	0.3	8.5	0.3
325	45.9	1.8	33.9	1.3	57.3	2.3	30.6	1.2

It was reported previously in Section 6.2 that the dominant reaction over Ni metals is methanol decomposition reaction. Therefore, an abundance of CO was noticed in the reformate gases with Ni containing catalysts compared to the gas composition from the 10%Cu catalyst. The Cu species doesn't easily dissociate CO at low temperature [149, 309-311]. Thus, the influence of Cu on carbon formation was noticed at 225°C. The low reactivity of CO dissociation at 225°C on the Ni-Cu catalyst surface is related to dilution of the active Ni sites by the inactive Cu atoms which will increase the carbon deposition formation on the Ni-Cu catalyst surface. The result is in good agreement with that reported for surface of Ni-Cu alloy [312]. It was reported that Cu surface energy is lower compared with Ni and the small size mismatch between Cu and Ni allows Cu atoms to segregate on the Ni-Cu surface causing the Ni sites responsible for carbon formation [312]. Increasing the reaction temperature will dilute the active Ni atoms with much less reactive copper atoms than Ni, reducing the

amount of carbon formed on Ni surface since it gives the opportunity for Ni metals to dissociate CO at high operation temperature [224].

According to previous studies [69, 306], methane and carbon coexist with H_2O, CO, CO_2 and H_2 in the methanol steam reforming reaction. The other compounds such as $HCOOCH_3$, HCHO and HCOOH are not detected in appreciable quantities since these species are only intermediate in the reforming mechanism [69, 306]. In the current study, the methanol steam reforming for prepared catalysts showed a negligible amount of CH_4 formation within the temperature range 225-325°C. Correspondingly, the possible reactions paths for carbon formation during the steam reforming reaction were reported as displayed in Eq. 6.12-6.14 [69, 306].

$CO + H_2 \rightleftharpoons C + H_2O$, $\Delta H°_{298}$= -172.0 kJ/mol (Eq. 6.12)

$CO_2 + 2H_2 \rightleftharpoons C + 2H_2O$, $\Delta H°_{298}$= -87.0 kJ/mol (Eq. 6.13)

$CH_4 \rightleftharpoons C + 2H_2$, $\Delta H°_{298}$= +75 kJ/mol (Eq. 6.14)

It could be concluded that carbon formation on the surface of the prepared catalyst can occur via the reactions in Eq. 6.12 and Eq. 6.13 since both reactions are thermodynamically favourable at low temperatures due to large decreases in Gibbs free energy and both reactions are exothermic according to the literature [69, 306]. On the other hand, the carbon formation from methane in Eq. 6.14 is thermodynamically unlikely at low temperatures and no methane was evident in the reported reactions in Sections 6.1 and 6.2.

6.4 Long-term methanol steam reforming test for 10%Cu, 7%Cu-3%Ni and 5%Cu-5%Ni catalysts

Methanol steam reforming reaction was carried out for the prepared 10%Cu, 7%Cu-3%Ni and 5%Cu-5%Ni catalysts in order to study long-term operation effects on the product yield. The reaction was carried out under same operating conditions as mentioned previously for the short-term catalyst tests in Section 6.1. The reaction temperature was fixed at 325°C and S/C was 1.7. The test was performed for 20 hours within three days by switching the reaction furnace on and off in campaigns, running for average 7 hours per day and shutting down the reaction furnace by leaving the catalyst under nitrogen overnight. The reason for choosing a high temperature for the long-term test is to study the temperature effects and operation time on the product yield and on the catalyst structure. The 3%Cu-7%Ni catalyst was excluded in the long-term study due to adverse effects of high Ni content on methanol reaction products as discussed in Section 6.2.

Figure 6.18 shows hydrogen produced within 20 hours for all tested catalysts. All catalysts revealed a high stability for hydrogen production. The prepared 10%Cu catalyst showed an increase in hydrogen production after one hour of operation and achieved an average hydrogen yield of 1.91 mol/mol-CH_3OH. For instance, the 7%Cu-3%Ni catalyst has revealed an increasing and decreasing trend within period of operation which explains that several reactions are occurring simultaneously on the active sites of the catalyst, which are strongly dependent on partial pressure of the products. The 5%Cu-5%Ni catalyst showed more stability for hydrogen production than the 10%Cu and 7%Cu-3%Ni catalysts.

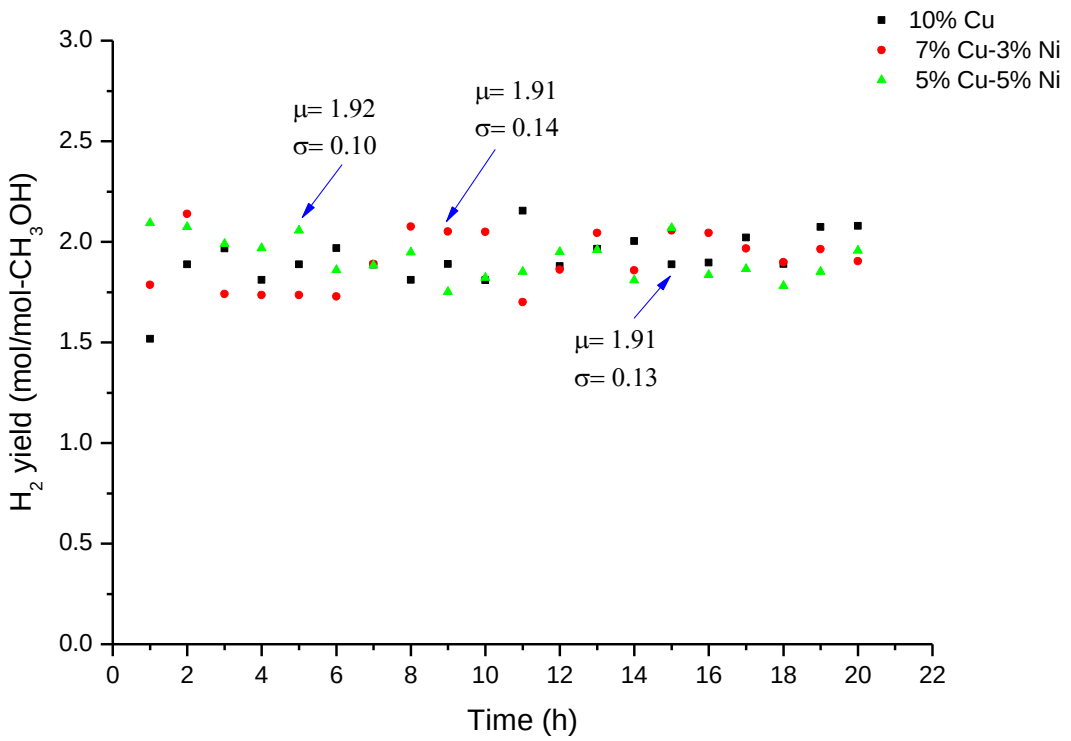

Figure 6.18. Hydrogen yield at 325°C and S/C of 1.7 for 20 hours run for 10%Cu, 7%Cu-3%Ni and 5%Cu-5%Ni methanol catalysts, the values in the graph represent the average (μ) and variation (σ) for 20 hours run.

Figures 6.19 and 6.20 show the amount of carbon oxides produced. Both CO_2 and CO showed an opposite trend. The amount of CO_2 decreased with time and the amount of CO increased. 10%Cu showed stability for CO production (0.07 mol/mol-CH_3OH) with only varying 0.02 mol/mol-CH_3OH over the course of the reaction, this amount is less than the predicted by equilibrium calculation (0.12 mol/mol-CH_3OH) indicating that CO is produced via reverse water gas shift reaction. The 7%Cu-3%Ni and 5%Cu-5%Ni showed a large increase in the amount of the CO produced. This effect occurs since some of the CO_2 produced via steam reforming reaction is consumed in the reverse water gas shift reaction to produce CO and additional amount of CO is produced from the decomposition reaction at 325°C. Both bimetallic

catalysts showed an increasing trend in CO (Figure 6.20) and a decreasing trend in CO_2 (Figure 6.19) for 14 hours then they showed stabilized production trend.

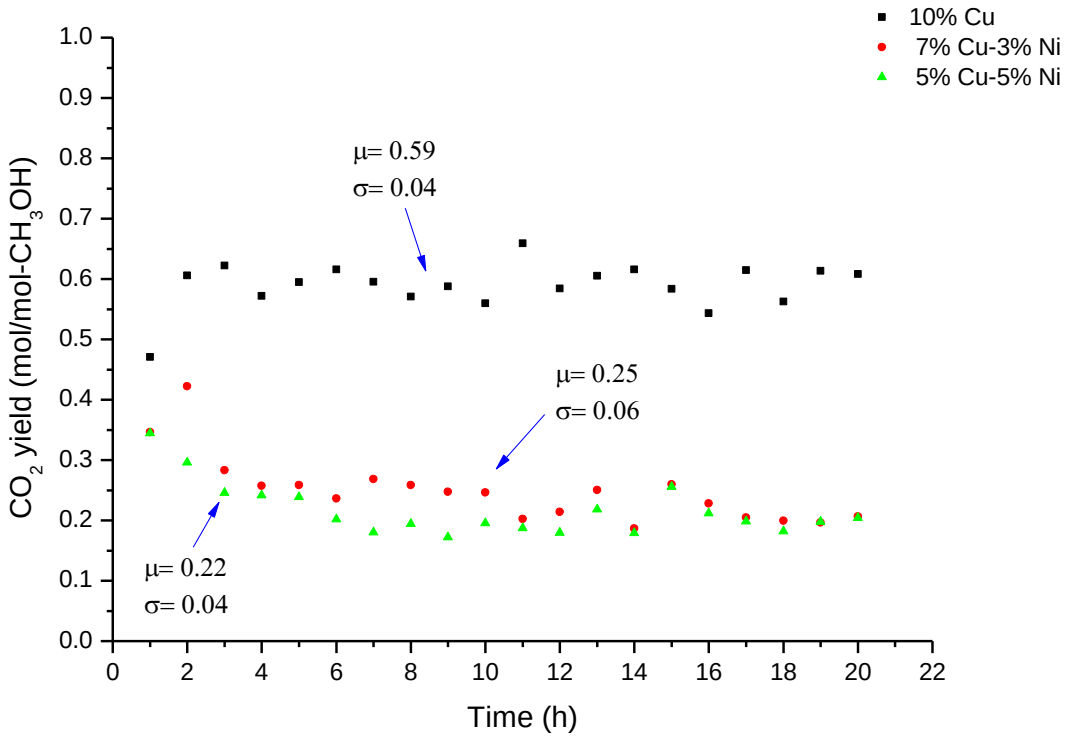

Figure 6.19. CO_2 yield at 325°C and S/C of 1.7 for 20 hours run for 10%Cu, 7%Cu-3%Ni and 5%Cu-5%Ni methanol catalysts, the values in the graph represent the average (μ) and variation (σ) for 20 hours run.

In order to study the effects of long-term operation on the catalyst structure, SEM images for the 10%Cu, 7%Cu-3%Ni and 5%Cu-5%Ni catalysts are shown in Figure 6.21. The 10%Cu catalyst in Figure 6.20a showed a long crack (highlighted by a marked black circle) on the support after 20 hours run in addition to shades of white agglomeration (highlighted by a marked green circle) throughout the support. The 7%Cu-3%Ni in Figure 6.21b showed holes on the support (highlighted by a marked black circle) due to the high operating temperature. The 5%Cu-5%Ni catalyst has shown significant metal agglomeration (highlighted by a marked green circle) [313] after 20 hours run as indicated in Figure 6.21c. This negative effect of the long-term

run on the catalyst structure can be related to the catalyst deactivation by thermal sintering [57, 74, 80] at 325°C which can be avoided by running the reaction at a temperature below 300°C [80] .

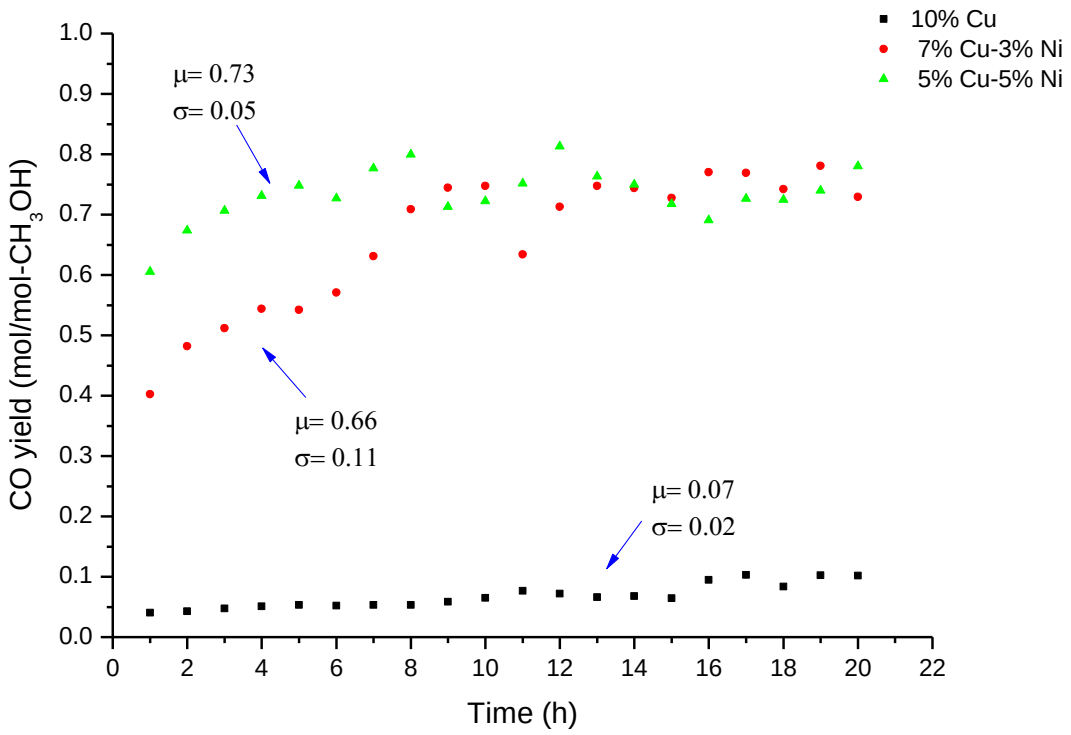

Figure 6.20. CO yield at 325°C and S/C of 1.7 for 20 hours run for 10%Cu, 7%Cu-3%Ni and 5%Cu-5%Ni methanol catalysts, the values in the graph represent the average (μ) and variation (σ) for 20 hours run.

The TGA results of the 10%Cu determined 32.1 mg of carbon deposition with carbon selectivity of 0.3%. The 7%Cu-3%Ni showed 77.1 mg carbon deposition and 0.6% carbon selectivity, and the 5%Cu-5%Ni showed 34.7 mg carbon deposition and 0.3% selectivity for carbon. The TGA analysis of the used methanol catalyst for long-term showed less carbon selectivity for 20 hours run in comparison with the short-test (4 hours) mentioned in Section 6.4.4. It could be that carbon removal was involved within the reaction duration.

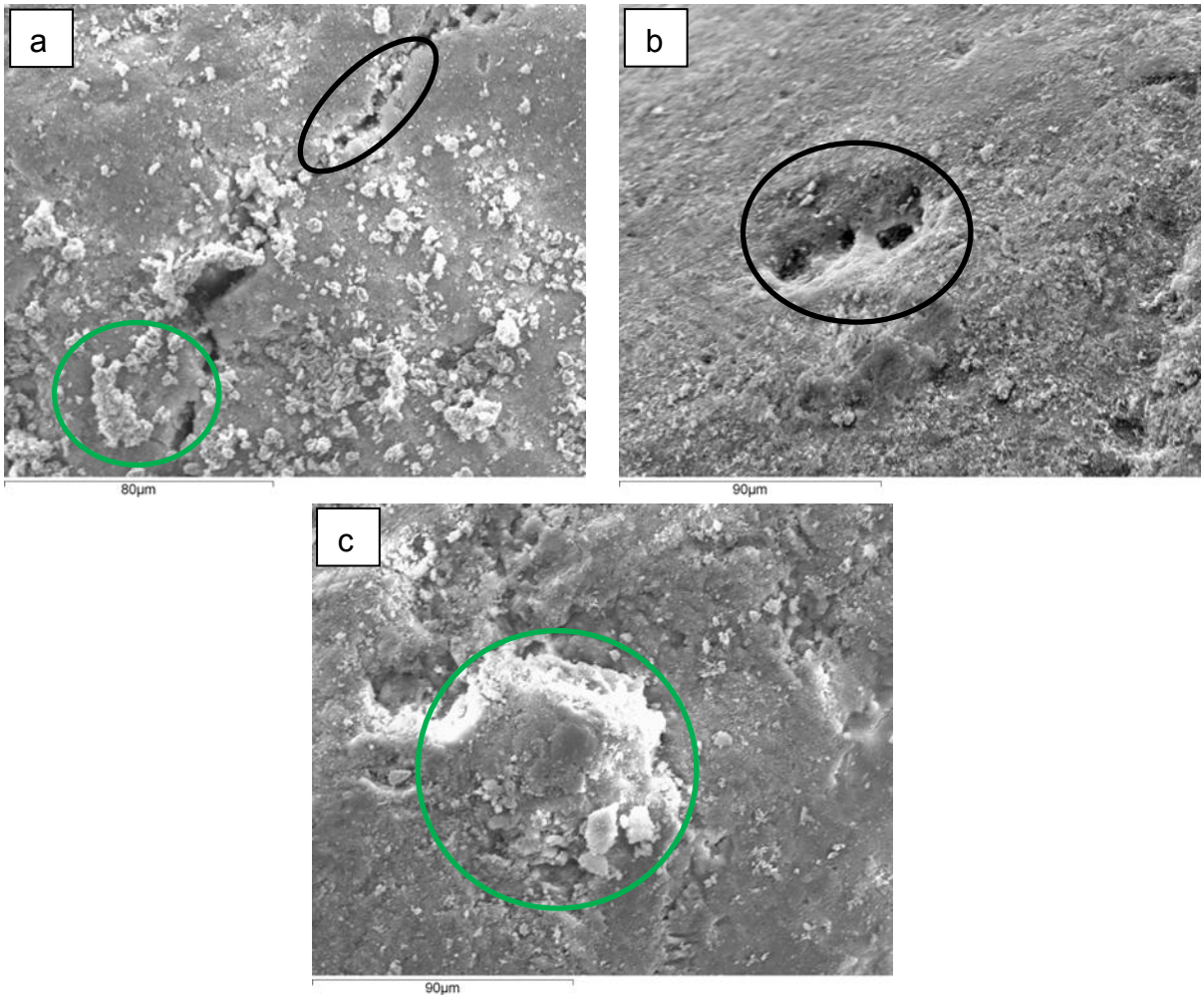

Figure 6.21. SEM images of the used methanol catalysts reacted at 325°C for 20 hours run: a) 10%Cu, b) 7%Cu-3%Ni and c) 5%Cu-5%Ni.

6.5 Chapter summary

The methanol catalytic activity measurements were performed for the prepared catalyst samples in order to study the effects of temperature (225-325°C), steam to carbon ratio (S/C of 1.3 and 1.7) and Ni metals content on Cu-based methanol reforming catalyst. For monometallic 10%Cu catalyst, the methanol conversion decreased from 92% at 225°C to 73% at 325°C. The amount of hydrogen produced decreased with increasing the temperature, the hydrogen yield changed from 2.7 mol/mol-CH_3OH at 225°C to 2.0 mol/mol-CH_3OH at 325°C for S/C= 1.7. It was found that for S/C of 1.7, the amount of CO is nearly equal or slightly greater than the

calculated equilibrium value at temperature 300-325°C, providing that the decomposition reaction is responsible for CO production in parallel with reverse water gas shift reaction.

The increasing Ni metals content had a positive effect on methanol conversion and showed a high methanol conversion at 300-325°C. The methanol conversion was high for 5%Cu-5%Ni and 7%Cu-3%Ni (98.5%) at 325°C which could possibly be explained by the active decomposition reaction. It was shown that 10%Cu catalyst produced the highest amount of H_2 (2.7 mol/mol-CH_3OH at 225°C) compared to other prepared bimetallic catalysts within the temperature range 225-275°C. The increase of Ni metals content showed an adverse effect on the amount of hydrogen produced. The maximum hydrogen yield of 2.2 mol/mol-CH_3OH was observed over 5%Cu-5%Ni catalyst at 325°C. The bimetallic nature of the prepared catalyst showed a negative effect on the amount of CO_2 produced. Increasing the amount of Ni metals content from 3% to 7% led to a big decrease for CO_2 and an increase for CO. A negligible amount of CH_4 was produced over bimetallic catalyst compared with carrying out the methanol reforming reaction over 10%Ni or over physical mixture of single metal 10%Ni and 10%Cu catalyst.

The spent methanol reforming catalysts were characterized in order to study the catalyst properties after the reaction. The SEM images of the reacted catalyst at 325°C showed more species agglomeration than that at 225°C and the SEM images displayed cracks. The reacted catalyst displayed lower BET surface area (89-98 m^2/g) than the fresh prepared catalyst (120-128 m^2/g). The XRD patterns for reacted catalyst revealed a possible crystallite growth with increasing the reaction temperature to 325°C. The prepared catalyst was less susceptible for carbon

formation at S/C of 1.7 than S/C of 1.3. The decrease in carbon formation by increasing the Ni content was attributed to the dilution effect of less active copper atoms with active Ni atoms, giving the opportunity for Ni metals to dissociate CO at high operation temperature as it was less carbon selectivity (1.2% for 3%Cu-7%Ni) than 10%Cu catalyst (1.8%) at 325°C and S/C of 1.7.

Finally, during the long-term stability test, all catalysts revealed a high stability for hydrogen production. The bimetallic catalysts showed an increasing trend in CO and a decreasing trend in CO_2 for 12 hours, and then the trend was stabilized. The SEM of the long-term spent catalyst displayed cracks and holes on the support and large agglomeration of particles was formed. The TGA analysis of the used methanol catalyst for long-term showed less carbon selectivity for 20 hours run in comparison with the short-test (4 hours).

CHAPTER 7

METHANE STEAM REFORMING

This chapter describes the research carried out for the methane steam reforming reaction over in-house prepared catalysts (10%Cu, 7%Ni-3%Cu, 5%Ni-5%Cu and 3%Ni-7%Cu). The reaction was carried out in a fixed bed reactor to study the catalyst reactivity under various operating conditions which will be discussed in Section 7.1. The reactions were carried out for 4 hours at various temperatures of 500, 550, 600, 650 and 700°C at atmospheric pressure. A constant flow rate of CH_4 at 25 ml/min and steam to carbon ratios of 2 and 3 were applied to the reaction system in order to study the fuel conversion and the catalyst selectivity for products. The effects of Cu content in a bimetallic Ni-Cu catalyst (Section 7.2) were also studied and compared with 10%Ni monometallic catalyst for methane steam reforming reaction.

The spent catalyst was characterized and comparisons with a freshly prepared catalyst are drawn and discussed in Section 7.3. The morphology and textural properties of the used catalysts were probed by SEM. The surface areas of the used catalysts at the high (700°C) and low (500°C) temperatures was determined by nitrogen adsorption-desorption analysis. Crystallite size and its phase were determined using XRD. The amount of carbon formation was studied for all used catalyst samples.

Finally, a long-term reaction test for 20 hours duration is also reported in Section 7.4 for selected in-house prepared catalysts, in order to investigate the catalytic behaviour during a long-term operation.

7.1 Effects of methane reaction temperature and steam over prepared 10%Ni/Al_2O_3 catalyst

The catalytic activity measurements were performed in the packed fixed bed reactor as discussed earlier in Chapter 3. The experiments were performed at low methane steam reforming temperature range of 500-700°C, with the S/C ratio of 2 and 3 and atmospheric pressure. The gas hourly space velocity (GHSV) was 1067.4 h^{-1} for methane steam reforming at S/C of 2 and 1388.9 h^{-1} at S/C of 3. The methane ratios of 2-3 were used in order to reduce the coke formation [152]. Both effects from increasing the reaction temperature and increasing the amount of water in the reactants upon the product produced were compared to the calculated equilibrium product yields.

In order to study conversions and products yields; an elemental analysis using reactor exit concentrations of CO, CO_2, CH_4 and H_2 and the inlet flow of methane was performed. The unmeasured H_2O was calculated. The total molar flow of carbon entering the reactor from methane equals the carbon leaving the reactor outlet. The accumulation of coke is assumed zero in the carbon balance as shown in Eq. 7.1. The carbon balance Eq. 7.1 contains one unknown, $\dot{n}_{out,dry}$.

$$\left(y_{CO} + y_{CO_2} + y_{CH_4}\right) \times \dot{n}_{out,dry} = 1 \times \dot{n}_{CH_4,in} \quad \text{(Eq. 7.1)}$$

$y_i = mol\ \ fraction\ of\ species\ i.$

$\dot{n} = total\ \ molar\ \ flow\ rate\ \ (mol/\min)$

$\dot{n}_i = molar\ \ flow\ rate\ of\ species\ \ i\ \ (mol/\min)$

where, in and out subscribts denote releveant mol enetring or leaving the reaction.

The hydrogen balance analysis was performed as shown in Eq. 7.2. Hydrogen entering the reaction from water and methane equals the hydrogen leaving the reaction. The Eq. 7.2 contains two unknowns, $\dot{n}_{out,dry}$, $\dot{n}_{H_2O,out}$.

$$\left(2y_{H_2} + 4y_{CH_4}\right) \times \dot{n}_{out,dry} + 2 \times \dot{n}_{H_2O,out} = 4 \times \dot{n}_{CH_4,in} + 2 \times \dot{n}_{H_2O,in} \quad \text{(Eq. 7.2)}$$

$y_i = mol\ \ fraction\ of\ species\ i.$

$\dot{n} = total\ molar\ flow\ rate\ (mol/\min)$

$\dot{n}_i = molar\ \ flow\ rate\ of\ species\ i\ (mol/\min)$

From the above elemental analysis, the unknown $\dot{n}_{out,dry}$ was measured in the experiment from bubble meter after water condensation and $\dot{n}_{H_2O,out}$ was calculated.

The conversions for methane and water were obtained by Eq.7.3-7.4 and displayed in Figure 7.1:

$$x_{CH_4} = \frac{\dot{n}_{CH_4,in} - \dot{n}_{CH_4,out}}{\dot{n}_{CH_4,in}} \quad \text{(Eq. 7.3)}$$

$$x_{H_2O} = \frac{\dot{n}_{H_2O,in} - \dot{n}_{H_2O,out}}{\dot{n}_{H_2O,in}} \quad \text{(Eq. 7.4)}$$

The molar flow rates of products from the reaction were calculated by:

$$\dot{n}_{i,out} = y_i \times \dot{n}_{out,dry} \quad \text{(Eq. 7.5)}$$

The products yields for hydrogen, carbon dioxide and carbon monoxide were obtained in mol/min per mol/min of methane as shown in Eq.7.6-7.8 and presented in Figures 7.2-7.4.

$$H_2 yield = \frac{\dot{n}_{H_2,out}}{\dot{n}_{CH_4,in}} \quad \text{(Eq. 7.6)}$$

$$CO_2 yield = \frac{\dot{n}_{CO_2,out}}{\dot{n}_{CH_4,in}} \quad \text{(Eq. 7.7)}$$

$$CO\ yield = \frac{\dot{n}_{CO,out}}{\dot{n}_{CH_4,in}} \quad \text{(Eq. 7.8)}$$

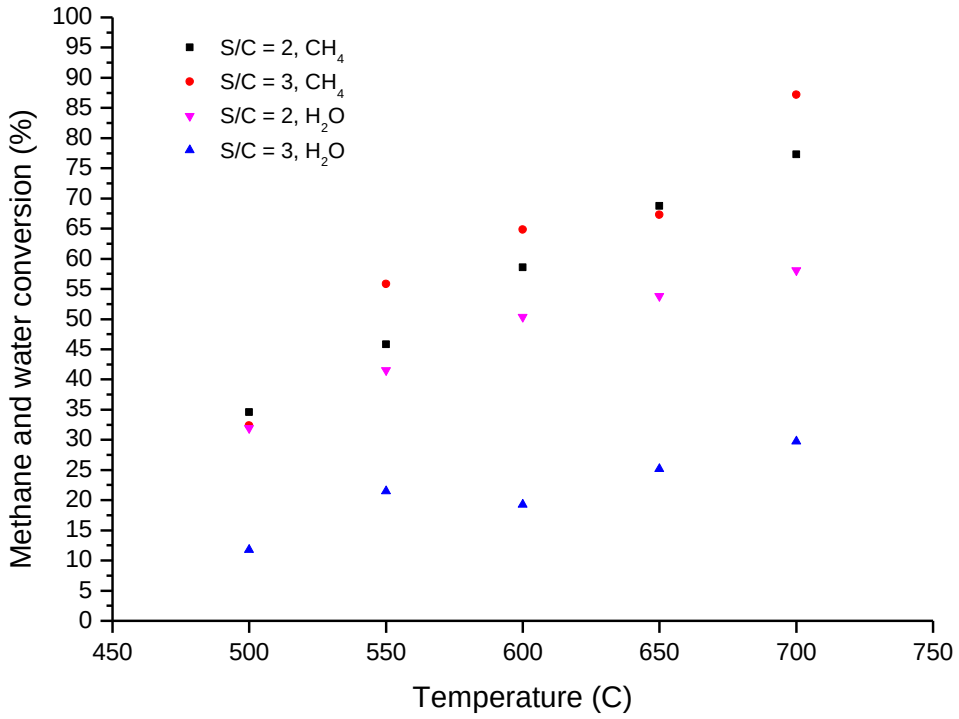

Figure 7.1. Methane and water conversions for 10%Ni/Al_2O_3 methane catalyst within 500-700°C for the S/C of 2 and 3.

It is clear from Figure 7.1 that the conversion of methane increases with increasing temperature. The conversion of methane was observed to increase from 32% at 500°C to 87% at 700°C for S/C of 3. The results obtained support that the methane reforming reaction is an endothermic process which is enhanced at high temperatures. It was also observed experimentally that increasing the amount of water in the reactants from S/C of 2 to 3 only shows a very small effect on methane conversion. It was reported previously in Chapter 2 that methane conversion

increases by only a very small amount with increasing amount of steam in the reactants, or even decreases with additional steam at some temperatures investigated as displayed in Figure 7.1. The amount of water consumed was less than predicted by equilibrium analysis (Figure 4.9) for S/C of 3 and nearly equal for S/C of 2. This is due to longer contact time (residence time) for S/C of 2 (3.37 s) than S/C of 3 (2.59 s).

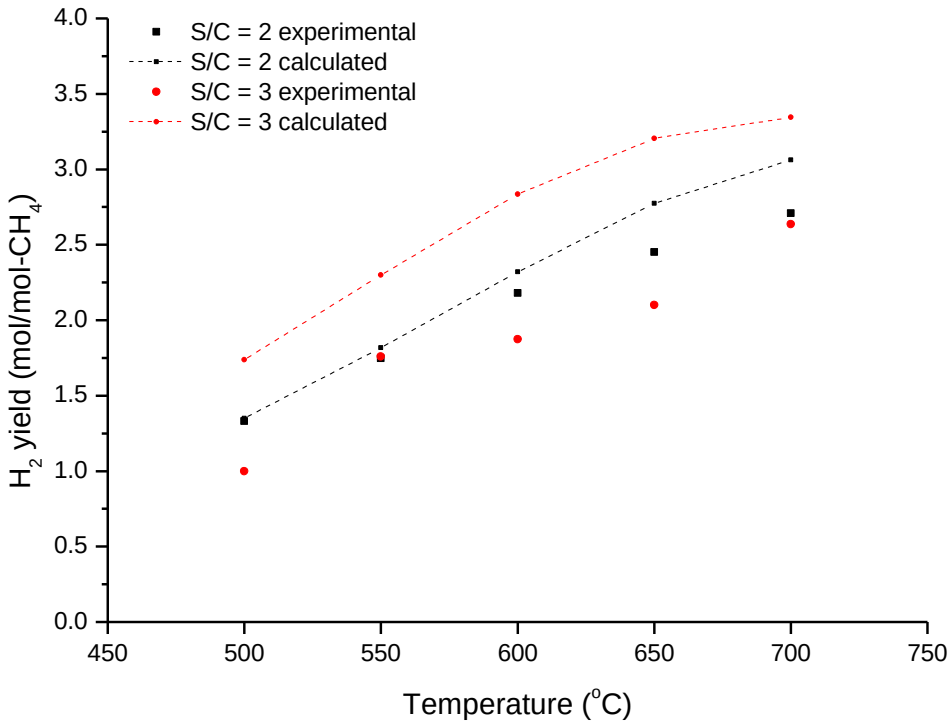

Figure 7.2. Experimental and calculated H_2 yield for 10%Ni/Al_2O_3 methane catalyst within 500-700°C for the S/C of 2 and 3.

It is shown in Figure 7.2 that the amount of hydrogen produced increases with increasing the temperature. The experimental results follow the same trend as the hydrogen yield obtained from equilibrium calculations and approach the calculated equilibrium values at 500-700°C for S/C of 2. However, the yield of hydrogen produced experimentally for S/C of 3 is less than the calculated results since the amount of water consumed was less than predicted by equilibrium calculations.

There was a slight increase in water conversion for S/C of 3 in Figure 7.1 which would indicate increasing contribution of thermal decomposition in the experiment. The experiments showed a maximum hydrogen yield of 2.7 mol/mol-CH_4 at 700°C and S/C of 2, and a minimum hydrogen yield of 1.0 mol/mol-CH_4 at 500°C and S/C of 3.

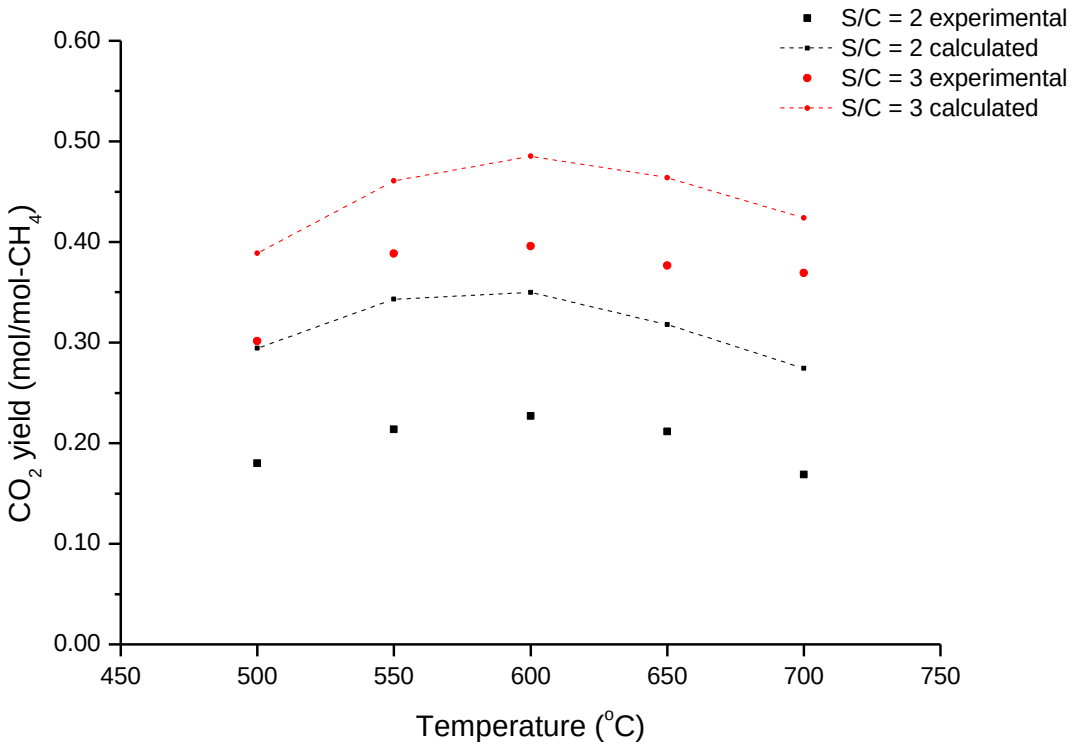

Figure 7.3. Experimental and calculated CO_2 yield for 10%Ni/Al_2O_3 methane catalyst within 500 -700°C for S/C of 2 and 3.

Figure 7.3 shows the amount of CO_2 produced. The CO_2 produced increases with increasing the temperature reaching a maximum yield at 600°C (0.40 mol/mol-CH_4 for S/C of 3 and 0.23 mol/mol-CH_4 for S/C of 2), then it decreases at temperatures 650-700°C. From Figure 7.3, the CO_2 content rises with increasing S/C ratio according to the water gas shift reaction equilibrium, since the reaction moves towards the products [265]. The amount of CO_2 was observed to decrease at 650-700°C due to less favourable water gas shift reaction.

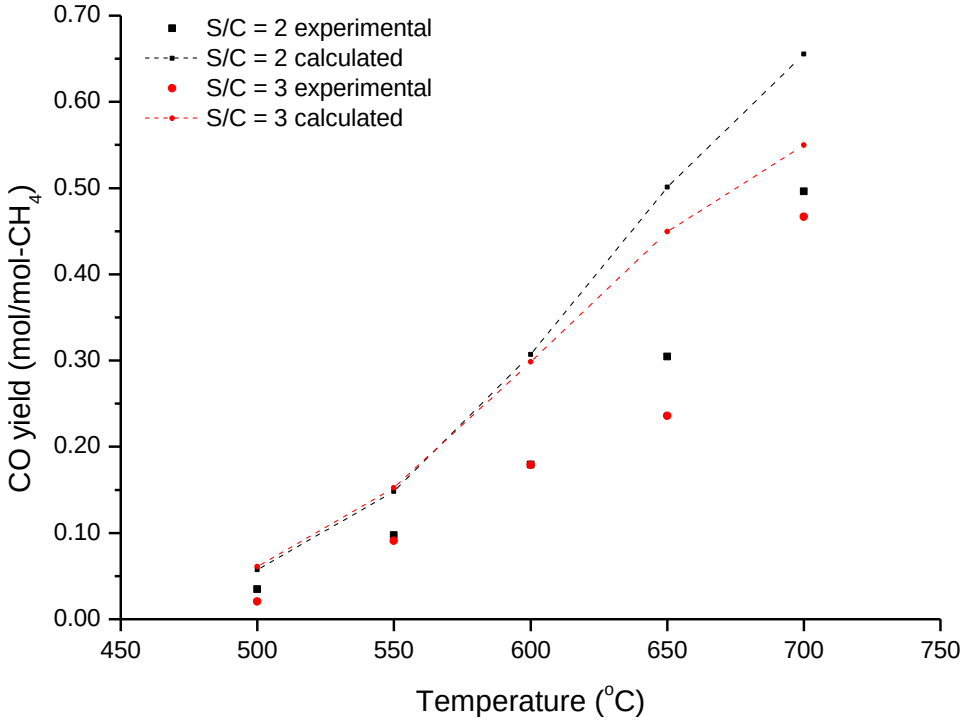

Figure 7.4. Experimental and calculated CO yield for 10%Ni/Al_2O_3 methane catalyst within 500-700°C for the S/C of 2 and 3.

Figure 7.4 shows that the CO produced increased with increasing temperature. It was also shown experimentally that increasing the molar ratio of water in the reactants from 2 to 3 only reveals a small reduction on the amount of CO produced at 650-700°C. The amount of CO increased from 0.02 mol/mol-CH_4 to 0.47 mol/mol-CH_4 within the temperature range 500-700°C for S/C of 3. This explains that CO is produced by increasing the reaction temperature via both methane reaction and reverse water gas shift reaction [168-171]. The CO yield that appears in the product is very low (0.02 mol/mol-CH_4) at 500°C due to the favourable water gas shift reaction. This coincides with performing methane steam reforming for low temperature PEMFC applications as even a very low concentration of CO can poison such kinds of fuel cells.

In conclusion, the methane steam reforming over monometallic catalyst 10%Ni/Al_2O_3 was carried out over the temperature range from 500°C to 700°C at atmospheric pressure. The results showed that methane steam reforming and water gas shift are the main reactions producing CO_2, CO and hydrogen [169, 170, 265]. The increase in temperature from 500°C to 700°C showed an increase in methane conversion and hydrogen produced. The amount of CO_2 increased to maximum at 600 °C then decreased since the effects of water gas shift reaction decease at high temperature. Furthermore, more CO is produced via the reverse water gas shift reaction and methane steam reforming reactions [192]. The experiments achieved a maximum hydrogen amount of 2.7 mol/mol-CH_4 at 700°C and S/C of 2. The positive effect of increasing steam to carbon ratio was observed in the amount of CO_2 produced via water gas shift reaction since the increase in the amount of water would enhance CO_2 production [57, 192]. Finally, the methane reaction showed high conversion at high temperature, corresponding to effective activation of C-H [187], and therefore, the reaction path is thought to be independent of the H_2O partial pressure [171].

7.2 Effects of Cu content on methane steam reforming

In this section, the effects of Cu content in the prepared catalysts (7%Ni-3%Cu, 5%Ni-5%Cu and 3%Ni-7%Cu) on product yield and conversion are compared with results of the 10%Ni catalyst. The reactions were carried out for catalysts in the range of temperatures from 500°C to 700°C with the S/C of 3 at atmospheric pressure.

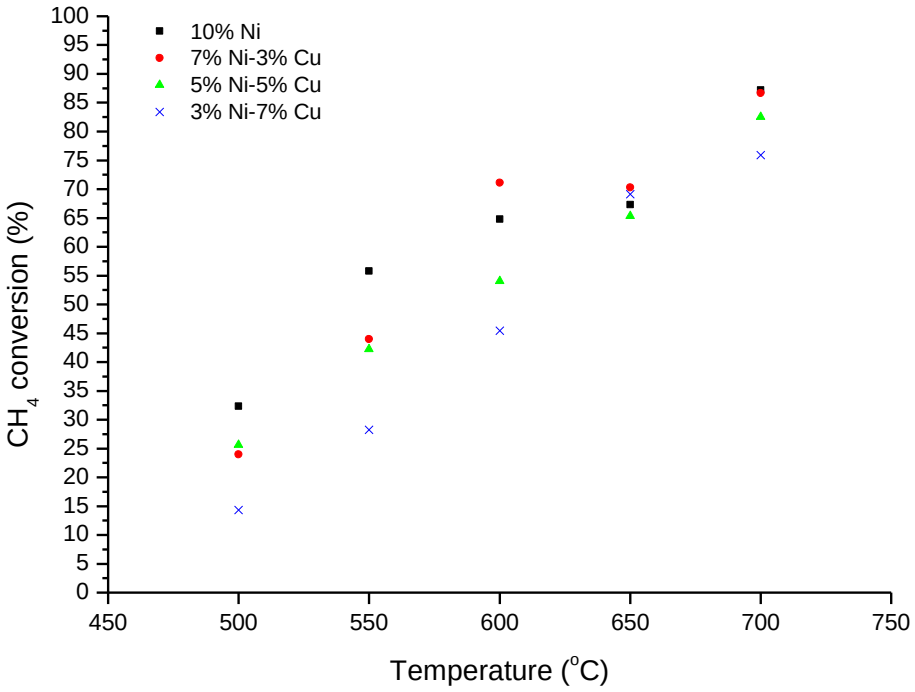

Figure 7.5. Methane conversion within 500-700°C and S/C of 3 for 10%Ni, 7%Ni-3%Cu, 5%Ni-5%Cu and 3%Ni-7%Cu methane catalysts.

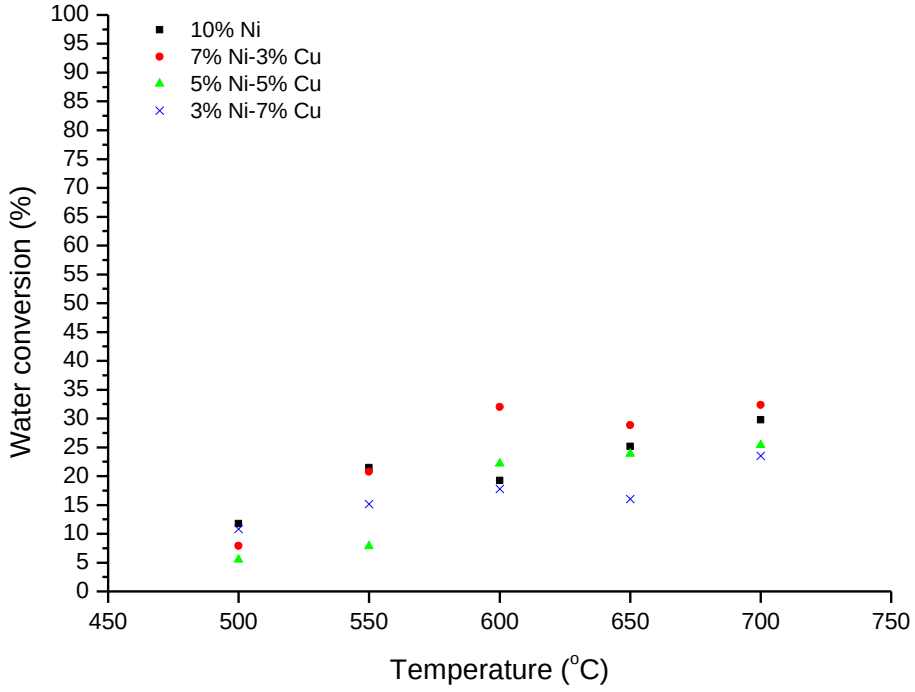

Figure 7.6. Water conversion within 500-700°C and S/C of 3 for 10%Ni, 7%Ni-3%Cu, 5%Ni-5%Cu and 3%Ni-7%Cu methane catalysts.

The methane and water conversions are displayed in Figure 7.5 and Figure 7.6, respectively. All prepared catalysts showed an increase in methane conversion with increasing the reaction temperature. The effects of increasing Cu content in the catalyst have negative effects on methane conversion within the range 500-550°C. The bimetallic catalysts showed lower methane conversion within the range 500-550°C with respect to the 10%Ni monometallic catalyst. 7%Ni-3%Cu displayed a slightly higher conversion ratio than 10%Ni at 600°C, while the other bimetallic catalysts (5%Ni-5%Cu and 3%Ni-7%Cu) gave lower conversion than 10%Ni. The effect of the small amount of Cu content (3%) displayed a good conversion compared to other prepared catalysts. This enhancement could be attributed to the synergistic effect between Cu and Ni metal due to bimetallic Ni-Cu alloy formation. The Cu existence would enhance the water gas shift reaction by consuming CO via water gas shift reaction as observed in Figure 7.6, while more CO is produced from methane reaction. Thus, removing CO via the water gas shift reaction is thought to increase CO as product in the methane reaction leading to CH_4 consumption. The low methane conversion for 5%Ni-5%Cu and 3%Ni-7%Cu catalysts compared with 7%Ni-3%Cu at 600°C is attributed to the fact that methane conversion occurs over the Ni surface only and the water consumption was higher for 7%Ni-3%Cu than other prepared catalysts. No methane conversion over the 10% Cu catalyst was detected experimentally and this will be discussed later in this section. In other words, Cu would be responsible for the water gas shift reaction after the methane reaction took place over the Ni surface.

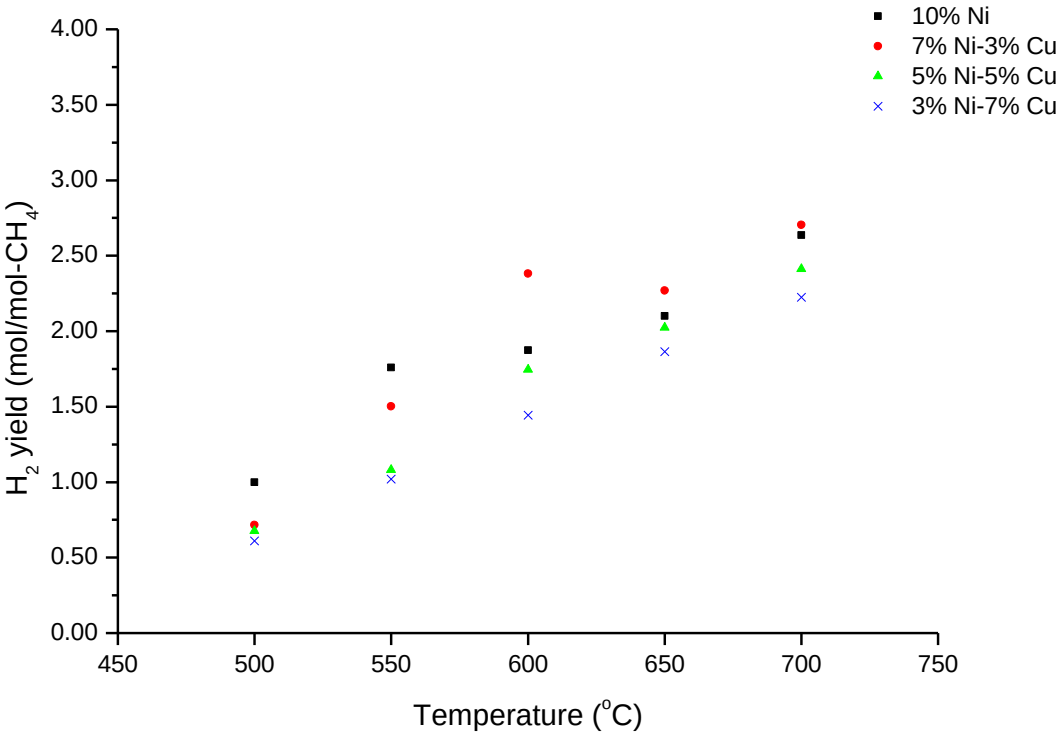

Figure 7.7. Hydrogen yield within 500-700°C and S/C of 3 for 10%Ni, 7%Ni-3%Cu, 5%Ni-5%Cu and 3%Ni-7%Cu methane catalysts.

The steam reforming reaction on various prepared catalysts showed that 10%Ni produced the highest amount of hydrogen within the range of temperatures 500-550°C compared to the other prepared catalysts, as shown in Figure 7.7. This is considered to be due to a high conversion of CH_4 (Figure 7.5) to CO_2 and hydrogen over 10%Ni catalyst. The 10wt.% of Ni content would enhance the ability of the catalyst for activating C-H bonds during methane steam reforming. It was observed that adding 3%Cu to the Ni catalyst increases the hydrogen yield at 600°C (2.4 mol/mol-CH_4). This indicates that 7%Ni-3%Cu is selective for hydrogen production due to both the effects of water gas shift reaction over active Cu and steam methane reforming reaction over Ni, because hydrogen is produced in both reactions. Figure 7.7 shows that adding more Cu metals to the catalyst (≥ 5 wt. %) makes the catalyst

less selective to hydrogen, as also observed for the catalysts 5%Ni-5%Cu and 3%Ni-7%Cu at 500-600°C. Thus, the low content of Ni would decrease the methane conversion and the produced hydrogen. This is considered to be due to Cu which increases the water gas shift reaction and less activity for the steam reforming of methane was observed as explained later in this section. The increase in the Cu content from 3wt.% to 7wt.% displayed small effects on the hydrogen amount produced within the temperature range 650-700°C, since the methane steam reforming reaction is thermodynamically favoured at high reaction temperature.

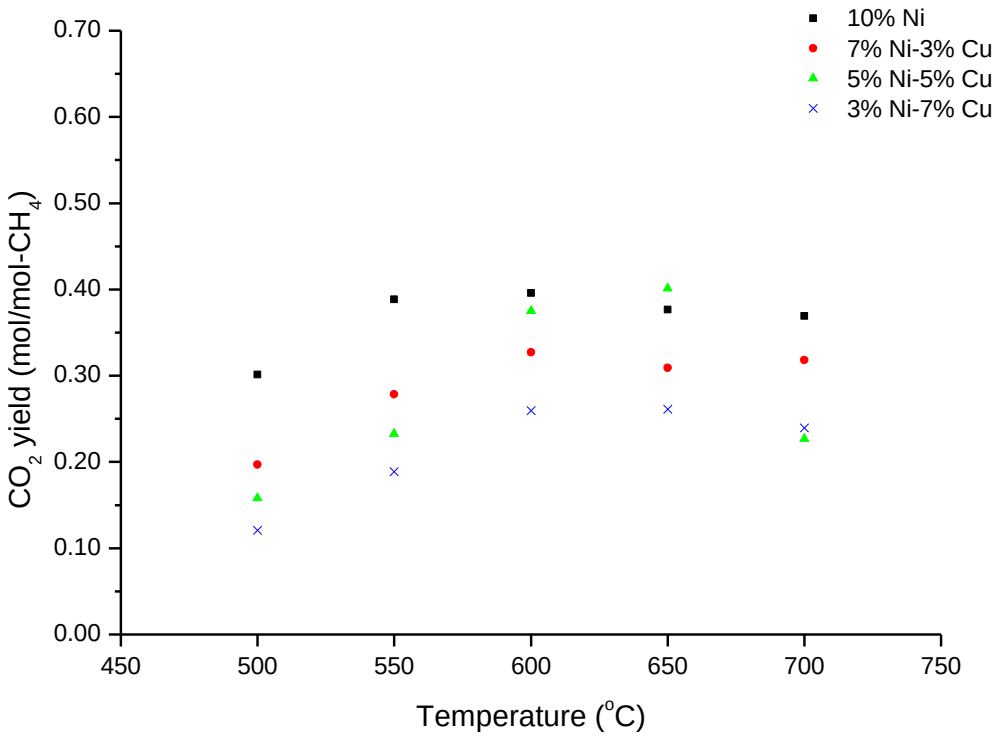

Figure 7.8. CO_2 yield within 500-700°C and S/C of 3 for 10%Ni, 7%Ni-3%Cu, 5%Ni-5%Cu and 3%Ni-7%Cu methane catalysts.

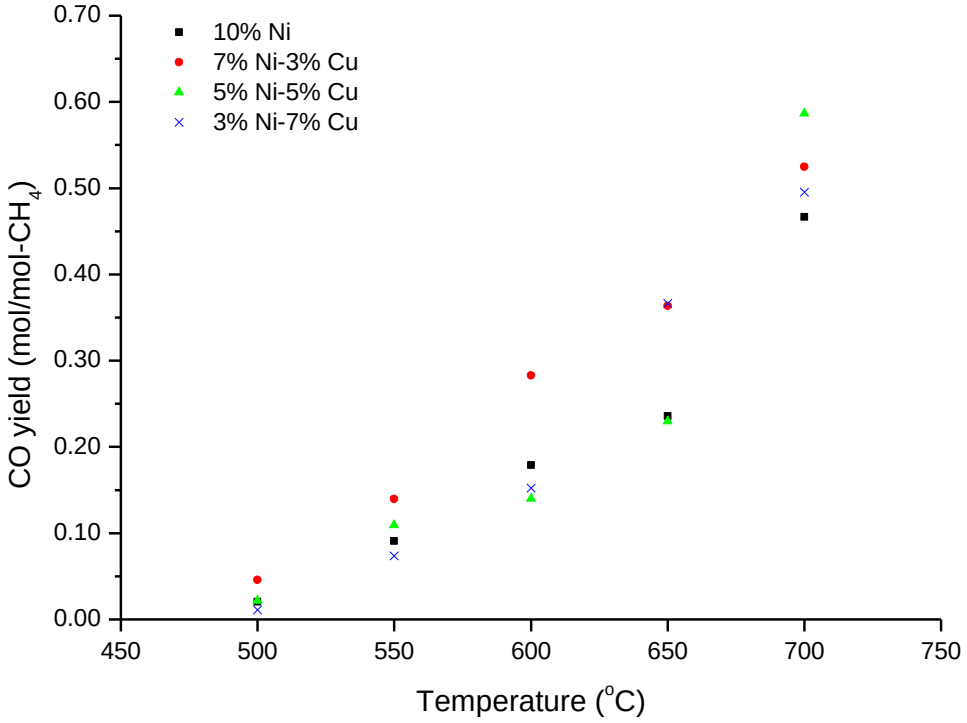

Figure 7.9. CO yield within 500-700°C and S/C of 3 for 10%Ni, 7%Ni-3%Cu, 5%Ni-5%Cu and 3%Ni-7%Cu methane catalysts.

The carbon oxides yields are shown in Figures 7.8 and 7.9, respectively, as a function of temperature for various catalysts. The 10%Ni and 5%Ni-5%Cu catalysts produced the highest amount of CO_2 compared to other bimetallic catalysts. All prepared catalysts showed an increase in the produced CO_2 with increasing temperature up to 600°C, then a slight drop within 650-700°C . This can be related to the water gas shift reaction at such operating temperatures (500-600°C), then the reaction becomes more selective for methane steam reforming reaction and reverse waster gas shift reaction that consumes CO_2 to CO in the range 650-700°C.

From Figure 7.9, the amount of CO produced increases with increasing the reaction temperature for all the prepared catalysts. The effects of increasing the Cu content on bimetallic Ni-Cu catalyst for methane steam reforming showed a similar trend to the 10%Ni catalyst being observed. The CO is produced by both reverse water gas

shift reaction and methane steam reforming reaction [212-215]. For instance, it was observed that 5%Ni-5%Cu catalyst at 700°C produced more CO than 10%Ni. This means that Cu catalyst at high reaction temperature favours reverse water gas shift reaction and further CO is produced from the activated methane reaction. On the other hand, 5%Ni-5%Cu catalyst within 600-650°C showed less CO produced than 700°C which explains less favoured reverse water gas shift reaction as well as less favoured methane steam reforming reaction. From Figure 7.9, it is observed that low reaction temperatures (500-600°C) produced a low amount of CO which emphasize the advantage of using the low operating temperature for fuel cell applications.

Table 7.1. Methane steam reforming reaction over 10%Cu and physical mixture of single metal 10%Cu and 10%Ni catalysts.

	10%Cu	**10%Ni, 10%Cu***	**10%Ni, 10%Cu***	**10%Ni, 10%Cu***
Temperature (°C)	700	700	600	500
S/C	3	3	3	3
Methane conversion (%)	9.7	87.0	55.8	28.6
Water conversion (%)	0.00	15.1	14.8	10.1
H_2 yield	0.08	2.19	1.56	0.87
CO_2 yield	0.01	0.23	0.24	0.17
CO yield	0.00	0.56	0.23	0.04

*Physical mixture of single metal (1.5 g of 10%Cu and 1.5 g of 10%Ni).

The methane steam reforming was also performed over 10%Cu catalyst at 700°C. It is noticed form Table 7.1 that there is no activity for the steam reforming of methane and only a small amount of hydrogen and CO_2 was observed. This explains that methane conversion does not occur over Cu. The methane reaction mechanism reviewed in Chapter 2 suggested that CH_4 derived intermediates chemisorb on the catalyst surface and then react with water species. Thus, the initial reactivity of the

catalyst metal towards C-H bond activation is the governing process which could not occur (catalysed) over the Cu surface.

The methane reaction was also performed over a physical mixture of single metals of 10%Ni and 10%Cu catalysts. From Table 7.1, the methane steam reforming reaction converts CH_4 to hydrogen and CO. The CO produced from the methane reaction reacts with steam to produce CO_2 and additional hydrogen, the composition depending upon the reaction temperature. The addition of Cu into the reactor tube enhanced the water gas shift reaction at 500°C and 600°C. The activity of methane reaction displayed high conversion with increasing the reaction temperature up to 700°C. At this temperature, the methane reaction is more active than the water gas shift reaction since a significant amount of CO is produced. As mentioned previously in this section, the small amount of Cu addition (3wt.%) enhanced the water gas shift reaction and methane reforming reaction for 7%Ni-3%Cu catalyst at 600°C as displayed in Figures 7.5 and 7.7. The methane reaction over the physical mixture of single metal 10%Ni and 10%Cu catalysts at 600°C agrees with the current finding as observed from Table 7.1. The high activity of methane conversion (71.1%) and hydrogen yield (2.40 mol/mol-CH_4) in bimetallic 7%Ni-3%Cu catalyst at 600°C in comparison with physical mixture of single metal 10%Ni and 10%Cu catalysts at same temperature is referred to the removal process of CO via water gas shift reaction which is produced from methane reaction. Accordingly, the methane conversion increases as well the amount of hydrogen.

The differences also between carrying the methane reaction over single metal and the addition of Cu into catalyst formulation is that the single metal would be more

susceptible for deactivation by carbon deposition than bimetallic catalyst as will be investigated in Section 7.3.4.

From the above results, it can be concluded that the methane reaction is active within the range 650-700°C for all prepared catalysts since a high amount of CO and hydrogen are produced and the methane conversion increased. The methane reaction depends on the prior activation of C-H bonds which was noted to occur mainly over the temperature range 650-700°C on all the prepared catalysts [171, 187]. For 7%Ni-3%Cu, the high activity for methane conversion and hydrogen yield were observed at 600°C compared to monometallic Ni and other bimetallic catalysts. This is due to synergetic effect between Cu and Ni metal which would enhance the water gas shift reaction and the methane reforming reaction.

7.3 Characterization of used methane steam reforming catalysts

In this section, characterization results and discussion are presented for the spent catalysts in order to understand how the catalyst properties may change during the reaction. The morphology of the used catalyst operated at 500°C and 700°C and S/C of 3 was examined using SEM. Then the catalyst surface area (determined using the BET method) and pore size were calculated using nitrogen adsorption-desorption isotherm data. The crystallite phase and size were estimated using XRD analysis. Finally, the TGA measurement was performed in order to study the carbon formation on the catalyst surface.

7.3.1 SEM of used methane catalysts

The morphological of the spent catalysts of (10%Ni, 7%Ni-3%Cu, 5%Ni-5%Cu and 3%Ni-7%Cu) operated at 500°C and 700°C at S/C of 3 are shown in Figures 7.10 and 7.11, respectively.

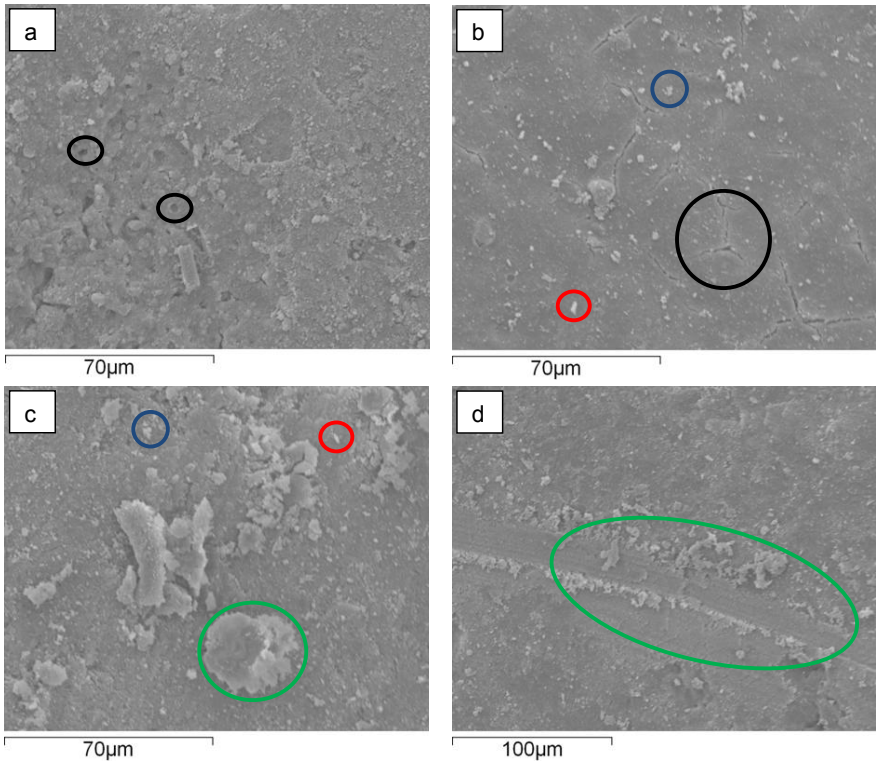

Figure 7.10. SEM images of the used methane catalysts reacted at 500°C and S/C of 3: a) 10%Ni, b) 7%Ni-3%Cu, c) 5%Ni-5%Cu and d) 3%Ni-7%Cu.

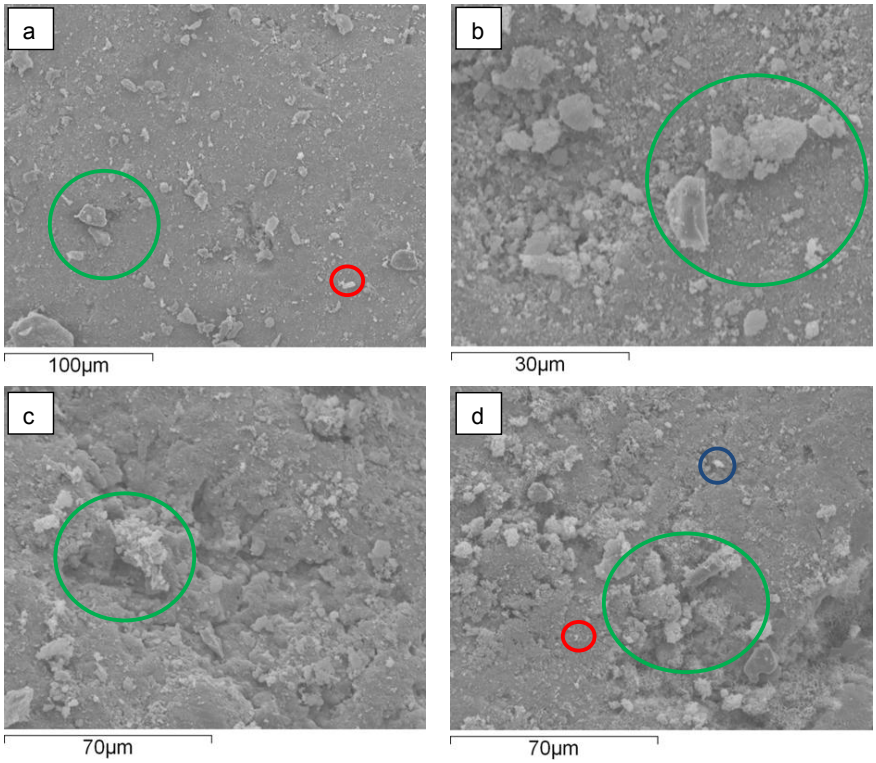

Figure 7.11 SEM images of the used methane catalysts reacted at 700°C and S/C of 3: a) 10%Ni, b) 7%Ni-3%Cu, c) 5%Ni-5%Cu and d)3%Ni-7%Cu.

The 10%Ni used catalyst reacted at 500°C in Figure 7.10a shows cracks (highlighted by a marked black circle) over a grey Al_2O_3 support. The SEM image of 10%Ni spent catalyst reacted at 700°C in Figure 7.11a showed bright white spots which represent Ni species (highlighted by a marked red circle) distributed over grey Al_2O_3 support with more agglomeration (highlighted by a marked green circle) being observed to have appeared on the catalyst compared to 10%Ni used catalyst reacted at 500°C.

The surface morphology of the used 7%Ni-3%Cu catalyst reacted at 500°C is showed in Figure 7.10b. Shades of white spots which correspond to Cu species (highlighted by a marked blue circle) and bright white spots which display Ni species (highlighted by a marked red circle) are observed and distributed on Al_2O_3 support with some cracks appearing on the support (highlighted by a marked black circle). Figure 7.11b displays the used 7%Ni-3%Cu catalyst operated at 700°C in the reaction, from which it is observed that the agglomerates of particles (highlighted by a marked green circle) appear on the catalyst surface compared to 7%Ni-3%Cu reacted at 500°C.

The SEM image of the used 5%Ni-5%Cu reacted at 500°C in Figure 7.10c shows shades of white spots (highlighted by a marked blue circle) which represent Cu species and bright white spots (highlighted by a marked red circle) which display Ni species over grey Al_2O_3 support with agglomeration of particles (highlighted by a marked green circle). The used 5%Ni-5%Cu catalyst reacted at 700°C as displayed in Figure 7.11c showed similar morphology as in Figure 7.10c with cracks and particle agglomeration (highlighted by a marked green circle) being observed.

SEM images displayed in Figure 7.10d for used 3%Ni-7%Cu reacted at 500°C showed changes on the catalyst surface texture of the support with agglomeration

along the support (highlighted by a marked green circle). From Figure 7.11d, the shades of white spots which correspond to Cu species (highlighted by a marked blue circle) and bright white spots which represent Ni species (highlighted by a marked red circle) are observed with agglomerates (highlighted by a marked green circle) over the support.

7.3.2 Nitrogen adsorption-desorption for the used methane catalysts

The changes to the catalyst surface and pore diameter after the reaction were studied and compared with the fresh catalyst in order to understand the effects of the reaction on catalyst characteristics. Therefore, the used catalyst reacted at 500°C and 700°C at S/C of 3 were investigated using nitrogen adsorption-desorption analysis. The isotherm adsorption- desorption graphs for used catalyst are shown in Figures 7.12 and 7.13.

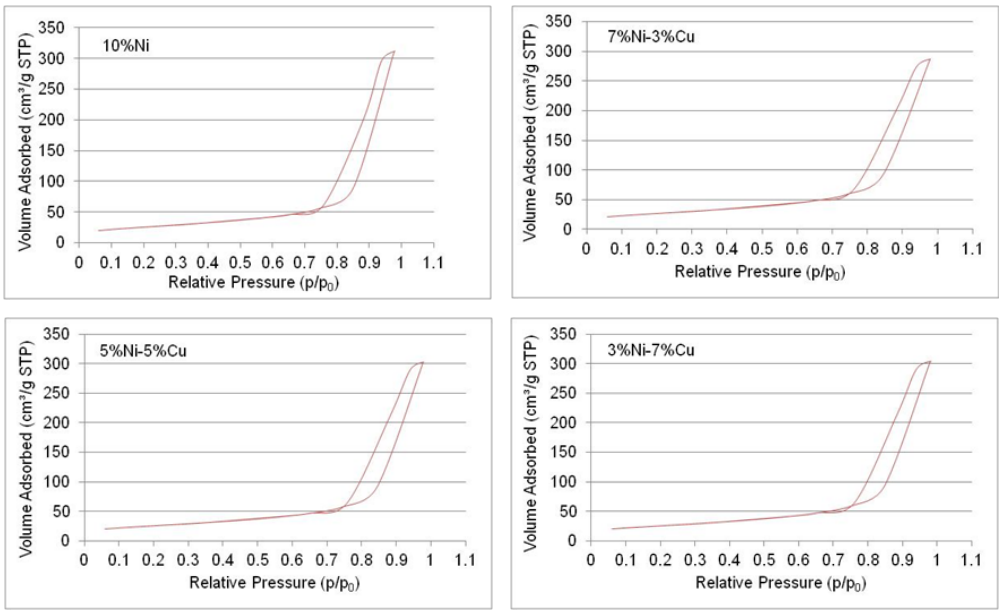

Figure 7.12. The sorption isotherms of nitrogen at 77K for the used methane catalysts reacted at 500°C and S/C of 3.

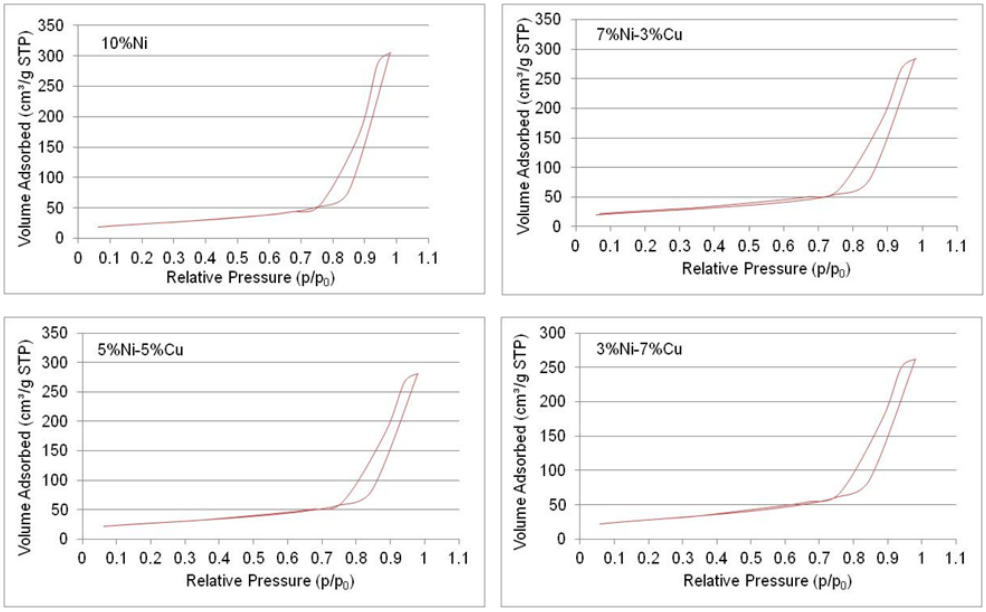

Figure 7.13. The sorption isotherms of nitrogen at 77K for the used methane catalysts reacted at 700°C and S/C of 3.

The adsorption-desorption isotherm for the used catalysts at 500°C and 700°C showed a low nitrogen uptake at a low relative pressure ($P/P_0 < 0.75$). The increase in adsorption with the increase in relative pressure was obtained at ($0.85 < P/P_0 < 0.98$). Based on the isotherm classification discussed in Figures 3.3 and 3.4, illustrated in Chapter 3, the used catalysts were found to be of Type V and with hysteresis Type H1 [273]. This means that, the used catalysts reacted at temperatures 500°C and 700°C could be classified as displaying mesoporosity with low energy of adsorption, including regular and even pore distribution in the Al_2O_3 support [273]. The isotherms obtained for catalyst reacted in methane reforming are similar to those reported for methanol reforming in Chapter 6. This is as expected, because the same type of Al_2O_3 support was used to prepare the catalyst. Thus, the increase in the reaction temperature up to 700°C revealed high catalyst resistance to sintering. As discussed in Chapter 2, the major drawback of Ni-γ-Al_2O_3 is its instability, which becomes significant at temperatures above 700°C due to thermal deterioration of γ-Al_2O_3 leading to sintering and pore blockage. This could also cause surface area loss

which was not observed in the current results due to low reaction temperature below the point where instability occurs.

Comparing the isotherm for the fresh catalysts in Figure 5.3, illustrated in Section 5.2 of Chapter 5, with the used catalyst in Figures 7.12 and 7.13, the used catalysts displayed a lower volume of adsorption. This might be related to the blockage in the pores of the corresponding Al_2O_3 support of the reacted catalyst, leading to a reduction in the volume of nitrogen adsorbed. Both types of the used catalysts showed a similar adsorption-desorption isotherm, indicating that the reaction temperature increases from 500°C to 700°C has only a minor effect on the catalyst change with respect to the surface area and pore size. Furthermore, the analysis of nitrogen adsorption-desorption has shown that the used catalyst indicated negligible microporous volume. The BET surface area calculations using the linearised form of BET equation (Eq. 3.4), discussed in Chapter 3, showed that the used catalysts had a lower surface area than the fresh catalysts as summarized in Table 7.2. This can be related to pore-blockage of the support after the reaction.

For 10%Ni and 7%Ni-3%Cu catalysts (Table 7.2); the used catalysts operated at 700°C showed lower surface area than the used catalysts operated at 500°C. This justifies the negative effect of high operating temperature on the catalyst surface area. By contrast, 5%Ni-5%Cu and 3%Ni-7%Cu catalysts showed that the used catalyst operated at 700°C have higher surface area than the used catalyst operated at 500°C (Table 7.2). For such high Cu loading catalyst (3%Ni-7%Cu), it is suggested that Cu metal particles distributed over the pore mouths are engaged in the water gas shift reaction at the lower temperature of 500°C to a greater extent than at 700°C, which makes the catalyst more susceptible to deactivation due to pore

coverage. The Cu has lower reactivity towards CO dissociation at a low temperature compared to a high temperature and therefore the influence of high Cu content on carbon deposits would be reasonable.

Table 7.2. BET surface area for the fresh and used methane catalysts reacted at 500°C and 700°C at S/C of 3.

	10%Ni	**7%Ni-3%Cu**	**5%Ni-5%Cu**	**3%Ni-7%Cu**
Surface area, fresh (m^2/g)	122	125	128	125
Surface area, reacted at 500°C (m^2/g)	93.3	97.1	93.2	91.7
Surface area, reacted at 700°C (m^2/g)	86.1	89.0	95.0	100
Pore diameter, fresh (nm)	19.9	19.8	19.6	20.1
Pore diameter, reacted at 500°C (nm)	20.1	18.3	20.1	20.5
Pore diameter, reacted at 700°C (nm)	21.9	19.8	18.4	16.1

7.3.3 XRD analysis for the used methane steam reforming catalysts

The XRD patterns for the used catalysts operated at 500°C and 700°C and S/C of 3 are shown in Figures 7.14 and 7.15. The differences in XRD patterns between the fresh (Figure 5.6, illustrated in Section 5.4 of Chapter 5) and the spent catalyst can be identified below. Comparing the XRD patterns for fresh catalyst and used catalyst revealed the presence of the oxide phase of metals in the fresh catalyst. The XRD patterns for used methane reforming catalysts did not show any evidence for a metal oxide phase, which explains that the catalyst did not oxidize after 4 hours reaction [80, 306, 307].

The XRD patterns of all used catalysts showed peaks related to the metallic phases of Ni or Cu and peaks related to γ-Al_2O_3 and the traces of θ-Al_2O_3. The results

obtained for spent catalysts following methane reforming are similar to the results for the used methanol catalysts reported in Section 6.3.3 of Chapter 6. However, the XRD patterns in used methane reforming catalyst showed less diffuse patterns due to possible metal crystallite growth at high reaction temperature. The metal crystallite stability decreases with decreasing the melting temperature of the metals and is affected by the interaction between metal and its support.

The 10%Ni catalyst showed XRD patterns of Ni metals at 2θ= 44°and 52° and the average crystallite size of Ni was 17.4 nm. In Figures 7.14 and 7.15, the bimetallic used catalysts showed patterns related to metallic Ni and metallic Cu and for Ni-Cu [211]. The average crystallite size of bimetallic catalysts is 16.8 nm at 2θ= 37°. The XRD patterns for the used catalyst reacted at 500°C and 700°C showed similar patterns and the effects of raising the reaction temperature displayed that the pattern lines are sharper and less diffuse than the ones at lower temperature. For all XRD patterns, the oxide phase of metals was not detected except for aluminates related to the alumina catalyst support.

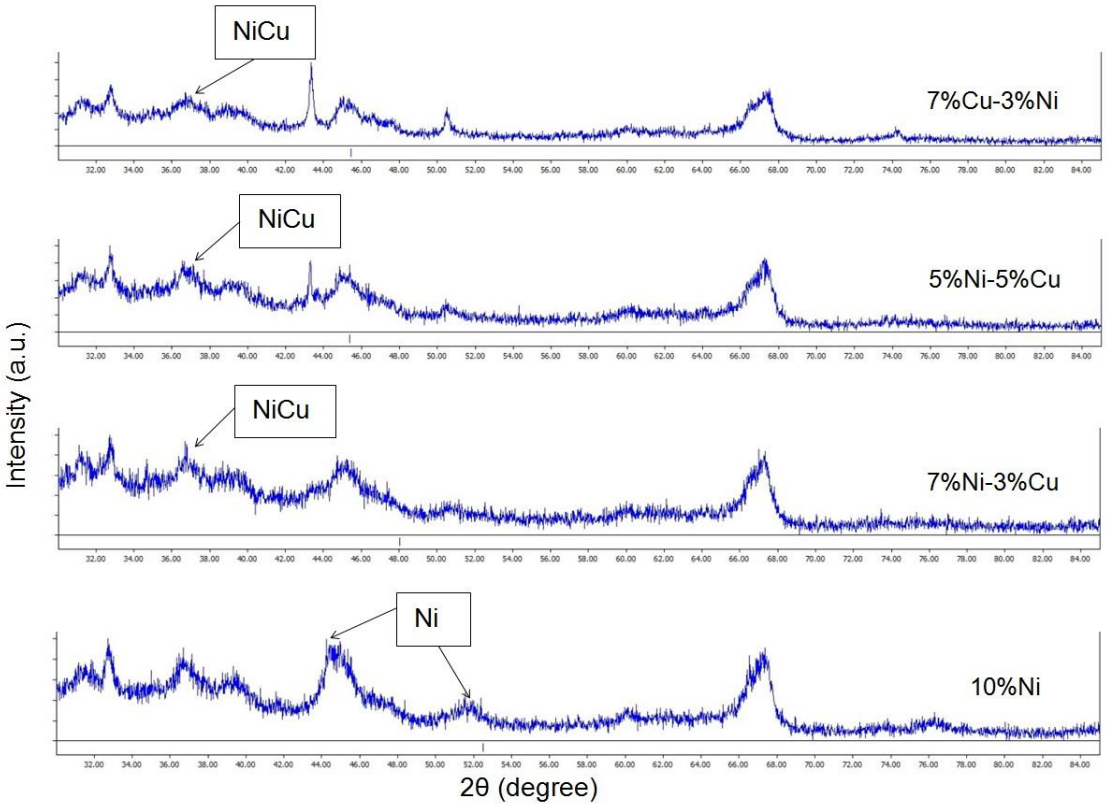

Figure 7.14. XRD patterns for the used methane catalysts reacted at 500°C and S/C of 3.

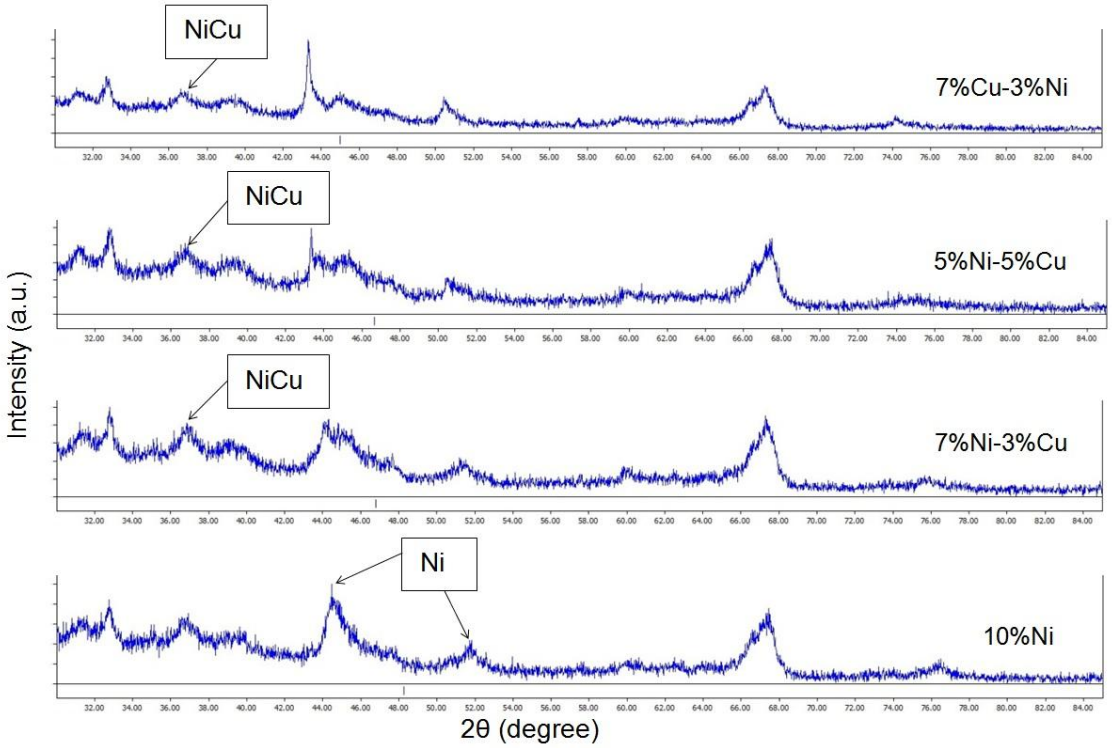

Figure 7.15. XRD patterns for the used methane catalysts reacted at 700°C and S/C of 3.

7.3.4 Carbon formation analysis for used methane steam reforming catalysts

The carbon formation is a major cause of catalyst deactivation during methane steam reforming as discussed in Chapter 2. The carbon deposition on the catalyst surface could lead to reduction in the catalyst activity and the selectivity for hydrogen produced. Carbon is formed on the surface by the catalytic reaction, which leads to hydrocarbon species adsorption and dehydrogenation [178, 212, 238, 239] as discussed in Section 2.6 of Chapter 2. The carbon is deposited on the catalyst surface mainly through the reactions of methane decomposition (Eq. 2.20), CO decomposition (Eq. 2.21) and CO reduction (Eq. 2.22) [169]. Increasing the amount of steam in the reactants in the range of 2-5 was suggested in order to reduce the amount of carbon formed on the catalyst surface [242].

The TGA discussed in Section 3.2.8 of Chapter 3 was carried out to study the amount of carbon formation on the catalyst during the reaction for all operated catalysts in the range 500-700°C and S/C of 2 and 3. This was achieved by introducing air into 20 mg of the used sample and heating the sample in the oven from 25°C to 900°C at a ramp rate of 10°C/min. A typical TGA plot for the operated catalyst is shown in Figure 7.16. The mass loss in Figure 7.16 represents the two counteracting effects of carbon burn off and metal oxidation. Therefore, the carbon formation was calculated. The measured mass loss by TGA is assumed as sum of complete metal oxidation to NiO and Cu_2O as shown in Eq. 6.9 and Eq. 6.10 (displayed in Chapter 6), respectively, and carbon burn off. The mass gain is calculated from wt. % of metal loading. The mass of oxygen, based on stoichiometry, that reacts to form NiO and Cu_2O was calculated and deducted from the value obtained from TGA curve. The remainder gives an estimate of carbon formation. The calculation assumed that the catalyst was fully reduced before performing TGA.

Then, the accumulated carbon in grams for the reaction duration was calculated as well as the catalyst selectivity for solid carbon (Sel_C) was estimated as shown in Eq. 7.9.

$$Sel_C\ (\%) = 100 \times \frac{n_{carbon}}{n_{CH_4,in}} \qquad \text{(Eq. 7.9)}$$

Where n_i *is total moles for reaction duration for species* i (mol)

The total mass change with the increase in the temperature is shown in Figure 7.16. The first peak at temperature 61.7°C (99.14%) shows the loss in the moisture on the catalyst. The prepared catalyst showed a continuous drop in the mass until the temperature reached 900°C. The mass change (4.57 wt.%) in Figure 7.16 represents the total amount of carbon removed and mass gain due to oxidation of metals of the catalyst at 532.7°C. The calculated accumulated solid carbon within the reaction duration (four hours) was 77.3 mg with catalyst selectivity for carbon was 2.4%.

It was valuable to compare the carbon formation of the prepared catalyst with the commercial nickel catalyst, discussed in Chapter 5, operated at the same conditions. The same TGA analysis was performed and the result is presented in Figure 7.17. It can be noticed that commercial catalyst has a higher mass change (85.28 wt.%) at 648.8°C. The calculated accumulated solid carbon within reaction duration was 2.23 g with catalyst selectivity for carbon was 69.5%. Comparing the two TGA graphs, the prepared catalyst is significantly less susceptible to carbon formation than the commercial nickel catalyst. In fact, the commercial Ni catalyst, which was characterized in Chapter 5, contains 40wt.% of Ni. The carbon formation increases with increasing Ni content in the catalyst [183-185]. Nickel catalyst above 20wt.% would be more susceptible to deactivation due to active site blocking and particle

sintering. The Ni particle diameter between 60-100 nm would be more effective for carbon growth on the catalyst surface because the carbon diffusion rate being slower due to longer diffusion paths [248, 314-316]. Table 5.2 in Section 5.3 of Chapter 5 displayed Ni particle diameter of 78 nm for commercial catalyst.

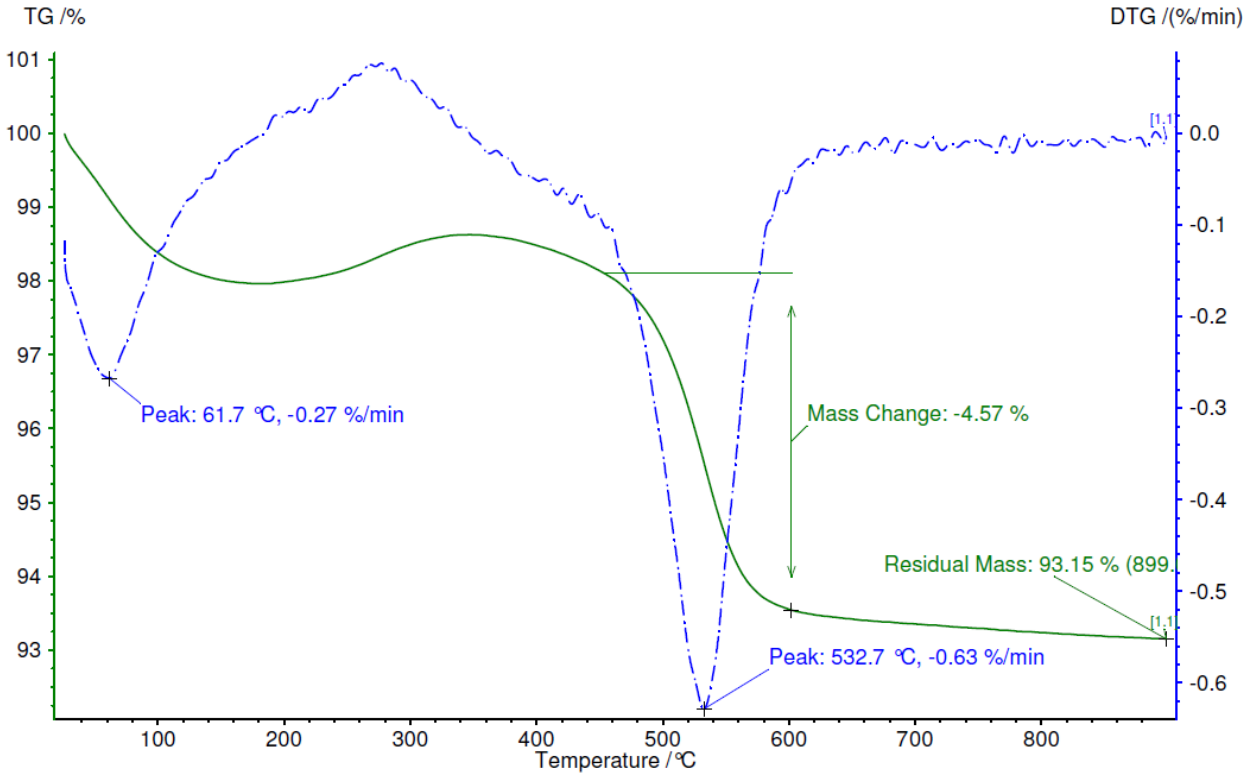

Figure 7.16. Typical TGA graph for the spent methane 5%Ni-5%Cu catalyst operated at 650°C and S/C of 2, the primary TG axis presents the percentage mass loss and the secondary Derivative Thermo Gravimetric (DTG) axis presents the derivative of percentage mass loss with respect to time as obtained from the NETZSCH software.

Tables 7.3 and 7.4 explain the amount of carbon formation occurring over the spent catalysts for methane steam reforming. It can be observed from Tables 7.3 and 7.4 that carbon formation depends on the particular catalyst and operating conditions during the reaction. For instance, the bimetallic catalysts reacted at 500°C and S/C of 2 displayed lower coke than catalysts operated at S/C of 3 at the same temperature. According to Table 2.6 in Section 2.6.1 of Chapter 2, polymerization of CH_4 radicals

would be possible at 500°C at the beginning of the reaction resulting in active site blocking. In contrast, the samples operated at 700°C and S/C of 3 showed less carbon formation than the operated catalysts at S/C of 2 at the same temperature. It was observed in this case that the formation of carbon would be minimized by increasing the steam to carbon ratio at high reaction temperature. Increasing the steam to carbon ratio produces effects in agreement with the reported literature regarding reduction of the carbon formation at high reaction temperature since the amount of steam would avoid the reactions (Eq. 2.20-2.22) which are responsible for producing carbon [242, 317].

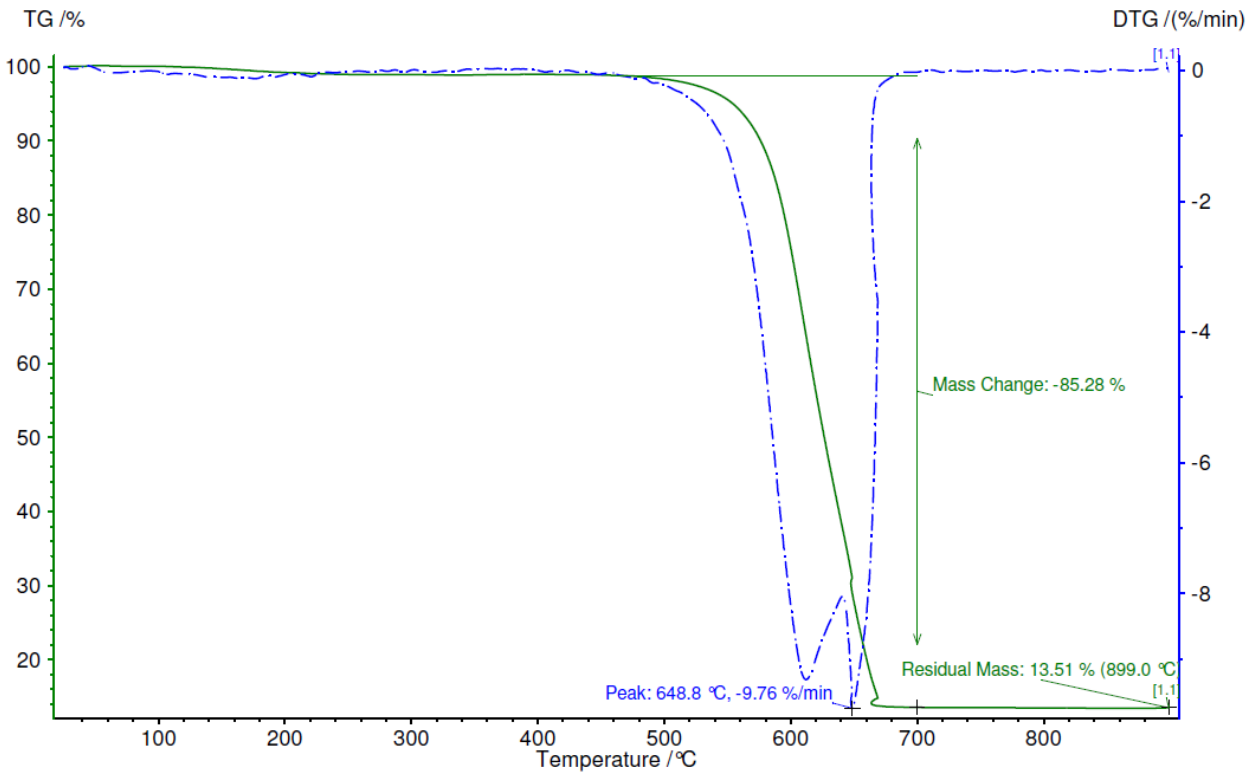

Figure 7.17. Typical TGA graph for the spent methane nickel commercial catalyst operated at 650°C and S/C of 2, the primary TG axis presents the percentage mass loss and the secondary DTG axis presents the derivative of percentage mass loss with respect to time as obtained from the NETZSCH software.

Table 7.3. Carbon deposition and selectivity on the used methane catalysts reacted at 500-700°C and S/C of 2.

	10%Ni		**7%Ni-3%Cu**		**5%Ni-5%Cu**		**3%Ni-7%Cu**	
T (°C)	Carbon amount (mg)	Sel_C (%)	Carbon amount (mg)	Sel_C (%)	Carbon amount (mg)	Sel_C (%)	Carbon amount (mg)	Sel_C (%)
500	59.1	1.8	24.4	0.8	49.5	1.5	26.5	0.8
550	63.0	2.0	54.6	1.7	10.1	0.3	15.0	0.5
600	40.9	1.3	38.2	1.2	44.3	1.4	95.1	3.0
650	57.3	1.8	55.8	1.7	65.0	2.0	37.5	1.2
700	17.5	0.5	236.2	7.4	105.5	3.3	204.6	6.4

Table 7.4. Carbon deposition and selectivity on the used methane catalysts reacted at 500-700°C and S/C of 3.

	10%Ni		**7%Ni-3%Cu**		**5%Ni-5%Cu**		**3%Ni-7%Cu**	
T (°C)	Carbon amount (mg)	Sel_C (%)	Carbon amount (mg)	Sel_C (%)	Carbon amount (mg)	Sel_C (%)	Carbon amount (mg)	Sel_C (%)
500	38.8	1.2	118.3	3.7	56.6	1.8	78.3	2.4
550	21.7	0.7	46.9	1.5	58.4	1.8	65.7	2.0
600	146.5	4.6	56.5	1.8	29.9	0.9	71.7	2.2
650	21.7	0.7	45.0	1.4	80.9	2.5	55.8	1.7
700	37.9	1.2	31.3	1.0	24.5	0.8	108.0	3.4

According to the Section 2.6 of Chapter 2, the carbon formation displayed in Tables 7.2 and 7.3 can be related to several routes. The catalyst was tested at low methane steam reforming temperature (500-700°C). It was suggested that an unstable carbide [243] intermediate forms on the supported Ni, Ni-Cu catalysts and remains attached to the metal and only the bulk carbide decomposes to form carbon [240, 243]. The carbon formed via hydrocarbon decomposition (Eq. 2.20) was reported at temperatures above 600°C [240]. In this case, a carbon atom diffuses rapidly through the carbide layer forming a constant carbon concentration within the metal particles. This can be inferred from the TGA results for catalysts operated at 700°C and S/C of 2, at which the highest amount of carbon was formed in comparison with the other used catalysts.

The effect of bimetallic catalyst could be noticed as the catalyst reacted at 600°C and S/C of 3. The amount of carbon formed for bimetallic catalyst was less than monometallic 10%Ni catalyst. In fact, both methane steam reforming reaction and water gas shift reaction were active as discussed previously in Section 7.2. Thus, the effect of Cu was to enhance the water gas shift reaction as well as reducing the carbon formation. The Cu in Ni-Cu catalysts was thought to block or decrease the carbon formed via the methane decomposition reaction (Eq. 2.20). It was reported that Cu would control the number of active sites (ensemble size) which are responsible for carbon formation as discussed in Chapter 2. The small formed ensembles from the dilution of the Ni surface with Cu atoms would reduce the amount of adsorbed carbon species on the Ni-Cu surface. Therefore, the synergetic effect between Cu and Ni metals was thought to have a stabilizing effect by controlling the catalyst structure properties.

7.4 Long-term methane steam reforming test for 10%Ni, 7%Ni-3%Cu and 5%Ni-5%Cu catalysts

Methane steam reforming reaction for 20 hours was carried out for prepared 10%Ni, 7%Ni-3%Cu and 5%Ni-5%Cu catalysts in order to study the long-term operation effects on the product yield. The reaction was carried out under the same operating conditions as those mentioned previously for the short duration runs in Sections 7.1 and 7.2. The reaction temperature was fixed at 700°C and S/C was 2 for 10%Ni and 5%Ni-5%Cu. The reaction temperature for 7%Ni-3%Cu was 600°C and S/C of 2.

The test was performed for 20 hours spread over three days by switching on and off in campaigns, running for average ca. 7 hours per day and shutting down the reaction furnace by leaving the catalyst under nitrogen overnight. As mentioned

previously in Section 7.2, the methane steam reforming process strongly depends on the reaction temperature at which C-H bond is activated. Therefore, the reason for choosing a high temperature for the long-term test is to study the effects of temperature and operation time on the product yield and on the catalyst structure. For 7%Ni-3%Cu, the operation temperature of 600°C was chosen since the amount of hydrogen produced showed its optimum value in Figure 7.7. The low steam to carbon ratio was selected to perform this test in order to study the effect of low steam and long operation time on carbon formation. The 3%Ni-7%Cu catalyst was excluded in the long-term study due to adverse effects of high Cu content on methane reaction as discussed in Section 7.2.

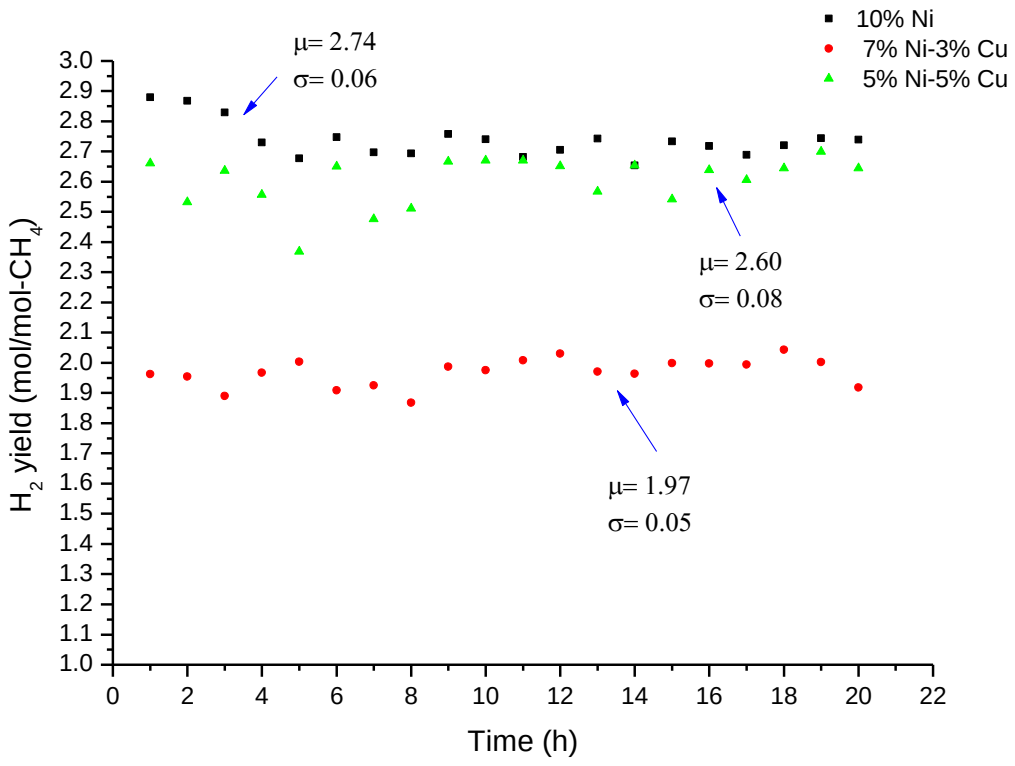

Figure 7.18. Hydrogen yield for 20 hours run at 700°C and S/C of 2 for 10%Ni, 5%Ni-5%Cu methane catalysts and at 600°C and S/C of 2 for 7%Ni-3%Cu methane catalyst, the values in the graph represent the average (μ) and variation (σ) for 20 hours run.

Figure 7.18 shows hydrogen produced within 20 hours for all tested catalysts. 10%Ni catalyst showed the high activity to produce hydrogen in comparison with 7%Ni-3%Cu and 5%Ni-5%Cu catalysts. The produced hydrogen displayed a stable trend versus time and no significant decay in hydrogen yield was observed. For 10%Ni catalyst, the maximum hydrogen yield was 2.88 mol/mol-CH_4 at first hour of the run then after that the hydrogen yield declined to an average value of 2.74 mol/mol-CH_4. The average hydrogen yield for 7%Ni-3%Cu was 1.97 mol/mol-CH_4 and for 5%Ni-5%Cu was 2.60 mol/mol-CH_4.

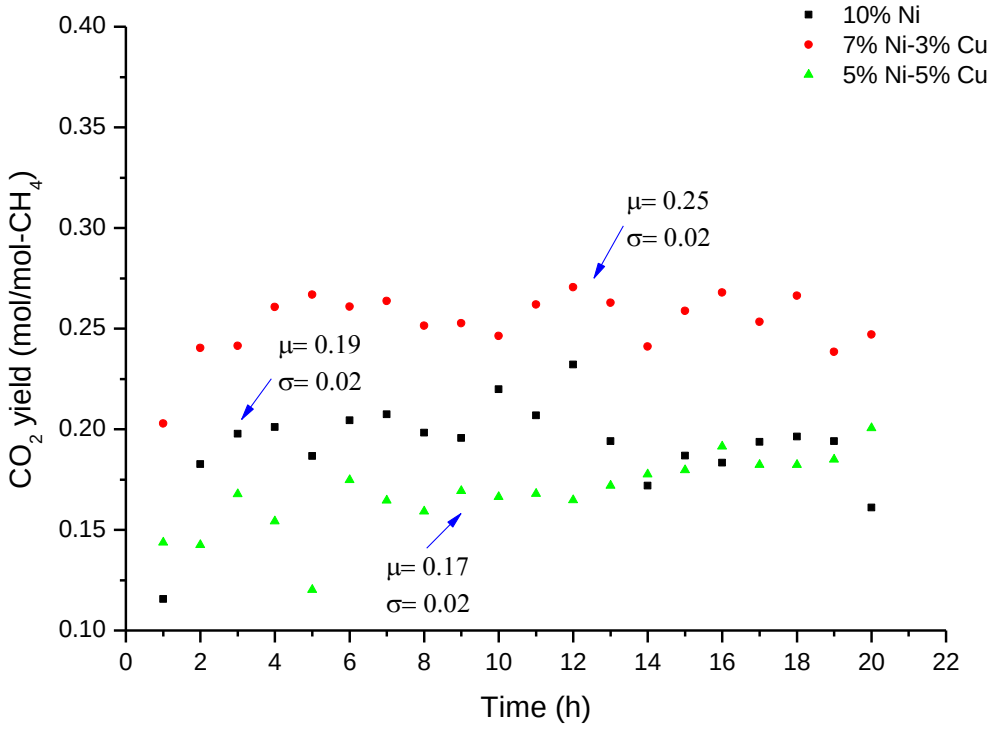

Figure 7.19. CO_2 yield for 20 hours run at 700°C and S/C of 2 for 10%Ni, 5%Ni-5%Cu methane catalysts and at 600°C and S/C of 2 for 7%Ni-3%Cu methane catalyst, the values in the graph represent the average (μ) and variation (σ) for 20 hours run.

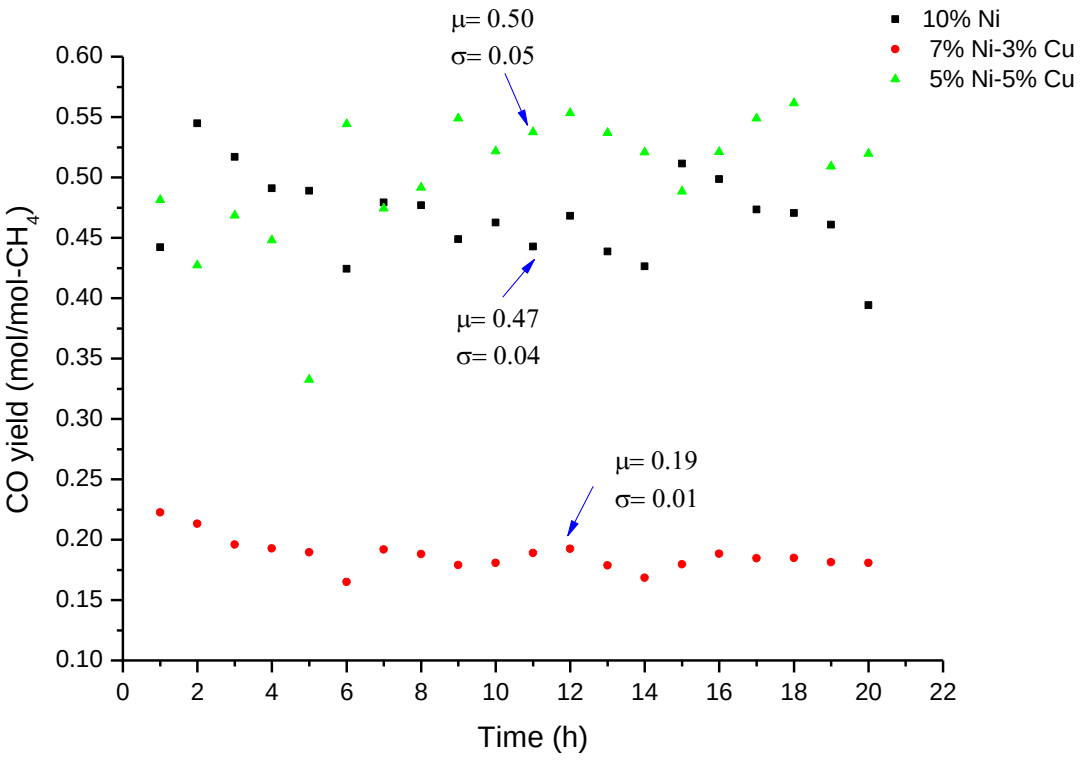

Figure 7.20. CO yield for 20 hours run at 700°C and S/C of 2 for 10%Ni, 5%Ni-5%Cu methane catalysts and at 600°C and S/C of 2 for 7%Ni-3%Cu methane catalyst, the values in the graph represent the average (μ) and variation (σ) for 20 hours run.

Figures 7.19 and 7.20 show the produced carbon oxides. Both CO_2 and CO showed an opposite trend. A stable trend for both CO_2 and CO was observed for 7%Ni-3%Cu at 600°C, the average CO yield for 7%Ni-3%Cu was 0.19 mol/mol-CH_4 with 0.01 mol/mol-CH_4 variation. However, the 10% Ni showed an increase in the produced CO_2 in the first 12 hours then decayed after a period of time of 1.5 h operation. On the other hand, 5%Ni-5%Cu showed a stable CO_2 trend and unstable CO yield for the first 10 hours run then thereafter the produced CO was stabilised. It can be inferred that the Cu content in Ni-Cu catalysts leads to a change in the ratio between CO and CO_2, which plays a role of stabilizing and controlling the amount of produced CO_2 with respect to CO. It can also be noticed that 5%Ni-5%Cu catalysts did not show a stable pattern for CO production in the course of 10 hours run. This indicates

that high Cu content in Ni-Cu catalyst will enhance the reverse water gas shift reaction on Cu metal sites and also the high content of Ni will be responsible for the methane reaction which produces more CO at 700°C. It can also observed from Figure 7.20 that the reaction temperature has a strong influence on the amount of produced CO in the methane reforming reaction, as it can be minimized by decreasing the reaction temperature and improving the Ni catalyst by introducing specific amounts of Cu metals up to 3wt.%.

In order to study the effects of long term study on the catalyst structure, SEM images for the 10%Ni, 7%Ni-3%Cu and 5%Ni-5%Cu catalysts are shown in Figure 7.21. The 10%Ni catalyst in Figure 7.21a displayed an agglomeration of Ni (highlighted by a marked green circle) as well as the cluster of Ni species being seen on the catalyst surface (highlighted by a marked black circle). The 7%Ni-3%Cu in Figure 7.21b showed agglomeration of metal particles over the support (highlighted by a marked green circle) and formed clusters (highlighted by a marked black circle). The 5%Ni-5%Cu catalyst in Figure 7.21c displayed shaded white patches which represent Cu species (highlighted by a marked blue circle) and bright white patches which correspond to Ni species (highlighted by a marked red circle) distributed non-uniformly on the surface of the Al_2O_3 support. Clearly observed agglomeration of particles (highlighted by a marked green circle) was formed, which can be related to thermal Cu sintering [57, 74, 80, 313] and Ni sintering due to high reaction temperature and long period reaction [248, 249, 259].

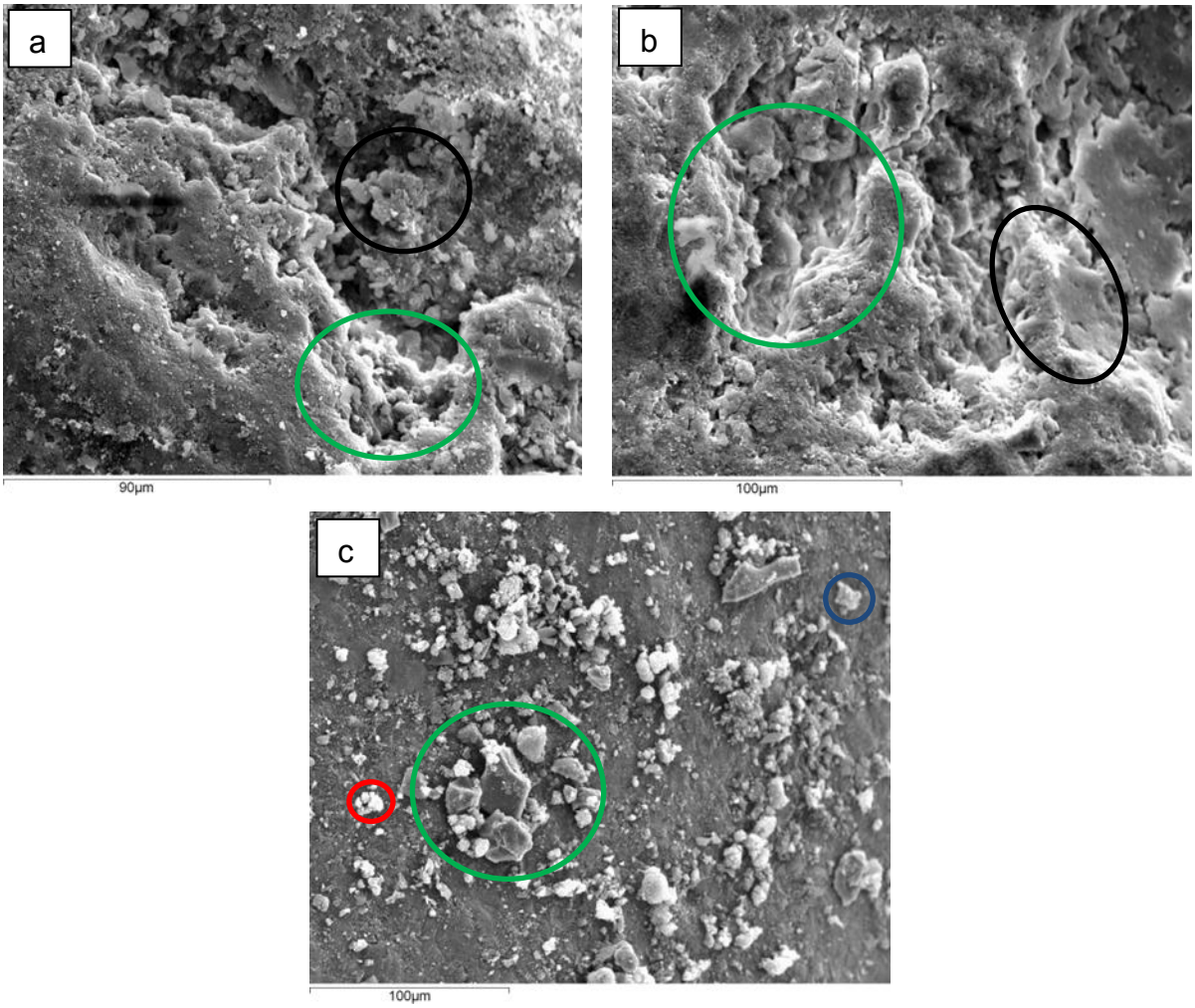

Figure 7.21. SEM images of the used 10%Ni and 5%Ni-5%Cu methane catalysts reacted at 700°C and S/C of 2 for 20 hours run and 7%Ni-3%Cu methane catalyst reacted at 600°C and S/C of 2 for 20 hours: a) 10%Ni, b) 7%Ni-3%Cu and c) 5%Ni-5%Cu.

From the TGA results of the 10%Ni sample the carbon deposition was 251.2 mg with carbon selectivity of 1.6%. The 7%Ni-3%Cu showed 111.4 mg of carbon deposition with 0.7% carbon selectivity, and the 5%Ni-5%Cu showed 780 mg of carbon deposition with selectivity 4.8% selectivity for carbon. The 5%Ni-5%Cu displaying the highest carbon formation among other tested catalysts. The results of the long-term test revealed a significant change of carbon deposition for methane steam reforming in comparison with the shorter period of testing mentioned in Table 7.3 in Section 7.3.4. This is interpreted by the fact that carbon deposition is a slow process and requires time until carbon is formed on the catalyst surface [243, 251] at

operated temperatures of 600°C and 700°C. The high amount of carbon formed on 5%Ni-5%Cu is thought to be due to high Cu content, through which both methane and reverse water gas shift reactions produce CO that subsequently decomposed to carbon at such an operation temperature [216-218], as explained in Eq. 2.21-2.22 in Chapter 2. It can be concluded that a high Cu loading (≥ 5wt.%) on Ni catalyst and high reaction temperature will affect the produced CO as well as the amount of carbon formation for a long period of operation.

7.5 Chapter summary

The methane catalytic activity measurements were applied for prepared catalyst in order to study the effects of temperature (500-700°C), steam to carbon ratio (S/C of 2 and 3) and Cu metal content on Ni-based methane reforming catalyst.

The methane reaction achieved a maximum reactivity with increasing the reaction temperature. The 10%Ni catalyst achieved a maximum of methane conversion of 87% at 700°C and S/C of 3. The maximum hydrogen yield was 2.7 mol/mol-CH_4 at 700°C and S/.C of 2. The reaction revealed an increase in the amount of CO produced with increasing the reaction temperature (0.02-0.47 mol/mol-CH_4) due to a high selectivity for reverse water gas shift reaction.

The effect of Cu metal content in the Ni catalyst revealed major changes in product distribution and catalytic reaction activity over the temperature range 500-600°C. The Ni-Cu catalyst had enhanced the water gas shift reaction. The 7%Ni-3%Cu revealed the highest conversion of 71.1% and produced the maximum amount of hydrogen 2.4 mol/mol-CH_4 among the other prepared catalysts at 600°C and S/C of 3. The Ni-Cu catalyst showed a high amount of CO at temperatures in the range 650-700°C than 10%Ni catalyst and it was referred to reverse water gas shift reaction and methane

steam reforming reaction at such operating temperature. The reaction was also performed for a physical mixture of 10%Ni and 10% Cu catalysts and compared with Ni-Cu catalysts. The results revealed an enhancement in reaction reactivity for products in Ni-Cu catalyst compared with physical mixture of 10%Ni and 10% Cu catalysts.

The spent methane reforming catalysts were characterized in order to study the catalyst properties after the reaction. The SEM revealed cracks appearing in the catalyst structure as well as agglomeration of particles. The calculated BET surface area for reacted catalyst revealed lower surface area (89-100 m^2/g) than fresh catalyst (120-128m^2/g). The XRD patterns for reacted methane catalyst at 700°C were less diffuse than the reacted catalysts at 500°C indicating crystallite growth at high reaction temperature.

The reacted methane catalyst showed carbon formation. A lower carbon formation was observed for operated catalyst at S/C of 2 than S/C of 3 at 500°C. This was related to polymerization of CH_4 radicals at the beginning of the reaction. On the other hand, the carbon formation was less at S/C of 3 than S/C of 2 at 700°C as it was related to the fact that increasing steam would avoid the reactions responsible for carbon production. The effect of Cu content in Ni catalyst was observed for reacted catalyst at 600°C and S/C of 3. The bimetallic reacted Ni-Cu catalysts revealed less carbon selectivity (0.9% for 5%Ni-5%Cu) than 10%Ni (4.6%) catalyst. The Cu content would control the number of active sites which are responsible for carbon formation.

Finally, the long-term stability showed that all tested catalysts had a high stability for hydrogen production within 20 hours run. The SEM of the long-term spent catalyst

showed large agglomeration of metal particles. The TGA analysis of spent methane catalysts for long-term test showed a significant change of carbon deposition in comparison with the short period test (4 hours), this was interpreted due to the fact that carbon deposition is a slow process and requires time until carbon is formed on the catalyst surface at 700°C.

CHAPTER 8

CONCLUSIONS AND FUTURE WORK RECOMMENDATIONS

8.1 Conclusions

This thesis reported the study of hydrogen production by methanol and methane steam reforming. The various loadings of bimetallic, 7%Cu-3%Ni/Al_2O_3, 5%Cu-5%Ni/Al_2O_3 and 7%Ni-3%Cu/Al_2O_3 catalysts, were synthesized using impregnation method and were compared with the prepared monometallic 10%Cu/Al_2O_3 and 10%Ni/Al_2O_3 catalysts. The aims of the work described in this thesis are:

- Synthesize and evaluate the prepared catalysts for methanol and methane steam reforming.
- Characterize the physical and chemical properties of the prepared catalysts before and after reactions.
- State the role of the bimetallic nature of Ni-Cu metals on the catalytic reaction performances.

The key findings of catalysts characteristics that are applied in methanol and methane steam reforming reactions over prepared catalysts were determined. The SEM of 10%Cu catalyst had a uniform distribution of copper species over Al_2O_3 support compared with 10%Ni catalyst. The SEM analysis for Ni-Cu bimetallic catalysts indicated evenly distributed metals species over the Al_2O_3 support but increasing the Ni loadings from 3wt.% to 7wt.% gave some agglomerates of metal species. The results of nitrogen adsorption-desorption revealed a Type IV adsorption isotherm and Type H1 hysteresis for all prepared catalysts suggesting that the catalyst exhibited mesoporous properties with high energy of adsorption and regular even pores without interconnection of channels in the support. However, the calculated BET surface area for the impregnated catalysts (120-128 m^2/g) had a

lower surface area than the support without metals impregnated (142 m^2/g) suggesting that Ni and /or Cu metals could block pores of Al_2O_3 support. The dispersion of the prepared catalysts was determined using CO chemisorption. This method had some limitations related to dispersion results obtained for bimetallic catalyst. It determines the total number of metal sites irrespective of the individual metal components on the surface of the catalyst. The analysis gave that the monometallic catalysts with low metal loadings of 3%Cu (4.31%) and 3%Ni (6.56%) have higher metal dispersion than 10%Cu (0.92%) or 10%Ni (1.74%). The bimetallic 7%Ni-3%Cu (1.95%) and 7%Cu-3%Ni (1.38%) catalysts revealed that increasing the Cu loading to 7wt.% decreases the bimetallic catalyst dispersion due to a decrease in the amount of CO chemisorbed. This was attributed to some Cu metal particles becoming inaccessible to the adsorption gas because they could be part of large clusters of metal or have become trapped in pores which are not accessible to the outside surface of the catalyst. However, XRD analysis for the prepared bimetallic catalysts indicated the formation of $Ni_xCu_{1-x}O$, NiO and CuO phases. The calculated average crystallite size from Scherrer formula for NiO in the 10% Ni catalyst was 17.8 nm, for CuO in 10%Cu catalyst was 17.9 nm and average crystallite size $Ni_xCu_{1-x}O$ in bimetallic catalyst was 16.7 nm. In addition, results of TPR suggested that bimetallic catalysts had a new hydrogen uptake peak. It was related to the reduction of NiCuO and has been attributed previously in literature to Ni-Cu alloy formation. The TPR profile revealed that 10%Cu could be reduced at 250°C, 10%Ni at 650°C, 7%Cu-3%Ni at 350°C, 5%Cu-5%Ni at 380°C and 7%Ni-3%Cu at 425°C.

The methanol steam reforming was evaluated over prepared catalysts at temperatures 225-325°C and S/C of 1.3 and 1.7. The monometallic 10%Cu catalyst achieved a maximum methanol conversion (92%) at 225°C and S/C of 1.7. The

amount of hydrogen produced decreased with increasing the temperature, the hydrogen yield changed from 2.7 mol/mol-CH_3OH at 225°C to 2.0 mol/mol-CH_3OH at 325°C for S/C= 1.7. The obtained amount of CO was nearly equal or slightly greater than the calculated equilibrium value at temperature 300-325°C, providing that the decomposition reaction is responsible for CO production in parallel with reverse water gas shift reaction. The influence of bimetallic catalyst on the methanol reaction was also evaluated. It was found that the impregnation of Ni to Cu had a strong influence upon the amount of CO_2 or CO by controlling the dominant reactions paths. The decomposition reaction on the metallic phase of Ni-Cu was responsible for significant amount of CO produced at temperatures 225-325°C compared to 10%Cu catalyst. The effects of the Ni-Cu alloy phase on the reaction for all bimetallic catalysts were noticed from the negligible amounts of CH_4 compared to the methanol reaction over 10%Ni or over physical mixture of single metal 10%Ni and 10%Cu catalyst, where significant amounts of CH_4 were produced due to CO_2 or CO hydrogenation. The highest amount of hydrogen produced within bimetallic catalysts was 2.2 mol/mol-CH_3OH for 5%Cu-5%Ni at 325°C and S/C of 1.7. The maximum methanol conversion was 98.5% for 7%Cu-3%Ni at 325°C and S/C of 1.7.

The methanol steam reforming catalyst was examined after the reaction. The SEM images showed cracks on the reacted catalyst and it displayed agglomeration of metals due to Cu sintering as it was more significant with a catalyst reacted at 325°C than catalysts reacted at 225°C. Moreover, the nitrogen adsorption-desorption isotherm determined even pores distribution in the Al_2O_3 support with low energy of adsorption compared with fresh catalysts due to blockage in the pores of the Al_2O_3 for reacted catalysts. The BET surface area calculations for reacted catalysts were in the range of 89-98 m^2/g. The XRD patterns for reacted catalyst displayed a possible

crystallite growth with increasing the reaction temperature to 325°C. From XRD, it was indicated that bimetallic phase of alloy Ni-Cu depends on Ni concentration in Cu and it increases with the increase of the Ni content and this will form Ni rich alloy or Cu rich alloy in the Ni-Cu catalyst. Generally, the carbon formation for reacted catalyst decreased with increasing S/C from 1.3 to 1.7. The bimetallic Ni-Cu catalysts revealed less carbon selectivity (1.2% for 3%Cu-7%Ni) during reaction than 10%Cu catalyst (1.8%) at 325°C and S/C of 1.7. This effect was attributed to the dilution effect of less active copper atoms with active Ni atoms, giving the opportunity for Ni metals to dissociate CO at high operation temperature. The reacted commercial $Cu/ZnO/Al_2O_3$ catalyst exhibited significantly higher carbon selectivity (6.2%) than the prepared catalysts (3.2%). It was concluded according to the literature that highly loaded catalyst (50%wt.Cu) was found to cause deactivation due to carbon deposition since the diffusion rate is being slower on larger particles (334 nm for commercial catalyst) due to longer diffusion path compared with smaller particles (75 nm for prepared catalyst).

The Methane steam reforming was also evaluated over prepared catalysts at temperatures 500-700°C and S/C of 2 and 3. The monometallic 10%Ni catalyst achieved maximum conversion of 87% at 700°C and S/C of 3. Thus, according to the literature, the methane reaction path depends on chemisorbed carbon produced via C-H bonds activation which becomes very active at high reaction temperature. The maximum hydrogen yield was 2.7 mol/mol-CH_4 at 700°C and S/.C of 2. Moreover, the reaction revealed an increase in the amount of CO produced with increasing the reaction temperature (0.02-0.47 mol/mol-CH_4) due to a high selectivity for reverse water gas shift reaction. The influence of bimetallic Ni-Cu catalyst on methane reaction was also examined. The synergetic effect between Cu and Ni metal was

found due to bimetallic Ni-Cu alloy formation since Ni-Cu catalyst had enhanced the water gas shift reaction and methane reforming at temperatures 500-600°C. Impregnating Ni catalyst with 3wt.% of Cu increased the conversion of methane and amount of hydrogen produced. The 7%Ni-3%Cu revealed the highest conversion of 71.1% and produced the maximum amount of hydrogen 2.4 mol/mol-CH_4 among the other prepared catalysts at 600°C and S/C of 3. It was also found that Cu addition (up to 7wt.%) in Ni catalyst had a strong effect on CO amount by enhancing the reactivity of the water gas shift reaction so the amount of CO_2 increased at temperatures in the range 500-600°C . In this case, the CO produced from methane reaction is consumed by the activated water gas shift reaction. The methane reaction performed over bimetallic catalyst was compared with 10%Cu and physical mixture of 10%Ni and 10% Cu catalysts. It was suggested that reaction over bimetallic Ni-Cu catalyst is determined by derived intermediates from CH_4 activation then it reacts with water species as it is enhanced by the presence of Cu in the Ni-Cu catalyst. The bimetallic catalysts showed a high amount of CO at temperatures in the range 650-700°C than 10%Ni catalyst since the reverse water gas shift is favoured at such operating temperatures for Cu containing catalysts.

The methane steam reforming catalysts were investigated after the reaction. The SEM images of reacted catalysts at temperatures 500°C and 700°C exhibited cracks and agglomeration of metals. The nitrogen adsorption-desorption revealed similar results as for reacted methanol reforming catalysts since the used Al_2O_3 support displayed strong resistivity for sintering with increasing the reaction temperature up to 700°C. This agrees with the literature as the support instability due to thermal deterioration and sintering occurs at temperature above 700°C. Moreover, the BET surface area calculations for reacted methane reforming catalysts were in the range

89-100 m^2/g. On contrast, the XRD patterns for reacted methane catalyst at 700°C were less diffuse than the reacted catalysts at 500°C indicating crystallite growth at high reaction temperature. According to the literature, the crystallite stability decreases with decreasing the melting temperature of the metals. Therefore, the crystallite growth was expected to be higher in methane reacted catalysts compared to reacted methanol catalysts. The reacted methane reforming catalysts showed carbon formation, the extent of which depends on the catalyst composition and operating conditions. The reacted catalysts displayed lower coke formation at 500°C for S/C of 2 than S/C of 3. The high carbon formation for S/C of 3 was related to the polymerization of CH_4 radicals at the beginning of the reaction, resulting in the active site blocking. On contrast, the carbon formation was less at S/C of 3 than S/C of 2 at 700°C. This was related to the fact that increasing steam would avoid the reactions responsible for carbon production. The bimetallic effect of Ni-Cu catalyst regarding reducing carbon formation was noticed at 600°C and S/C of 3. The bimetallic reacted Ni-Cu catalysts revealed less carbon selectivity (0.9% for 5%Ni-5%Cu) than 10%Ni (4.6%) catalyst. This was attributed to synergetic effect between Cu and Ni metals as it is thought that Cu provides a stabilizing agent by forming Ni-Cu alloy by controlling the catalyst structure. As mentioned in the literature, Cu would control the number of active sites (ensemble size) which are responsible for carbon formation. Therefore, Ni-Cu alloy thought to block or decrease the carbon formation via methane decomposition reaction. The reacted commercial nickel catalyst (40%wt.Ni/Al_2O_3) exhibited significantly higher carbon selectivity (69.5%)

than prepared catalysts (2.4%). This agrees with literature that Ni catalyst loaded above 20wt.% of Ni metals would be more susceptible to deactivation due to active site blocking and particle sintering.

8.2 Recommendations for future work

Based on the conclusions drawn of the work presented in the previous chapters, the following issues could provide potential progress to the work introduced in this thesis:

- Catalyst preparation requires further investigation. It would be useful to prepare the catalyst using dual impregnation. This requires impregnating the calcined monometallic copper catalyst with nickel metals then performing the calcination again for bimetallic Ni-Cu catalyst.
- The prepared Ni-Cu/Al_2O_3 catalyst can be enhanced by adding Cr or Ce as promoter since this could increase the catalyst activity and hydrogen production selectivity.
- In the future, the aim of Ni-Cu alloy in steam reforming of methanol and methane could be explored by investigating in situ infrared spectroscopy for the reacted catalysts. This will facilitate understanding the reaction pathway and products formation.
- Further characterization techniques would be helpful to understand the catalyst properties. Diffuse Reflectance Infrared Fourier Transform (DRIFTS) would be useful to explore the nature of coke deposits on the catalyst and the nature of the active species. It would be also useful to study the acidity of the prepared catalysts by using Temperature Programmed Desorption (TPD) in order to determine the acidity effect on the reaction. Performing Transmission Electron Microscopy (TEM) would enable the display of the nanometres size of metals particles for fresh and reacted catalysts in order to compare them.
- It is recommended to perform XRD analysis and nitrogen adsorption-desorption analysis for reduced catalyst so the accurate comparison between

the unreacted, reduced and consumed catalysts could be obtained regarding the crystallite size using XRD and surface area from BET calculation.

- Kinetics studies are required to understand more about the Ni_x-C_y/Al_2O_3 catalysts and further key parameters such as activation energy and rate of reaction should be investigated.
- A further investigation regarding the effect of changing the methanol and methane fuels flow rate on the reformate composition. This will allow understanding the influence upon hydrogen production rate, selectivity and activity of Ni_x-Cu_y/Al_2O_3 catalysts.
- The use of Ni_x-Cu_y/Al_2O_3 catalysts at temperatures above 325°C for methanol steam reforming and below 500°C for methane would give a further understanding of the reformate composition and carbon formation at such operating conditions.
- It was found that reacted catalysts at the top of the bed experienced more carbon formation than at the bottom of the bed. Therefore, it would be useful to perform the reaction over a multilayer catalyst bed by keeping a gap between the catalysts in the bed and investigate further this finding.
- It is desirable to perform a long-term stability test for the prepared catalysts for 100 hours. This would give further exploration about the catalyst stability, activity, selectivity and resistivity to carbon formation.
- The experimental rig was designed to provide hydrogen for fuel cell. It would be useful to couple SOFC with the experimental rig as external reformer. This will give a further insight into studying the dynamic effects on hydrogen production and catalytic reaction performance.

CHAPTER 9

APPENDICES

9.1 CO chemisorption equations

SF_{calc} , GMW_{calc}, SA_{calc} and D_{calc} are determined using the following equations:

$$SF_{calc} = \left[\left(\frac{F_1 \times SF_1}{W_{atomic1}} \right) + \left(\frac{F_2 \times SF_2}{W_{atomic2}} \right) + ... + \left(\frac{F_N \times SF_N}{W_{atomicN}} \right) \right] . GMW_{calc} \quad \text{(Eq. 9.1)}$$

Where:
SF_{calc} : calculated stoichiometry factor
SF_N : stoichiometry factor for metal N
F_1 : fraction of sample weight for metal N
$W_{atomic1}$: gram molecular weight of first metal (g/g-mole)
GMW_{calc} : gram molecular weight (g/g-mole)

$$GMW_{calc} = \frac{1}{\left(\frac{F_1}{W_{atomic1}} \right) + \left(\frac{F_2}{W_{atomic2}} \right) + ... + \left(\frac{F_N}{W_{atomicN}} \right)} \quad \text{(Eq. 9.2)}$$

Where:
GMW_{calc} : gram molecular weight (g/g-mole)
F_N : fraction of sample weight for metal N
$W_{atomicN}$: gram Molecular Weight of first metal (g/g-mole)

$$SA_{calc} = \left[\left(\frac{F_1 \times SA_1}{W_{atomic1}} \right) + \left(\frac{F_2 \times SA_2}{W_{atomic2}} \right) + ... + \left(\frac{F_N \times SA_N}{W_{atomicN}} \right) \right] . GMW_{calc} \quad \text{(Eq. 9.3)}$$

Where:
SA_{calc} : calculated cross-sectional area
F_N : fraction of sample weight for metal N
SA_N : cross-sectional area for metal N
$W_{atomicN}$: gram molecular weight of first metal (g/g-mole)

$$D_{calc} = \left[\left(\frac{F_1 \times D_1}{W_{atomic1}} \right) + \left(\frac{F_2 \times D_2}{W_{atomic2}} \right) + ... + \left(\frac{F_N \times D_N}{W_{atomicN}} \right) \right] . GMW_{calc} \quad \text{(Eq. 9.4)}$$

Where:
D_{calc} : calculated density
F_N : fraction of sample weight for metal N
D_N : density for metal N
$W_{atomicN}$: gram molecular weight of first metal (g/g-mole)

9.2 BET Calculation

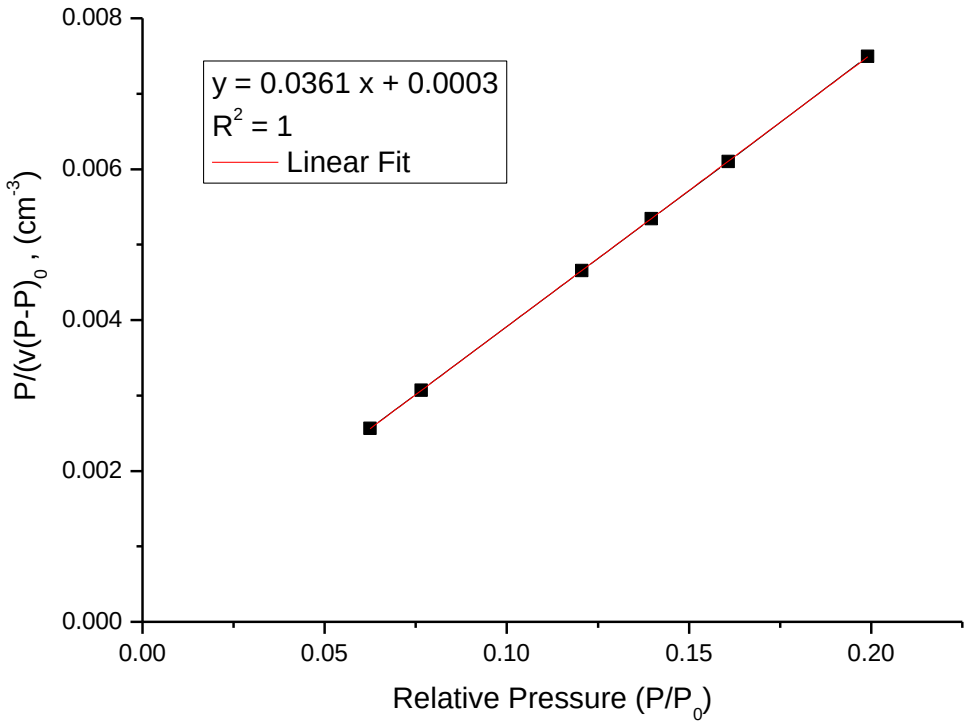

Figure 9.1. Typical fit for the BET plot.

Table 9.1. Example for BET calculations using linearized form of BET equation.

Parameter	Description	Equation	Constants	Values	Unit
Slope				0.0361	$1/cm^3$
Intercept				0.0003	
V_m	Volume of monolayer	*1/(intercept+slope)*		27.47	cm^3
n_m	Number of moles in monolayer	v_m / V_N	V_N=22.4X10^{-3} m^3, molar gas volume at STP	1.23	mole
Area per gram of catalyst	Area of catalyst	$n_m . б . N_A$	$б^0$=16.2X10^{-20} m^2, N_2 molecule surface area , N_A =6.02X10^{23} mol^{-1} , Avogadro's constant	119.61	m^2/g

9.3 GC Calibration

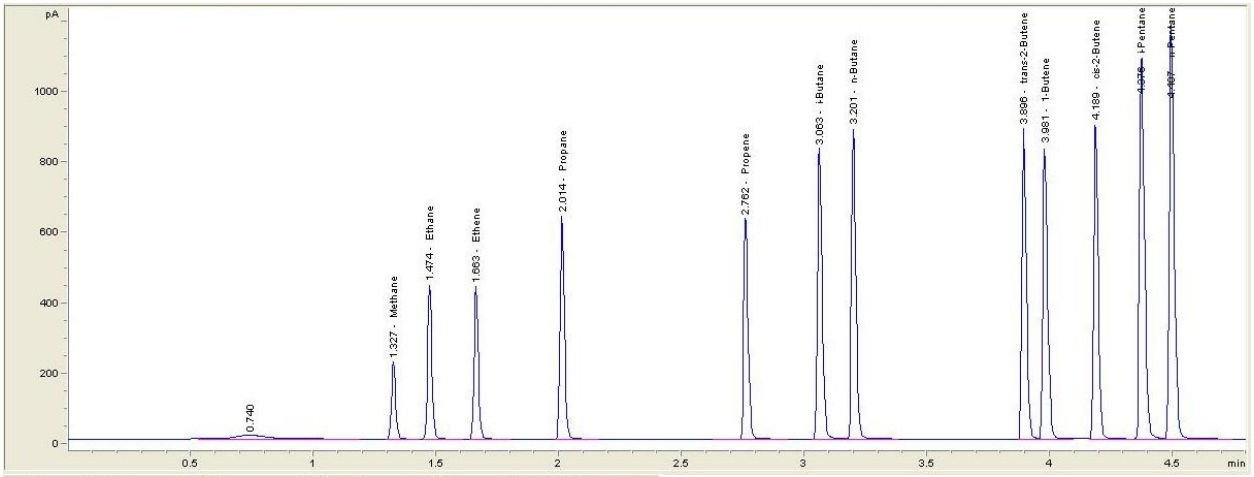

#	Time	Area	Height	Width	Area%	Symmetry
1	0.74	108.6	11	0.1391	0.925	0.85
2	1.327	262.2	217.5	0.0191	2.234	0.832
3	1.474	514.3	438.6	0.0187	4.381	0.828
4	1.663	508.7	432.8	0.0187	4.333	0.798
5	2.014	774.5	634.9	0.0192	6.597	0.776
6	2.762	771	627.3	0.0183	6.567	0.646
7	3.063	1083.7	826.3	0.0203	9.230	0.636
8	3.201	1123.6	884.9	0.0198	9.570	0.66
9	3.896	1118	885.3	0.0197	9.523	0.645
10	3.981	1124.6	831.5	0.0208	9.578	0.598
11	4.189	1139.9	896.1	0.0198	9.709	0.664
12	4.376	1563	1088.4	0.0218	13.313	0.578
13	4.497	1648.7	1177.2	0.0213	14.043	0.587

Figure 9.2. FID calibration.

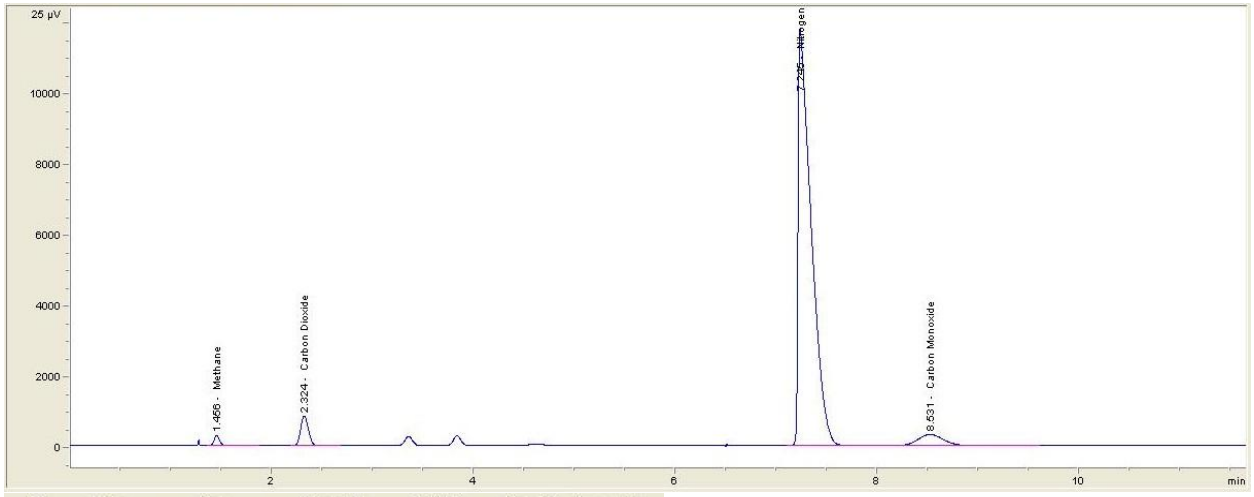

#	Time	Area	Height	Width	Area%	Symmetry
1	1.456	1097.4	279.3	0.0618	0.940	0.876
2	2.324	4390	834.5	0.0814	3.759	0.812
3	7.245	105751.7	11730.7	0.1292	90.545	0.178
4	8.531	5555.3	312.7	0.2792	4.756	0.852

Figure 9.3. TCD2 calibration.

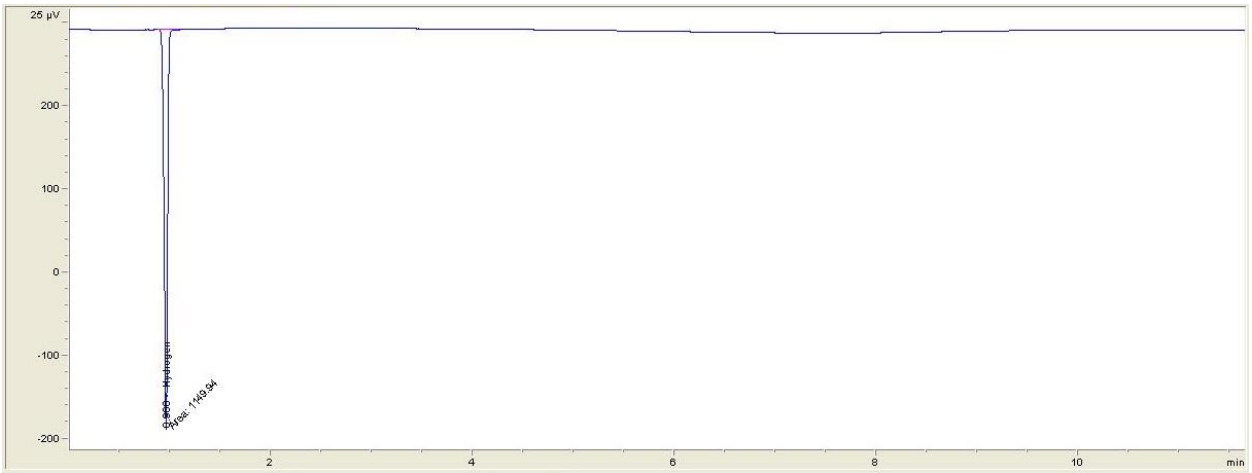

#	Time	Area	Height	Width	Area%	Symmetry
1	0.966	1149.9	483.4	0.0396	100.000	0

Figure 9.4. TCD3 calibration.

Table 9.2. Standard calibration gas composition.

Gas	Percentage of the gas in the mixture
N-Pentane	1%
CIS-2-Butene	1%
N-Butane	1%
Isobutane	1%
Propylene	1%
Carbon dioxide	3%
Ethane	1%
Methane	1%
Isopentane	1%
Trans-2-Butene	1%
1-Butene	1%
Propane	1%
Nitrogen	Balance
Hydrogen	1%
Ethylene	1%
Carbon monoxide	4%

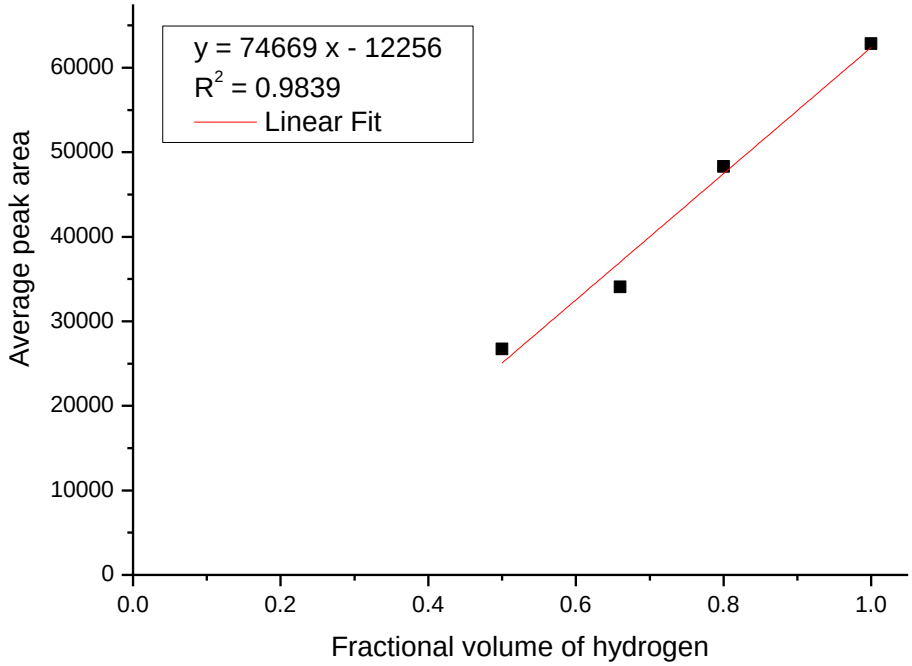

Figure 9.5. GC calibration curve for hydrogen.

9.4 Gibbs free energy of substances

Table 9.3. Gibbs free energy values of formation for various substances [318].

T (K)	ΔG H_2 (kJ)	ΔG CO_2 (kJ)	ΔG CO (kJ)	ΔG H_2O (kJ)	ΔG CH_4 (kJ)	ΔG C (kJ)	ΔG CH_3OH (kJ)
298.15	0	-394.364	-137.180	-228.620	-50.757	671.228	-162.448
300	0	-394.370	-137.345	-228.538	-50.607	670.946	-162.208
400	0	-394.646	-146.354	-223.951	-42.036	655.537	-148.654
500	0	-394.903	-155.426	-219.113	-32.714	639.900	-134.250
600	0	-395.139	-164.494	-214.081	-22.851	624.137	-119.255
700	0	-395.347	-173.522	-208.898	-12.596	608.306	-103.843
800	0	-395.527	-182.494	-203.595	-2.057	592.442	-88.138
900	0	-395.680	-191.408	-198.193	8.685	576.565	-72.229
1000	0	-395.810	-200.261	-192.713	19.572	560.688	-56.178
1100	0	-395.918	-209.056	-187.168	30.562	544.818	
1200	0	-396.007	-217.796	-181.572	41.624	528.960	
1300	0	-396.079	-226.482	-175.934	52.736	513.118	
1400	0	-396.136	-235.118	-170.260	63.880	497.293	
1500	0	-396.179	-243.707	-164.559	75.044	481.486	

Table 9.4. Gibbs free energy calculations for water gas shift reaction.

T (K)	ΔG H_2 (kJ)	ΔG CO_2 (kJ)	ΔG CO (kJ)	ΔG H_2O (kJ)	ΔG_{WGS} (kJ)
298.15	0.000	-394.36	-137.180	-228.620	-28.564
300.00	0.000	-394.37	-137.345	-228.538	-28.487
400.00	0.000	-394.65	-146.354	-223.951	-24.341
500.00	0.000	-394.90	-155.426	-219.113	-20.364
600.00	0.000	-395.14	-164.494	-214.081	-16.564
700.00	0.000	-395.35	-173.522	-208.898	-12.927
800.00	0.000	-395.53	-182.494	-203.595	-9.438
900.00	0.000	-395.68	-191.408	-198.193	-6.079
1000.00	0.000	-395.81	-200.261	-192.713	-2.836

Where:

$$\Delta G_{WGS} = \left(\Delta G_{H_2} + \Delta G_{CO_2}\right) - 1 \cdot \left(\Delta G_{CO} + \Delta G_{H_2O}\right) \quad \text{(Eq. 9.5)}$$

9.5 Equilibrium analysis for methanol steam reforming

Table 9.5. Equilibrium analysis of methanol steam reforming at various methanol reaction temperatures at S/C of 1.3, excluding He as inert gas.

P	(bar)	1	1	1	1	1
T	(°C)	225	250	275	300	325
mol fraction	CH_4	0.26381	0.26122	0.25748	0.25232	0.24547
mol fraction	CO	0.00001	0.0000	0.00007	0.00016	0.00034
mol fraction	CO_2	0.09144	0.09281	0.09476	0.09744	0.10092
mol fraction	H_2	0.01052	0.01725	0.02695	0.04032	0.05796
mol fraction	H_2O	0.63422	0.62869	0.62073	0.60977	0.59531
mol fraction	C	0	0	0	0	0
mol fraction	He	0	0	0	0	0
C balance	total equilibrium moles	2.81484	2.82438	2.83841	2.85780	2.88409
conversion %	CH_3OH	100.00	100.00	100.00	100.00	100.00
conversion %	H_2O	0.00	0.00	0.00	0.00	0.00
yield (mol/mol)	CH_4	0.74	0.74	0.73	0.72	0.71
yield (mol/mol)	CO	0.00	0.00	0.00	0.00	0.00
yield (mol/mol)	CO_2	0.26	0.26	0.27	0.28	0.29
yield (mol/mol)	H_2	0.03	0.05	0.08	0.12	0.17

Table 9.6. Equilibrium analysis of methanol steam reforming at various methanol reaction temperatures at S/C of 1.7, excluding He as inert gas.

P	(bar)	1	1	1	1	1
T	(°C)	225	250	275	300	325
mol fraction	CH_4	0.23038	0.22783	0.22416	0.21911	0.21244
mol fraction	CO	0.00001	0.0000	0.00006	0.00014	0.00029
mol fraction	CO_2	0.08041	0.08186	0.08393	0.08676	0.09044
mol fraction	H_2	0.01086	0.01779	0.02776	0.04145	0.05945
mol fraction	H_2O	0.67833	0.67249	0.66409	0.65255	0.63738
mol fraction	C	0	0	0	0	0
mol fraction	He	0	0	0	0	0
C balance	total equilibrium moles	3.21750	3.22883	3.24517	3.26787	3.29848
conversion %	CH_3OH	100.00	100.00	100.00	100.00	100.00
conversion %	H_2O	0.00	0.00	0.00	0.00	0.00
yield (mol/mol)	CH_4	0.74	0.74	0.73	0.72	0.70
yield (mol/mol)	CO	0.00	0.00	0.00	0.00	0.00
yield (mol/mol)	CO_2	0.26	0.26	0.27	0.28	0.30
yield (mol/mol)	H_2	0.03	0.06	0.09	0.14	0.20

Table 9.7. Equilibrium analysis of methanol steam reforming at various methanol reaction temperatures at S/C of 1.3, CO and CO_2 as potential carbon products, excluding He as inert gas.

P	(bar)	1	1	1	1	1
T	(°C)	225	250	275	300	325
mol fraction	CH_4	0	0	0	0	0
mol fraction	CO	0.01284	0.0184	0.02489	0.03214	0.03993
mol fraction	CO_2	0.21972	0.21416	0.20767	0.20042	0.19263
mol fraction	H_2	0.68483	0.67928	0.67278	0.66553	0.65774
mol fraction	H_2O	0.08261	0.08816	0.09466	0.10191	0.1097
mol fraction	C	0	0	0	0	0
mol fraction	He	0	0	0	0	0
C balance	total equilibrium moles	4.29997	4.30015	4.29997	4.29997	4.29997
conversion %	CH_3OH	100.00	100.00	100.00	100.00	100.00
conversion %	H_2O	72.68	70.84	68.69	66.29	63.71
yield (mol/mol)	CH_4	0.00	0.00	0.00	0.00	0.00
yield (mol/mol)	CO	0.06	0.08	0.11	0.14	0.17
yield (mol/mol)	CO_2	0.94	0.92	0.89	0.86	0.83
yield (mol/mol)	H_2	2.94	2.92	2.89	2.86	2.83

Table 9.8. Equilibrium analysis of methanol steam reforming at various methanol reaction temperatures at S/C of 1.7, CO and CO_2 as potential carbon products, excluding He as inert gas.

P	(bar)	1	1	1	1	1
T	(°C)	225	250	275	300	325
mol fraction	CH_4	0	0	0	0	0
mol fraction	CO	0.00595	0.0091	0.01301	0.01781	0.02337
mol fraction	CO_2	0.20681	0.20372	0.19976	0.19495	0.1894
mol fraction	H_2	0.63235	0.62925	0.62529	0.62048	0.61493
mol fraction	H_2O	0.15489	0.15798	0.16194	0.16675	0.17231
mol fraction	C	0	0	0	0	0
mol fraction	He	0	0	0	0	0
C balance	total equilibrium moles	4.70013	4.69991	4.69991	4.70013	4.69991
conversion %	CH_3OH	0.00	0.00	0.00	0.00	0.00
conversion %	H_2O	57.18	56.32	55.23	53.90	52.36
yield (mol/mol)	CH_4	0.00	0.00	0.00	0.00	0.00
yield (mol/mol)	CO	0.03	0.04	0.06	0.08	0.11
yield (mol/mol)	CO_2	0.97	0.96	0.94	0.92	0.89
yield (mol/mol)	H_2	2.97	2.96	2.94	2.92	2.89

Table 9.9. Equilibrium analysis of methanol steam reforming at various methanol reaction temperatures at S/C of 1.3, including He as inert gas.

P	(bar)	1	1	1	1	1
T	(°C)	225	250	275	300	325
mol fraction	CH_4	0.23311	0.23078	0.22741	0.22277	0.21663
mol fraction	CO	0.00001	0.0000	0.00007	0.00015	0.00032
mol fraction	CO_2	0.08099	0.08231	0.08419	0.08676	0.0901
mol fraction	H_2	0.00989	0.0162	0.02529	0.03781	0.05431
mol fraction	H_2O	0.56047	0.55552	0.5484	0.5386	0.5257
mol fraction	C	0	0	0	0	0
mol fraction	He	0.11553	0.11517	0.11464	0.1139	0.11294
C balance	total equilibrium moles	3.18360	3.19366	3.20852	3.22914	3.25680
conversion %	CH_3OH	100.00	100.00	100.00	100.00	100.00
conversion %	H_2O	0.00	0.00	0.00	0.00	0.00
yield (mol/mol)	CH_4	0.74	0.74	0.73	0.72	0.71
yield (mol/mol)	CO	0.00	0.00	0.00	0.00	0.00
yield (mol/mol)	CO_2	0.26	0.26	0.27	0.28	0.29
yield (mol/mol)	H_2	0.03	0.05	0.08	0.12	0.18

Table 9.10. Equilibrium analysis of methanol steam reforming at various methanol reaction temperatures at S/C of 1.7, including He as inert gas.

P	(bar)	1	1	1	1	1
T	(°C)	225	250	275	300	325
mol fraction	CH_4	0.20438	0.20207	0.19875	0.19417	0.18815
mol fraction	CO	0.00001	0.0000	0.00006	0.00013	0.00028
mol fraction	CO_2	0.07153	0.07292	0.07491	0.07762	0.08114
mol fraction	H_2	0.01023	0.01674	0.0261	0.03894	0.05581
mol fraction	H_2O	0.60192	0.59668	0.58915	0.57883	0.56528
mol fraction	C	0	0	0	0	0
mol fraction	He	0.11193	0.11156	0.11103	0.11031	0.10935
C balance	total equilibrium moles	3.62424	3.63623	3.65337	3.67755	3.70961
conversion %	CH_3OH	100.00	100.00	100.00	100.00	100.00
conversion %	H_2O	0.00	0.00	0.00	0.00	0.00
yield (mol/mol)	CH_4	0.74	0.73	0.73	0.71	0.70
yield (mol/mol)	CO	0.00	0.00	0.00	0.00	0.00
yield (mol/mol)	CO_2	0.26	0.27	0.27	0.29	0.30
yield (mol/mol)	H_2	0.04	0.06	0.10	0.14	0.21

Table 9.11. Equilibrium analysis of methanol steam reforming at various methanol reaction temperatures at S/C of 1.3, CO and CO_2 as potential carbon products, including He as inert gas.

P	(bar)	1	1	1	1	1
T	(°C)	225	250	275	300	325
mol fraction	CH_4	0	0	0	0	0
mol fraction	CO	0.01183	0.0169	0.02293	0.02961	0.03679
mol fraction	CO_2	0.20241	0.19729	0.1913	0.18463	0.17745
mol fraction	H_2	0.63087	0.62576	0.61977	0.61309	0.60591
mol fraction	H_2O	0.0761	0.08121	0.0872	0.09388	0.10106
mol fraction	C	0	0	0	0	0
mol fraction	He	0.0788	0.0788	0.0788	0.0788	0.0788
C balance	total equilibrium moles	4.66766	4.66788	4.66788	4.66766	4.66766
conversion %	CH_3OH	100.00	100.00	100.00	100.00	100.00
conversion %	H_2O	72.68	70.84	68.69	66.29	63.71
yield (mol/mol)	CH_4	0.00	0.00	0.00	0.00	0.00
yield (mol/mol)	CO	0.06	0.08	0.11	0.14	0.17
yield (mol/mol)	CO_2	0.94	0.92	0.89	0.86	0.83
yield (mol/mol)	H_2	2.94	2.92	2.89	2.86	2.83

Table 9.12. Equilibrium analysis of methanol steam reforming at various methanol reaction temperatures at S/C of 1.7, CO and CO_2 as potential carbon products, including He as inert gas.

P	(bar)	1	1	1	1	1
T	(°C)	225	250	275	300	325
mol fraction	CH_4	0	0	0	0	0
mol fraction	CO	0.00548	0.0083	0.01197	0.0164	0.02151
mol fraction	CO_2	0.19038	0.18753	0.18389	0.17946	0.17435
mol fraction	H_2	0.58211	0.57926	0.57561	0.57119	0.56607
mol fraction	H_2O	0.14258	0.14543	0.14908	0.1535	0.15862
mol fraction	C	0	0	0	0	0
mol fraction	He	0.07945	0.07945	0.07945	0.07945	0.07945
C balance	total equilibrium moles	5.10569	5.10569	5.10569	5.10569	5.10569
conversion %	CH_3OH	100.00	100.00	100.00	100.00	100.00
conversion %	H_2O	57.18	56.32	55.23	53.90	52.36
yield (mol/mol)	CH_4	0.00	0.00	0.00	0.00	0.00
yield (mol/mol)	CO	0.03	0.04	0.06	0.08	0.11
yield (mol/mol)	CO_2	0.97	0.96	0.94	0.92	0.89
yield (mol/mol)	H_2	2.97	2.96	2.94	2.92	2.89

9.6 Equilibrium analysis for methane steam reforming

Table 9.13. Equilibrium analysis of methane steam reforming at various methane reaction temperatures at S/C of 2, excluding He as inert gas.

P	(bar)	1	1	1	1	1
T	(°C)	500	550	600	650	700
mol fraction	CH_4	0.17883	0.13181	0.08343	0.04194	0.016
mol fraction	CO	0.01461	0.0355	0.06873	0.10585	0.13365
mol fraction	CO_2	0.07808	0.08544	0.08121	0.06899	0.05676
mol fraction	H_2	0.35618	0.44817	0.53104	0.5935	0.62796
mol fraction	H_2O	0.37228	0.2991	0.23559	0.18973	0.16564
mol fraction	C	0	0	0	0	0
mol fraction	He	0	0	0	0	0
C balance	total equilibrium moles	3.68297	3.95695	4.28504	4.61297	4.84473
conversion %	CH_4	34.14	47.84	64.25	80.65	92.25
conversion %	H_2O	31.45	40.82	49.52	56.24	59.88
yield (mol/mol)	CO	0.05	0.14	0.29	0.49	0.65
yield (mol/mol)	CO_2	0.29	0.34	0.35	0.32	0.27
yield (mol/mol)	H_2	1.31	1.77	2.28	2.74	3.04

Table 9.14. Equilibrium analysis of methane steam reforming at various methane reaction temperatures at S/C of 3, excluding He as inert gas.

P	(bar)	1	1	1	1	1
T	(°C)	500	550	600	650	700
mol fraction	CH_4	0.1147	0.07649	0.04096	0.01606	0.00484
mol fraction	CO	0.01196	0.0282	0.0524	0.07629	0.09212
mol fraction	CO_2	0.07823	0.08747	0.08695	0.07967	0.07132
mol fraction	H_2	0.34883	0.43448	0.50502	0.54755	0.56164
mol fraction	H_2O	0.44627	0.37336	0.31465	0.28043	0.27008
mol fraction	C	0	0	0	0	0
mol fraction	He	0	0	0	0	0
C balance	total equilibrium moles	4.88067	5.20400	5.54600	5.81328	5.94248
conversion %	CH_4	44.02	60.19	77.28	90.66	97.12
conversion %	H_2O	27.40	35.23	41.83	45.66	46.50
yield (mol/mol)	CO	0.06	0.15	0.29	0.44	0.55
yield (mol/mol)	CO_2	0.38	0.46	0.48	0.46	0.42
yield (mol/mol)	H_2	1.70	2.26	2.80	3.18	3.34

Table 9.15. Equilibrium analysis of methane steam reforming at various methane reaction temperatures at S/C of 2, including He as inert gas.

P	(bar)	1	1	1	1	1
T	(°C)	500	550	600	650	700
mol fraction	CH_4	0.16114	0.11823	0.07407	0.03656	0.01362
mol fraction	CO	0.01426	0.0344	0.06623	0.10104	0.12651
mol fraction	CO_2	0.07315	0.07974	0.07551	0.06412	0.05296
mol fraction	H_2	0.33538	0.42231	0.50074	0.55958	0.59136
mol fraction	H_2O	0.33654	0.2709	0.21438	0.17415	0.15376
mol fraction	C	0	0	0	0	0
mol fraction	He	0.07954	0.07437	0.06906	0.06455	0.06179
C balance	total equilibrium moles	4.02334	4.30274	4.63371	4.95737	5.17893
conversion %	CH_4	35.17	49.13	65.68	81.88	92.95
conversion %	H_2O	32.30	41.72	50.33	56.83	60.18
yield (mol/mol)	CO	0.06	0.15	0.31	0.50	0.66
yield (mol/mol)	CO_2	0.29	0.34	0.35	0.32	0.27
yield (mol/mol)	H_2	1.35	1.82	2.32	2.77	3.06

Table 9.16. Equilibrium analysis of methane steam reforming at various methane reaction temperatures at S/C of 3, including He as inert gas.

P	(bar)	1	1	1	1	1
T	(°C)	500	550	600	650	700
mol fraction	CH_4	0.10539	0.06973	0.03678	0.0141	0.00418
mol fraction	CO	0.01172	0.0275	0.05068	0.0731	0.08773
mol fraction	CO_2	0.07447	0.08307	0.08241	0.07549	0.06764
mol fraction	H_2	0.33304	0.41475	0.48168	0.52125	0.53376
mol fraction	H_2O	0.41407	0.34726	0.2941	0.264	0.25563
mol fraction	C	0	0	0	0	0
mol fraction	He	0.06131	0.05769	0.05436	0.05206	0.05106
C balance	total equilibrium moles	5.21975	5.54662	5.88685	6.14666	6.26763
conversion %	CH_4	44.99	61.32	78.35	91.33	97.38
conversion %	H_2O	27.96	35.80	42.29	45.91	46.59
yield (mol/mol)	CO	0.06	0.15	0.30	0.45	0.55
yield (mol/mol)	CO_2	0.39	0.46	0.49	0.46	0.42
yield (mol/mol)	H_2	1.74	2.30	2.84	3.20	3.35

9.7 EDS

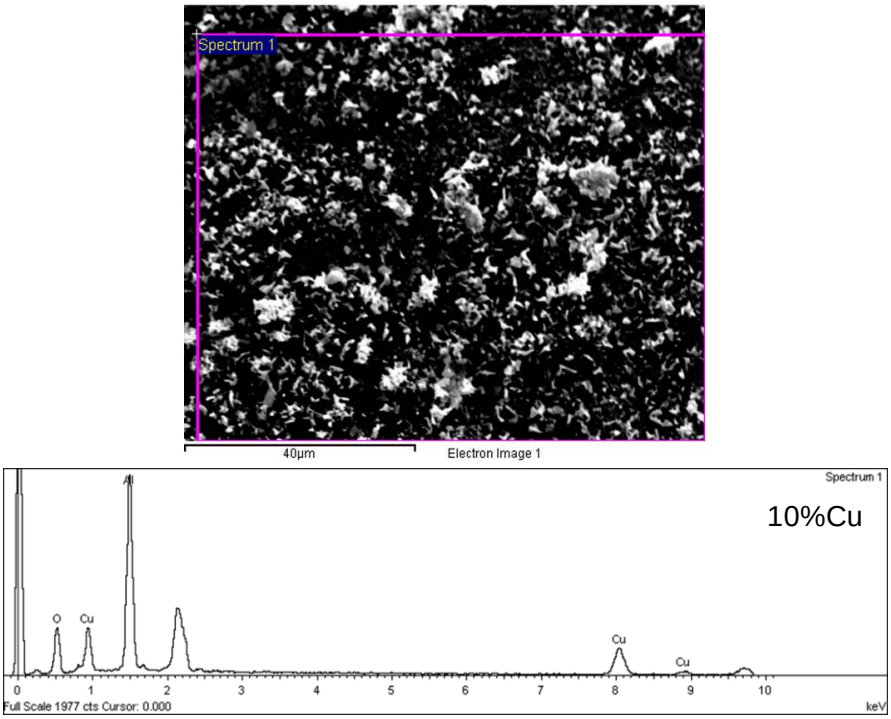

Figure 9.6. EDS for 10%Cu catalyst.

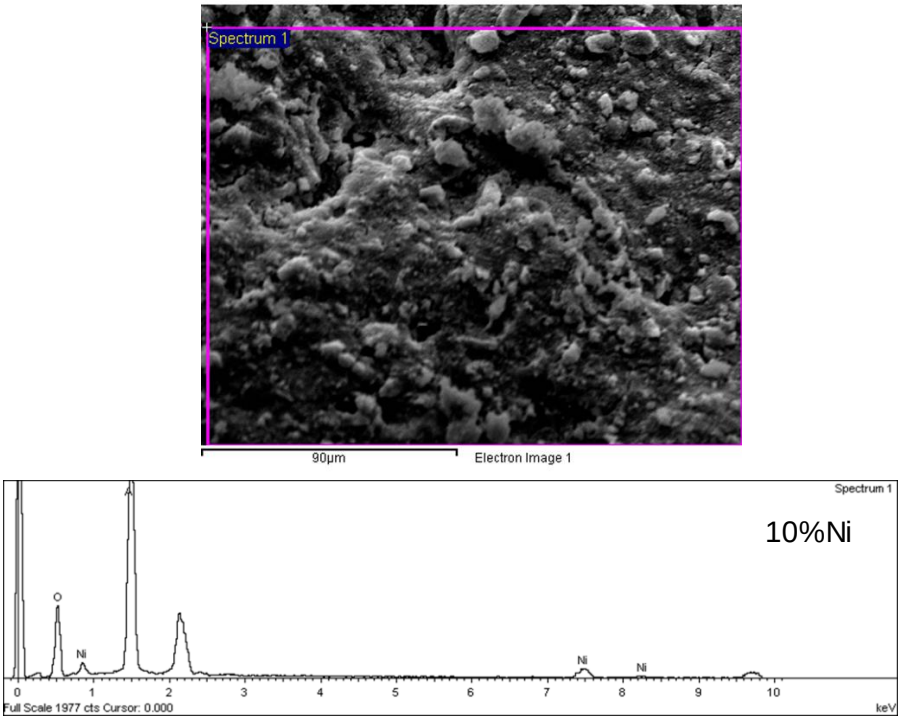

Figure 9.7. EDS for 10%Ni catalyst.

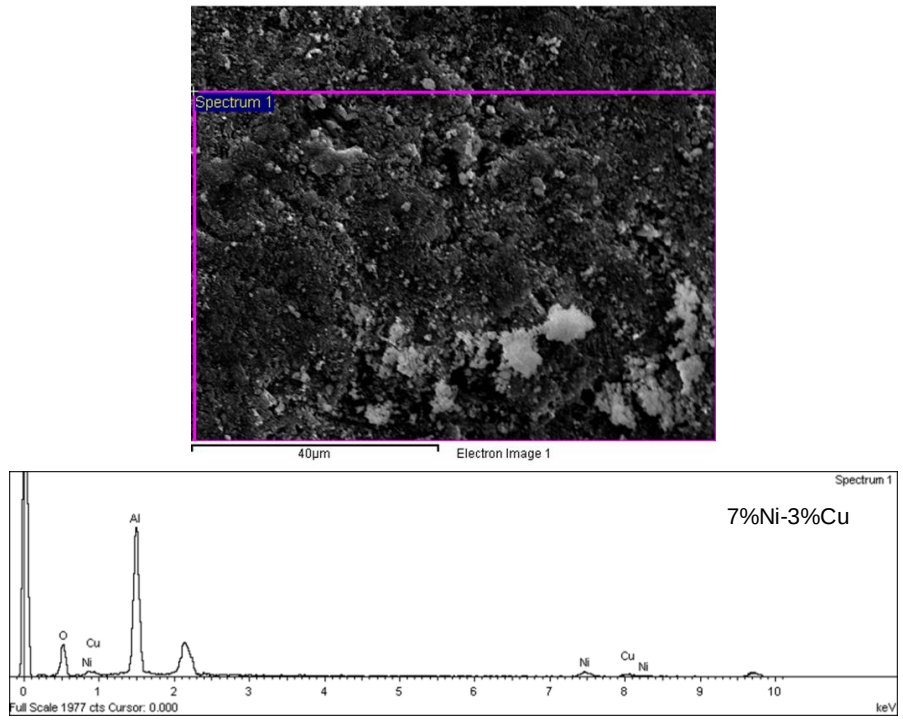

Figure 9.8. EDS for 7%Ni-3%Cu catalyst.

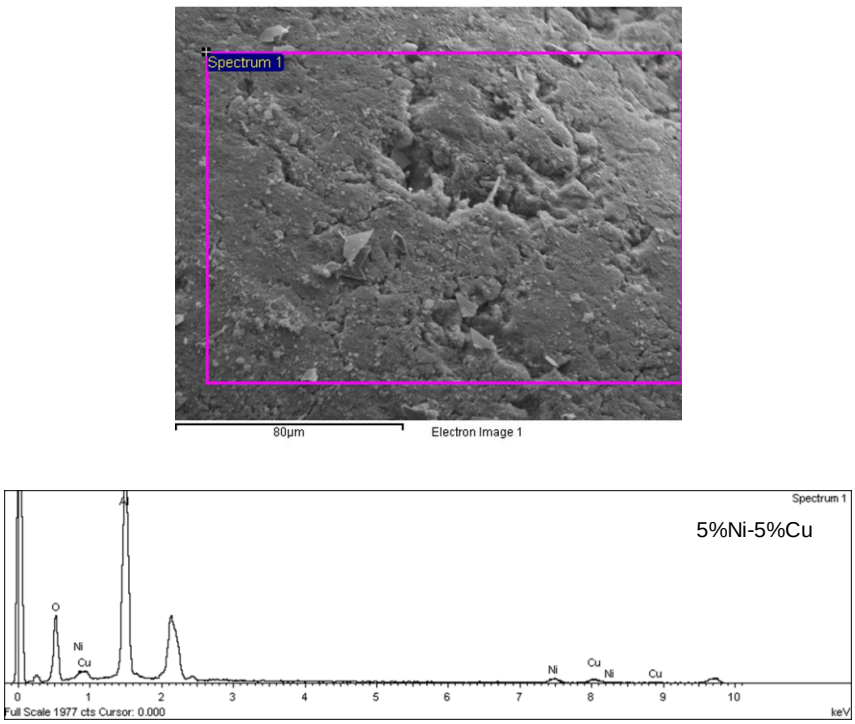

Figure 9.9. EDS for 5%Ni-5%Cu catalyst.

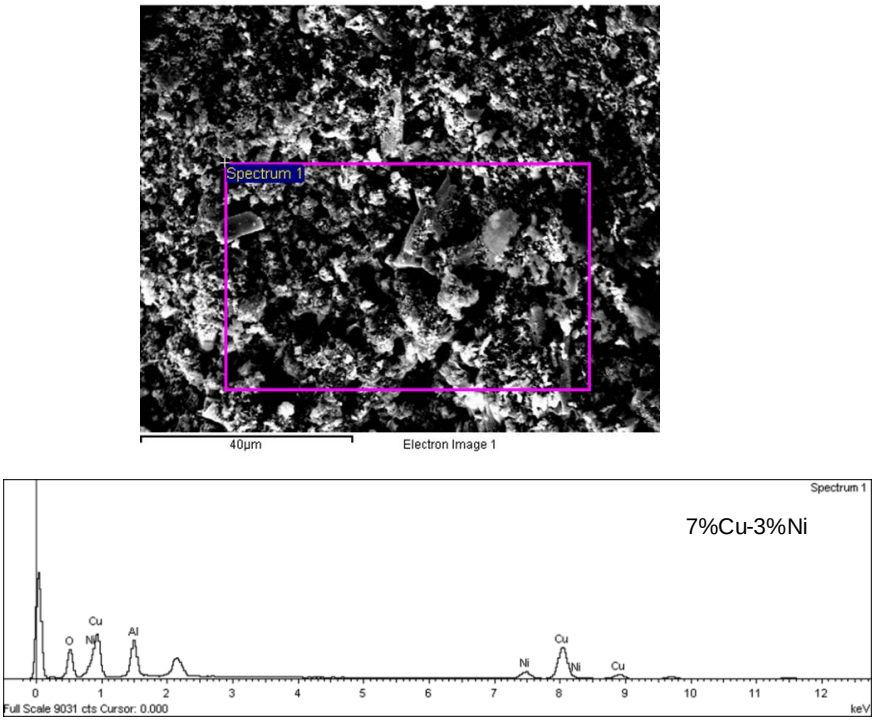

Figure 9.10. EDS for 7%Cu-3%Ni catalyst.

9.8 Methanol steam reforming catalysts

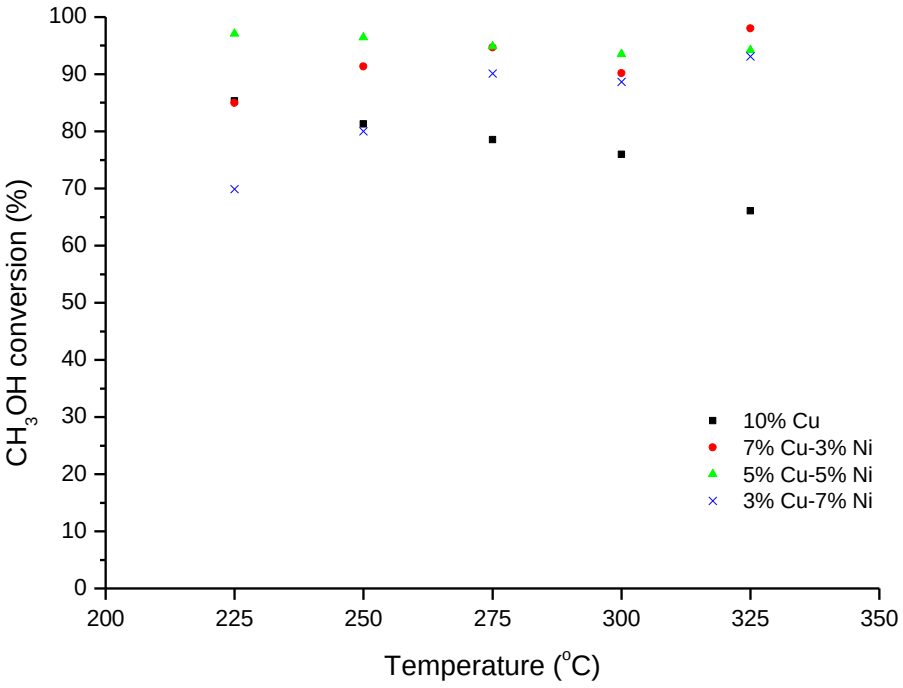

Figure 9.11. Methanol conversion within 225-325°C and S/C of 1.3 for 10%Cu, 7%Cu-3%Ni, 5%Cu-5%Ni and 3%Cu-7%Ni methanol catalysts.

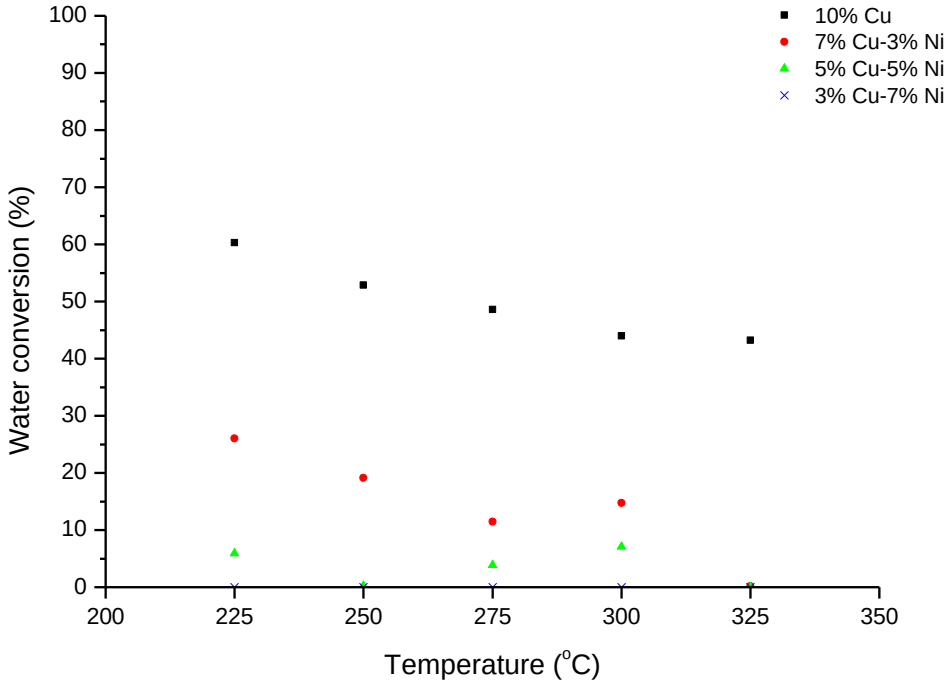

Figure 9.12. Water conversion within 225-325°C and S/C of 1.3 for 10%Cu, 7%Cu-3%Ni, 5%Cu-5%Ni and 3%Cu-7%Ni methanol catalysts

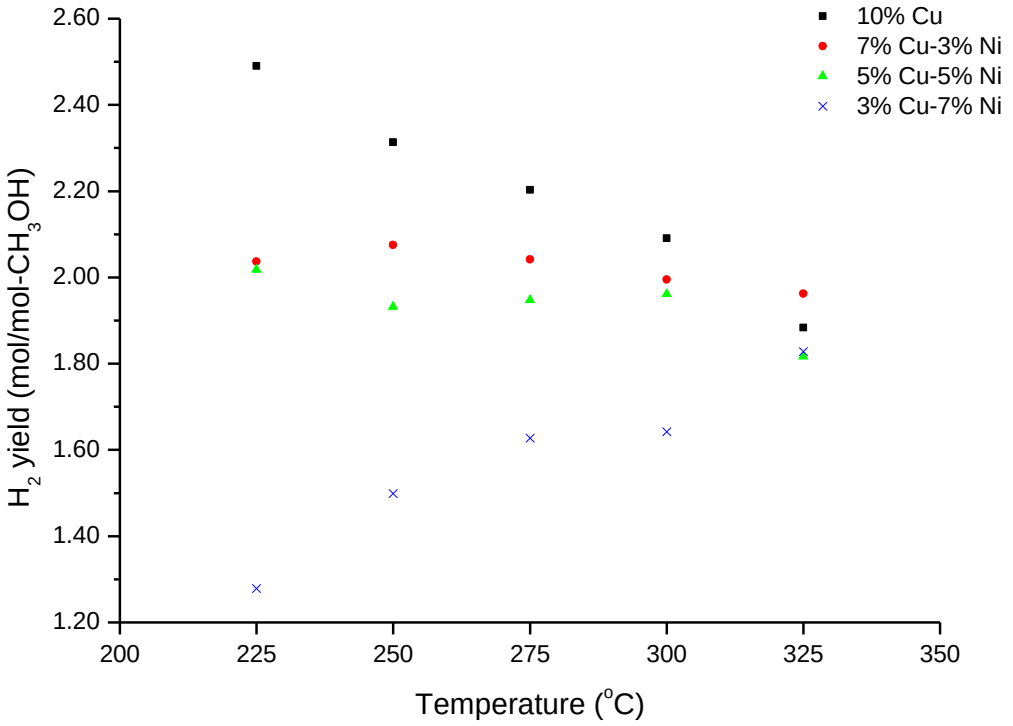

Figure 9.13. Hydrogen yield within 225-325°C and S/C of 1.3 for 10%Cu, 7%Cu-3%Ni, 5%Cu-5%Ni and 3%Cu-7%Ni methanol catalysts.

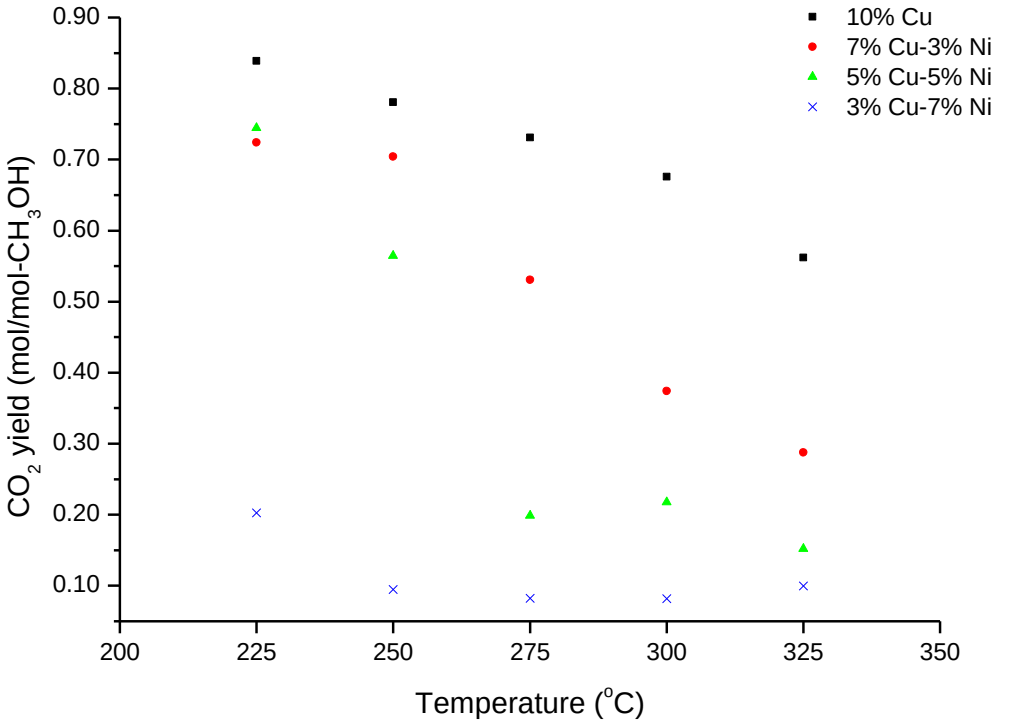

Figure 9.14. CO_2 yield within 225-325°C and S/C of 1.3 for 10%Cu, 7%Cu-3%Ni, 5%Cu-5%Ni and 3%Cu-7%Ni methanol catalysts.

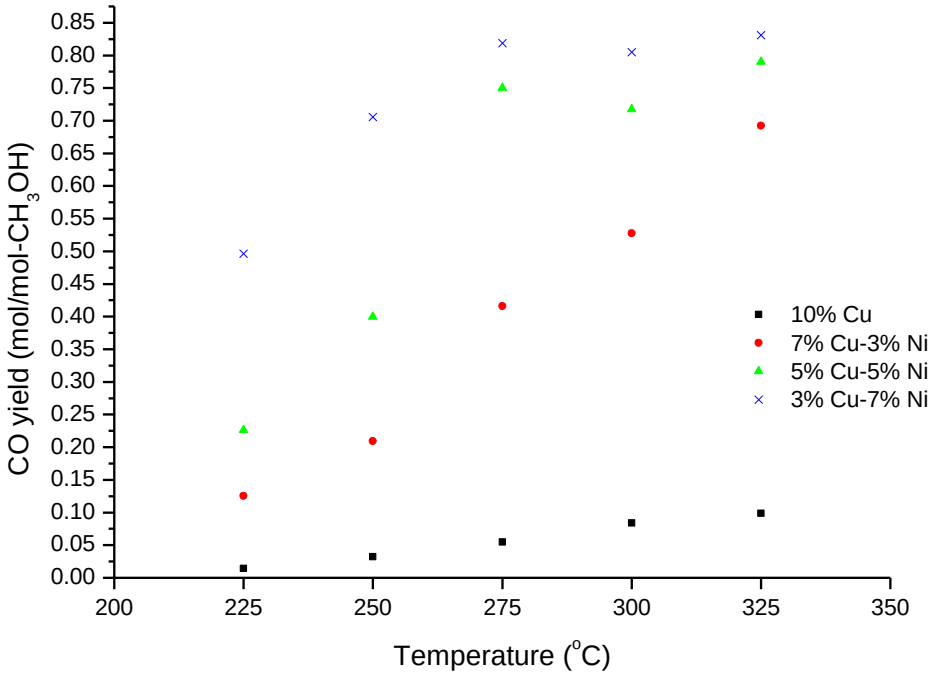

Figure 9.15. CO yield within 225-325°C and S/C of 1.3 for 10%Cu, 7%Cu-3%Ni, 5%Cu-5%Ni and 3%Cu-7%Ni methanol catalysts.

9.9 Methane steam reforming catalysts

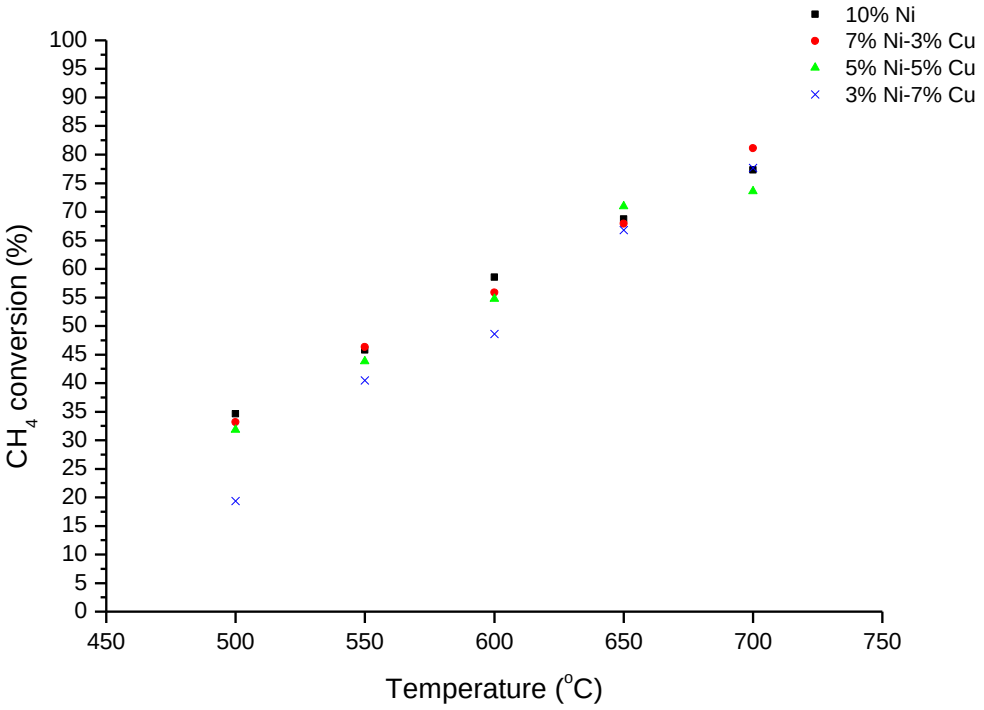

Figure 9.16. Methane conversion within 500-700°C and S/C of 2 for 10%Ni, 7%Ni-3%Cu, 5%Ni-5%Cu and 3%Ni-7%Cu methane catalysts.

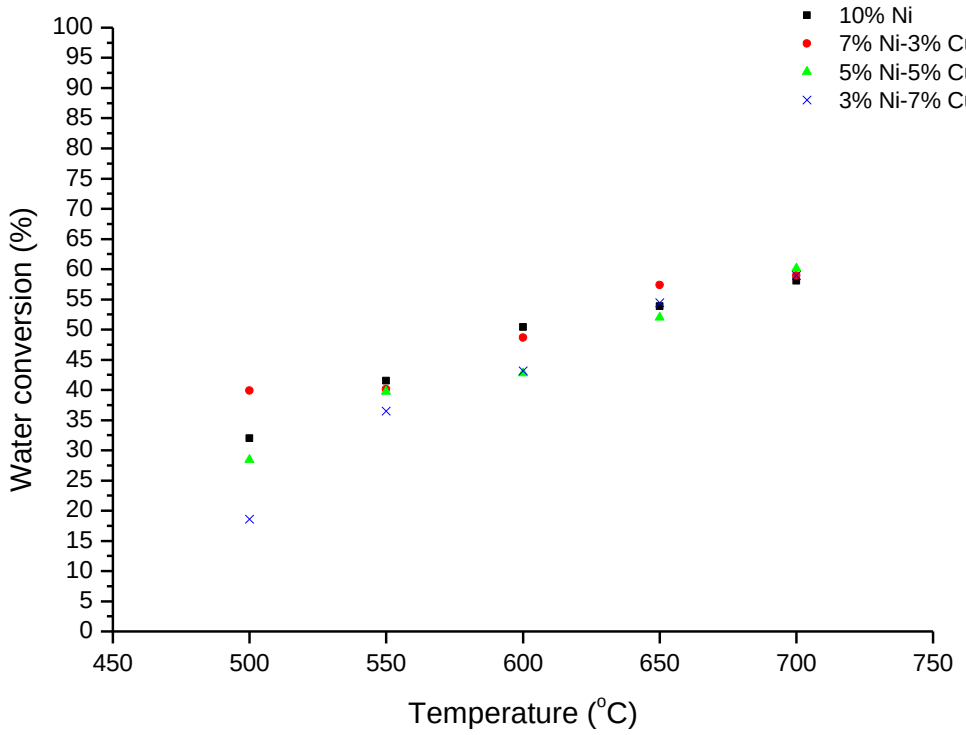

Figure 9.17. Water conversion within 500-700°C and S/C of 2 for 10%Ni, 7%Ni-3%Cu, 5%Ni-5%Cu and 3%Ni-7%Cu methane catalysts.

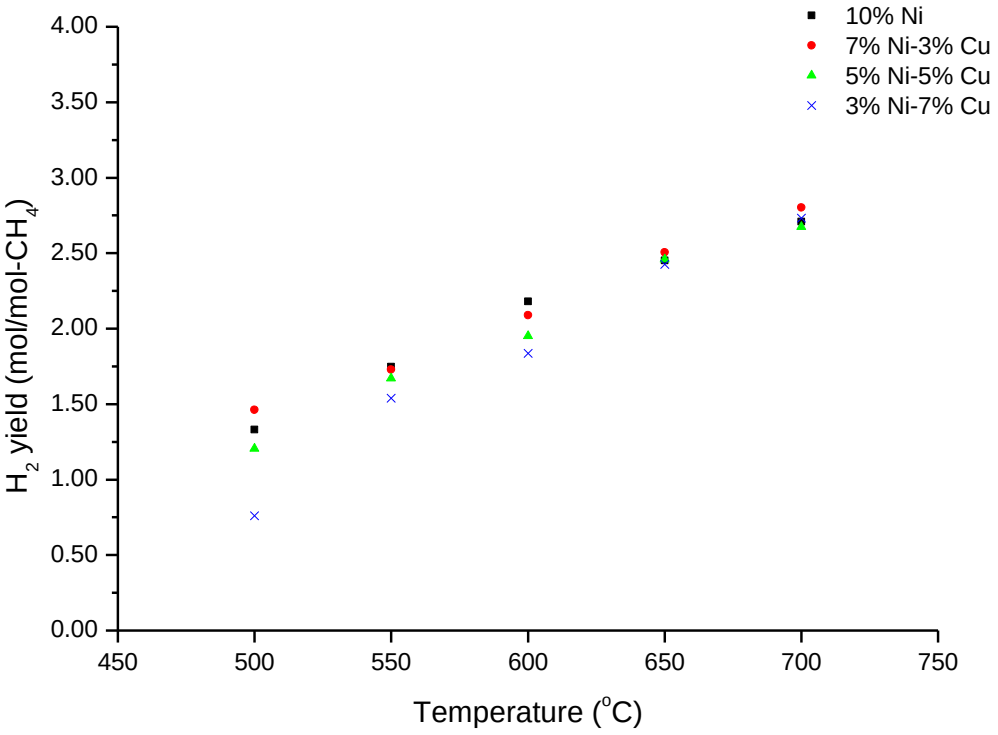

Figure 9.18. Hydrogen yield within 500-700°C and S/C of 2 for 10%Ni, 7%Ni-3%Cu, 5%Ni-5%Cu and 3%Ni-7%Cu methane catalysts.

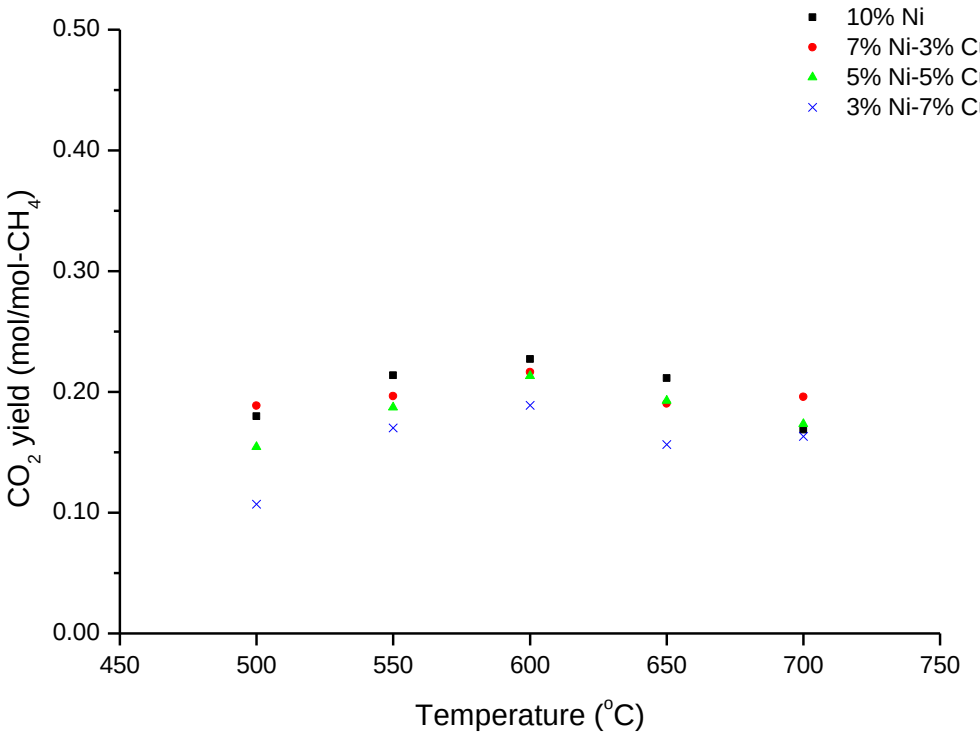

Figure 9.19. CO_2 yield within 500-700°C and S/C of 2 for 10%Ni, 7%Ni-3%Cu, 5%Ni-5%Cu and 3%Ni-7%Cu methane catalysts.

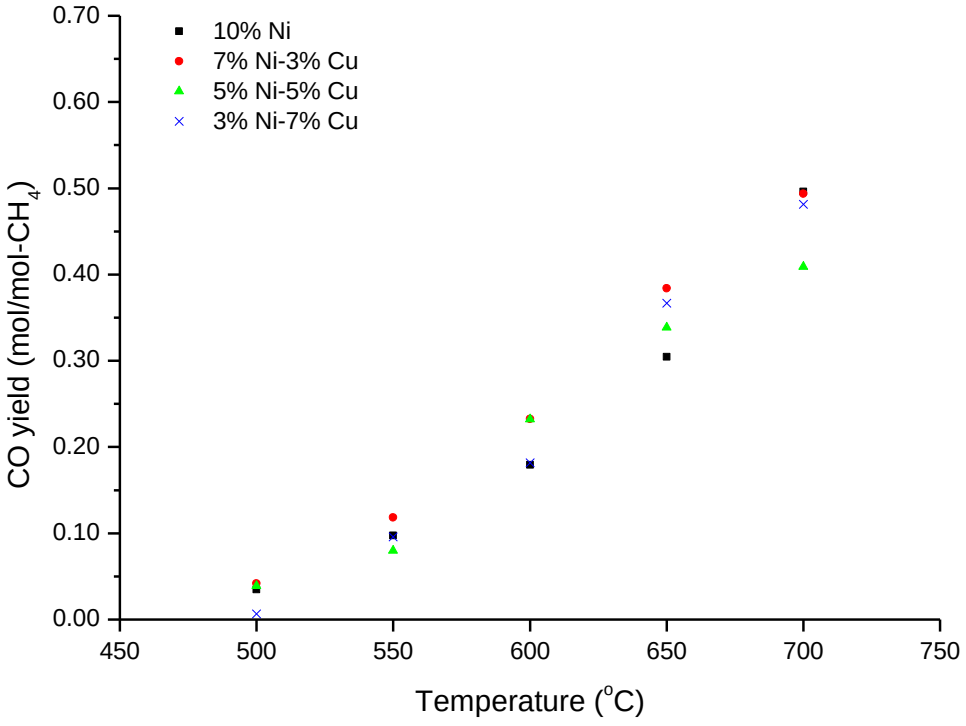

Figure 9.20. CO yield within 500-700°C and S/C of 2 for 10%Ni, 7%Ni-3%Cu, 5%Ni-5%Cu and 3%Ni-7%Cu methane catalyst.

REFERENCES

1. Hirsch, R.L., R. Bezdek, and R. Wendling, *Peaking of world oil production: impacts, mitigation, & risk management. A report prepared for the government of the United States of America*. February 2005.
2. Dunn, S., *Hydrogen futures: Toward a sustainable energy system.* International Journal of Hydrogen Energy, 2002. **27**(3): p. 235-264.
3. Ball, M. and M. Wietschel, *The future of hydrogen – opportunities and challenges.* International Journal of Hydrogen Energy, 2009. **34**(2): p. 615-627.
4. Jörissen, L. *Fuel cells in future energy systems*. in *International Summer School for PEM Fuel Cells Application and Integration*. 2011. Izmir, Turkey.
5. Larminie, J. and A. Dicks, *Fuel cell systems explained*. 2 ed. 2003: Wiley.
6. Choudhury, A., H. Chandra, and A. Arora, *Application of solid oxide fuel cell technology for power generation—A review.* Renewable and Sustainable Energy Reviews, 2013. **20**(0): p. 430-442.
7. Stambouli, A.B. and E. Traversa, *Solid oxide fuel cells (SOFCs): A review of an environmentally clean and efficient source of energy.* Renewable and Sustainable Energy Reviews, 2002. **6**(5): p. 433-455.
8. Wang, Y., et al., *A review of polymer electrolyte membrane fuel cells: Technology, applications, and needs on fundamental research.* Applied Energy, 2011. **88**(4): p. 981-1007.
9. Oldani, C. *Fuel cell membranes*. in *International Summer School for PEM Fuel Cells Application and Integration*. 2011. Izmir, Turkey.
10. *Comparsion of fuel cell technologies , energy efficiency and renewable energy- fuel cell technologies program*. U.S Depeartment of Energy.

11. Steinberger-Wilckens, R. *An introduction to fuel cells : Status and applications of fuel cell technology and competing technologies and the market place*. in *Joint European Summer School for fuel cell and hydrogen technology.* . 2011. Viterbo, Italy.

12. Zhang, X., et al., *A review of integration strategies for solid oxide fuel cells.* Journal of Power Sources, 2010. **195**(3): p. 685-702.

13. Andújar, J.M. and F. Segura, *Fuel cells: History and updating. A walk along two centuries.* Renewable and Sustainable Energy Reviews, 2009. **13**(9): p. 2309-2322.

14. Das, S.K., A. Reis, and K.J. Berry, *Experimental evaluation of CO poisoning on the performance of a high temperature proton exchange membrane fuel cell.* Journal of Power Sources, 2009. **193**(2): p. 691-698.

15. McConnell, V.P., *High-temperature PEM fuel cells: Hotter, simpler, cheaper.* Fuel Cells Bulletin, 2009. **2009**(12): p. 12-16.

16. Lemus, R.G. and J.M. Martínez Duart, *Updated hydrogen production costs and parities for conventional and renewable technologies.* International Journal of Hydrogen Energy, 2010. **35**(9): p. 3929-3936.

17. Mueller-Langer, F., et al., *Techno-economic assessment of hydrogen production processes for the hydrogen economy for the short and medium term.* International Journal of Hydrogen Energy, 2007. **32**(16): p. 3797-3810.

18. Balat, M., *Potential importance of hydrogen as a future solution to environmental and transportation problems.* International Journal of Hydrogen Energy, 2008. **33**(15): p. 4013-4029.

19. Ewan, B.C.R. and R.W.K. Allen, *A figure of merit assessment of the routes to hydrogen.* International Journal of Hydrogen Energy, 2005. **30**(8): p. 809-819.

20. F. Brown, L., *A comparative study of fuels for on-board hydrogen production for fuel-cell-powered automobiles.* International Journal of Hydrogen Energy, 2001. **26**(4): p. 381-397.

21. Navarro, R.M., M.A. Peña, and J.L.G. Fierro, *Hydrogen production reactions from carbon feedstocks: Fossil fuels and biomass.* Chemical Reviews, 2007. **107**(10): p. 3952-3991.

22. Arzamendi, G., et al., *Integration of methanol steam reforming and combustion in a microchannel reactor for H_2 production: A CFD simulation study.* Catalysis Today, 2009. **143**(1–2): p. 25-31.

23. Agrell, J., et al., *Production of hydrogen from methanol over Cu/ZnO catalysts promoted by ZrO_2 and Al_2O_3.* Journal of Catalysis, 2003. **219**(2): p. 389-403.

24. *Biofuels*, in *Biodiesel*. 2008. p. 39-64.

25. Palo, D.R., R.A. Dagle, and J.D. Holladay, *Methanol Steam Reforming for Hydrogen Production.* Chemical Reviews, 2007. **107**(10): p. 3992-4021.

26. *Transport Biofuels: Their Characteristics, Production and Costs*, in *Biofuels for Road Transport*. 2009. p. 1-48.

27. Hamelinck, C.N. and A.P.C. Faaij, *Future prospects for production of methanol and hydrogen from biomass.* Journal of Power Sources, 2002. **111**(1): p. 1-22.

28. Satyapal, S., et al., *The U.S. Department of Energy's National Hydrogen Storage Project: Progress towards meeting hydrogen-powered vehicle requirements.* Catalysis Today, 2007. **120**(3–4): p. 246-256.

29. Sakintuna, B., F. Lamari-Darkrim, and M. Hirscher, *Metal hydride materials for solid hydrogen storage: A review.* International Journal of Hydrogen Energy, 2007. **32**(9): p. 1121-1140.

30. *Hydrogen as an energy carrier*. 2006, Royal Belgian Academy Council of Applied Science Brussel.

31. Bowman, R. and N. stetson, *Hydrogen stoarge materials 2007-2009*. 2009, DOE Hydrogen and Fuel Cells Program Record.

32. Kolb, G., *Fuel Processing For Fuel Cells*. 2008, Weinheim: Wiley-VCH.

33. Xuan, J., et al., *A review of biomass-derived fuel processors for fuel cell systems.* Renewable and Sustainable Energy Reviews, 2009. **13**(6–7): p. 1301-1313.

34. Ahmed, S., R. Kumar, and M. Krumpelt, *Fuel processing for fuel cell power systems.* Fuel Cells Bulletin, 1999. **2**(12): p. 4-7.

35. Qi, A., B. Peppley, and K. Karan, *Integrated fuel processors for fuel cell application: A review.* Fuel Processing Technology, 2007. **88**(1): p. 3-22.

36. Ni, M., D.Y.C. Leung, and M.K.H. Leung, *A review on reforming bio-ethanol for hydrogen production.* International Journal of Hydrogen Energy, 2007. **32**(15): p. 3238-3247.

37. Abbas, H.F. and W.M.A. Wan Daud, *Hydrogen production by methane decomposition: A review.* International Journal of Hydrogen Energy, 2010. **35**(3): p. 1160-1190.

38. Snytnikov, P.V., et al., *Catalysts for hydrogen production in a multifuel processor by methanol, dimethyl ether and bioethanol steam reforming for fuel cell applications.* International Journal of Hydrogen Energy, 2012. **37**(21): p. 16388-16396.

39. Badmaev, S.D. and P.V. Snytnikov, *Hydrogen production from dimethyl ether and bioethanol for fuel cell applications.* International Journal of Hydrogen Energy, 2008. **33**(12): p. 3026-3030.

40. Steinberg, M., *Production of hydrogen and methanol from natural gas with reduced CO_2 emission.* International Journal of Hydrogen Energy, 1998. **23**(6): p. 419-425.

41. Wang, X., et al., *Steam reforming of dimethyl ether over Cu–Ni/γ-Al_2O_3 bi-functional catalyst prepared by deposition–precipitation method.* International Journal of Hydrogen Energy, 2010. **35**(9): p. 4060-4068.

42. Roh, H.-S. and K.-W. Jun, *Low temperature methane steam reforming for hydrogen production for fuel cells.* Bull. Korean Chem. Soc, 2009. **30**(1): p. 153.

43. Terazaki, T., et al., *Development of multi-layered microreactor with methanol reformer for small PEMFC.* Journal of Power Sources, 2005. **145**(2): p. 691-696.

44. Palo, D.R., et al., *Fuel processor development for a soldier-portable fuel cell system*, in *Microreaction Technology*, M. Matlosz, W. Ehrfeld, and J. Baselt, Editors. 2001, Springer Berlin Heidelberg. p. 359-367.

45. http://www.ultracell-llc.com/products.php [Accessed 2nd May 2014].

46. Bowers, B., et al., *Advanced onboard fuel processor for PEM Fuel cell vehicles.* SAE Technical Paper, 2006.

47. Bowers, B., et al., *Multi-fuel PEM fuel cell power plant for vehicles.* SAE Technical Paper, 2009.

48. Irving, P.M. and J.S. Pickles, *Operational requirements for a multi-fuel processor that generates hydrogen from Bio- and petroleum-based fuels for both SOFC and PEM fuel cells.* ECS Transactions, 2007. **5**(1): p. 665-671.

49. Sjardin, M., K.J. Damen, and A.P.C. Faaij, *Techno-economic prospects of small-scale membrane reactors in a future hydrogen-fuelled transportation sector.* Energy, 2006. **31**(14): p. 2523-2555.

50. Schmid, H.P. and J.A. Wünning, *FLOX® steam reforming for PEM fuel cell systems.* Fuel Cells, 2004. **4**(4): p. 256-263.

51. http://www.ballard.com/ [Accessed 2nd May 2014].

52. Ogden, J., *Review of small stationary reformers for hydrogen production*. 2002, Center for energy and environmental studies.

53. Pettersson, L.J. and R. Westerholm, *State of the art of multi-fuel reformers for fuel cell vehicles: problem identification and research needs.* International Journal of Hydrogen Energy, 2001. **26**(3): p. 243-264.

54. Meyer, A., C. Schroll, and R. Lesieur, *Development and Evaluation of Multi-Fuel Fuel Cell Power Plant for Transportation Applications.* SAE Technical Paper, 2000.

55. Bowers, B., et al., *Multi-fuel PEM fuel cell power plant for vehicles.* SAE Technical Paper 2009.

56. Reed, J., et al., *A multi-function compact fuel reforming reactor for fuel cell applications.* Fuel, 2010. **89**(5): p. 949-957.

57. Twigg, M.V., *Catalyst Handbook*. Second ed. 1989, London: Wolfe publishing Ltd.

58. Peppley, B.A., *Catalytic steam reforming of methanol using a commercial copper oxide/zinc oxide/aluminum oxide low temperature shift catalyst*. 1993, Queen's University at Kingston (Canada): Canada. p. 123.

59. OhI, G.L., J.L. Stein, and G.E. Smith, *Fundamental factors in the design of a fast-responding methanol-to-hydrogen steam reformer for transportation*

applications. Journal of Energy Resources Technology, 1996. **118**(2): p. 112-119.

60. Xuan, J., et al., *A review of biomass-derived fuel processors for fuel cell systems.* Renewable and Sustainable Energy Reviews, 2009. **13**(6-7): p. 1301-1313.
61. Nahar, G. and V. Dupont, *Hydrogen via steam reforming of liquid biofeedstock.* Biofuels, 2012. **3**(2): p. 167-191.
62. Little, A., *Multi-fuel reformers for fuel cells used in transportation. Phase 1: Multi-fuel reformers*. 1994: Cambridge.
63. Demirbas, A., *Biofuels*, in *Biodiesel*. 2008, Springer London. p. 39-64.
64. Arzamendi, G., et al., *Integration of methanol steam reforming and combustion in a microchannel reactor for H_2 production: A CFD simulation study.* Catalysis Today, 2009. **143**(1-2): p. 25-31.
65. Richardson, J.T., *Principles of Catalyst Development*. 1989, New York: Plenum press.
66. Fogler, H.S., *Elements of chemical reaction engineering*. 3 ed. 1999: Prentice Hall PTR.
67. Pearce, R. and W.R. Patterson, *Catalysis and chemical processes*. 1981, Glasgow: Blackie & Son Ltd.
68. Cronk. *http://guweb2.gonzaga.edu/faculty/cronk/CHEM240/images/reaction_coordinate_catalyst_lg.gif* [Accessed 2nd May 2014].
69. Lwin, Y., et al., *Hydrogen production from steam-methanol reforming: Thermodynamic analysis.* International Journal of Hydrogen Energy, 2000. **25**(1): p. 47-53.

70. Peppley, B.A., et al., *Methanol-steam reforming on Cu/ZnO/Al_2O_3 catalysts. Part 2. A comprehensive kinetic model.* Applied Catalysis A: General, 1999. **179**(1-2): p. 31-49.

71. Peppley, B.A., et al., *Methanol-steam reforming on Cu/ZnO/Al_2O_3. Part 1: the reaction network.* Applied Catalysis A: General, 1999. **179**(1-2): p. 21-29.

72. Agarwal, V., S. Patel, and K.K. Pant, *H_2 production by steam reforming of methanol over Cu/ZnO/Al_2O_3 catalysts: transient deactivation kinetics modeling.* Applied Catalysis A: General, 2005. **279**(1–2): p. 155-164.

73. Purnama, H., et al., *CO formation/selectivity for steam reforming of methanol with a commercial CuO/ZnO/Al_2O_3 catalyst.* Applied Catalysis A: General, 2004. **259**(1): p. 83-94.

74. Basile, A., et al., *Hydrogen production by methanol steam reforming carried out in membrane reactor on Cu/Zn/Mg-based catalyst.* Catalysis Today, 2008. **137**(1): p. 17-22.

75. Amphlett, J.C., et al., *Hydrogen production by steam reforming of methanol for polymer electrolyte fuel cells.* International Journal of Hydrogen Energy, 1994. **19**(2): p. 131-137.

76. Peters, R., H.G. Düsterwald, and B. Höhlein, *Investigation of a methanol reformer concept considering the particular impact of dynamics and long-term stability for use in a fuel-cell-powered passenger car.* Journal of Power Sources, 2000. **86**(1–2): p. 507-514.

77. Peppley, B., *Catalytic Steam Reforming of Methanol Using a commercial CuO/ZnO/Al_2O_3 Low Temperature Shift Catalyst*, in *Chemical Engineering*. 1993, Queen's University: Kingston.

78. Amphlett, J.C., et al., *Hydrogen production by the catalytic steam reforming of methanol part 1: The thermodynamics.* The Canadian Journal of Chemical Engineering, 1981. **59**(6): p. 720-727.

79. Amphlett, J.C., et al., *Hydrogen production by the catalytic steam reforming of methanol: Part 2: Kinetics of methanol decomposition using girdler G66B catalyst.* The Canadian Journal of Chemical Engineering, 1985. **63**(4): p. 605-611.

80. Twigg, M.V. and M.S. Spencer, *Deactivation of copper metal catalysts for methanol decomposition, methanol steam reforming and methanol synthesis.* Topics in Catalysis, 2003. **22**(3/4): p. 191-203.

81. Jiang, C.J., *Studies of the production of hydrogen from methanol steam reforming at low temperatures*. 1992, University of New South Wales (Australia): Australia.

82. Agrell, J., H. Birgersson, and M. Boutonnet, *Steam reforming of methanol over a $Cu/ZnO/Al_2O_3$ catalyst: a kinetic analysis and strategies for suppression of CO formation.* Journal of Power Sources, 2002. **106**(1-2): p. 249-257.

83. Trimm, D.L. and Z.I. Oensan, *Onboard fuel conversion for hydrogen-fuel-cell-driven vehicles.* Catalysis Reviews: Science and Engineering, 2001. **43**(1): p. 31-84.

84. Lindström, B. and L.J. Pettersson, *Hydrogen generation by steam reforming of methanol over copper-based catalysts for fuel cell applications.* International Journal of Hydrogen Energy, 2001. **26**(9): p. 923-933.

85. Regalbuto, J., *Catalyst Preperation:Science and Engineering*. 2006, CRC Press: USA.

86. Fierro, G., et al., *Study of the reducibility of copper in CuO-ZnO catalysts by temperature-programmed reduction.* Applied Catalysis A: General, 1996. **137**(2): p. 327-348.

87. Agarwal, V., S. Patel, and K.K. Pant, *H_2 production by steam reforming of methanol over Cu/ZnO/Al_2O_3 catalysts: transient deactivation kinetics modeling.* Applied Catalysis A: General, 2005. **279**(1-2): p. 155-164.

88. Breen, J.P. and J.R.H. Ross, *Methanol reforming for fuel-cell applications: development of zirconia-containing Cu-Zn-Al catalysts.* Catalysis Today, 1999. **51**(3-4): p. 521-533.

89. Huang, G., et al., *Steam reforming of methanol over CuO/ZnO/CeO_2/ZrO_2/Al_2O_3 catalysts.* Applied Catalysis A: General, 2009. **358**(1): p. 7-12.

90. Ginés, M.J.L., et al., *Activity and structure-sensitivity of the water-gas shift reaction over CuZnAl mixed oxide catalysts.* Applied Catalysis A: General, 1995. **131**(2): p. 283-296.

91. Men, Y., et al., *Steam reforming of methanol over Cu/CeO_2/γ-Al_2O_3 catalysts in a microchannel reactor.* Applied Catalysis A: General, 2004. **277**(1-2): p. 83-90.

92. Patel, S. and K.K. Pant, *Selective production of hydrogen via oxidative steam reforming of methanol using Cu-Zn-Ce-Al oxide catalysts.* Chemical Engineering Science, 2007. **62**(18-20 SPEC. ISS.): p. 5436-5443.

93. Liu, Y., et al., *Highly active copper/ceria catalysts for steam reforming of methanol.* Applied Catalysis A: General, 2002. **223**(1-2): p. 137-145.

94. Oİˆnsan, Z.I., *Catalytic processes for clean hydrogen production from hydrocarbons.* Turkish Journal of Chemistry, 2007. **31**(5): p. 531-550.

95. Oguchi, H., et al., *Steam reforming of methanol over Cu/CeO_2/ZrO_2 catalysts.* Applied Catalysis A: General, 2005. **281**(1-2): p. 69-73.

96. Yaseneva, P., et al., *Hydrogen production by steam reforming of methanol over Cu-CeZrYOx-based catalysts.* Catalysis Today, 2008. **138**(3-4): p. 175-182.

97. Cheng, W.-H., et al., *Supported Cu Catalysts with Yttria-Doped Ceria for Steam Reforming of Methanol.* Topics in Catalysis, 2003. **22**(3/4): p. 225-233.

98. Matter, P.H., D.J. Braden, and U.S. Ozkan, *Steam reforming of methanol to H_2 over nonreduced Zr-containing CuO/ZnO catalysts.* Journal of Catalysis, 2004. **223**(2): p. 340-351.

99. Matter, P.H. and U.S. Ozkan, *Effect of pretreatment conditions on Cu/Zn/Zr-based catalysts for the steam reforming of methanol to H_2.* Journal of Catalysis, 2005. **234**(2): p. 463-475.

100. Velu, S., et al., *Oxidative steam reforming of methanol over CuZnAl(Zr)-oxide catalysts for the selective production of hydrogen for fuel cells: Catalyst characterization and performance evaluation.* Journal of Catalysis, 2000. **194**(2): p. 373-384.

101. Wu, G.-S., et al., *The Role of the Promoters in Cu Based Catalysts for Methanol Steam Reforming.* Catalysis Letters, 2009. **130**(1/2): p. 177-184.

102. Yong-Feng, L., D. Xin-Fa, and L. Wei-Ming, *Effects of ZrO_2-promoter on catalytic performance of CuZnAlO catalysts for production of hydrogen by steam reforming of methanol.* International Journal of Hydrogen Energy, 2004. **29**(15): p. 1617-1621.

103. Purnama, H., et al., *Activity and selectivity of a nanostructured CuO/ZrO_2 catalyst in the steam reforming of methanol.* Catalysis Letters, 2004. **94**(1/2): p. 61-68.

104. Ritzkopf, I., et al., *Decreased CO production in methanol steam reforming over Cu/ZrO_2 catalysts prepared by the microemulsion technique.* Applied Catalysis A: General, 2006. **302**(2): p. 215-223.

105. Jones, S.D. and H.E. Hagelin-Weaver, *Steam reforming of methanol over CeO_2- and ZrO_2-promoted Cu-ZnO catalysts supported on nanoparticle Al_2O_3.* Applied Catalysis B: Environmental, 2009. **90**(1-2): p. 195-204.

106. Matsumura, Y. and H. Ishibe, *High temperature steam reforming of methanol over $Cu/ZnO/ZrO_2$ catalysts.* Applied Catalysis B: Environmental, 2009. **91**(1-2): p. 524-532.

107. Gribovskii, A.G., et al., *Efficiency of Zn/TiO_2 catalyst operation in a microchannel reactor in methanol steam reforming.* Kinetics and Catalysis, 2009. **50**(1): p. 11-17.

108. Huang, X., L. Ma, and M.S. Wainwright, *The influence of Cr, Zn and Co additives on the performance of skeletal copper catalysts for methanol synthesis and related reactions.* Applied Catalysis A: General, 2004. **257**(2): p. 235-243.

109. Ma, L., et al., *Cr_2O_3 promoted skeletal Cu catalysts for the reactions of methanol steam reforming and water gas shift.* Catalysis Today, 2000. **63**(2-4): p. 499-505.

110. Lindström, B., L.J. Pettersson, and P. Govind Menon, *Activity and characterization of Cu/Zn, Cu/Cr and Cu/Zr on γ-alumina for methanol*

reforming for fuel cell vehicles. Applied Catalysis A: General, 2002. **234**(1-2): p. 111-125.

111. Idem, R.O. and N.N. Bakhshi, *Production of hydrogen from methanol over promoted coprecipitated Cu-Al catalysts: The effects of various promoters and catalyst activation methods.* Industrial and Engineering Chemistry Research, 1995. **34**(5): p. 1548-1557.
112. Kearns, L.M., et al., *Hydrogen production via methanol - Steam reforming using catalysts containing a hydrotalcite phase structure.* ACS Division of Fuel Chemistry, Preprints, 1999. **44**(4): p. 905-908.
113. Takahashi, T., M. Inoue, and T. Kai, *Effect of metal composition on hydrogen selectivity in steam reforming of methanol over catalysts prepared from amorphous alloys.* Applied Catalysis A: General, 2001. **218**(1-2): p. 189-195.
114. Manzoli, M., A. Chiorino, and F. Boccuzzi, *Decomposition and combined reforming of methanol to hydrogen: a FTIR and QMS study on Cu and Au catalysts supported on ZnO and TiO_2.* Applied Catalysis B: Environmental, 2005. **57**(3): p. 201-209.
115. Papavasiliou, J., G. Avgouropoulos, and T. Ioannides, *Steam reforming of methanol over copper-manganese spinel oxide catalysts.* Catalysis Communications, 2005. **6**(7): p. 497-501.
116. Papavasiliou, J., G. Avgouropoulos, and T. Ioannides, *Steady-state isotopic transient kinetic analysis of steam reforming of methanol over Cu-based catalysts.* Applied Catalysis B: Environmental, 2009. **88**(3-4): p. 490-496.
117. Iwasa, N. and N. Takezawa, *New Supported Pd and Pt Alloy Catalysts for Steam Reforming and Dehydrogenation of Methanol.* Topics in Catalysis, 2003. **22**(3/4): p. 215-224.

118. Iwasa, N., et al., *Methanol Synthesis from CO_2 Under Atmospheric Pressure over Supported Pd Catalysts.* Catalysis Letters, 2004. **96**(1/2): p. 75-78.

119. Iwasa, N., et al., *Steam reforming of methanol over Pd/ZnO: Effect of the formation of PdZn alloys upon the reaction.* Applied Catalysis A: General, 1995. **125**(1): p. 145-157.

120. Iwasa, N., et al., *Steam reforming of methanol over Pd-Zn catalysts.* Reaction Kinetics and Catalysis Letters, 2000. **69**(2): p. 355-360.

121. Iwasa, N., et al., *Effect of Zn addition to supported Pd catalysts in the steam reforming of methanol.* Applied Catalysis A: General, 2003. **248**(1-2): p. 153-160.

122. Cao, C., et al., *Kinetic studies of methanol steam reforming over Pd/ZnO catalyst using a microchannel reactor.* Applied Catalysis A: General, 2004. **262**(1): p. 19-29.

123. Ranganathan, E.S., S.K. Bej, and L.T. Thompson, *Methanol steam reforming over Pd/ZnO and Pd/CeO2 catalysts.* Applied Catalysis A: General, 2005. **289**(2): p. 153-162.

124. Karim, A., T. Conant, and A. Datye, *The role of PdZn alloy formation and particle size on the selectivity for steam reforming of methanol.* Journal of Catalysis, 2006. **243**(2): p. 420-427.

125. Agrell, J., et al., *Production of hydrogen by partial oxidation of methanol over ZnO-supported palladium catalysts prepared by microemulsion technique.* Applied Catalysis A: General, 2003. **242**(2): p. 233-245.

126. Penner, S., et al., *Pd/Ga_2O_3 methanol steam reforming catalysts: Part I. Morphology, composition and structural aspects.* Applied Catalysis A: General, 2009. **358**(2): p. 193-202.

127. Lorenz, H., et al., *Pd/Ga_2O_3 methanol steam reforming catalysts: Part II. Catalytic selectivity.* Applied Catalysis A: General, 2009. **358**(2): p. 203-210.

128. Penner, S., et al., *Growth and structural stability of well-ordered PdZn alloy nanoparticles.* Journal of Catalysis, 2006. **241**(1): p. 14-19.

129. Tolmacsov, P., A. Gazsi, and F. Solymosi, *Decomposition and reforming of methanol on Pt metals supported by carbon Norit.* Applied Catalysis A: General, 2009. **362**(1-2): p. 58-61.

130. Qi, C., J.C. Amphlett, and B.A. Peppley, *K (Na)-promoted Ni, Al layered double hydroxide catalysts for the steam reforming of methanol.* Journal of Power Sources, 2007. **171**(2): p. 842-849.

131. Qi, C., J.C. Amphlett, and B.A. Peppley, *Hydrogen production by methanol reforming on NiAl layered double hydroxide derived catalyst: Effect of the pretreatment of the catalyst.* International Journal of Hydrogen Energy, 2007. **32**(18): p. 5098-5102.

132. Qi, C., J. Amphlett, and B. Peppley, *H_2 production via the steam reforming of methanol over NiAl-layered double hydroxide derived catalysts.* Catalysis Surveys from Asia, 2009. **13**(1): p. 16-21.

133. Qi, C., J.C. Amphlett, and B.A. Peppley, *Product composition as a function of temperature over NiAl-layered double hydroxide derived catalysts in steam reforming of methanol.* Applied Catalysis A: General, 2006. **302**(2): p. 237-243.

134. Jacobs, G. and B.H. Davis, *In situ DRIFTS investigation of the steam reforming of methanol over Pt/ceria.* Applied Catalysis A: General, 2005. **285**(1-2): p. 43-49.

135. Suwa, Y., et al., *Comparative study between Zn–Pd/C and Pd/ZnO catalysts for steam reforming of methanol.* Applied Catalysis A: General, 2004. **267**(1–2): p. 9-16.

136. Sá, S., et al., *Catalysts for methanol steam reforming—A review.* Applied Catalysis B: Environmental, 2010. **99**(1–2): p. 43-57.

137. Takezawa, N. and N. Iwasa, *Steam reforming and dehydrogenation of methanol: Difference in the catalytic functions of copper and group VIII metals.* Catalysis Today, 1997. **36**(1): p. 45-56.

138. Günter, M.M., et al., *Redox behavior of copper oxide/zinc oxide catalysts in the steam reforming of methanol studied by in situ x-ray diffraction and absorption spectroscopy.* Journal of Catalysis, 2001. **203**(1): p. 133-149.

139. Okamoto, Y., et al., *Surface characterization of copper (II) oxide-zinc oxide methanol-synthesis catalysts by x-ray photoelectron spectroscopy. 2. Reduced catalysts.* The Journal of Physical Chemistry, 1983. **87**(19): p. 3747-3754.

140. Frank, B., et al., *Steam reforming of methanol over copper-containing catalysts: Influence of support material on microkinetics.* Journal of Catalysis, 2007. **246**(1): p. 177-192.

141. Iwasa, N. and N. Takezawa, *New supported Pd and Pt alloy catalysts for steam reforming and dehydrogenation of methanol.* Topics in Catalysis, 2003. **22**(3-4): p. 215-224.

142. Iwasa, N., et al., *New catalytic functions of Pd–Zn, Pd–Ga, Pd–In, Pt–Zn, Pt–Ga and Pt–In alloys in the conversions of methanol.* Catalysis Letters, 1998. **54**(3): p. 119-123.

143. Xia, G., et al., *Development of highly active Pd-ZnO/Al_2O_3 catalysts for microscale fuel processor applications.* Chemical Engineering & Technology, 2005. **28**(4): p. 515-519.

144. Patel, S. and K.K. Pant, *Influence of preparation method on performance of Cu(Zn)(Zr)-alumina catalysts for the hydrogen production via steam reforming of methanol.* Journal of Porous Materials, 2006. **13**(3): p. 373-378.

145. Carrero, A., J.A. Calles, and A.J. Vizcaíno, *Hydrogen production by ethanol steam reforming over Cu-Ni/SBA-15 supported catalysts prepared by direct synthesis and impregnation.* Applied Catalysis A: General, 2007. **327**(1): p. 82-94.

146. Vizcaíno, A.J., A. Carrero, and J.A. Calles, *Hydrogen production by ethanol steam reforming over Cu–Ni supported catalysts.* International Journal of Hydrogen Energy, 2007. **32**(10–11): p. 1450-1461.

147. Mariño, F., et al., *Hydrogen production from steam reforming of bioethanol using Cu/Ni/K/γ-Al_2O_3 catalysts. Effect of Ni.* International Journal of Hydrogen Energy, 2001. **26**(7): p. 665-668.

148. Liao, P.-H. and H.-M. Yang, *Preparation of catalyst Ni–Cu/CNTs by chemical reduction with formaldehyde for steam reforming of methanol.* Catalysis Letters, 2008. **121**(3-4): p. 274-282.

149. De Rogatis, L., et al., *Ni_xCu_y/Al_2O_3 based catalysts for hydrogen production.* Energy & Environmental Science, 2008. **1**(4): p. 501-509.

150. Wu, H., et al., *Ni-Based Catalysts for Low Temperature Methane Steam Reforming: Recent Results on Ni-Au and Comparison with Other Bi-Metallic Systems.* Catalysts, 2013. **3**(2): p. 563-583.

151. Khzouz, M., et al., *Characterization and activity test of commercial Ni/Al_2O_3, $Cu/ZnO/Al_2O_3$ and prepared $Ni–Cu/Al_2O_3$ catalysts for hydrogen production from methane and methanol fuels.* International Journal of Hydrogen Energy, 2013. **38**(3): p. 1664-1675.

152. Angeli, S.D., et al., *State of the art catalysts for CH_4 steam reforming at low temperature.* International Journal of Hydrogen Energy, 2014. **39**(5): p. 1979-1997.

153. Thurgood, C.P., et al., *Deactivation of $Cu/ZnO/Al_2O_3$ Catalyst: Evolution of Site Concentrations with Time.* Topics in Catalysis, 2003. **22**(3/4): p. 253-259.

154. Jones, S.D., L.M. Neal, and H.E. Hagelin-Weaver, *Steam reforming of methanol using Cu-ZnO catalysts supported on nanoparticle alumina.* Applied Catalysis B: Environmental, 2008. **84**(3-4): p. 631-642.

155. Choi, Y. and H.G. Stenger, *Fuel cell grade hydrogen from methanol on a commercial $Cu/ZnO/Al_2O_3$ catalyst.* Applied Catalysis B: Environmental, 2002. **38**(4): p. 259-269.

156. Lindström, B. and L.J. Pettersson, *Deactivation of copper-based catalysts for fuel cell applications.* Catalysis Letters, 2001. **74**(1-2): p. 27-30.

157. Santacesaria, E. and S. Carrá, *Kinetics of catalytic steam reforming of methanol in a cstr reactor.* Applied Catalysis, 1983. **5**(3): p. 345-358.

158. Lee, J.K., J.B. Ko, and D.H. Kim, *Methanol steam reforming over $Cu/ZnO/Al_2O_3$ catalyst: kinetics and effectiveness factor.* Applied Catalysis A: General, 2004. **278**(1): p. 25-35.

159. Patel, S. and K.K. Pant, *Experimental study and mechanistic kinetic modeling for selective production of hydrogen via catalytic steam reforming of methanol.* Chemical Engineering Science, 2007. **62**(18–20): p. 5425-5435.

160. Takahashi, K., N. Takezawa, and H. Kobayashi, *The mechanism of steam reforming of methanol over a copper-silica catalyst.* Applied Catalysis, 1982. **2**(6): p. 363-366.

161. Tesser, R., M. Di Serio, and E. Santacesaria, *Methanol steam reforming: A comparison of different kinetics in the simulation of a packed bed reactor.* Chemical Engineering Journal, 2009. **154**(1–3): p. 69-75.

162. Busca, G., et al., *Hydrogen from alcohols: IR and flow reactor studies.* Catalysis Today, 2009. **143**(1-2): p. 2-8.

163. Jiang, C.J., et al., *Kinetic mechanism for the reaction between methanol and water over a Cu-ZnO-Al_2O_3 catalyst.* Applied Catalysis A: General, 1993. **97**(2): p. 145-158.

164. Jiang, C.J., et al., *Kinetic study of steam reforming of methanol over copper-based catalysts.* Applied Catalysis A: General, 1993. **93**(2): p. 245-255.

165. Jacobs, G. and B.H. Davis, *In situ DRIFTS investigation of the steam reforming of methanol over Pt/ceria.* Applied Catalysis A: General, 2005. **285**(1–2): p. 43-49.

166. Iwasa, N., et al., *Methanol synthesis from CO_2 under atmospheric pressure over supported pd catalysts.* Catalysis Letters, 2004. **96**(1-2): p. 75-78.

167. Iwasa, N., et al., *Effect of Zn addition to supported Pd catalysts in the steam reforming of methanol.* Applied Catalysis A: General, 2003. **248**(1–2): p. 153-160.

168. Rostrup-Nielsen, J., *Reaction kinetics and scale-up of catalytic processes.* Journal of Molecular Catalysis A: Chemical, 2000. **163**(1–2): p. 157-162.

169. Rostrup-Nielsen, J.R., J. Sehested, and J.K. Nørskov, *Hydrogen and synthesis gas by steam- and CO_2 reforming*, in *Advances in Catalysis*. 2002, Academic Press. p. 65-139.

170. Xu, J. and G.F. Froment, *Methane steam reforming, methanation and water-gas shift: I. Intrinsic kinetics.* AIChE Journal, 1989. **35**(1): p. 88-96.

171. Wei, J. and E. Iglesia, *Isotopic and kinetic assessment of the mechanism of reactions of CH_4 with CO_2 or H_2O to form synthesis gas and carbon on nickel catalysts.* Journal of Catalysis, 2004. **224**(2): p. 370-383.

172. Joensen, F. and J.R. Rostrup-Nielsen, *Conversion of hydrocarbons and alcohols for fuel cells.* Journal of Power Sources, 2002. **105**(2): p. 195-201.

173. Rostrup-Nielsen, J.R., *Conversion of hydrocarbons and alcohols for fuel cells.* Physical Chemistry Chemical Physics, 2001. **3**(3): p. 283-288.

174. Rostrup-Nielsen, J.R., *Production of synthesis gas.* Catalysis Today, 1993. **18**(4): p. 305-324.

175. Rostrup-Nielsen, J.R., L.J. Christiansen, and J.H. Bak Hansen, *Activity of steam reforming catalysts: Role and assessment.* Applied Catalysis, 1988. **43**(2): p. 287-303.

176. Abild-Pedersen, F., et al., *Methane activation on Ni(1 1 1): Effects of poisons and step defects.* Surface Science, 2005. **590**(2–3): p. 127-137.

177. Jones, G., et al., *First principles calculations and experimental insight into methane steam reforming over transition metal catalysts.* Journal of Catalysis, 2008. **259**(1): p. 147-160.

178. Bengaard, H.S., et al., *Steam reforming and graphite formation on Ni catalysts.* Journal of Catalysis, 2002. **209**(2): p. 365-384.

179. Goula, M., A. Lemonidou, and A. Efstathiou, *Characterization of carbonaceous species formed during reforming of CH_4 with CO_2 over Ni/CaO-Al_2O_3 catalysts studied by various transient techniques.* Journal of Catalysis, 1996. **161**(2): p. 626-640.

180. Borowiecki, T., A. Gołębiowski, and B. Stasińska, *Effects of small MoO_3 additions on the properties of nickel catalysts for the steam reforming of hydrocarbons.* Applied Catalysis A: General, 1997. **153**(1–2): p. 141-156.

181. Zhao, B., et al., *Synthesis of flower-Like NiO and effects of morphology on its catalytic properties.* The Journal of Physical Chemistry C, 2009. **113**(32): p. 14440-14447.

182. Yu, Z., et al., *Effect of catalyst preparation on the carbon nanotube growth rate.* Catalysis Today, 2005. **100**(3–4): p. 261-267.

183. Liguras, D.K., D.I. Kondarides, and X.E. Verykios, *Production of hydrogen for fuel cells by steam reforming of ethanol over supported noble metal catalysts.* Applied Catalysis B: Environmental, 2003. **43**(4): p. 345-354.

184. Rostrupnielsen, J.R. and J.H.B. Hansen, *CO_2-reforming of methane over transition metals.* Journal of Catalysis, 1993. **144**(1): p. 38-49.

185. McMinn, T.E., F.C. Moates, and J.T. Richardson, *Catalytic steam reforming of chlorocarbons: catalyst deactivation.* Applied Catalysis B: Environmental, 2001. **31**(2): p. 93-105.

186. Smith, D.J. and L.D. Marks, *Direct lattice imaging of small metal particles.* Philosophical Magazine A, 1981. **44**(3): p. 735-740.

187. Wei, J. and E. Iglesia, *Structural requirements and reaction pathways in methane activation and chemical conversion catalyzed by rhodium.* Journal of Catalysis, 2004. **225**(1): p. 116-127.

188. Souza, M.M.V.M., O.R. Macedo Neto, and M. Schmal, *Synthesis gas production from natural gas on supported Pt catalysts.* Journal of Natural Gas Chemistry, 2006. **15**(1): p. 21-27.

189. Yokota, S., K. Okumura, and M. Niwa, *Support effect of metal oxide on Rh catalysts in the CH_4-CO_2 reforming reaction.* Catalysis Letters, 2002. **84**(1-2): p. 131-134.

190. Keghouche, N., et al., *Radiation-induced synthesis of α-Al_2O_3 supported nickel clusters: Characterization and catalytic properties.* Radiation Physics and Chemistry, 2005. **74**(3–4): p. 185-200.

191. Wang, S. and G.Q.M. Lu, *CO_2 reforming of methane on Ni catalysts: Effects of the support phase and preparation technique.* Applied Catalysis B: Environmental, 1998. **16**(3): p. 269-277.

192. Matsumura, Y. and T. Nakamori, *Steam reforming of methane over nickel catalysts at low reaction temperature.* Applied Catalysis A: General, 2004. **258**(1): p. 107-114.

193. Zhang, Q.-H., Y. Li, and B.-Q. Xu, *Reforming of methane and coalbed methane over nanocomposite Ni/ZrO_2 catalyst.* Catalysis Today, 2004. **98**(4): p. 601-605.

194. Siswana, N.P., D.L. Trimm, and N.W. Cant. *Metal-support interactions in steam reforming*. in *Studies in Surface Science and Catalysis*. 1998. Elsevier.

195. Dong, W.-S., et al., *Methane reforming over Ni/Ce-ZrO2 catalysts: effect of nickel content.* Applied Catalysis A: General, 2002. **226**(1–2): p. 63-72.

196. Oh, Y.-S., et al., *A highly active catalyst, Ni/Ce–ZrO_2/θ-Al_2O_3, for on-site H_2 generation by steam methane reforming: pretreatment effect.* International Journal of Hydrogen Energy, 2003. **28**(12): p. 1387-1392.

197. Roh, H.-S., K.-W. Jun, and S.-E. Park, *Methane-reforming reactions over Ni/Ce-ZrO_2/θ-Al_2O_3 catalysts.* Applied Catalysis A: General, 2003. **251**(2): p. 275-283.

198. Bradford, M.C.J. and M.A. Vannice, *Catalytic reforming of methane with carbon dioxide over nickel catalysts I. Catalyst characterization and activity.* Applied Catalysis A: General, 1996. **142**(1): p. 73-96.

199. Kusakabe, K., et al., *Methane steam reforming over Ce–ZrO_2-supported noble metal catalysts at low temperature.* Fuel Processing Technology, 2004. **86**(3): p. 319-326.

200. Horiuchi, T., et al., *Suppression of carbon deposition in the CO_2-reforming of CH_4 by adding basic metal oxides to a Ni/Al_2O_3 catalyst.* Applied Catalysis A: General, 1996. **144**(1–2): p. 111-120.

201. Foletto, E.L., R.W. Alves, and S.L. Jahn, *Preparation of Ni/Pt catalysts supported on spinel ($MgAl_2O_4$) for methane reforming.* Journal of Power Sources, 2006. **161**(1): p. 531-534.

202. Borowiecki, T., et al., *Oxidation–reduction of Ni/Al_2O_3 steam reforming catalysts promoted with Mo.* Applied Catalysis A: General, 2004. **274**(1–2): p. 259-267.

203. Borowiecki, T., G. Giecko, and M. Panczyk, *Effects of small MoO_3 additions on the properties of nickel catalysts for the steam reforming of hydrocarbons: II. Ni-Mo/Al_2O_3 catalysts in reforming, hydrogenolysis and cracking of n-butane.* Applied Catalysis A: General, 2002. **230**(1–2): p. 85-97.

204. Takahashi, R., et al., *Addition of zirconia in Ni/SiO_2 catalyst for improvement of steam resistance.* Applied Catalysis A: General, 2004. **273**(1–2): p. 211-215.

205. Cheekatamarla, P.K. and C.M. Finnerty, *Reforming catalysts for hydrogen generation in fuel cell applications.* Journal of Power Sources, 2006. **160**(1): p. 490-499.

206. Choudhary, V.R., B.S. Uphade, and A.S. Mamman, *Large enhancement in methane-to-syngas conversion activity of supported Ni catalysts due to precoating of catalyst supports with MgO, CaO or rare-earth oxide.* Catalysis Letters, 1995. **32**(3-4): p. 387-390.

207. Jeong, J.H., et al., *Ru-doped Ni catalysts effective for the steam reforming of methane without the pre-reduction treatment with H_2.* Applied Catalysis A: General, 2006. **302**(2): p. 151-156.

208. Vaidya, P.D. and A.E. Rodrigues, *Kinetics of steam reforming of ethanol over a Ru/Al_2O_3 catalyst.* Industrial & Engineering Chemistry Research, 2006. **45**(19): p. 6614-6618.

209. Ishihara, A., et al., *Addition effect of ruthenium on nickel steam reforming catalysts.* Fuel, 2005. **84**(12–13): p. 1462-1468.

210. Craciun, R., W. Daniell, and H. Knözinger, *The effect of CeO_2 structure on the activity of supported Pd catalysts used for methane steam reforming.* Applied Catalysis A: General, 2002. **230**(1–2): p. 153-168.

211. De Rogatis, L., et al., *Methane partial oxidation on NiCu-based catalysts.* Catalysis Today, 2009. **145**(1–2): p. 176-185.

212. Rostrup-Nielsen, J.R., *Sulfur-passivated nickel catalysts for carbon-free steam reforming of methane.* Journal of Catalysis, 1984. **85**(1): p. 31-43.

213. Andersen, N.T., et al., *Statistical models for ensemble control by alloying and poisoning of catalysts: I. Mathematical assumptions and derivations.* Journal of Catalysis, 1987. **104**(2): p. 454-465.

214. Nishiyama, Y. and Y. Tamai, *Carbon formation on copper-nickel alloys from benzene.* Journal of Catalysis, 1974. **33**(1): p. 98-107.

215. Ponec, V. *Catalysis by alloys in hydrocarbon reactions*. in *Advances in Catalysis*. 1983. Academic Press.

216. Bernardo, C.A., I. Alstrup, and J.R. Rostrup-Nielsen, *Carbon deposition and methane steam reforming on silica-supported Ni-Cu catalysts.* Journal of Catalysis, 1985. **96**(2): p. 517-534.

217. McLeod, A.S. and L.F. Gladden, *Relating metal particle geometry to the selectivity and activity of supported-metal catalysts: A monte carlo study.* Journal of Catalysis, 1998. **173**(1): p. 43-52.

218. Alstrup, I., *A new model explaining carbon filament growth on nickel, iron, and Ni-Cu alloy catalysts.* Journal of Catalysis, 1988. **109**(2): p. 241-251.

219. Huang, T.-J., T.-C. Yu, and S.-Y. Jhao, *Weighting variation of water−gas shift in steam reforming of methane over supported Ni and Ni−Cu catalysts.* Industrial & Engineering Chemistry Research, 2005. **45**(1): p. 150-156.

220. Chen, J., et al., *Production of COx-free hydrogen and nanocarbon by direct decomposition of undiluted methane on Ni–Cu–alumina catalysts.* Applied Catalysis A: General, 2004. **269**(1–2): p. 179-186.

221. Takenaka, S., et al., *Methane decomposition into hydrogen and carbon nanofibers over supported Pd–Ni catalysts.* Journal of Catalysis, 2003. **220**(2): p. 468-477.

222. Li, Y., et al., *Simultaneous production of hydrogen and nanocarbon from decomposition of methane on a nickel-based catalyst.* Energy & Fuels, 2000. **14**(6): p. 1188-1194.

223. Alstrup, I. and M. Teresa Tavares, *The kinetics of carbon formation from CH_4 + H_2 on a silica-supported nickel catalyst.* Journal of Catalysis, 1992. **135**(1): p. 147-155.

224. Alstrup, I., et al., *Carbon formation on nickel and nickel-copper alloy catalysts.* 1998.

225. Kim, M.S., N.M. Rodriguez, and R.T.K. Baker, *The interaction of hydrocarbons with copper□nickel and nickel in the formation of carbon filaments.* Journal of Catalysis, 1991. **131**(1): p. 60-73.

226. Kim, M.S., N.M. Rodriguez, and R.T.K. Baker, *The role of interfacial phenomena in the structure of carbon deposits.* Journal of Catalysis, 1992. **134**(1): p. 253-268.

227. Echegoyen, Y., et al., *Thermo catalytic decomposition of methane over Ni–Mg and Ni–Cu–Mg catalysts: Effect of catalyst preparation method.* Applied Catalysis A: General, 2007. **333**(2): p. 229-237.

228. Echegoyen, Y., et al., *Hydrogen production by thermocatalytic decomposition of methane over Ni-Al and Ni-Cu-Al catalysts: Effect of calcination temperature.* Journal of Power Sources, 2007. **169**(1): p. 150-157.

229. Lázaro, M.J., et al., *Decomposition of methane over Ni-SiO2 and Ni-Cu-SiO2 catalysts: Effect of catalyst preparation method.* Applied Catalysis A: General, 2007. **329**(0): p. 22-29.

230. Suelves, I., et al., *Characterization of NiAl and NiCuAl catalysts prepared by different methods for hydrogen production by thermo catalytic decomposition of methane.* Catalysis Today, 2006. **116**(3): p. 271-280.

231. Moliner, R., et al., *Ni–Mg and Ni–Cu–Mg catalysts for simultaneous production of hydrogen and carbon nanofibers: The effect of calcination temperature.* International Journal of Hydrogen Energy, 2008. **33**(6): p. 1719-1728.

232. Li, J., et al., *Active Nb_2O_5-supported nickel and nickel–copper catalysts for methane decomposition to hydrogen and filamentous carbon.* Journal of Molecular Catalysis A: Chemical, 2004. **221**(1–2): p. 105-112.

233. Wang, H. and R.T.K. Baker, *Decomposition of methane over a Ni−Cu−MgO catalyst to produce hydrogen and carbon nanofibers.* The Journal of Physical Chemistry B, 2004. **108**(52): p. 20273-20277.

234. Sinfelt, J.H., J.L. Carter, and D.J.C. Yates, *Catalytic hydrogenolysis and dehydrogenation over copper-nickel alloys.* Journal of Catalysis, 1972. **24**(2): p. 283-296.

235. Sachtler, W.M.H. and P. Van Der Plank, *The role of individual surface atoms in chemisorption and catalysis by nickel-copper alloys.* Surface Science, 1969. **18**(1): p. 62-79.

236. Cadenhead, D. and N. Wagner, *Low-temperature hydrogen adsorption on copper-nickel alloys.* The Journal of Physical Chemistry, 1968. **72**(8): p. 2775-2781.

237. Hall, W.K. and P.H. Emmett, *The hydrogenation of benzene over copper–nickel alloys.* The Journal of Physical Chemistry, 1958. **62**(7): p. 816-821.

238. Sidjabat, O. and D.L. Trimm, *Nickel–magnesia catalysts for the steam reforming of light hydrocarbons.* Topics in Catalysis, 2000. **11-12**(1-4): p. 279-282.

239. Trimm, D.L., *The formation and removal of coke from nickel catalyst.* Catalysis Reviews, 1977. **16**(1): p. 155-189.

240. Bartholomew, C.H., *Carbon deposition in steam reforming and methanation.* Catalysis Reviews, 1982. **24**(1): p. 67-112.

241. Rostrup-Nielsen, J. and D.L. Trimm, *Mechanisms of carbon formation on nickel-containing catalysts.* Journal of Catalysis, 1977. **48**(1–3): p. 155-165.

242. Trimm, D.L., *Coke formation and minimisation during steam reforming reactions.* Catalysis Today, 1997. **37**(3): p. 233-238.

243. Trimm, D.L., *Catalysts for the control of coking during steam reforming.* Catalysis Today, 1999. **49**(1–3): p. 3-10.

244. Helveg, S., et al., *Atomic-scale imaging of carbon nanofibre growth.* Nature, 2004. **427**(6973): p. 426-429.

245. Takehira, K., et al., *Steam reforming of CH_4 over supported Ni catalysts prepared from a Mg–Al hydrotalcite-like anionic clay.* Physical Chemistry Chemical Physics, 2003. **5**(17): p. 3801-3810.

246. Numaguchi, T., K. Shoji, and S. Yoshida, *Hydrogen effect on α-Al_2O_3 supported Ni catalyst for steam methane reforming reaction.* Applied Catalysis A: General, 1995. **133**(2): p. 241-262.

247. Mărginean, P. and A. Olariu, *Effect of heat treatment on the properties of nickel/chromia and nickel/alumina catalysts.* Applied Catalysis A: General, 1996. **140**(1): p. 59-72.

248. Bartholomew, C.H., *Mechanisms of catalyst deactivation.* Applied Catalysis A: General, 2001. **212**(1–2): p. 17-60.

249. Wynblatt, P. and N.A. Gjostein, *Supported metal crystallites.* Progress in Solid State Chemistry, 1975. **9**(0): p. 21-58.

250. Armor, J.N. and D.J. Martenak, *Studying carbon formation at elevated pressure.* Applied Catalysis A: General, 2001. **206**(2): p. 231-236.

251. Beebe, T.P., et al., *Kinetics of the activated dissociative adsorption of methane on the low index planes of nickel single crystal surfaces.* The Journal of Chemical Physics, 1987. **87**(4): p. 2305-2315.

252. Rostrup-Nielsen, J.R., *Promotion by poisoning*, in *Studies in Surface Science and Catalysis*, H.B. Calvin and B.B. John, Editors. 1991, Elsevier. p. 85-101.

253. Cooper, B.J. and D.L. Trimm, *Carbon deposition from propylene on polycrystalline and single crystal iron.* Journal of Catalysis, 1980. **62**(1): p. 35-43.

254. Rostrup-Nielsen, J.R., *New aspects of syngas production and use.* Catalysis Today, 2000. **63**(2–4): p. 159-164.

255. Aparicio, L.M., *Transient isotopic studies and microkinetic modeling of methane reforming over nickel catalysts.* Journal of Catalysis, 1997. **165**(2): p. 262-274.

256. Alstrup, I., et al. *Promotion of steam reforming catalysts*. in *Studies in Surface Science and Catalysis*. 1998. Elsevier.

257. Rostrup-Nielsen, J.R., *Industrial relevance of coking.* Catalysis Today, 1997. **37**(3): p. 225-232.

258. Bartholomew, C.H., *Sintering kinetics of supported metals: new perspectives from a unifying GPLE treatment.* Applied Catalysis A: General, 1993. **107**(1): p. 1-57.

259. Sehested, J., et al., *Sintering of nickel steam-reforming catalysts: effects of temperature and steam and hydrogen pressures.* Journal of Catalysis, 2004. **223**(2): p. 432-443.

260. Sehested, J., *Four challenges for nickel steam-reforming catalysts.* Catalysis Today, 2006. **111**(1–2): p. 103-110.

261. Sehested, J., *Sintering of nickel steam-reforming catalysts.* Journal of Catalysis, 2003. **217**(2): p. 417-426.

262. Sehested, J., et al., *Sintering of nickel steam-reforming catalysts on $MgAl_2O_4$ spinel supports.* Journal of Catalysis, 2001. **197**(1): p. 200-209.

263. Campbell, C.T., S.C. Parker, and D.E. Starr, *The effect of size-dependent nanoparticle energetics on catalyst sintering.* Science, 2002. **298**(5594): p. 811-814.

264. Chen, D., et al., *Deactivation during carbon dioxide reforming of methane over Ni catalyst: microkinetic analysis.* Chemical Engineering Science, 2001. **56**(4): p. 1371-1379.

265. Yablonskii, G.v., et al., *Kinetic models of catalytic reactions*. 1991: Access Online via Elsevier.

266. Jarosch, K., T. El Solh, and H.I. de Lasa, *Modelling the catalytic steam reforming of methane: discrimination between kinetic expressions using sequentially designed experiments.* Chemical Engineering Science, 2002. **57**(16): p. 3439-3451.

267. Chalk, S.G., et al., *The US Department of Energy – investing in clean transport.* Journal of Power Sources, 1998. **71**(1–2): p. 26-35.

268. Irving, P., et al., *Catalytic micro-reactor systems for hydrogen generation*, in *Microreaction Technology*, M. Matlosz, W. Ehrfeld, and J. Baselt, Editors. 2001, Springer Berlin Heidelberg. p. 286-294.

269. Ahmed, S., et al., *A gasoline fuel processor designed to study quick-start performance.* Journal of Power Sources, 2006. **154**(1): p. 214-222.

270. Micromeritics, *AutoChem II 2920 Automated Catalyst Characterization System*, M.I. Corporation, Editor. 2006.

271. Webb, P., *Introduction to chemical adsorption analytical techniques and their applications to catalysis.* MIC Technical Publications, 2003.

272. Brunauer, S., P.H. Emmett, and E. Teller, *Adsorption of gases in multimolecular layers.* Contribution from the bureau of chemistry and soils and george washington university, 1938.

273. Condon, J.B., *Surface area and porosity determinations by physisorption: measurements and theory*. 2006, USA: Elsevier.

274. Gregg, S.J. and K.S.W. Sing, *Adsorption, surface area and porosity*. 1982, New York: Academic Press.

275. Sing, K.S.W., et al., *Reporting phhysisorption data for gas/solid systems with special reference to the determination of surface area and porosity.* Pure & App. Chem, 1984. **57**(4): p. 603-619.

276. Chorkendorff, I. and J.W. Niemantsverdriet, *Concepts of modern catalysis and kinetics*. 2007, Wiley-VCH.

277. HARRICK, *The praying mantis™ user's manual*. 2010, Harrick scientific products, INC.: New York.

278. NETZSCH, *Operating instructions TG 209 F1 iris*. NETZSCH-Gerätebau GmbH: Gemany.

279. Post, E., *Principles of TG, DSC, STA and EGA*, ed. N.G. GmbH. 2009, Germany: NETZSCH.

280. Agilent, *Agilent 7890A gas chromatograph-operating guide*. 2007, Agilent Technologies: USA.

281. Wang, C., *Parallel GC for complete refinery gas analysis- application hydrocarbon processing*. 2007, Agilent Technologies: USA.

282. Idem, R. and N. Bakhshi, *Production of hydrogen from methanol. 1. Catalyst characterization studies.* Ind. Eng. Chem. Res., 1994. **33**: p. 2047-2055.

283. Lua, A.C. and H.Y. Wang, *Decomposition of methane over unsupported porous nickel and alloy catalyst.* Applied Catalysis B: Environmental, 2013. **132–133**(0): p. 469-478.

284. Wang, L.-C., et al., *Production of hydrogen by steam reforming of methanol over Cu/ZnO catalysts prepared via a practical soft reactive grinding route based on dry oxalate-precursor synthesis.* Journal of Catalysis, 2007. **246**(1): p. 193-204.

285. Pérez-Hernández, R., et al., *Catalytic steam reforming of methanol to produce hydrogen on supported metal catalysts*. Hydrogen Energy - Challenges and Perspectives. 2012.

286. Shastri, A.G. and J. Schwank, *Metal dispersion of bimetallic catalysts via stepwise chemisorption and surface titration: I. Ru-AuSiO_2.* Journal of Catalysis, 1985. **95**(1): p. 271-283.

287. Batista, J., et al., *On the structural characteristics of γ-alumina-supported Pd–Cu bimetallic catalysts.* Applied Catalysis A: General, 2001. **217**(1–2): p. 55-68.

288. Chandler, B.D., et al., *Preparation and characterization of supported bimetallic Pt–Au particle catalysts from molecular cluster and chloride salt precursors.* Journal of Catalysis, 1999. **187**(2): p. 367-384.

289. Li, Y., Q. Fu, and M. Flytzani-Stephanopoulos, *Low-temperature water-gas shift reaction over Cu- and Ni-loaded cerium oxide catalysts.* Applied Catalysis B: Environmental, 2000. **27**(3): p. 179-191.

290. Skoda, F., et al., *Surface characterization of palladium-copper bimetallic catalysts by FTIR spectroscopy and test reactions.* Catalysis Letters, 1994. **29**(1-2): p. 159-168.

291. Fernández-García, M., J.A. Anderson, and G.L. Haller, *Alloy formation and stability in Pd-Cu bimetallic catalysts.* Journal of Physical Chemistry, 1996. **100**(40): p. 16247-16254.

292. Yao, C.-Z., et al., *Effect of preparation method on the hydrogen production from methanol steam reforming over binary Cu/ZrO_2 catalysts.* Applied Catalysis A: General, 2006. **297**(2): p. 151-158.

293. Shishido, T., et al., *Active Cu/ZnO and $Cu/ZnO/Al_2O_3$ catalysts prepared by homogeneous precipitation method in steam reforming of methanol.* Applied Catalysis A: General, 2004. **263**(2): p. 249-253.

294. Shishido, T., et al., *Production of hydrogen from methanol over Cu/ZnO and $Cu/ZnO/Al_2O_3$ catalysts prepared by homogeneous precipitation: Steam reforming and oxidative steam reforming.* Journal of Molecular Catalysis A: Chemical, 2007. **268**(1–2): p. 185-194.

295. Águila, G., et al., *A novel method for preparing high surface area copper zirconia catalysts: Influence of the preparation variables.* Applied Catalysis A: General, 2009. **360**(1): p. 98-105.

296. Oliveira, E.L.G., C.A. Grande, and A.E. Rodrigues, *Methane steam reforming in large pore catalyst.* Chemical Engineering Science, 2010. **65**(5): p. 1539-1550.

297. Seo, J.G., et al., *Effect of preparation method of mesoporous $Ni–Al_2O_3$ catalysts on their catalytic activity for hydrogen production by steam reforming*

of liquefied natural gas (LNG). International Journal of Hydrogen Energy, 2009. **34**(13): p. 5409-5416.

298. Sohlberg, K., S.J. Pennycook, and S.T. Pantelides, *Hydrogen and the structure of the transition aluminas.* Journal of the American Chemical Society, 1999. **121**(33): p. 7493-7499.

299. Ryczkowski, J., *IR spectroscopy in catalysis.* Catalysis Today, 2001. **68**(4): p. 263-381.

300. Edwards, J.F. and G.L. Schrader, *Infrared spectroscopy of copper/zinc oxide catalysts for the water-gas shift reaction and methanol synthesis.* The Journal of Physical Chemistry, 1984. **88**(23): p. 5620-5624.

301. Roh, H.-S., et al., *Highly active and stable Ni/Ce–ZrO_2 catalyst for H_2 production from methane.* Journal of Molecular Catalysis A: Chemical, 2002. **181**(1–2): p. 137-142.

302. Ye, J., et al., *Lanthanum modified Ni/γ-Al_2O_3 catalysts for partial oxidation of methane.* Journal of Rare Earths, 2006. **24**(3): p. 302-308.

303. Seo, J.G., et al., *Effect of calcination temperature of mesoporous alumina xerogel (AX) supports on hydrogen production by steam reforming of liquefied natural gas (LNG) over Ni/AX catalysts.* International Journal of Hydrogen Energy, 2008. **33**(24): p. 7427-7434.

304. Youn, M.H., et al., *Role and effect of molybdenum on the performance of Ni-Mo/γ-Al_2O_3 catalysts in the hydrogen production by auto-thermal reforming of ethanol.* Journal of Molecular Catalysis A: Chemical, 2007. **261**(2): p. 276-281.

305. Lee, J.-H., et al., *Stabilization of Ni/Al_2O_3 catalyst by Cu addition for CO_2 reforming of methane.* Applied Catalysis A: General, 2004. **269**(1–2): p. 1-6.

306. Faungnawakij, K., R. Kikuchi, and K. Eguchi, *Thermodynamic evaluation of methanol steam reforming for hydrogen production.* Journal of Power Sources, 2006. **161**(1): p. 87-94.

307. Matsumura, Y. and H. Ishibe, *High temperature steam reforming of methanol over Cu/ZnO/ZrO_2 catalysts.* Applied Catalysis B: Environmental, 2009. **91**(1–2): p. 524-532.

308. Shaikhutdinov, S.K., et al., *Coprecipitated Ni.Al and Ni.Cu.Al catalysts for methane decomposition and carbon deposition I. Genesis of Calcined and reduced catalysts.* Applied Catalysis A: General, 1995. **126**(1): p. 125-139.

309. Ponec, V., *Selectivity in the syngas reactions: The role of supports and promoters in the activation of CO and in the stabilization of intermediates*. Studies in Surface Science and Catalysis. Vol. Volume 64. 1991: Elsevier. 117-157.

310. Schwank, J., *Bimetallic catalysts for CO activation*, in *Studies in Surface Science and Catalysis*. 1991, Elsevier. p. 225-264.

311. Ponec, V. and G.C. Bond, *Catalysis by metals and alloys*. Vol. 95. 1995: Elsevier.

312. Ferrando, R., J. Jellinek, and R.L. Johnston, *Nanoalloys: From theory to applications of alloy clusters and nanoparticles.* Chemical Reviews, 2008. **108**(3): p. 845-910.

313. Idem, R.O. and N.N. Bakhshi, *Production of hydrogen from methanol. 2. Experimental studies.* Industrial & Engineering Chemistry Research, 2002. **33**(9): p. 2056-2065.

314. Baker, R.T.K., *Catalytic growth of carbon filaments.* Carbon, 1989. **27**(3): p. 315-323.

315. Kuijpers, E.G.M., et al., *The reversible decomposition of methane on a $NiSiO_2$ catalyst.* Journal of Catalysis, 1981. **72**(1): p. 75-82.

316. Matsukata, M., T. Matsushita, and K. Ueyama, *A novel hydrogen/syngas production process: Catalytic activity and stability of $NiSiO_2$.* Chemical Engineering Science, 1996. **51**(11): p. 2769-2774.

317. Sasaki, K. and Y. Teraoka *Equilibria in Fuel Cell Gases: I. Equilibrium compositions and reforming conditions.* Journal of The Electrochemical Society, 2003. **150**(7): p. A878-A884.

318. Barin, I., *Thermochemical data of pure substances*. 1995, VCH Publishers: Weinheim